SYNTHESIS OF POTENTIAL NEW CONTRAST AGENTS FOR APPLICATIONS ACROSS MULTIPLE IMAGING MODALITIES

Emilie Marie Sophie Patit-Tha Brun

Thesis submitted to the University of Ottawa
in partial Fulfillment of the requirements for the Degree of

Doctorate in Philosophy in Chemistry

Department of Chemistry and Biomolecular Sciences

Faculty of Science

University of Ottawa

Supervisor: Adam J. Shuhendler, PhD
Co-Supervisor: Cory Harris, PhD

Examining Board: Jaclyn Brusso, PhD, Chemistry and Biomolecular Sciences
Gerd Melkus, PhD, Radiology
Benjamin Rotstein, PhD, Biochemistry, Microbiology and Immunology

External Examiner: Eric Price, BSc, PhD, Department of Chemistry, University of Saskatchewan

ABSTRACT

The imaging field comprises a wide array of techniques, driving the creation and innovation of contrast agents and probes. The increasing prevalence of diseases and the detection of new conditions have driven the development and adjustment of contrast agents to aid in detection, treatment and the improvement of patient outcomes. Magnetic resonance imaging (MRI) is a non-invasive imaging technique known for producing high-resolution images. To enhance resolution and improve image visualization, contrast agents can be employed to assist in the detection and diagnosis of diseases such as tumors or cancers. This thesis explores the development and application of multiple imaging modalities through the creation of diverse probes designed for specific diagnostic and therapeutic applications. The research focuses on the design, synthesis and characterization of various imaging probes, each optimized for techniques such as MRI, chemical exchange saturation transfer (CEST)-MRI, magnetic resonance fingerprinting (MRF) and optical imaging. We have identified and characterized a hydrazone-CEST MRI probe capable of mapping vitamin B_6 metabolism, with applications in lung cancer models. Additionally, we have developed a novel method for combining two lanthanides within the same complex to test their potential as gadolinium-based contrast agents in MRI and MRF imaging, as well as in optical imaging, using the emissive properties of europium(III). Building on this chemistry, the plan was to incorporate the radioisotope lutetium-177 into our complex for potential future application as a targeted radionuclide therapy agent against glioblastoma. Furthermore, we attempted to develop a THC-based probe for both Δ^8 and Δ^9 isomers to assess their ability to track biodistribution within the endocannabinoid system and their receptors engagement. This research contributes to the advancement of medical imaging technologies by demonstrating the adaptability and effectiveness of multiple imaging modalities and the designed probes for each application.

Dedication

To my Bon-Papa, Dr Philippe Brun.

Acknowledgements

The realization of this thesis would not have been possible without my amazing supervisor Dr Adam Shuhendler. Five years ago, you took a chance on a non-English-speaking French student and you were one of the few who believed in me. You gave me the opportunity to be where I am today and helped me grow into the scientist I always wanted to be. A few lines are not enough to express my deepest gratitude and respect for you. Even if you think I am angry all the time, I just want to say thank you for bringing me where I am today.

I would also like to thank my co-supervisor, Dr Cory Harris, who helped me during this thesis, and shared his knowledge about plants and cannabis specifically. Your guidance in the plant field has been invaluable.

I extend my heartfelt thanks to all my lab mates, and past members, especially Aidan, Dominic, Claudia, Clara, Reda and Halimo, for their collaboration and for creating a stimulating and fun work environment. Our lab has expanded over the years, but your support and our tea times make this PhD journey less stressful (if it's possible) and helped me to come to the lab every day.

My parents, Mae Lek and Patrice, I can never be grateful enough for all the support and love you have provided me throughout my life. You have always pushed me to be better and discover the world. Xavier and Isabelle, thank you for encouraging me to learn English. I wouldn't be in Canada or have the opportunities I had without your support.

And last but not least, to my wonderful husband, Jérôme Fromaget, who already had an extra name to my list, thank you ! You have supported me more than a decade now with your constant motivation and belief in me. I wouldn't been able to do this without you by my side.

Table of Contents

List of Figures

List of Tables

List of Symbols, Nomenclature and Abbreviations

2-AG – 2-Arachidonoyl Glycerol

2-HYNIC – 2 Hydrazinonicotinic Acid

%MTRasym – Percentage Magnetization Transfer Ratio Asymmetry

5-HT3A – Serotonin 3A Receptor

AA – Arachidonic Acid

AEA – *N*-Arachidonoylethanolamine

Alloc – Allyloxycarbonyl

APT – Amide Proton Transfer

BBr_3 – Boron Tribomide

BF_3/Et_2O – Boron Trifluoride Etherate

BMI – Body Mass Index

CB – Cannabinoid Receptor

CBD – Cannabidiol

$CDCl_3$ – Deuterated Chloroform

CDDP – Cis-Diammine-Platinum (II) Dichloride

CEST – Chemical Exchange Saturation Transfer

CHQ – 2-cyano-6-hydroxyquinoline

CNS – Central Nervous System

CT – Computed Tomography

CuAAC – Copper(I)-catalyzed Alkyne-Azide Cycloaddition

CV – Column Volume

D_2O – Heavy Water

DBCO – Dibenzocyclooctyne

DCM – Dichloromethane

DiaCEST – Diamagnetic CEST

DIPEA – N,N-Diisopropylethylamine

DMEM – Dulbecco's Modified Eagle Medium

DMF – Dimethylformamide

DMSO-D_6 – Deuterated Dimethyl Sulfoxide

DOTA – 1,4,7,10-tetraazacyclododecane-*N*,*N'*,*N''*,*N'''*-tetraacetic acid

DTPA – Diethylenetriaminepentaacetic acid

DTT – Dithiothreitol

Dy(III) – Dysprosium(III)

ECS – Endocannabinoid System

EI – Electron Impact

Er(III) – Erbium(III)

ESI – Electrospray Ionisation

Et_2O – Diethyl Ether

EtOAc – Ethyl Acetate

Eu(III) – Europium(III)

FA – Flip Angle

FAAH – Fatty Acid Amide Hydrolase

FBS – Fetal Bovine Serum

FCC – Flash Column Chromatography

FDG – Fluorodeoxyglucose

FID – Free Induction Decay

FMN – Flavin Mononucleotide

FOV – Field of View

GAG – Glycosaminoglycan

GBCA – Gadolinium-Based Contrast Agent

GBM – Glioblastoma Multiforme

Gd(III) – Gadolinium(III)

GPCR – G-Protein-Coupled Receptor

HBTU – Hexafluorophosphate Benzotriazole Tetramethyl Uronium

HCl – Hydrochloric Acid

Ho(III) – Holmium(III)

HOBt – 1-Hydroxybenzotriazole

HPLC – High Performed Liquid Chromatography

HRMS – High-Resolution Mass Spectrometry

IR-bSSFP – Inversion-Recovery balanced Steady State Free-Precession

K_2CO_3 – Potassium Carbonate

KF – Potassium Fluoride

LC-MS – Liquid Chromatography-Mass Spectrometry

Lu(III) – Lutetium(III)

MAG – Monoacylglycerol lipase

MeOH – Methanol

Mp – Melting Point

MRF – Magnetic Resonance Fingerprinting

MRI – Magnetic Resonance Imaging

MT – Magnetization Transfer

Na_2SO_4 – Sodium Sulfate

NA^3 – *N*-Amino Anthranilic Acid

NaI – Sodium Iodide

$NaHCO_3$ – Sodium Bicarbonate

NaOD – Sodium Deuteroxide

NETs – Neuroendocrine Tumors

NMR – Nuclear Magnetic Resonance

NSF – Nephrogenic Systemic Fibrosis

PA – Pyridoxic Acid

PARACEST – Paramagnetic Chemical Exchange Saturation Transfer

PBS – Phosphate Buffer Saline

$Pd(PPh_3)_4$ – Tetrakis(triphenylphosphine)palladium

PDXK – Pyridoxal Kinase

PDXP – Pyridoxal Phosphatase

PET-CT – Positron Emission Tomography-Computed Tomography

PL – Pyridoxal

PLP – Pyridoxal 5'-Phosphate

PN – Pyridoxine

PNPO – Pyridoxine 5'-Phosphate Oxidase

ppm – Parts Per Million

PPRγ – Peroxisome Proliferator-activated Receptor γ

PRE – Paramagnetic Relaxation Enhancement

PSMA – Prostate Specific Membrane Antigen

p-TSA – p-Toluenesulfonic Acid

RARE – Refocused Echoes

RF – Radiofrequency

ROI – Region Of Interest

ROS – Reactive Oxygen Species

RT – Room Temperature

SNR – Signal-to-Noise Ratio

SPAAC – Strain-Promoted Azide Alkyne Cycloaddition

SPECT – Single Photon Emission Computed Tomography

ST – Saturation Transfer

Tb(III) – Terbium(III)

TBAF – Tetra-n-butylammonium Fluoride

TE – Echo Time

TFA – Trifluoroacetic Acid

THC – Tetrahydrocannabinol

THCA – Tetrahydrocannabinolic acid

THF – Tetrahydrofuran

TLC – Thin-Layer Chromatography

Tm(III) – Thulium(III)

TMS – Tetramethylsilane

TMSCl – Trimethylsilyl Chloride

TPN1 – Thyamine Pyrophosphate Carrier 1

TR – Repetition Time

TRPV – Transient Receptor Potential Vanilloid

TRT – Targeted Radionucide Therapy

UPLC-HILIC-Z-ESI – High Performance Hydrophilic Interaction Liquid Interaction-ESI

US – UltraSound

WASSR – Water Saturation Shift Referencing

Yb(III) – Ytterbium(III)

Chapter 1: Introduction

1.1. Molecular imaging modalities

1.1.1. Origins

The field of medical diagnostic imaging began at the end of the 19th century, in 1895, when Wilhem Conrad Röntgen produced one of the first images of the inside of a live human body using X-rays [1, 2]. By penetrating solid object and revealing internal structures, with a Crookes cathode ray tube, Röntgen's discovery transformed the fields of physics and medicine. With the first Nobel Prize in Physics in 1901 [3, 4] he provided a non-invasive way to visualize the human body, which leads to the development of various imaging tools based on X-rays or the introduction of new technologies over the following century. This include computed tomography (CT), single photon emission computed tomography (SPECT), ultrasound (US) and magnetic resonance imaging (MRI) [5].

One of the most significant advancement was computed tomography (CT), introduced by Godfrey Hounsfield and Allan M. Cormarck [6]. CT is considered as a sectional imaging technique because it employs tomography, allowing for a fast and precise representation of the anatomy. CT scans use X-rays to create detailed cross-sectional images of the body [7]. By applying a computed reconstruction algorithm to two dimensional radiographs taken from many different directions, CT provides three-dimensional images of the object [8, 9].

On the other hand, single photon emission computed tomography (SPECT) is recognized as an nuclear medicine technique based the utilization of nuclides which decay by emitting single

gamma rays [5]. This technique generates images that illustrates the three-dimensional distribution of an administered radiotracer [10] offering insights about the blood flow, metabolism and other physiological processes [11].

Compared to some imaging techniques, ultrasound (US) imaging is a non-invasive and radiation free method that creates images of internal biological tissues using high-frequency sound waves. These sound waves are generated by converting electrical energy through a transducer [12]. This imaging technique is widely used in medical fields such as obstetrics [13, 14], cardiology [15] or abdominal imaging [16].

One major innovation was magnetic resonance imaging (MRI), developed more than 50 years ago. It is a non-invasive and versatile imaging method [17] that uses strong magnetic field to produce high-resolution images of the body's internal structures [5] and to investigate human anatomy, physiology and pathophysiology [18]. Its capacity to differentiate between various types of tissues and provided detailed images makes it indispensable in diagnosing a wide range of conditions, from cancers [19, 20] to neurological injuries [21, 22] or following disease progression [23, 24].

Nowadays, medical imaging becomes crucial for improving patient outcomes by enabling accurate and early diagnosis, guiding specialized treatments plans and supporting minimally invasive procedures [25]. Imaging enhances patient safety by offering non-invasive options and identifying potential risks before procedures. Overall, medical imaging contributes to more effective and high-quality patient care, ultimately improving prognoses and quality of life for the patient [25, 26].

1.1.2. Magnetic Resonance Imaging

Magnetic resonance imaging (MRI), developed in 1973 by Paul Lauterbur [27], is a medical application of nuclear magnetic resonance (NMR) based on the magnetic resonance of water protons through a powerful magnet and radiofrequency (RF) energy [17, 18]. The abundance of water protons in various tissues allows the visualization of mobile hydrogen nuclei and their distribution throughout the body. Due to their high sensitivity and concentration in the body, water protons are the primary imaging target, providing the highest contrast when excited [28]. Protons are characterized by a spin angular momentum and magnetic properties which make them in constant movement around their axes [29]. When exposed to an external magnetic field (B_0), protons will align either parallel or anti-parallel to this field, acting like magnetic dipoles. The parallel alignment to B_0 corresponds to a lower energy state while the anti-parallel alignment corresponds to a higher energy state. Although these two populations of protons are almost equally populated, the remaining population difference results in a net bulk magnetization vector (M_z) that aligned parallel to B_0 [30].

The frequency at which protons, or spins, rotate around the direction of the external magnetic field is defined as the Larmor frequency, or resonance frequency, which is proportional to the strength of the magnetic field [31]. This net magnetization vector does not produce a measurable signal on its own. Therefore, a radiofrequency energy pulse (B_1) at the Larmor frequency is applied perpendicular to B_0. This pulse causes the protons to absorb energy, inducing a transition between the two energy levels [5]. Protons are stimulated and disrupted, forcing them to realign with the static magnetic field B_0 at specific angles, known as flip angles, typically 90º or 180º [29, 30]. When the radiofrequency pulse is turned off, protons returns to their original alignment with the magnetic

field, which is called relaxation (Figure 1.1), and release electromagnetic energy known as free induction decay (FID). Several RF pulses are applied to generate multiple FID, which are then averaged to improve the signal-to-noise ratio (SNR). Different types of images can be generated by changing the sequence of RF pulses applied [29].

Images of the internal structures of the body are created through variations in the magnetic field strength across space, known as gradients. These gradients determine the location of signals within the body. The use of magnetic field gradients enable precise spatial encoding of the signals emitted by protons [29]. These gradients, generated by specialized gradient coils, vary the magnetic field linearly within the imaging volume. This allows for the selection of specific slices and the encoding of spatial information along different axes [29]. Slice-selective excitation is based on the selective excitation of spins in a well-defined slice of tissue or section of the body within the imaging volume [31]. By varying the magnetic field along an axis perpendicular to the chosen slice plane, only protons in the specific slice will resonate at the frequency of the applied RF pulse [31]. To obtain information from the individual pixels in a slice, phase and frequency encoding gradients are used. Phase encoding occurs between the application of the RF excitation pulse and the readout of the signal. This involves a short, temporary change in the magnetic field, causing a phase shift of the spinning protons. This phase shift, which depends on the duration of the gradient application, provides spatial information [30, 32]. However, to differentiate between pixels with the same phase encoding, a frequency encoding gradient can be used. The application of this gradient causes a shift in the resonance frequency of the protons, leading to different precessional frequencies and enabling the distinction between protons [30]. The data collected through these processes are stored in a format called k-space [31], which can be transformed into an image using Fourier transformation [30].

The echo time (TE) corresponds to the amount of time between the application of the radiofrequency pulse and the centered peak of the received echo signal. The repetition time (TR), on the other hand, corresponds to the repetition time interval between multiple application of 90º RF pulse to the same slice [32]. Both parameters, measured in milliseconds, will affect the relaxation time of the tissues, influencing the contrast of the image. Fourier transformation is applied to the averaged FID signals to generate the MRI image or frequency spectrum [29]. Two types of relaxation processes can be observed: longitudinal (T_1) and transverse (T_2) relaxation.

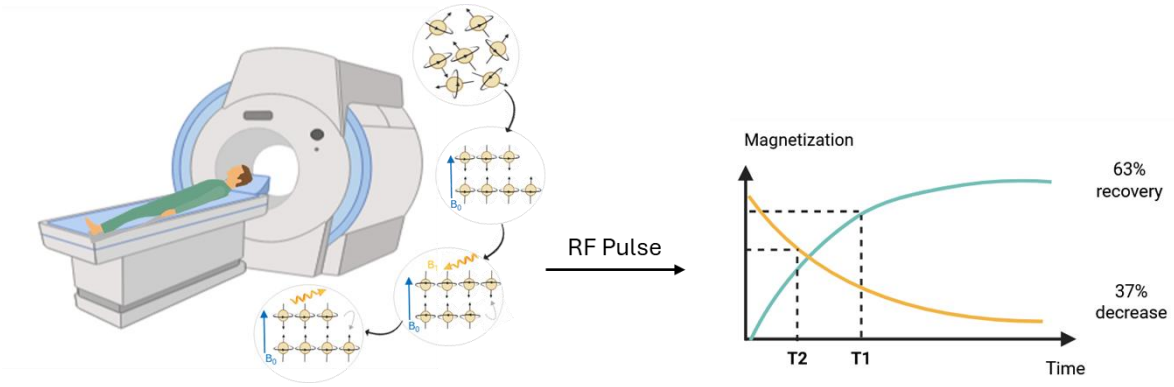

Figure 1.1 Overview of the MRI principle. Protons align with the magnetic field (B_0), are excited by an RF pulse (B_1), and emit signals during relaxation, characterized by T_1 and T_2 times, which are processed to form images.

T_1, or spin-lattice relaxation, involves the realignment of the longitudinal magnetization with the external magnetic field after being disturbed by a radiofrequency pulse. Once the radiofrequency pulse is turned off, the excited protons begin to return to their lower energy state by releasing the excess of energy absorbed from the RF pulse [30]. This energy is transferred to the

surrounding molecular environment, known as lattice, which includes the surrounding molecules and the overall thermal environment of the tissue [33]. As the protons return to their lower energy state, the longitudinal component of the net magnetization M_z recovers exponentially. This recovery is characterized by the time constant T_1, which varies depending on the tissue type. Tissues with shorter T_1 relaxation times recover their longitudinal magnetization more quickly, while those with longer T_1 times recover more slowly [32]. T_1-weighted images are generated by using short TR and TE values. Using a shorter TR limits the recovery of the longitudinal magnetization, which amplifies the contrast differences between tissues with different T_1 relaxation times. In contrast, a longer TR allows the longitudinal magnetization to fully recover between spins excitation states, leading to a contrast that is only based on the water proton density present in the tissue [32].

T_2, or spin-spin relaxation, involves the decay of the transverse magnetization of protons after being excited by an RF pulse. Initially, the excited protons spin at their Larmor frequency. However, due to interactions between neighboring spins, spin-spin interactions, and minor differences in the local magnetic field, these protons begin to lose their phase coherence. This dephasing leads to a gradual decline in the transverse magnetization over time. This decay is characterized by the time constant T_2 [32, 34], which is always shorter than the T_1 time, although it varies among different tissues [30]. On the other hand, T_2-weigthed images are generated by using longer TE and TR values. The contrast in images is obtained by increasing the TE value, which allows more time for the transverse magnetization to decay. This enhances the contrast between tissues with different T_2 relaxation times but similar proton densities [32].

1.2. Advanced imaging techniques

1.2.1. Magnetic Resonance Fingerprinting

While magnetic resonance imaging is considered as a qualitative imaging technique, magnetic resonance fingerprinting (MRF) is designated as a multiparametric quantitative tissue characterization technique [35]. MRF uses a pseudorandomized acquisition process to capture the unique signal evolution of each voxel, also known as "fingerprint" or voxel fingerprinting, from various materials or tissues. These fingerprints are generated using the inversion recovery balanced steady state free-precession (IR-bSSFP), which enhances tissue contrast, allowing differentiation between various tissue types, and achieves a high signal-to-noise ratio by maintaining a steady state of magnetization. The fingerprints are sensitive to T_1, T_2 and static magnetic field B_0 inhomogeneity [36].

Unlike traditional MRI, which reconstructs images by repeating the same acquisition parameters over time, MRF continuously varies parameters like flip angle (FA), phases of RF pulses, echo time (TE), repetition time (TR) during the scanning process [37]. This variation generates a specific signal for each tissue [38], enabling the examination of multiple magnetic resonance parameters in a single scan [39]. The generated fingerprints are then compared to a pre-computed library of simulated signal evolutions, known as the dictionary. These signal evolutions represent the expected responses of different tissues to the varied acquisition parameters used in MRF. Each entry in the dictionary corresponds to a unique combination of tissue properties, including proton density and T_1/T_2 relaxation times [37]. When a match is found through a pattern recognition algorithm that predict spin behavior and signal evolution during the acquisition, the

tissue properties used to create the simulated fingerprint are recognized as the actual properties of the tissue in that specific voxel. This process provides both quantitative and anatomic information [38].

Due to its ability to provide quantitative tissue characterization, MRF possesses a wide range of applications, including cardiovascular imaging. For example, cardiac MRF has been used to quantify T_1 and T_2 relaxation times in the myocardium [40] and to study patients with nonischemic cardiomyopathy [41]. Relaxometries values of T_1 and T_2 have been estimated through MRF for different brain regions in both men and women of various ages, revealing regional differences in the brain [42]. MRF has also been applied in the detection of different intra-axial brain tumors, such as gliomas and metastases, suggesting its potential as a quantifiable diagnostic tool [43]. Despite being a recent imaging method, MRF has found applications in multiple areas, including the diagnosis of epilepsy [44] or the identification of high-grade prostate cancers [45]. All these application require the generation of specific parameters and dictionaries to adapt the analysis to the tested conditions. This adaptation ensures that the quantitative maps generated by MRF are clinically relevant and provide meaningful information for diagnosis and treatment planning.

1.2.2. Chemical Exchange Saturation Transfer

Considered as a novel MRI contrast mechanism, chemical exchange saturation transfer (CEST) was first introduced by Wolff and Balaban in 1989 with the principle of magnetization transfer [46]. It provides more metabolic information compared to clinical imaging techniques by indirect detection of lowly-concentration labile protons [47]. Compared to MRI, which obtained signals by exciting bulk water protons, CEST is based on the saturation of exchangeable protons. These protons exchange between exogenous, introduced as contrast agents, or endogenous, present in tissues, molecules and bulk water, resonating at different frequencies [48, 49]. The labile protons are located on functional groups of molecules, such as amines, amides, alcohols or guanidinium protons [17]. Since CEST depends on the contrast agent environment, the CEST effect is dependent on different physiological parameters like pH [50, 51], enzyme activity [52], concentration or temperature [48]. Saturation transfer (ST) is induced by a long, weak, off resonance RF pulse targeted at the Larmor frequency [48] through a process called magnetization transfer (MT). This process induced a decrease of magnetization and, consequently, the water signal. For CEST to be effective, the equilibrium exchange rate (k_{ex}) must be equal to or smaller than the chemical shift difference (Δ_{CS}) between solvent (water) and solute (CEST contrast agent), i.e., $k_{ex} < \Delta_{CS}$ [53, 54].

A representation of the remaining signal intensity of water protons as a function of the frequency offset of the applied RF saturation pulse ($\Delta\omega$), which is the difference in frequency between the saturation pulse and the resonance frequency of water protons, is defined by the Z-spectrum or CEST spectrum (Figure 1.2A) [28]. The Z-spectrum is a plot of S_{sat}/S_0 where S_{sat} is water signal intensity with saturation, and S_0, water signal intensity without saturation [48]. In the Z-spectrum, an intense peak corresponds to the direct saturation of the bulk water signal, while other

peaks represent the CEST signal of the studied contrast agent [17]. Once the Z-spectrum indicates a reduction in the water signal intensity, it is considered as a negative contrast mechanism. Therefore, a smaller Z value suggests a stronger CEST effect [17, 55].

The direct water saturation effect refers to the reduction in the water signal intensity caused by the direct application of the RF saturation pulse to water protons [56] which can interfere with the detection of CEST signals. To address this issue, a magnetization transfer ratio asymmetry (MTR_{asym}) analysis is performed (Figure 1.2B). MTR_{asym} uses the symmetry of the direct saturation around the water frequency [28, 56]. The signal intensities are designated as S_{sat} (-Δω) and S_{sat} (+Δω) obtained by saturating frequencies Δω downfield and upfield from the water proton resonance frequency, respectively [28, 57].

$$MTR_{asym} = \frac{S_{sat}\,(-\Delta\omega) - S_{sat}\,(+\Delta\omega)}{S_0}$$

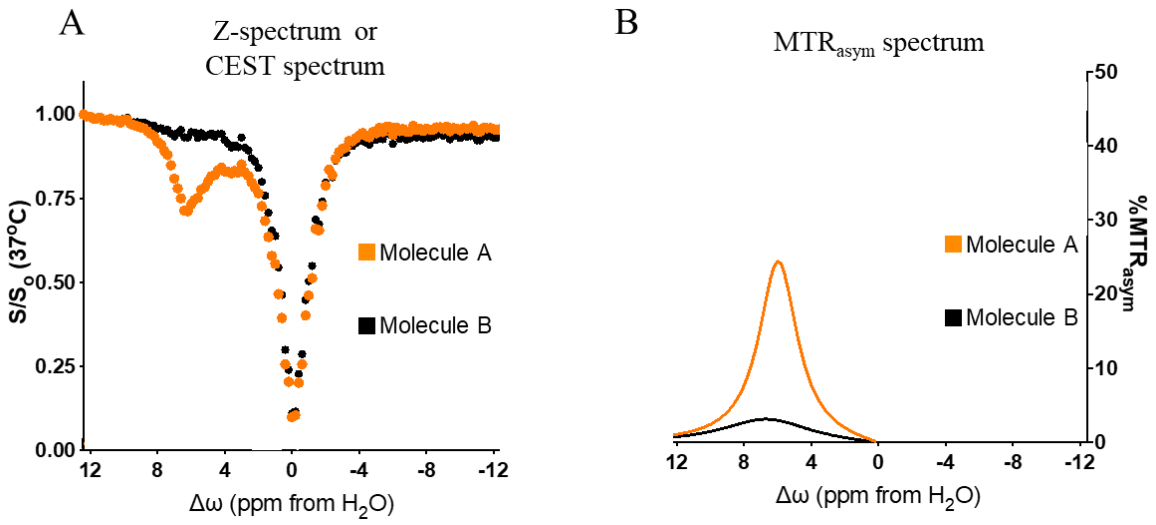

Figure 1.2 Schematic diagram of chemical exchange saturation transfer. (A) Z-spectrum or CEST spectrum representing the signal from two different molecules (A & B) (~ 6 ppm) and the water peak (0 ppm). (B) MTR_{asym} spectrum represented by the magnetization transfer ratio asymmetry analysis of the CEST spectrum to remove the side effect of the direct water saturation.

The exchangeable protons from CEST agents can be classified into two types: paramagnetic CEST (paraCEST) agents, which incorporate paramagnetic ions like lanthanides and can shift the labile proton signal from the bulk water resonance by tens to hundreds of ppm [58], and diamagnetic CEST (diaCEST) agents, which include -NH, $-NH_2$, or -OH groups. These agents present a chemical shift difference (Δ_{CS}) of less than 10 ppm from water [53, 58]. One well-known type of diaCEST is amide proton transfer (APT), which relies on the chemical exchange between bulk water protons and amide groups in proteins and peptides overexpressed in some type of cancers [28]. APT has been useful in detecting and characterizing different cancers, such as breast cancer [59], bladder cancer [60], brain tumors [61] or determining the histological grade of rectal cancer [62], for examples.

On the other hand, amino acids, including peptides, contain amine protons that can be considered as diaCEST agents. This is the case of glutamate, an abundant neurotransmitter in the central nervous system, which can provide information for neurological studies and neurodegenerative diseases [28]. Applications of glutamate as a diaCEST agent include research on Alzheimer's [63], Parkinson's [64], Huntington's [65] diseases, or even schizophrenia [66], making it an ideal diaCEST agent for neurological research or disease diagnosis. Another diaCEST amino agent can be creatinine, a derivative amino acid synthesized in the liver, kidneys, and pancreas. Creatinine is considered as an interesting biomarker in muscle physiology [67, 68].

Even though some metabolites have chemical shifts close to water, they have been studied as diaCEST agents for their hydroxyl protons. Examples include glucose, glycogen and glycosaminoglycans (GAGs) [28]. Glucose uptake and metabolism [69] can be tracked with glucoCEST, particularly in cancers such as the head and neck cancer [70], or breast cancer [71]. GlycoCEST can be used for diagnosing and monitoring glycogen metabolism disorders [57], including conditions like obesity, insulin resistance and type 2 diabetes with abnormal glycogen levels [48]. Additionally, hydroxyl proton diaCEST imaging can detect cartilage damage and degeneration, like osteoarthritis, using GagCEST [72], [73]. In this context, GAG quantification serves as a potential biomarker for osteoarthritis [57].

1.3. Lanthanides in medicine

1.3.1. Lanthanide-Based Contrast Agents

MRI presents a relatively low sensitivity compared to other imaging techniques, estimated in the higher micromolar range. To improve the visualization of some tissue, studies have demonstrated that the injection of contrast agents, particularly paramagnetic metal ions such as lanthanides, enhances the intensity of water proton signals between voxels [74]. Chelated to avoid toxicity from free lanthanides ions, some examples like Gd-DTPA-BMA and Dy-DTPA-BMA agents demonstrated to be efficient contrast agent for cardiac and cerebral imaging [75]. For *in vivo* application, lanthanides (III) must have high thermodynamic and kinetic stability to ensure that the complex remains intact and functional in the body. This is why lanthanides(III) ions need to bind to organic ligand with seven or eight coordination sites, like for example DTPA (diethylenetriaminepentaacetic acid), a heptadentate ligand, or DOTA (1,4,7,10-tetraazacyclododecane-*N*,*N'*,*N''*,*N'''*-tetraacetic acid), an octadentate ligand [76]. Lanthanides(III) ions, comprising 15 different metals, are considered paramagnetic due to the presence of one to seven unpaired electrons in their *4f* orbitals, except for lanthanum(III) and lutetium(III). This electronic configuration contributes to the magnetic properties of the metal ion [76, 77]. Paramagnetic lanthanides can be categorized in two classes: gadolinium-based contrast agent (GBCA), which enhance the longitudinal relaxation rate of water protons, and CEST agents, which reduce water signal by transferring saturated magnetization from exchangeable protons [74, 58].

GBCAs, used in clinical MRI since 1988 with the first gadolinium(III) (Gd) DTPA complex (Magnevist ®) [78, 79], are based on the chelation of gadolinium(III) ions in a +3-oxidation state that

binds to water molecule. Known for its strong paramagnetic properties, Gd(III) shortens both T_1 and T_2 relaxation times [17]. To measure how effectively a contrast agent, like GBCA, decreases T_1 or T_2 relaxation times of water protons as a function of Gd(III) concentration, the longitudinal relaxivity r_1 or transverse relaxivity r_2 are used [17]. Those parameters, measured in $mM^{-1}.s^{-1}$, represent the increase in the relaxation rate $R_{1/2}$ (= 1 / $T_{1/2}$) of water protons per millimolar concentration of the paramagnetic contrast agent [80]. This results in increased signal intensity on T_1-weighted images, a phenomenon known as paramagnetic relaxation enhancement (PRE), and decreased signal intensity for T_2 -weighted images [81, 82].

Multiple physicochemical parameters influence relaxivity and can impact the ligand design for contrast agents. One key parameter is the hydration number (q), which represents the number of water molecules in the inner sphere that are directly coordinated to the Gd(III) ion. A higher hydration number generally leads to higher r_1 value since more water molecule interact with the paramagnetic lanthanide(III) ion, enhancing the relaxation rate. Another parameter is the tumbling rate (τ_R), also known as the rotational correlation time, which refers to how fast the molecules rotates in solution [79]. While smaller GBCA molecules presented low relaxivity, macromolecular Gd(III) complexes demonstrate higher relaxivities values by reducing the tumbling rate of the molecule and increasing the interaction between water protons with the lanthanide(III) ion [83]. This allows an enhancement in the relaxation rate which improves image contrast [84]. Additionally, the water residency time (τ_M) represents the average time a water molecule coordinated to the Gd(III) ion remains bound before exchanging with a bulk water molecule. It is estimated that one molecule of GBCA can relax around 10 million water molecules per second [79, 82].

GBCAs, which are excreted through the kidneys, are in general considered safe for patients with normal renal function. However, in some cases, they have been associated with nephrogenic

systemic fibrosis (NSF), with few cases reported in the 2000s. NSF happens in patients with poor kidney function, due to the release of free gadolinium [81], and has led to increased interest in developing new methods and safer contrast agents [58].

Dysprosium(III), another paramagnetic lanthanide ion, is considered as a negative contrast agent [85] for *in vivo* T_2-weighted images through a mechanism known as Curie spin relaxation [86]. This effect is particularly pronounced due to dysprosium (Dy)(III)'s magnetic moment and short electronic relaxation time, which enhance T_2 relaxation. The Curie spin relaxation effect increases with the magnetic field strength, making Dy(III) complexes especially effective at higher fields [87]. Another factor influencing T_2 relaxation is the water residency time (τ_M). Some Dy(III) complexes, despite having similar rotational correlation times (τ_R), show the highest T_2 enhancement when having the slowest water exchange rate at higher magnetic field [85]. Vander Elst et al. [85] showed that the transverse relaxivity r_2 of their tested complexes depends on both the square of the magnetic field and the water residency time (τ_M). Therefore, Dy(III) based complexes with long τ_M values are considered effective negative contrast agents at high magnetic fields [86] due to their efficient transverse relaxivity r_2 [87].

Additionally, lanthanides can be used as paraCEST agents due to their paramagnetic properties, modifying the signal of labile protons, causing it to shift from the bulk water resonance by more than tens of ppm [58]. One particular feature of these probes is their ability to be designed to respond to specific biological conditions such as pH, temperature, concentrations or enzyme activity [58, 54]. Among these, applications of ytterbium (Yb)(III) based paraCEST contrast agents, such as Yb-DOTAM-Gly have shown a change in the net saturation transfer effect from 70 % to 10 % in a 6.0 to 8.8 pH range [88]. A thulium(III)-DOTA derivative was also synthesized by coupling it with a DEVD peptide sequence, allowing the suppression of the CEST signal after caspase-3

activation [89]. This capability highlights the potential of paraCEST agents to monitor biological processes, offering insights into disease progression and therapeutic responses.

1.3.2. Lutetium as a therapeutic agent

Lutetium (Lu)(III), with its most stable oxidation state of +3, is another lanthanide widely used in the imaging field. Certain isotopic forms of lutetium(III) can be radioactive, with lutetium-177 (^{177}Lu) presenting particular interest in the field of nuclear medicine due to its therapeutic and imaging properties. These characteristics make ^{177}Lu an ideal agent for application as a targeted radionuclide therapy (TRT) agent, also known as radiopharmaceutical therapy [90, 91]. Based on the emission of different types of particles, including β ones, this specialized form of radiation therapy delivers targeted radiation to cancer cells [92]. In TRT, the radionuclide is conjugated to molecules that specifically target receptors or antigens expressed on cancer cells. These molecules can be small molecules, peptides, proteins and antibodies [93, 94].

^{177}Lu is a radioactive isotope with a half-life of 6.65 days, which is long enough to allow for effective therapeutic use while being short enough to minimize prolonged radiation exposure to the patient [95]. Produced through the irradiation of isotopically enriched ^{176}Lu or ^{176}Yb with reactor neutrons [96], ^{177}Lu decays in the majority of events to the stable ground state of the isotope 177 hafnium, emitting β^- particles and low-energy γ photons in the process [93]. The emission of both γ rays and β particles makes ^{177}Lu a versatile theranostic agent, suitable for both diagnostic and therapeutic purposes. The γ rays, with their high abundance of photon emissions, are used in diagnostic molecular imaging to track the biodistribution and uptake of the radionuclide in the

body [97]. Conversely, the β particles induce the therapeutic effect of ^{177}Lu. Low-energy β particles are used for the treatment of leukemias, lymphomas or metastases, while high-energy β particles are employed for the treatment of solid tumors [95]. These particles travel short distance in tissue, with a maximum path length of 1.5 mm [90], delivering a high dose of radiation to targeted cells while minimizing damage to the surrounding healthy tissue [93].

One of the most well-established applications of ^{177}Lu is as a peptide receptor TRT [92] in the treatment of neuroendocrine tumors (NETs), which are known to overexpressed somatostatin receptors [98]. This application has led to the development of ^{177}Lu-DOTATATE (Lutathera), approved in both Europe and the United-States [99, 100]. This radioisotope is complexed to DOTATATE, a somatostatin analog designed to inhibit somatostatin receptors [95]. DOTATATE is a fourteen amino acid cyclic peptide, similar to the non-radioactive eight amino acid analog octreotide [98]. In a clinical study involving 52 patients with advanced pancreatic NETs, ^{177}Lu-DOTATATE demonstrating significant antitumor activity [101]. Further clinical studies on 310 patients with gastroenteropancreatic tumors, treated with a cumulative activity of up to 27.8-29.6 GBq of ^{177}Lu-DOTATATE, revealed complete and partial tumor remission in 2% and 28% of patients, respectively [102]. The unique properties of ^{177}Lu-DOTATATE have led to its application across various types of NETs, including midgut NETs [103], but also improving progression-free survival and quality of life by reducing hormone secretion [104].

Another type of cancer that benefits from ^{177}Lu therapy is prostate cancer through the targeting of prostate-specific membrane antigen (PSMA). PSMA is a transmembrane protein overexpressed on the surface of prostate cancer cells [98], making the binding to radioactive isotopes PSMA-targeting molecules an excellent target for TRT [105]. Initially, a radiolabeled PSMA monoclonal antibody, J591,was synthesized to target the extracellular domain before being internalized

through endocytosis. However, this approach led to hematotoxicity, possibly due to the large molecular size of the antibody [106]. To address this issue, smaller ^{177}Lu radiolabeled molecules were developed, such as [^{177}Lu]-PSMA-617. This compound is primarily used in the treatment of metastatic castration-resistant prostate cancer and has been shown to increase survival rates in men with this condition [107, 108].

^{177}Lu is a versatile and effective theranostic agent with applications mostly in both neuroendocrine tumors and prostate cancer. Its targeted delivery, dual emission properties, and clinical efficacy make it a valuable tool in the field of nuclear medicine, offering improved outcomes and quality of life for patients with advanced cancers [92, 94].

1.4. Biological Basis For Targets of Molecular Imaging Described In This Thesis

1.4.1. Vitamin B_6

Vitamin B_6 includes multiple vitamers that are derivative of 2-methyl-3-hydroxy-5-hydroxymethyl-pyridine. These vitamers include pyridoxine (PN), pyridoxal (PL), pyridoxamine (PM) and their respective 5'-phosphates, with pyridoxal-5'phosphate (PLP) being the metabolically active form [109].

Considered as an essential nutrient by finding its source in fish, liver, meat, cereals or nuts [110], metabolism of vitamin B_6 involves several key steps that ensures its efficient utilization by the body. Non-phosphorylated B_6 vitamers are primarily absorbed in the intestine through a plasma membrane transporter [111]. The TPN1 transporter, a member of the purine cytosine permease family [112], is located on the plasma membrane and functions as a proton symporter with high affinity for

PN, facilitating its transport into intestinal cells [113]. Once absorbed, vitamers are either transported directly to the liver for metabolism or undergo metabolic modifications before being transported [114]. Pyridoxamine, pyridoxine and pyridoxal are phosphorylated by pyridoxal kinase (PDXK) to form their respective phosphorylated derivatives. The flavin mononucleotide (FMN)-dependent enzyme pyridox(am)ine phosphate 5'-oxidase (PNPO) then oxidizes these phosphorylated forms to produce pyridoxal 5'-phosphate. Conversely, PN can first be oxidized first by PNPO to form PL, which is then phosphorylated by PDXK to form PLP [111, 115]. If vitamin B_6 levels exceed biological requirements, PLP is dephosphorylated by PDXP to form PL. This PL is subsequently oxidized to pyridoxic acid (PA) by an aldehyde oxidase before excretion through the urine (Figure 1.3) [116].

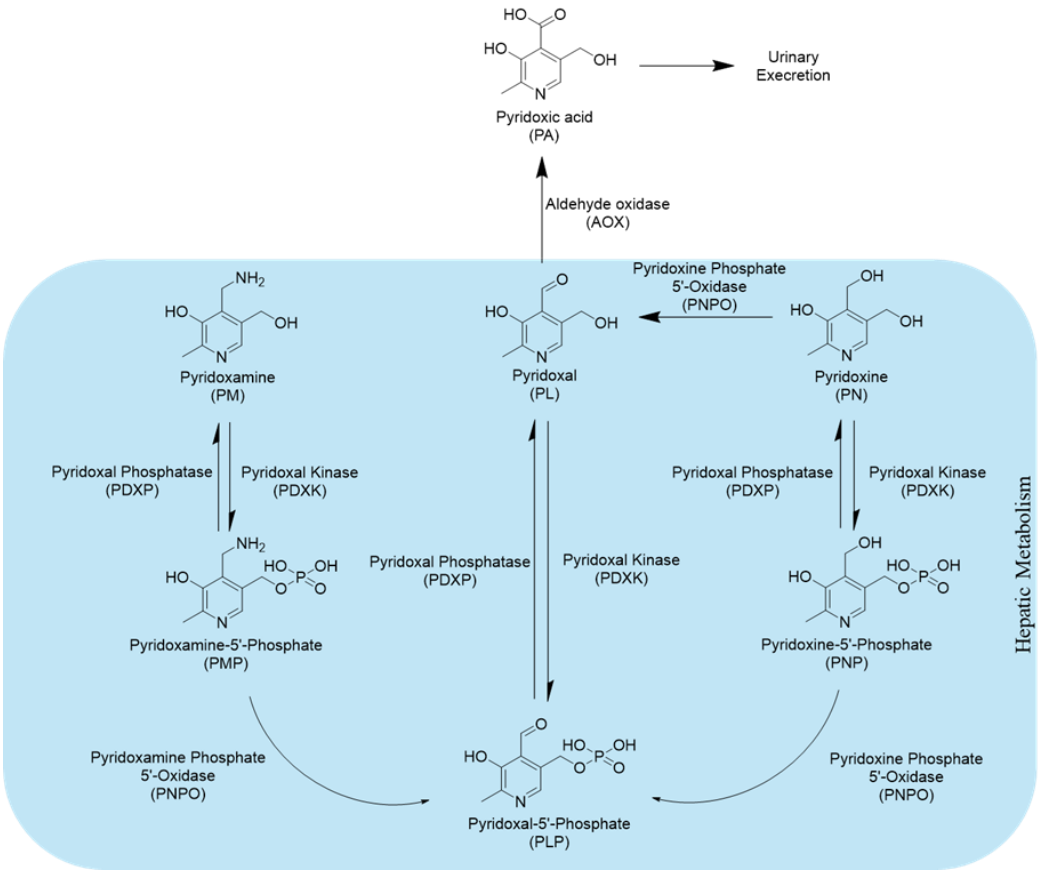

Figure 1.3 Metabolic pathway of vitamin B_6 and synthesis of pyridoxal 5'-phosphate (PLP). Conversion of B_6 vitamers (pyridoxine, pyridoxal, pyridoxamine) into the active form, pyridoxal 5'-phosphate (PLP). Key enzymes include pyridoxal kinase (PDXK) and pyridoxal phosphatase (PDXP).

PLP is involved in over 140 biochemical pathways, including amino acid and neurotransmitter metabolism, folate and 1-carbon metabolism, protein and polyamine synthesis, carbohydrate and lipid metabolism, mitochondrial function and erythropoiesis [111]. Its structure presents an aldehyde group, which enables it to function as a cofactor for enzymes by reacting with the amino groups of amino acids resulting in a Schiff base. This Schiff base is essential for the majority of enzyme-catalyzed reactions that require PLP [117]. Beyond its enzymatic roles, PLP has nonenzymatic

functions such as acting as antioxidants in fungus at similar rates to vitamins C and E [118]. Other studies demonstrate that PLP exhibits antiepileptic activity by inhibiting the activation of P2X7 receptors [119, 120].

PLP possesses antioxidant properties that help neutralize reactive oxygen species (ROS), which are known to cause DNA damage and contribute to cancer development [115]. Many cancers are treated with cis-diammine-platinum (II) dichloride (CDDP), or cisplatin, although chemoresistance is observed in some cancers, such as lung cancer [121]. Studies have shown that the metabolism of PN is involved in the adaptation and cytotoxic response of non-small cell lung carcinoma to perturbation in homeostasis, such as heat shock, hypoxia, or nutrient deprivation [122]. Additionally, PN, depending on PDXK levels, intensifies CDDP cytotoxicity *in vitro* and *in vivo* of non-small cell lung carcinoma through DNA damage [123]. Preclinical studies have demonstrated that lung cancer cells with higher levels of PLP (the active form) reveal increased sensitivity to CDDP treatment. *In vivo* experiments have shown that co-administering PN with CDDP in mice enhances the drug's anti-tumor effectiveness by elevating intracellular B_6 vitamer concentrations, leading to increased cancer cell death when levels are higher than normal [121, 124]. Conversely, lung cancer cells with higher levels of PL (inactive form) display resistance to CDDP [115].

The metabolism of vitamin B_6 and its role in lung cancer, particularly its involvement in chemoresistance to cisplatin, have been investigated. However, few imaging studies have been conducted to visually highlight these findings or to demonstrate the metabolic pathways of vitamin B_6 in cancer applications. The first PN-based Gd (III) complex has been synthesized in 2024 by Ortos-Arroyo et al. [125] and studied for its potential use as a contrast agent for MRI, focusing on its crystallographic, magnetic and relaxometric properties. The analysis revealed that this complex

shows higher relaxivity values compared to the commercially available Gd (III)-based contrast agent [125].

1.4.2. Cannabinoids

Cannabis sativa produces over 750 compounds, which can be regrouped in different classes. One of these classes is cannabinoids, which includes more than 100 terpenophenolic secondary metabolites. Among these, Δ^9-tetrahydrocannabinol (THC) is the main psychoactive ingredients [126]. It is produced through a decarboxylation reaction from Δ^9-tetrahydrocannabinolic acid (THCA), obtained from nonpsychoactive *C. sativa* extracts [127, 128]. Due to its psychoactive properties, the consumption of cannabis is associated with both pathological and behavioral toxicity [129]. Other side effects, such as psychotic symptoms, euphoria, altered perception, increased anxiety or cognitive deficits [130] have been observed in healthy candidates after exposure to THC [131].

The effects of THC are primarily mediated through its interaction with the body's endocannabinoid system. This system consists of endogenous cannabinoid receptors, known as CB_1 and CB_2 receptors, a G-protein-coupled receptor (GPCR) [132] localized in the presynaptic junction [133]. CB_1 receptors are predominantly found in the brain and central nervous system but are also present in the heart, blood vessel, liver, lungs and the digestive system. In contrast, CB_2 receptors are mainly located in cells related to the immune system, which is why this receptor is involved in inflammatory conditions and the regulation of the immune system [127].

These receptors are naturally formed in the body to interact with endogenous molecules. This led to the identification of *N*-arachidonoylethanolamine, or anandamide (AEA) and 2-arachidonoyl glycerol (2-AG) as the endogenous agonists, or lipids mediators, of these receptors, ultimately revealing the existence of the endocannabinoid system [134]. The production and activation of the endocannabinoid molecules depend on elevated levels of calcium ions and are synthesized on demand from lipid precursors in biological membranes [135]. Once produced, AEA and 2-AG travel retrogradely, or "backward", from the postsynaptic neuron to the presynaptic neuron, where they interact with CB_1 and CB_2 receptors inhibiting the release of neurotransmitter [136]. To prevent prolonged activation of cannabinoid receptors, AEA and 2-AG are degraded by fatty acid amide hydrolase (FAAH) and monoacylglycereol lipase (MAG) respectively [127]. FAAH, found in the postsynaptic neuron, degrades AEA into arachidonic acid (AA) and ethanolamine, while MAG, found in the presynaptic neuron, degrades 2-AG into arachidonic acid and glycerol (Figure 1.4) [133].

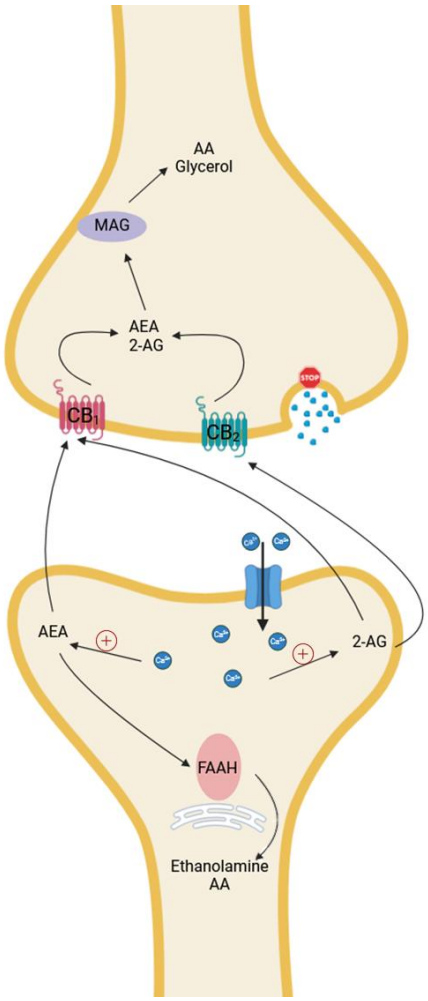

Figure 1.4 Endocannabinoid system (ECS) signaling pathway. Illustration of the endocannabinoid system, a complex network of receptors, endogenous ligands, and enzymes that regulates physiological processes. The ECS includes cannabinoids receptors, CB_1 and CB_2, endocannabinoids such as anandamide (AEA) and 2-arachidonoyl glycerol (2-AG), and enzymes responsible for their degradation, including fatty acid amide hydrolase (FAAH) and monoacylglycerol lipase (MAG).

Although other receptors in the endocannabinoid system, such as GPR55, transient receptor potential vanilloid (TRPV), peroxisome proliferator-activated receptor γ (PPRγ), or serotonin 3A receptor (5-HT3A), can be activated by endocannabinoids, including Δ^9-THC [136], interaction of Δ^9-THC with CB_1 receptors has been shown to induce hypothermia or catalepsy and analgesic properties [127]. However, interaction with CB_2 receptors induces anti-inflammatory properties. Other applications of THC have revealed its effectiveness in the treatment of neurodegenerative diseases of the central nervous system [137] and in managing chemotherapy-induced nausea and vomiting [133, 134]. Once THC enters the body, it undergoes a series of metabolic processes that ultimately lead to its elimination. Metabolism of THC primarily occurs in the liver where it is degraded by cytochrome P450 isoenzymes, including CYP2C9, CYP2C19, and CYP3A4 [129, 132]. The main metabolite of THC is 11-hydroxy-THC, which is also psychoactive [138]. Further metabolism converts 11-hydroxy-THC into 11-carboxy-THC, which is non-psychoactive. This metabolite then undergoes glucuronidation, making it more water-soluble and easier to excrete [139].

In addition to its metabolism and elimination, THC exhibits a unique property known as the depot effect. Due to its high lipophilicity, THC can accumulate in adipose tissues throughout the body. This accumulation creates a reserve of THC that can be gradually released back into the bloodstream over time, typically during lipolysis [140]. The subsequent release and redistribution of THC from adipose tissues can prolong its presence in the body. The depot effect is more pronounced in chronic users of cannabis, as repeated exposure can lead to significant accumulation of THC in fatty tissues [129, 141]. However, the specific impact of the patient's sex or age on the depot effect has not been extensively studied, even if it has been studies for other purposes such as the impact on the brain [142]. While it is known that body composition and metabolic rates can vary depending on the sex or age of the patients [143, 144], further research is needed to determine how

these factors influence THC accumulation in adipose tissues and redistribution. Moreover, it is worth considering whether the depot effect is impacted by the type of receptor engaged in the endocannabinoid system and its location in the body. CB_1 and CB_2 are distributed throughout various tissues and organs [127, 136]. The interaction of THC with these receptors may influence its metabolism, storage and subsequent release from adipose tissues [132].

1.5. Thesis Overview and Goals

The goal of this thesis is to design, synthesize, characterize and evaluate new potential contrast agents for application in the imaging field of MRI, MRF and CEST-MRI. To map vitamin B_6 metabolism, and more specifically its cofactor PLP, chapter 2 will discuss the synthesis, characterization and evaluation of a second generation probe known as 2-HYNIC. This probe exhibits selectivity for aromatic aldehydes and is considered a hydrazone-dependent CEST contrast agent. Chapter 3 will explore a new synthetic approach for the controlled synthesis of homo- and hetero-bislanthanide complexes based on a cyanohydroxyquinoline-cysteine condensation. Each complex will be synthesized and characterized, followed by testing their relaxivities through MRI and MRF, as well as their optical properties. Building on the same chemistry developed to combine lanthanides in a 1:1 ratio, chapter 4 will be based on the theranostic properties of lutetium to incorporate this lanthanide into a new homo-bislanthanide complex. This will create a potential targeted radionuclide therapy agent against glioblastoma. Finally, chapter 5 will focus on assessing the effect of physiological characteristics and receptor engagement by synthesizing and characterizing a new fluorinated THC-based probe. This probe will be used to evaluate the biodistribution of this potential radiotracer.

The overall goal of this thesis is to develop and evaluate innovative contrast agents and theranostic probes for advanced imaging techniques and targeted therapies. By achieving these goals, the thesis will enhance the understanding of biological processes though innovative imaging and therapeutic strategies.

1.6. Objectives

To achieve the overall goals of this thesis, which focus on the synthesis and characterization of potential contrast probes and radiotracers for application in MRI, MRF and CEST, the specific objectives are as follows:

- Map PLP metabolism: evaluate the efficacy of 2-HYNIC as a potential hydrazoCEST contrast agent. This includes assessing the formation of hydrazones from derived metabolites, evaluating the impact of pH and concentration on CEST signal production, and comparing the first generation probe (NA^3) with the second generation probe (2-HYNIC) in cell lines and tumor xenografts for application in lung cancer (Chapter 2).
- Combine lanthanides through an uncatalyzed aqueous click reaction: develop combinations of multiple lanthanides, ranging from europium to lutetium, together, and characterized them, evaluate their relaxivity values using MRF and test the optical properties of europium(III) as an emissive lanthanide ion (Chapter 3).
- Utilize lanthanides combination chemistry for radionuclide therapy: apply the chemistry developed to combine lanthanides by incorporating the radionuclide ^{177}lutetium. This includes developing a new synthesis to include an azide-modified-*L*-lysine on the complex,

allowing the addition of D-VAP and RI-VAP peptides for glioblastoma targeting through SPAAC chemistry (Chapter 4).

- Investigate the endocannabinoid system: gain a better understanding of the endocannabinoid system, as receptors are not limited to the brain but are also found in organs, connective tissues and immune cells. This includes the synthesis of two potentials radiotracers, [^{18}F]-ω-fluoro-Δ^8 THC and [^{18}F]-ω-fluoro-Δ^9 THC, by adding a radioactive fluorine (^{18}F) to the end of the aliphatic chain, optimizing the purification process of the different intermediates to obtain the most accurate signal from receptor engagement (Chapter 5).

1.7. Notes and References

(1) Bercovich, E.; Javitt, M. C. Medical Imaging: From Roentgen to the Digital Revolution, and Beyond. *Rambam Maimonides Med J* **2018**, *9* (4), e0034.

(2) Ritter, F.; Boskamp, T.; Homeyer, A.; Laue, H.; Schwier, M.; Link, F.; Peitgen, H.-O. Medical Image Analysis. *IEEE pulse* **2011**, *2*, 60–70.

(3) Singh, R. The Nobel Laureate W.C. Roentgen and His X-Rays. *Indian Journal of History of Science* **2016**, *51*.

(4) Mould, R. F. Invited Review: Röntgen and the Discovery of X-Rays. *Br J Radiol* **1995**, *68* (815), 1145–1176.

(5) James, M. L.; Gambhir, S. S. A Molecular Imaging Primer: Modalities, Imaging Agents, and Applications. *Physiol Rev* **2012**, *92* (2), 897–965.

(6) Martí-Bonmatí, L.; Sopena, R.; Bartumeus, P.; Sopena, P. Multimodality Imaging Techniques. *Contrast Media & Molecular Imaging* **2010**, *5* (4), 180–189.

(7) Withers, P. J.; Bouman, C.; Carmignato, S.; Cnudde, V.; Grimaldi, D.; Hagen, C. K.; Maire, E.; Manley, M.; Du Plessis, A.; Stock, S. R. X-Ray Computed Tomography. *Nat Rev Methods Primers* **2021**, *1* (1), 1–21.

(8) Jung, H. Basic Physical Principles and Clinical Applications of Computed Tomography. *Prog Med Phys* **2021**, *32* (1), 1–17.

(9) Hsieh, J.; Flohr, T. Computed Tomography Recent History and Future Perspectives. *JMI* **2021**, *8* (5), 052109.

(10) Hutton, B. F. SPECT Imaging: Basics and New Trends. In *Handbook of Particle Detection and Imaging*; Fleck, I., Titov, M., Grupen, C., Buvat, I., Eds.; Springer International Publishing: Cham, **2021**; 1217–1236.

(11) Hutton, B. F. The Origins of SPECT and SPECT/CT. *Eur J Nucl Med Mol Imaging* **2014**, *41* (1), 3–16.

(12) Jensen, J. A. Medical Ultrasound Imaging. *Progress in Biophysics and Molecular Biology* **2007**, *93* (1), 153–165.

(13) Harrison, B. P.; Crystal, C. S. Imaging Modalities in Obstetrics and Gynecology. *Emergency Medicine Clinics* **2003**, *21* (3), 711–735.

(14) Easter, S. R.; Hameed, A. B.; Shamshirsaz, A.; Fox, K.; Zelop, C. M. Point of Care Maternal Ultrasound in Obstetrics. *American Journal of Obstetrics and Gynecology* **2023**, *228* (5), 509.e1-509.e13.

(15) Aly, I.; Rizvi, A.; Roberts, W.; Khalid, S.; Kassem, M. W.; Salandy, S.; du Plessis, M.; Tubbs, R. S.; Loukas, M. Cardiac Ultrasound: An Anatomical and Clinical Review. *Translational Research in Anatomy* **2021**, *22*, 100083.

(16) Chau, S. S.; Beutler, B. D.; Grant, E. G.; Tchelepi, H. Ultrasound Innovations in Abdominal Radiology: Multiparametic Imaging in Liver Transplantation. *Abdom Radiol* **2025**, *50* (2), 679–692.

(17) Kubíček, V.; Tóth, É. Design and Function of Metal Complexes as Contrast Agents in MRI. In *Advances in Inorganic Chemistry*; van Eldik, R., Hubbard, C. D., Eds.; Academic Press, **2009**; *61*, 63–129.

(18) Yan, G.-P.; Robinson, L.; Hogg, P. Magnetic Resonance Imaging Contrast Agents: Overview and Perspectives. *Radiography* **2007**, *13*, e5–e19.

(19) Moffat, B. A.; Chenevert, T. L.; Meyer, C. R.; Mckeever, P. E.; Hall, D. E.; Hoff, B. A.; Johnson, T. D.; Rehemtulla, A.; Ross, B. D. The Functional Diffusion Map: An Imaging Biomarker for the Early Prediction of Cancer Treatment Outcome. *Neoplasia* **2006**, *8* (4), 259–267.

(20) Padhani, A. R.; Husband, J. E. Dynamic Contrast-Enhanced MRI Studies in Oncology with an Emphasis on Quantification, Validation and Human Studies. *Clin Radiol* **2001**, *56* (8), 607–620.

(21) Morinaga, A.; Ono, K.; Ikeda, T.; Ikeda, Y.; Shima, K.; Noguchi-Shinohara, M.; Samuraki, M.; Yanase, D.; Yoshita, M.; Iwasa, K.; Mastunari, I.; Yamada, M. A Comparison of the Diagnostic Sensitivity of MRI, CBF-SPECT, FDG-PET and Cerebrospinal Fluid Biomarkers for Detecting Alzheimer's Disease in a Memory Clinic. *Dement Geriatr Cogn Disord* **2010**, *30* (4), 285–292.

(22) Sun, C.; Veiseh, O.; Gunn, J.; Fang, C.; Hansen, S.; Lee, D.; Sze, R.; Ellenbogen, R. G.; Olson, J.; Zhang, M. *In Vivo* MRI Detection of Gliomas by Chlorotoxin-Conjugated Superparamagnetic Nanoprobes. *Small* **2008**, *4* (3), 372–379.

(23) Hodgson, R. J.; O'Connor, P.; Moots, R. MRI of Rheumatoid Arthritis Image Quantitation for the Assessment of Disease Activity, Progression and Response to Therapy. *Rheumatology (Oxford)* **2008**, *47* (1), 13–21.

(24) Kennel, S. J.; Davis, I. A.; Branning, J.; Pan, H.; Kabalka, G. W.; Paulus, M. J. High Resolution Computed Tomography and MRI for Monitoring Lung Tumor Growth in Mice Undergoing Radioimmunotherapy: Correlation with Histology. *Med Phys* **2000**, *27* (5), 1101–1107.

(25) Reviewer, P.; Reviewer, S. The Patient Experience in Medical Imaging: A Qualitative Systematic Review (Protocol). *JBI Evidence Synthesis* **2010**, *8* (8), 1.

(26) Smith-Bindman, R.; Kwan, M. L.; Marlow, E. C.; Theis, M. K.; Bolch, W.; Cheng, S. Y.; Bowles, E. J. A.; Duncan, J. R.; Greenlee, R. T.; Kushi, L. H.; Pole, J. D.; Rahm, A. K.; Stout, N. K.; Weinmann, S.; Miglioretti, D. L. Trends in Use of Medical Imaging in US Health Care Systems and in Ontario, Canada, 2000-2016. *JAMA* **2019**, *322* (9), 843–856.

(27) Lauterbur, P. C. Image Formation by Induced Local Interactions: Examples Employing Nuclear Magnetic Resonance. *Nature* **1973**, *242* (5394), 190–191.

(28) Wu, B.; Warnock, G.; Zaiss, M.; Lin, C.; Chen, M.; Zhou, Z.; Mu, L.; Nanz, D.; Tuura, R.; Delso, G. An Overview of CEST MRI for Non-MR Physicists. *EJNMMI Phys* **2016**, *3* (1), 19.

(29) Grover, V. P. B.; Tognarelli, J. M.; Crossey, M. M. E.; Cox, I. J.; Taylor-Robinson, S. D.; McPhail, M. J. W. Magnetic Resonance Imaging: Principles and Techniques: Lessons for Clinicians. *J Clin Exp Hepatol* **2015**, *5* (3), 246–255.

(30) van Geuns, R.-J. M.; Wielopolski, P. A.; de Bruin, H. G.; Rensing, B. J.; van Ooijen, P. M. A.; Hulshoff, M.; Oudkerk, M.; de Feyter, P. J. Basic Principles of Magnetic Resonance Imaging. *Progress in Cardiovascular Diseases* **1999**, *42* (2), 149–156.

(31) Brown, M. A.; Semelka, R. C. *MRI: Basic Principles and Application*; John Wiley & Sons**, 2015**.

(32) Jezzard, P.; Clare, S. Principles of Nuclear Magnetic Resonance and MRI. In *Functional Magnetic Resonance Imaging: An Introduction to Methods*; Jezzard, P., Matthews, P. M., Smith, S. M., Eds.; Oxford University Press, **2001**;

(33) Goldman, M. Formal Theory of Spin–Lattice Relaxation. *Journal of Magnetic Resonance* **2001**, *149* (2), 160–187.

(34) Bloch, F. Nuclear Induction. *Phys. Rev.* **1946**, *70* (7–8), 460–474.

(35) Bipin Mehta, B.; Coppo, S.; McGivney, D. F.; Hamilton, J. I.; Chen, Y.; Jiang, Y.; Ma, D.; Gulani, N. S. V.; Griswold, M. A. *M*agnetic resonance fingerprinting: a technical review. *Magn Reson Med* **2019**, 81, 25-46.

(36) Schmitt, P.; Griswold, M. A.; Jakob, P. M.; Kotas, M.; Gulani, V.; Flentje, M.; Haase, A. Inversion Recovery TrueFISP: Quantification of T(1), T(2), and Spin Density. *Magn Reson Med* **2004**, *51* (4), 661–667.

(37) Poorman, M. E.; Martin, M. N.; Ma, D.; McGivney, D. F.; Gulani, V.; Griswold, M. A.; Keenan, K. E. Magnetic Resonance Fingerprinting Part 1: Potential Uses, Current Challenges, and Recommendations. *J Magn Reson Imaging* **2020**, *51* (3), 675–692.

(38) Panda, A.; Mehta, B. B.; Coppo, S.; Jiang, Y.; Ma, D.; Seiberlich, N.; Griswold, M. A.; Gulani, V. Magnetic Resonance Fingerprinting – An Overview. *Current Opinion in Biomedical Engineering* **2017**, *3*, 56–66.

(39) Ma, D.; Gulani, V.; Seiberlich, N.; Liu, K.; Sunshine, J. L.; Duerk, J. L.; Griswold, M. A. Magnetic Resonance Fingerprinting. *Nature* **2013**, *495* (7440), 187–192.

(40) Hamilton, J. I.; Jiang, Y.; Chen, Y.; Ma, D.; Lo, W.-C.; Griswold, M.; Seiberlich, N. MR Fingerprinting for Rapid Quantification of Myocardial T1 , T2 , and Proton Spin Density. *Magn Reson Med* **2017**, *77* (4), 1446–1458.

(41) Liu, Y.; Hamilton, J.; Rajagopalan, S.; Seiberlich, N. Cardiac Magnetic Resonance Fingerprinting: Technical Overview and Initial Results. *JACC Cardiovasc Imaging* **2018**, *11* (12), 1837–1853.

(42) Badve, C.; Yu, A.; Rogers, M.; Ma, D.; Liu, Y.; Schluchter, M.; Sunshine, J.; Griswold, M.; Gulani, V. Simultaneous T1 and T2 Brain Relaxometry in Asymptomatic Volunteers Using Magnetic Resonance Fingerprinting. *Tomography* **2015**, *1* (2), 136–144.

(43) Badve, C.; Yu, A.; Dastmalchian, S.; Rogers, M.; Ma, D.; Jiang, Y.; Margevicius, S.; Pahwa, S.; Lu, Z.; Schluchter, M.; Sunshine, J.; Griswold, M.; Sloan, A.; Gulani, V. MR Fingerprinting of Adult Brain Tumors: Initial Experience. *AJNR Am J Neuroradiol* **2017**, *38* (3), 492–499.

(44) Liao, C.; Wang, K.; Cao, X.; Li, Y.; Wu, D.; Ye, H.; Ding, Q.; He, H.; Zhong, J. Detection of Lesions in Mesial Temporal Lobe Epilepsy by Using MR Fingerprinting. *Radiology* **2018**, *288* (3), 804–812.

(45) Yu, A. C.; Badve, C.; Ponsky, L. E.; Pahwa, S.; Dastmalchian, S.; Rogers, M.; Jiang, Y.; Margevicius, S.; Schluchter, M.; Tabayoyong, W.; Abouassaly, R.; McGivney, D.; Griswold, M. A.; Gulani, V. Development of a Combined MR Fingerprinting and Diffusion Examination for Prostate Cancer. *Radiology* **2017**, *283* (3), 729–738.

(46) Wolff, S. D.; Balaban, R. S. Magnetization Transfer Contrast (MTC) and Tissue Water Proton Relaxation *in Vivo*. *Magn Reson Med* **1989**, *10* (1), 135–144.

(47) Foo, L. S.; Yap, W.-S.; Hum, Y. C.; Manan, H. A.; Tee, Y. K. Analysis of Model-Based and Model-Free CEST Effect Quantification Methods for Different Medical Applications. *Journal of Magnetic Resonance* **2020**, *310*, 106648.

(48) Viswanathan, S.; Kovacs, Z.; Geen, K. N.; Ratnakar, S. J.; Sherry, A. D. Alternatives to Gadolinium-Based Metal Chelates for Magnetic Resonance Imaging. *Chem Rev* **2010**, 110, 2960-3018.

(49) Ward, K. M.; Aletras, A. H.; Balaban, R. S. A New Class of Contrast Agents for MRI Based on Proton Chemical Exchange Dependent Saturation Transfer (CEST). *J Magn Reson* **2000**, *143* (1), 79–87.

(50) Sun, P. Z.; Sorensen, A. G. Imaging pH Using the Chemical Exchange Saturation Transfer (CEST) MRI: Correction of Concomitant RF Irradiation Effects to Quantify CEST MRI for Chemical Exchange Rate and pH. *Magn Reson Med* **2008**, *60* (2), 390–397.

(51) Sun, P. Z.; Wang, E.; Cheung, J. S.; Zhang, X.; Benner, T.; Sorensen, A. G. Simulation and Optimization of Pulsed Radio Frequency Irradiation Scheme for Chemical Exchange Saturation Transfer (CEST) MRI-Demonstration of pH-Weighted Pulsed-Amide Proton CEST MRI in an Animal Model of Acute Cerebral Ischemia. *Magn Reson Med* **2011**, *66* (4), 1042–1048.

(52) Daryaei, I.; Ghaffari, M. M.; Jones, K. M.; Pagel, M. D. Detection of Alkaline Phosphatase Enzyme Activity with a CatalyCEST MRI Biosensor. *ACS Sens* **2016**, *1* (7), 857-861.

(53) Vinogradov, E.; Sherry, A. D.; Lenkinski, R. E. CEST: From Basic Principles to Applications, Challenges and Opportunities. *J Magn Reson* **2013**, *229*, 155–172.

(54) Soesbe, T. C.; Wu, Y.; Dean Sherry, A. Advantages of Paramagnetic Chemical Exchange Saturation Transfer (CEST) Complexes Having Slow to Intermediate Water Exchange Properties as Responsive MRI Agents. *NMR in Biomedicine* **2013**, *26* (7), 829–838.

(55) van Zijl, P. C. M.; Yadav, N. N. Chemical Exchange Saturation Transfer (CEST): What Is in a Name and What Isn't? *Magn Reson Med* **2011**, *65* (4), 927–948.

(56) Liu, G.; Song, X.; Chan, K. W. Y.; McMahon, M. T. Nuts and Bolts of Chemical Exchange Saturation Transfer MRI. *NMR Biomed* **2013**, *26* (7), 810–828.

(57) Kogan, F.; Hariharan, H.; Reddy, R. Chemical Exchange Saturation Transfer (CEST) Imaging: Description of Technique and Potential Clinical Applications. *Curr Radiol Rep* **2013**, *1* (2), 102–114.

(58) Wahsner, J.; Gale, E. M.; Rodríguez-Rodríguez, A.; Caravan, P. Chemistry of MRI Contrast Agents: Current Challenges and New Frontiers. *Chem. Rev.* **2019**, *119* (2), 957–1057.

(59) Kamitani, T.; Sagiyama, K.; Yamasaki, Y.; Hino, T.; Wada, T.; Kubo, M.; Akiyoshi, S.; Yamamoto, H.; Yabuuchi, H.; Ishigami, K. Amide Proton Transfer (APT) Imaging of Breast Cancers and Its Correlation with Biological Status. *Clinical Imaging* **2023**, *96*, 38–43.

(60) Kong, L.; Li, H.; Cai, Q.; Cao, W.; Chen, Y.; Weng, B.; Li, M.; Zhang, M.; Qian, L.; Guo, Y.; Ling, J.; Wen, Z.; Wang, H. Amide Proton Transfer-Weighted Imaging in Assessing the Aggressive and Proliferative Potential of Bladder Cancer. *Journal of Magnetic Resonance Imaging* **2025**, *61* (2), 704–712.

(61) Ying, Y.; Yahya, N.; Manan, H. A. Amide Proton Transfer MR Imaging in the Characterization of Brain Tumors: A Review Paper. *Journal of Radiation Research and Applied Sciences* **2024**, *17* (3), 101043.

(62) Meng, N.; Huang, Z.; Jiang, H.; Dai, B.; Shen, L.; Liu, X.; Wu, Y.; Yu, X.; Fu, F.; Li, Z.; Shen, Z.; Jiang, B.; Wang, M. Glucose Chemical Exchange Saturation Transfer MRI for Predicting the Histological Grade of Rectal Cancer: A Comparative Study with Amide Proton Transfer-Weighted and Diffusion-Weighted Imaging. *Insights Imaging* **2024**, *15* (1), 269.

(63) Haris, M.; Nath, K.; Cai, K.; Singh, A.; Crescenzi, R.; Kogan, F.; Verma, G.; Reddy, S.; Hariharan, H.; Melhem, E. R.; Reddy, R. Imaging of Glutamate Neurotransmitter Alterations in Alzheimer's Disease. *NMR in Biomedicine* **2013**, *26* (4), 386–391.

(64) Bagga, P.; Pickup, S.; Crescenzi, R.; Martinez, D.; Borthakur, A.; D'Aquilla, K.; Singh, A.; Verma, G.; Detre, J. A.; Greenberg, J.; Hariharan, H.; Reddy, R. *In Vivo* GluCEST MRI:

Reproducibility, Background Contribution and Source of Glutamate Changes in the MPTP Model of Parkinson's Disease. *Sci Rep* **2018**, *8* (1), 2883.

(65) Pépin, J.; Francelle, L.; Carrillo-de Sauvage, M.-A.; de Longprez, L.; Gipchtein, P.; Cambon, K.; Valette, J.; Brouillet, E.; Flament, J. *In Vivo* Imaging of Brain Glutamate Defects in a Knock-in Mouse Model of Huntington's Disease. *NeuroImage* **2016**, *139*, 53–64.

(66) Roalf, D. R.; Nanga, R. P. R.; Rupert, P. E.; Hariharan, H.; Quarmley, M.; Calkins, M. E.; Dress, E.; Prabhakaran, K.; Elliott, M. A.; Moberg, P. J.; Gur, R. C.; Gur, R. E.; Reddy, R.; Turetsky, B. I. Glutamate Imaging (GluCEST) Reveals Lower Brain GluCEST Contrast in Patients on the Psychosis Spectrum. *Mol Psychiatry* **2017**, *22* (9), 1298–1305.

(67) Kogan, F.; Haris, M.; Singh, A.; Cai, K.; Debrosse, C.; Nanga, R. P. R.; Hariharan, H.; Reddy, R. Method for High-Resolution Imaging of Creatine *in Vivo* Using Chemical Exchange Saturation Transfer. *Magn Reson Med* **2014**, *71* (1), 164–172.

(68) Kogan, F.; Haris, M.; Debrosse, C.; Singh, A.; Nanga, R. P.; Cai, K.; Hariharan, H.; Reddy, R. *In Vivo* Chemical Exchange Saturation Transfer Imaging of Creatine (CrCEST) in Skeletal Muscle at 3T. *J Magn Reson Imaging* **2014**, *40* (3), 596–602.

(69) Nasrallah, F. A.; Pagès, G.; Kuchel, P. W.; Golay, X.; Chuang, K.-H. Imaging Brain Deoxyglucose Uptake and Metabolism by glucoCEST MRI. *J Cereb Blood Flow Metab* **2013**, *33* (8), 1270–1278.

(70) Wang, J.; Weygand, J.; Hwang, K.-P.; Mohamed, A. S. R.; Ding, Y.; Fuller, C. D.; Lai, S. Y.; Frank, S. J.; Zhou, J. Magnetic Resonance Imaging of Glucose Uptake and Metabolism in Patients with Head and Neck Cancer. *Sci Rep* **2016**, *6* (1), 30618.

(71) Chan, K. W. Y.; McMahon, M. T.; Kato, Y.; Liu, G.; Bulte, J. W. M.; Bhujwalla, Z. M.; Artemov, D.; van Zijl, P. C. M. Natural D-Glucose as a Biodegradable MRI Contrast Agent for Detecting Cancer. *Magn Reson Med* **2012**, *68* (6), 1764–1773.

(72) Ling, W.; Regatte, R. R.; Navon, G.; Jerschow, A. Assessment of Glycosaminoglycan Concentration *in Vivo* by Chemical Exchange-Dependent Saturation Transfer (gagCEST). *Proc Natl Acad Sci U S A* **2008**, *105* (7), 2266–2270.

(73) Soellner, S. T.; Welsch, G. H.; Gelse, K.; Goldmann, A.; Kleyer, A.; Schett, G.; Pachowsky, M. L. gagCEST Imaging at 3 T MRI in Patients with Articular Cartilage Lesions of the Knee and Intraoperative Validation. *Osteoarthritis Cartilage* **2021**, *29* (8), 1163–1172.

(74) Aime, S.; Castelli, D. D.; Crich, S. G.; Gianolio, E.; Terreno, E. Pushing the Sensitivity Envelope of Lanthanide-Based Magnetic Resonance Imaging (MRI) Contrast Agents for Molecular Imaging Applications. *Acc. Chem. Res.* **2009**, *42* (7), 822–831.

(75) Fossheim, S.; Johansson, C.; Fahlvik, A. K.; Grace, D.; Klaveness, J. Lanthanide-Based Susceptibility Contrast Agents: Assessment of the Magnetic Properties. *Magnetic Resonance in Medicine* **1996**, *35* (2), 201–206.

(76) Peters, J. A.; Djanashvili, K.; Geraldes, C. F. G. C.; Platas-iglesias, C. Structure, Dynamics, and Computational Studies of Lanthanide-Based Contrast Agents. In *The Chemistry of Contrast Agents in Medical Magnetic Resonance Imaging*; John Wiley & Sons, Ltd, **2013**, 209–276.

(77) De Gregori da Rocha, J.; Cechinel, M. A. P.; Rocha, L. F.; Riella, H. G., Padoin, N.; Soares, C. Exploring the Potential of Rare Earth Doped Carbon Dots: Concepts and Applications. *ResearchGate* **2024**.

(78) Szomolanyi, P.; Rohrer, M.; Frenzel, T.; Noebauer-Huhmann, I. M.; Jost, G.; Endrikat, J.; Trattnig, S.; Pietsch, H. Comparison of the Relaxivities of Macrocyclic Gadolinium-Based Contrast Agents in Human Plasma at 1.5, 3, and 7 T, and Blood at 3 T. *Invest Radiol* **2019**, *54* (9), 559–564.

(79) Hermann, P.; Kotek, J.; Kubíček, V.; Lukeš, I. Gadolinium(III) Complexes as MRI Contrast Agents: Ligand Design and Properties of the Complexes. *Dalton Trans.* **2008**, No. 23, 3027–3047.

(80) Shen, Y.; Goerner, F. L.; Snyder, C.; Morelli, J. N.; Hao, D.; Hu, D.; Li, X.; Runge, V. M. T1 Relaxivities of Gadolinium-Based Magnetic Resonance Contrast Agents in Human Whole Blood at 1.5, 3, and 7 T: *Investigative Radiology* **2015**, *50* (5), 330–338.

(81) Do, C.; DeAguero, J.; Brearley, A.; Trejo, X.; Howard, T.; Escobar, G. P.; Wagner, B. Gadolinium-Based Contrast Agent Use, Their Safety, and Practice Evolution. *Kidney360* **2020**, *1* (6), 561.

(82) Li, H.; Meade, T. J. Molecular Magnetic Resonance Imaging with Gd(III)-Based Contrast Agents: Challenges and Key Advances. *J. Am. Chem. Soc.* **2019**, *141* (43), 17025–17041.

(83) Zhou, Z.; Lu, Z.-R. Gadolinium-Based Contrast Agents for Magnetic Resonance Cancer Imaging. *WIREs Nanomedicine and Nanobiotechnology* **2013**, *5* (1), 1–18.

(84) Zhang, J.; Dai, L.; He, L.; Bhattarai, A.; Chan, C.-M.; Tai, W. C.-S.; Vardhanabhuti, V.; Law, G.-L. Design and Synthesis of Chiral DOTA-Based MRI Contrast Agents with Remarkable Relaxivities. *Commun Chem* **2023**, *6* (1), 1–10.

(85) Vander Elst, L.; Roch, A.; Gillis, P.; Laurent, S.; Botteman, F.; Bulte, J. W. M.; Muller, R. N. Dy-DTPA Derivatives as Relaxation Agents for Very High Field MRI: The Beneficial Effect of Slow Water Exchange on the Transverse Relaxivities. *Magn Reson Med* **2002**, *47* (6), 1121–1130.

(86) Gómez-González, E.; Caro, C.; García-Martín, M. L.; Becerro, A. I.; Ocaña, M. Outstanding MRI Contrast with Dysprosium Phosphate Nanoparticles of Tuneable Size. *Nanoscale* **2022**, *14* (31), 11461–11470.

(87) Caravan, P.; Greenfield, M. T.; Bulte, J. W. Molecular Factors That Determine Curie Spin Relaxation in Dysprosium Complexes. *Magn Reson Med* **2001**, *46* (5), 917–922.

(88) Aime, S.; Barge, A.; Delli Castelli, D.; Fedeli, F.; Mortillaro, A.; Nielsen, F. U.; Terreno, E. Paramagnetic Lanthanide(III) Complexes as pH-Sensitive Chemical Exchange Saturation Transfer (CEST) Contrast Agents for MRI Applications. *Magn Reson Med* **2002**, *47* (4), 639–648.

(89) Yoo, B.; Pagel, M. D. A PARACEST MRI Contrast Agent to Detect Enzyme Activity. *J Am Chem Soc* **2006**, *128* (43), 14032–14033.

(90) Vogel, W. V.; van der Marck, S. C.; Versleijen, M. W. J. Challenges and Future Options for the Production of Lutetium-177. *Eur J Nucl Med Mol Imaging* **2021**, *48* (8), 2329–2335.

(91) Dash, A.; Knapp, F. F. (Russ); Pillai, M. R. A. Targeted Radionuclide Therapy - An Overview. *Current Radiopharmaceuticals* **2013**, *6* (3), 152–180.

(92) Sgouros, G.; Bodei, L.; McDevitt, M. R.; Nedrow, J. R. Radiopharmaceutical Therapy in Cancer: Clinical Advances and Challenges. *Nat Rev Drug Discov* **2020**, *19* (9), 589–608.

(93) Dash, A.; Pillai, M. R. A.; Knapp, F. F. Production of 177Lu for Targeted Radionuclide Therapy: Available Options. *Nucl Med Mol Imaging* **2015**, *49* (2), 85–107.

(94) Lepareur, N.; Ramée, B.; Mougin-Degraef, M.; Bourgeois, M. Clinical Advances and Perspectives in Targeted Radionuclide Therapy. *Pharmaceutics* **2023**, *15* (6), 1733.

(95) Gudkov, S. V.; Shilyagina, N. Y.; Vodeneev, V. A.; Zvyagin, A. V. Targeted Radionuclide Therapy of Human Tumors. *International Journal of Molecular Sciences* **2016**, *17* (1), 33.

(96) Kuznetsov, R. A.; Bobrovskaya, K. S.; Svetukhin, V. V.; Fomin, A. N.; Zhukov, A. V. Production of Lutetium-177: Process Aspects. *Radiochemistry* **2019**, *61* (4), 381–395.

(97) Banerjee, S.; Pillai, M. R. A.; Knapp, F. F. R. Lutetium-177 Therapeutic Radiopharmaceuticals: Linking Chemistry, Radiochemistry, and Practical Applications. *Chem Rev* **2015**, *115* (8), 2934–2974.

(98) Goldsmith, S. J. Targeted Radionuclide Therapy: A Historical and Personal Review. *Seminars in Nuclear Medicine* **2020**, *50* (1), 87–97.

(99) Mittra, E. S. Neuroendocrine Tumor Therapy: 177Lu-DOTATATE. *American Journal of Roentgenology* **2018**, *211* (2), 278–285.

(100) Das, S.; Al-Toubah ,Taymeyah; El-Haddad ,Ghassan; and Strosberg, J. 177Lu-DOTATATE for the Treatment of Gastroenteropancreatic Neuroendocrine Tumors. *Expert Review of Gastroenterology & Hepatology* **2019**, *13* (11), 1023–1031.

(101) Sansovini, M.; Severi, S.; Ambrosetti, A.; Monti, M.; Nanni, O.; Sarnelli, A.; Bodei, L.; Garaboldi, L.; Bartolomei, M.; Paganelli, G. Treatment with the Radiolabelled Somatostatin

Analog Lu-DOTATATE for Advanced Pancreatic Neuroendocrine Tumors. *Neuroendocrinology* **2013**, *97* (4), 347–354.

(102) Kwekkeboom, D. J.; de Herder, W. W.; Kam, B. L.; van Eijck, C. H.; van Essen, M.; Kooij, P. P.; Feelders, R. A.; van Aken, M. O.; Krenning, E. P. Treatment With the Radiolabeled Somatostatin Analog [177Lu-DOTA0,Tyr3]Octreotate: Toxicity, Efficacy, and Survival. *JCO* **2008**, *26* (13), 2124–2130.

(103) Strosberg, J.; El-Haddad, G.; Wolin, E.; Hendifar, A.; Yao, J.; Chasen, B.; Mittra, E.; Kunz, P. L.; Kulke, M. H.; Jacene, H.; Bushnell, D.; O'Dorisio, T. M.; Baum, R. P.; Kulkarni, H. R.; Caplin, M.; Lebtahi, R.; Hobday, T.; Delpassand, E.; Cutsem, E. V.; Benson, A.; Srirajaskanthan, R.; Pavel, M.; Mora, J.; Berlin, J.; Grande, E.; Reed, N.; Seregni, E.; Öberg, K.; Sierra, M. L.; Santoro, P.; Thevenet, T.; Erion, J. L.; Ruszniewski, P.; Kwekkeboom, D.; Krenning, E. Phase 3 Trial of 177Lu-Dotatate for Midgut Neuroendocrine Tumors. *New England Journal of Medicine* **2017**, *376* (2), 125–135.

(104) Strosberg, J.; Wolin, E.; Chasen, B.; Kulke, M.; Bushnell, D.; Caplin, M.; Baum, R. P.; Kunz, P.; Hobday, T.; Hendifar, A.; Oberg, K.; Sierra, M. L.; Thevenet, T.; Margalet, I.; Ruszniewski, P.; Krenning, E.; on behalf of the NETTER-1 Study Group. Health-Related Quality of Life in Patients With Progressive Midgut Neuroendocrine Tumors Treated With 177Lu-Dotatate in the Phase III NETTER-1 Trial. *JCO* **2018**, *36* (25), 2578–2584.

(105) Rahbar, K.; Afshar-Oromieh, A.; Jadvar, H.; Ahmadzadehfar, H. PSMA Theranostics: Current Status and Future Directions. *Mol Imaging* **2018**, *17*, 1536012118776068.

(106) Tagawa, S. T.; Milowsky, M. I.; Morris, M.; Vallabhajosula, S.; Christos, P.; Akhtar, N. H.; Osborne, J.; Goldsmith, S. J.; Larson, S.; Taskar, N. P.; Scher, H. I.; Bander, N. H.; Nanus, D.

M. Phase II Study of Lutetium-177 Labeled Anti-Prostate-Specific Membrane Antigen (PSMA) Monoclonal Antibody J591 for Metastatic Castration-Resistant Prostate Cancer. *Clin Cancer Res* **2013**, *19* (18), 5182–5191.

(107) Hofman, M. S.; Violet, J.; Hicks, R. J.; Ferdinandus, J.; Thang, S. P.; Akhurst, T.; Iravani, A.; Kong, G.; Kumar, A. R.; Murphy, D. G.; Eu, P.; Jackson, P.; Scalzo, M.; Williams, S. G.; Sandhu, S. [177Lu]-PSMA-617 Radionuclide Treatment in Patients with Metastatic Castration-Resistant Prostate Cancer (LuPSMA Trial): A Single-Centre, Single-Arm, Phase 2 Study. *The Lancet Oncology* **2018**, *19* (6), 825–833.

(108) Hofman, M. S.; Emmett, L.; Sandhu, S.; Iravani, A.; Joshua, A. M.; Goh, J. C.; Pattison, D. A.; Tan, T. H.; Kirkwood, I. D.; Ng, S.; Francis, R. J.; Gedye, C.; Rutherford, N. K.; Weickhardt, A.; Scott, A. M.; Lee, S.-T.; Kwan, E. M.; Azad, A. A.; Ramdave, S.; Redfern, A. D.; Macdonald, W.; Guminski, A.; Hsiao, E.; Chua, W.; Lin, P.; Zhang, A. Y.; McJannett, M. M.; Stockler, M. R.; Violet, J. A.; Williams, S. G.; Martin, A. J.; Davis, I. D.; TheraP Trial Investigators and the Australian and New Zealand Urogenital and Prostate Cancer Trials Group. [177Lu]Lu-PSMA-617 versus Cabazitaxel in Patients with Metastatic Castration-Resistant Prostate Cancer (TheraP): A Randomised, Open-Label, Phase 2 Trial. *Lancet* **2021**, *397* (10276), 797–804.

(109) Percudani, R.; Peracchi, A. The B6 Database: A Tool for the Description and Classification of Vitamin B6-Dependent Enzymatic Activities and of the Corresponding Protein Families. *BMC Bioinformatics* **2009**, *10* (1), 273.

(110) Venturelli, S.; Leischner, C.; Helling, T.; Burkard, M.; Marongiu, L. Vitamins as Possible Cancer Biomarkers: Significance and Limitations. *Nutrients* **2021**, *13* (11), 3914.

(111) Wilson, M. P.; Plecko, B.; Mills, P. B.; Clayton, P. T. Disorders Affecting Vitamin B6 Metabolism. *Journal of Inherited Metabolic Disease* **2019**, *42* (4), 629–646.

(112) Middleton, H. M. Intestinal Hydrolysis of Pyridoxal 5'-Phosphate *in Vitro* and *in Vivo* in the Rat. Effect of Amino Acids and Oligopeptides. *Dig Dis Sci* **1990**, *35* (1), 113–120.

(113) Stolz, J.; Vielreicher, M. Tpn1p, the Plasma Membrane Vitamin B6 Transporter of Saccharomyces Cerevisiae*. *Journal of Biological Chemistry* **2003**, *278* (21), 18990–18996.

(114) Albersen, M.; Bosma, M.; Knoers, N. V. V. A. M.; de Ruiter, B. H. B.; Diekman, E. F.; de Ruijter, J.; Visser, W. F.; de Koning, T. J.; Verhoeven-Duif, N. M. The Intestine Plays a Substantial Role in Human Vitamin B6 Metabolism: A Caco-2 Cell Model. *PLoS One* **2013**, *8* (1), e54113.

(115) Parra, M.; Stahl, S.; Hellman, H. Vitamin B6 and Its Role in Cell Metabolism and Physiology. *Cells* **2018**, *7* (7), 84.

(116) Stanulović, M.; Jeremić, V.; Leskovac, V.; Chaykin, S. New Pathway of Conversion of Pyridoxal to 4-Pyridoxic Acid. *Enzyme* **1976**, *21* (4), 357–369.

(117) Eliot, A. C.; Kirsch, J. F. Pyridoxal Phosphate Enzymes: Mechanistic, Structural, and Evolutionary Considerations. *Annu Rev Biochem* **2004**, *73*, 383–415.

(118) Bilski, P.; Li, M. Y.; Ehrenshaft, M.; Daub, M. E.; Chignell, C. F. Vitamin B6 (Pyridoxine) and Its Derivatives Are Efficient Singlet Oxygen Quenchers and Potential Fungal Antioxidants. *Photochem Photobiol* **2000**, *71* (2), 129–134.

(119) Klotz, K. A.; Lemke, J. R.; Korinthenberg, R.; Jacobs, J. Vitamin B6-Responsive Epilepsy Due to a Novel KCNQ2 Mutation. *Neuropediatrics* **2017**, *48* (3), 199–204.

(120) Thériault, O.; Poulin, H.; Thomas, G. R.; Friesen, A. D.; Al-Shaqha, W. A.; Chahine, M. Pyridoxal-5'-Phosphate (MC-1), a Vitamin B6 Derivative, Inhibits Expressed P2X Receptors. *Can J Physiol Pharmacol* **2014**, *92* (3), 189–196.

(121) Galluzzi, L.; Vitale, I.; Senovilla, L.; Olaussen, K. A.; Pinna, G.; Eisenberg, T.; Goubar, A.; Martins, I.; Michels, J.; Kratassiouk, G.; Carmona-Gutierrez, D.; Scoazec, M.; Vacchelli, E.; Schlemmer, F.; Kepp, O.; Shen, S.; Tailler, M.; Niso-Santano, M.; Morselli, E.; Criollo, A.; Adjemian, S.; Jemaà, M.; Chaba, K.; Pailleret, C.; Michaud, M.; Pietrocola, F.; Tajeddine, N.; Rouge, T. de L. M.; Araujo, N.; Morozova, N.; Robert, T.; Ripoche, H.; Commo, F.; Besse, B.; Validire, P.; Fouret, P.; Robin, A.; Dorvault, N.; Girard, P.; Gouy, S.; Pautier, P.; Jägemann, N.; Nickel, A.-C.; Marsili, S.; Paccard, C.; Servant, N.; Hupé, P.; Behrens, C.; Behnam-Motlagh, P.; Kohno, K.; Cremer, I.; Damotte, D.; Alifano, M.; Midttun, Ø.; Ueland, P. M.; Lazar, V.; Dessen, P.; Zischka, H.; Chatelut, E.; Castedo, M.; Madeo, F.; Barillot, E.; Thomale, J.; Wistuba, I. I.; Sautès-Fridman, C.; Zitvogel, L.; Soria, J.-C.; Harel-Bellan, A.; Kroemer, G. Prognostic Impact of Vitamin B6 Metabolism in Lung Cancer. *Cell Reports* **2012**, *2* (2), 257–269.

(122) Galluzzi, L.; Marsili ,Sabrina; Vitale ,Ilio; Senovilla ,Laura; Michels ,Judith; Garcia ,Pauline; Vacchelli ,Erika; Chatelut ,Etienne; Castedo ,Maria; and Kroemer, G. Vitamin B6 Metabolism Influences the Intracellular Accumulation of Cisplatin. *Cell Cycle* **2013**, *12* (3), 417–421.

(123) Aranda, F.; Bloy, N.; Pesquet, J.; Petit, B.; Chaba, K.; Sauvat, A.; Kepp, O.; Khadra, N.; Enot, D.; Pfirschke, C.; Pittet, M.; Zitvogel, L.; Kroemer, G.; Senovilla, L. Immune-Dependent Antineoplastic Effects of Cisplatin plus Pyridoxine in Non-Small-Cell Lung Cancer. *Oncogene* **2015**, *34* (23), 3053–3062.

(124) Johansson, M.; Relton, C.; Ueland, P. M.; Vollset, S. E.; Midttun, Ø.; Nygård, O.; Slimani, N.; Boffetta, P.; Jenab, M.; Clavel-Chapelon, F.; Boutron-Ruault, M. C.; Fagherazzi, G.; Kaaks, R.; Rohrmann, S.; Boeing, H.; Weikert, C.; Bas Buenode-Mesquita, H.; Ros, M. M.; Van Gils, C. H.; Peeters, P. H. M.; Agudo, A.; Barricarte, A.; Navarro, C.; Rodríguez, L.; Sánchez, M. J.; Larrañaga, N.; Khaw, K. T.; Wareham, N.; Allen, N. E.; Crowe, F.; Gallo, V.; Norat, T.; Krogh, V.; Masala, G.; Panico, S.; Sacerdote, C.; Tumino, R.; Trichopoulou, A.; Lagiou, P.; Trichopoulos, D.; Rasmuson, T.; Hallmans, G.; Riboli, E.; Vineis, P.; Brennan, P. Serum B Vitamin Levels and Risk of Lung Cancer. *JAMA* **2010**, *303* (23), 2377–2385.

(125) Orts-Arroyo, M.; Ten-Esteve, A.; Ginés-Cárdenas, S.; Cerdá-Alberich, L.; Martí-Bonmatí, L.; Martínez-Lillo, J. A Gadolinium(III) Complex Based on Pyridoxine Molecule with Single-Ion Magnet and Magnetic Resonance Imaging Properties. *International Journal of Molecular Sciences* **2024**, *25* (4), 2112.

(126) Upton, R.; ElSohly, M.; Romm. A.; Russo, E.; Sexton, M. *Cannabis Inflorescence: Cannabis Spp.; Standards of Identity, Analysis, and Quality Control*. American Herbal Pharmacopoeia: Scotts Valley, CA, **2014**.

(127) Richter, G.; Hazzah, T.; Hartsel, J. A.; Eades, J., Hickory, B.; Makriyannis, A. Cannabis Sativa: An Overview. *Nutraceuticals*; Academic Press, **2021**; 603–624.

(128) J. Bloemendal, V. R. L.; Hest, J. C. M. van; T. Rutjes, F. P. J. Synthetic Pathways to Tetrahydrocannabinol (THC): An Overview. *Organic & Biomolecular Chemistry* **2020**, *18* (17), 3203–3215.

(129) Grotenhermen, F. Pharmacokinetics and Pharmacodynamics of Cannabinoids. *Clin Pharmacokinet* **2003**, *42* (4), 327–360.

(130) Schwope, D. M.; Bosker, W. M.; Ramaekers, J. G.; Gorelick, D. A.; Huestis, M. A. Psychomotor Performance, Subjective and Physiological Effects and Whole Blood Δ^9-Tetrahydrocannabinol Concentrations in Heavy, Chronic Cannabis Smokers Following Acute Smoked Cannabis. *J Anal Toxicol* **2012**, *36* (6), 405–412.

(131) D'Souza, D. C.; Perry, E.; MacDougall, L.; Ammerman, Y.; Cooper, T.; Wu, Y.; Braley, G.; Gueorguieva, R.; Krystal, J. H. The Psychotomimetic Effects of Intravenous Delta-9-Tetrahydrocannabinol in Healthy Individuals: Implications for Psychosis. *Neuropsychopharmacol* **2004**, *29* (8), 1558–1572.

(132) Stella, N. THC and CBD: Similarities and Differences between Siblings. *Neuron* **2023**, *111* (3), 302–327.

(133) Vemuri, V. K.; Makriyannis, A. Medicinal Chemistry of Cannabinoids. *Clin Pharmacol Ther* **2015**, *97* (6), 553–558.

(134) Pacher, P.; Kogan, N. M.; Mechoulam, R. Beyond THC and Endocannabinoids. *Annual Review of Pharmacology and Toxicology* **2020**, *60*, 637–659.

(135) Maccarrone, M. Metabolism of the Endocannabinoid Anandamide: Open Questions after 25 Years. *Front Mol Neurosci* **2017**, *10*, 166.

(136) Pintori, N.; Caria, F.; De Luca, M. A.; Miliano, C. THC and CBD: Villain versus Hero? Insights into Adolescent Exposure. *International Journal of Molecular Sciences* **2023**, *24* (6), 5251.

(137) Hill, A. J.; Williams, C. M.; Whalley, B. J.; Stephens, G. J. Phytocannabinoids as Novel Therapeutic Agents in CNS Disorders. *Pharmacol Ther* **2012**, *133* (1), 79–97.

(138) Lemberger, L.; Crabtree, R. E.; Rowe, H. M. 11-Hydroxy- 9 -Tetrahydrocannabinol: Pharmacology, Disposition, and Metabolism of a Major Metabolite of Marihuana in Man. *Science* **1972**, *177* (4043), 62–64.

(139) Schwope, D. M.; Karschner, E. L.; Gorelick, D. A.; Huestis, M. A. Identification of Recent Cannabis Use: Whole-Blood and Plasma Free and Glucuronidated Cannabinoid Pharmacokinetics Following Controlled Smoked Cannabis Administration. *Clin Chem* **2011**, *57* (10), 1406–1414.

(140) Huestis, M. A. Human Cannabinoid Pharmacokinetics. *Chem Biodivers* **2007**, *4* (8), 1770–1804.

(141) Gunasekaran, N.; Long, L. E.; Dawson, B. L.; Hansen, G. H.; Richardson, D. P.; Li, K. M.; Arnold, J. C.; McGregor, I. S. Reintoxication: The Release of Fat-Stored Δ 9-Tetrahydrocannabinol (THC) into Blood Is Enhanced by Food Deprivation or ACTH Exposure. Br. J. Pharmacol. **2009**, *158* (5), 1330-7.

(142) Gorey, C.; Kuhns, L.; Smaragdi, E.; Kroon, E.; Cousijn, J. Age-Related Differences in the Impact of Cannabis Use on the Brain and Cognition: A Systematic Review. *European Archives of Psychiatry and Clinical Neuroscience* **2019**, *269* (1), 37.

(143) Forner-Piquer, I.; Giommi, C.; Sella, F.; Lombó, M.; Montik, N.; Dalla Valle, L.; Carnevali, O. Endocannabinoid System and Metabolism: The Influences of Sex. *International Journal of Molecular Sciences* **2024**, *25* (22), 11909.

(144) Wagner, E. J. Sex Differences in Cannabinoid-Regulated Biology: A Focus on Energy Homeostasis. *Frontiers in Neuroendocrinology* **2016**, *40*, 101–109.

Chapter 2: Mapping Vitamin B_6 Metabolism by Hydrazo-CEST Magnetic Resonance Imaging

Emilie Marie Sophie Patit-Tha Brun ‡[1, 2], Nicholas David Calvert ‡[1, 2], Mojmir Suchý [1, 2], Alexia Kirby [2, 3], Gerd Melkus [4, 5], Ruslan Garipov [6], Christina L. Addison [7, 8, 9] and Adam J. Shuhendler [1, 2, 3]*

[1]Dept. Chemistry & Biomolecular Sciences, University of Ottawa, Ottawa, Ontario, Canada. E-mail: adam.shuhendler@uottawa.ca

[2]University of Ottawa Heart Institute, Ottawa, Ontario, Canada

[3]Dept. Biology, University of Ottawa, Ottawa, Ontario, Canada

[4]Dept. Medical Imaging, The Ottawa Hospital, Ottawa, ON, Canada

[5]Dept. Radiology, University of Ottawa, Ottawa, Ontario, Canada

[6]MR Solutions Ltd, Guildford, Surrey, UK

[7]Cancer Therapeutics Program, Ottawa Hospital Research Institute, Ottawa, Canada

[8]Dept. Biochemistry, Microbiology and Immunology, University of Ottawa, Ottawa, Canada

[9]Dept. Medicine, University of Ottawa, Ottawa, Ontario, Canada

‡ Authors contributed equally to this work.

2.1. Overview of the Research Article Presented in this Chapter

A second generation probe, 2-hydrazinonicotinic acid (2-HYNIC) has been tested as a potential hydrazoCEST contrast agent. Previous studies reported a first generation probe, *N*-aminoanthranilic acid (NA^3), which demonstrated selectivity for aliphatic aldehydes. In the other hand, 2-HYNIC presents selectivity for aromatic aldehydes, such as vitamin B_6, producing higher CEST signal in the presence of pyridoxal 5'-phosphate. Following improvements in the purity and yield of the synthesis steps, the CEST-MRI properties of 2-HYNIC were thoroughly analyzed. *In vitro* and *in vivo* studies, using two lung cancer lines, were conducted with both generations of probes to evaluate the efficacy of 2-HYNIC as a contrast agent for mapping pyridoxal 5'-phosphate through MRI.

2.2. Author Contributions

E.M.S.P.B. and N.D.C contributed equally to this work. E.M.S.P.B. performed all the Z-spectra acquisition and analysis on the 300 MHz NMR at different concentrations and pH values. N.D.C performed *in vitro* and *in vivo* studies. M.S. was responsible for the synthesis and characterization of chemical compounds. A.K. performed animal studies including implementation and imaging.

2.3. Copyright

Brun E.M.S.P, Clavert N.D., Suchý M. et al. Mapping vitamin B_6 metabolism by hydrazoCEST magnetic resonance imaging. ***Chem. Commun.***, 2021,**57**, 10867-10870. https://doi.org/10.1039/D1CC03704H.

2.4. Abstract

A new CEST-MRI contrast agent, 2-HYNIC, capable of sensing aromatic aldehydes is reported. Pyridoxal 5'-phosphate, a key Vitamin B_6 metabolite necessary for >140 biotransformations was mapped by CEST-MRI *in vitro* and *in vivo* in lung cancer. 2-HYNIC provided access to this key biomarker associated with a variety of human diseases.

2.5. Introduction

Vitamin B_6, or pyridoxine (PN), is an essential nutrient obtained from our diet that is a coenzyme necessary for more than 140 biochemical transformations, including neurotransmitter, amino acid, and glycogen metabolism [1]. After ingestion, vitamin B_6 metabolism involves four protein-driven processes: (i) PN is actively taken up into cells by the transporter TPN1; (ii) intracellular PN is oxidized to the aldehyde pyridoxal (PL) by pyridoxine 5'-phosphate oxidase (PNPO); (iii) PL is phosphorylated to form the active coenzyme pyridoxal 5'-phosphate (PLP) by

pyridoxal kinase (PDXK); (iv) pyridoxal phosphatase (PDXP) can dephosphorylate PLP to PL (Figure 2.1) [1]. Any extracellular PLP can be salvaged through the action of PDXP and subsequent cell uptake by TPN1 [2]. Ultimately, this kinase-phosphatase-oxidase system regulates the intracellular pool of PLP available for metabolism, providing a sufficient supply to meet metabolic needs [3].

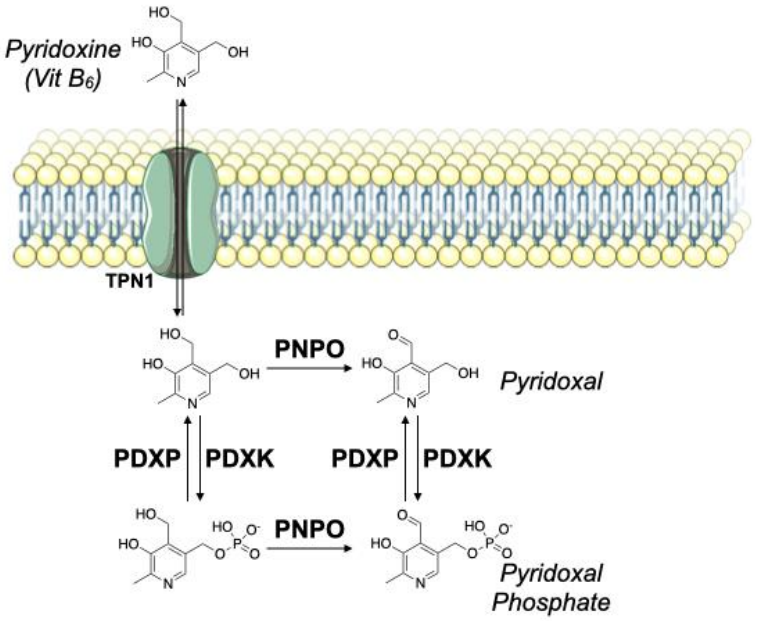

Figure 2.1 Uptake and metabolism of pyridoxine to generate pyridoxal (PL) and pyridoxal 5'-phosphate (PLP). PNPO: pyridoxine 5'-phosphate oxidase, PDXK: pyridoxal kinase, PDXP: pyridoxal phosphatase.

Because of its central role in the metabolism of key biochemicals essential for cell function, dysregulation of the PLP-to-PL balance has been associated with a variety of pathologies. PLP-dependant enzymes are critical for neurotransmitter biosynthesis, and deficiencies in PLP have been linked to neurodegeneration, pain and depression [4, 5]. Pyridoxine metabolic status is also

related to the severity of injury following neurotrauma, where vitamin B_6 supplementation is found to be neuroprotective [6]. Since the intracellular pool of PLP serves as a metabolic nexus, dysregulation of the kinase- phosphatase activity balance controlling this coenzyme (i.e. low PDXK, high PDXP) also conferred cancer cell resistance to exogenous chemical or physical stress (i.e. resistance to therapy) [7]. This effect was attributed to a general stress–resistance mechanism through the multi-pronged limitation of metabolism driven by PLP deprivation, since both PN and PDXK were necessary for cancer cell sensitization. Importantly, non-small cell lung cancer patients with low PDXK expression consistently had poorer prognoses across two patient cohorts [7]. The key role of the PDXK–PDXP activity balance in health and disease has been exploited for a range of clinical diagnoses through the measurement of plasma PLP concentrations [8]. However, the assumption that plasma levels of PLP approximate intracellular PLP levels is tenuous: plasma levels of PLP fluctuate with dietary intake, but intracellular levels remain constant and are under tight control of the kinase-phosphatase-oxidase system [9, 10, 11]; mutations in the kinase-phosphatase-oxidase system can occur, which would further alter intracellular PLP levels independently of plasma concentrations [12]; vitamin B_6 metabolism is sex-dependent [13]. Recently, a fluorogenic probe with high specificity for PLP has been reported and demonstrated to accurately measure intracellular PLP in cultured human cells [14], presenting the first *in vitro* assay capable of overcoming the limitations of plasma PLP measurements. While mapping PLP as a marker of the PDXK–PDXP activity balance in tissues and live organisms would be valuable to both understand the biochemistry of this coenzyme and to realize its potential as a diagnostic and prognostic biomarker, accessing intracellular PLP as an *in vivo* biomarker has remained elusive until now.

2.6. Results and Discussion

In the presented work we achieved the mapping of PLP levels *in vitro* and *in vivo* by chemical exchange saturation transfer magnetic resonance imaging (CEST-MRI), which builds upon our previous work developing aldehyde-conditional contrast agents [15, 16, 17]. With this HydrazoCEST approach, CEST signal is only produced after the reaction of the hydrazine-derived contrast agent with an aldehyde to form a hydrazone (Figure 2.2), affording aldehyde-directed activity-based sensing. The first-generation contrast agent was based on the *N*-amino anthranilic acid (**NA^3**) scaffold [17], which was previously shown to undergo rapid and catalyst-free formation of hydrazones under physiological conditions [17, 18, 19, 20]. By changing the core of the HydrazoCEST contrast agent from the first-generation **NA^3** to the second-generation 2-hydrazinonicotinic acid (**2-HYNIC**) core reported herein (Figure 2.2B), the signalling selectivity of these contrast agents could be tuned from favouring aliphatic aldehydes for NA^3, to favouring aromatic aldehydes for **2-HYNIC** (Figure 2.2C vs. D). The chemical synthesis of **2-HYNIC** and all hydrazones associated with this work can be found in supplementary information. We have previously found that a hydrogen bond between the proton on the proximal hydrazone nitrogen and the neighbouring carboxylate was necessary for CEST signal generation [17]. This hydrogen bond optimizes the exchange rate between the hydrazone and bulk water for CEST signal production, as has been reported in other classes of CEST-MRI contrast agents [21, 22, 23]. ^{1}H NMR and molecular modelling studies previously performed suggested that this key hydrogen bonding distance was minimized when the hydrazone was co-planar with the aromatic ring, *i.e.* the hydrazone favoured the *E*-conformation [17], and which were applied here to study the origin of the aromatic aldehyde selectivity of **2-HYNIC**. While the acetaldehyde-derived hydrazone of **NA^3** favours the *E*

conformation (Supplementary S2A), that of **2-HYNIC** favours the *Z* conformation (Supplementary S2B), which may account for the substantial reduction in CEST-MRI contrast production for aliphatic aldehydes using **2-HYNIC** *vs*. **NA^3** (Figure 2.2C *vs*. D). Conversely, only the 2-formyl- benzenesulfonic acid-derived hydrazone of **2-HYNIC** showed hydrazone proton peak broadening indicative of hydrogen bonding to the neighbouring carboxylate (Supplementary S2D *vs*. C). Overall, the *Z*-spectra obtained demonstrates the inversion of the signalling selectivity between first- and second-generation HydrazoCEST contrast agents, with **2-HYNIC** favouring signal production from hydrazones derived from aromatic aldehydes.

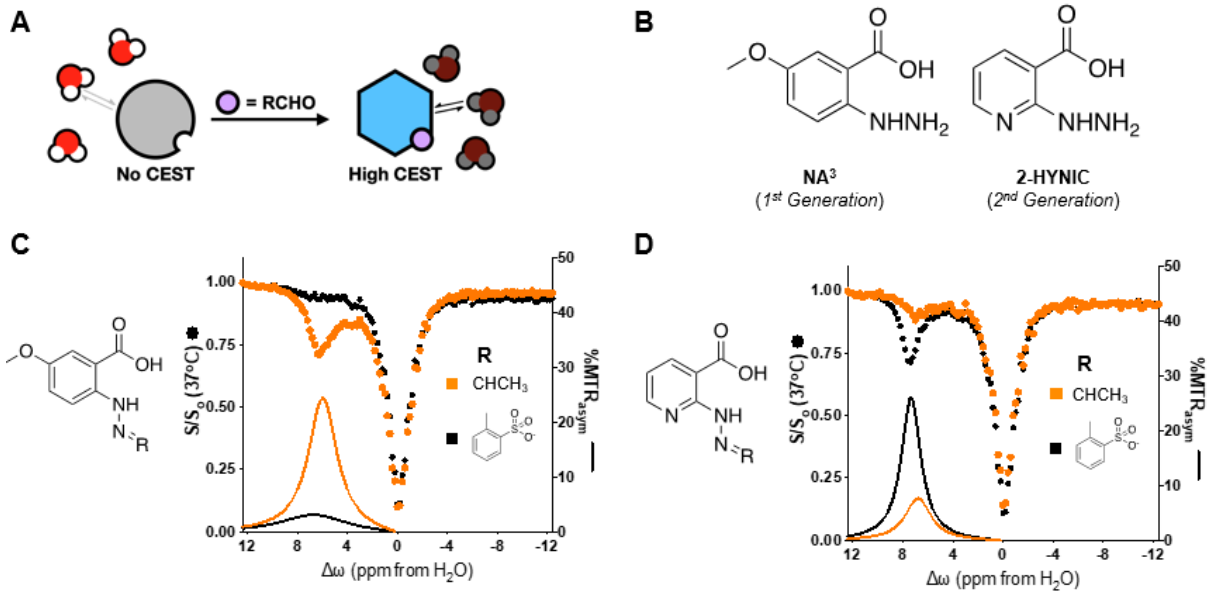

Figure 2.2 Aldehyde-dependent signalling selectivity of HydrazoCEST contrast agents. (A) CEST-MRI contrast is only produced from the hydrazone form of the contrast agent. (B) Chemical structure of the first-generation (**NA^3**) and second-generation (**2-HYNIC**) HydrazoCEST-MRI contrast agents. *Z*-Spectra (dots) and $\%MTR_{asym}$ (lines) for **NA^3** (C) and **2-HYNIC** (D) upon hydrazone formation with acetaldehyde (orange) or 2-formylbenzenesulfonic acid (black).

Given the ability of 2-HYNIC-derived hydrazones to provide substantial CEST-MRI contrast when bound to aromatic aldehydes, we next evaluated the signal production from hydrazones derived from the reaction of metabolites of vitamin B_6 with **NA^3** or **2-HYNIC** (Figure 2.3). While the **NA^3**-PL hydrazone produced negligible CEST contrast, the PLP-derived hydrazone resulted in $\%MTR_{asym}$ of approximately 10% (Figure 2.3A). A similar signal enhancement pattern was observed for the **2-HYNIC**-derived hydrazones, however at substantially greater contrast values: the PL hydrazone yielded a $\%MTR_{asym}$ of approximately 5% at 20 mM, while the PLP-derived hydrazone resulted in 12% and 28% at 20 and 40 mM, respectively (Figure 2.3B). In order to investigate the origin of the enhanced signal production from **2-HYNIC**-PLP hydrazones, the $\%MTR_{asym}$ was evaluated over the pH range 6.0 to 12.0 (Supplementary S3). While the **NA^3**-PL(P) and **2-HYNIC**-PL hydrazones showed a sigmoidal dependence of signal on pH with inflection points around pH 10.5 and 9.5, respectively, the **2-HYNIC**-PLP hydrazone maintained high signal production at pH > 7.5 (Supplementary S3B). UV spectra of the **2-HYNIC**-derived hydrazones were acquired from pH 7.5 to 10.0 (0.5 pH unit increments), with the PL-derived hydrazone showing an increase in the bathochromic absorption (λ_{abs} 325 → 385 nm) between pH 9.0 and 9.5 (Supplementary S3C and D). When the absorbance ratio at λ_{385} / λ_{325} was plotted as a function of pH, the sigmoidal curve with an inflection point between pH 9.0 and 9.5 for the PL-derived hydrazone was recapitulated, however the curve for the PLP-derived hydrazone remained relatively unchanged over the pH range evaluated (Supplementary S3E). These spectral data suggest that there is a conformational change in the **2-HYNIC**-PL hydrazone that increases absorption at λ = 385 nm at pH > 9.0, promoting enhanced CEST-MRI contrast. This conformational change was observed through density functional theory mechanical modelling of the **2-HYNIC**-PL and **2-HYNIC**-PLP hydrazones in aqueous

environments at pH 7.5 and 10.0 (Supplementary S4). The **2-HYNIC**-PL hydrazone switches from a twisted conformation at pH 7.5 with a 2.78 Å hydrogen bond distance between the hydrazone proton and neighboring carboxylate to a planar conformation at pH 10.0, reducing the hydrogen bond distance to 1.79 Å (Supplementary S4, top). The **2-HYNIC**-PLP hydrazone maintains a planar hydrazone conformation at both pH 7.5 and 10.0, keeping the hydrogen bond distance around 1.76 Å (Supplementary S4, bottom). Taken together, these data demonstrate that **2-HYNIC** can differentially report on the presence of PL and PLP, where PL-derived hydrazones are poor CEST-MRI contrast agents at physiological pH due to a nonplanar conformation, but those derived from PLP maintain a planar conformation and provide substantial CEST-MRI signal at physiological pH (Figure 2.3C).

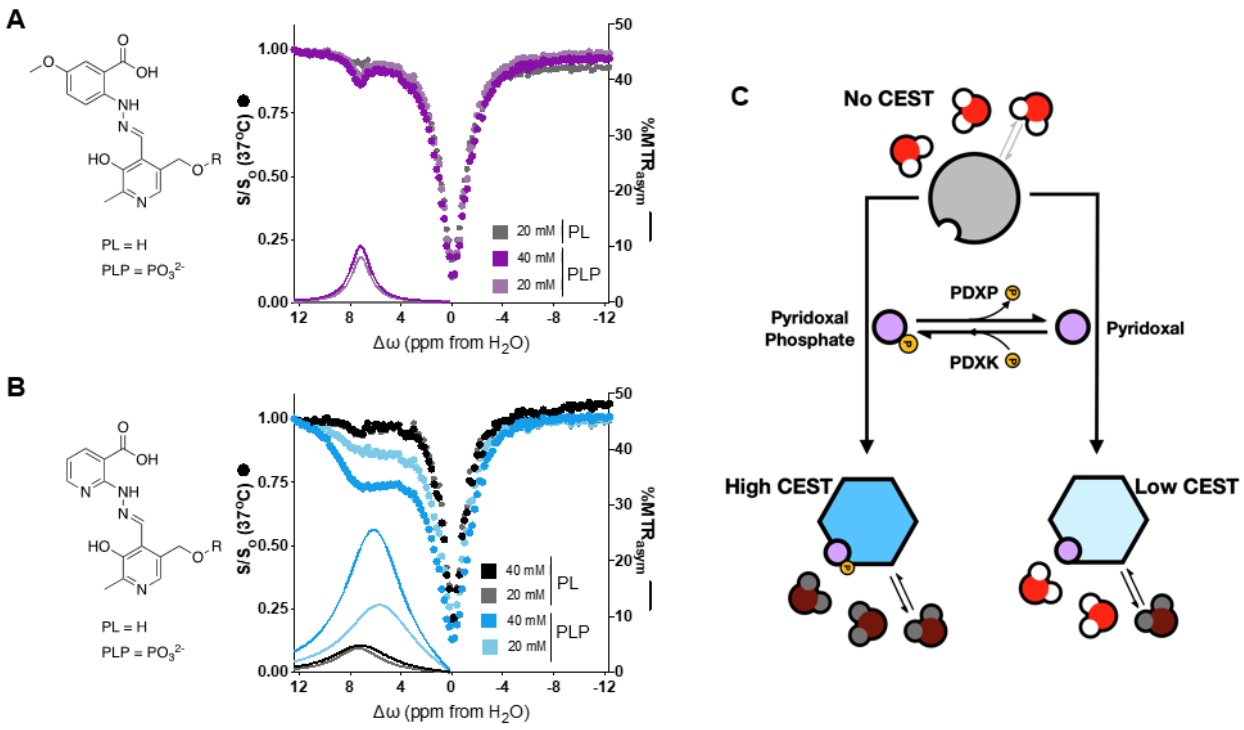

Figure 2.3 The ability of HydrazoCEST contrast agents to detect vitamin B_6 metabolites. (A) *Z*-Spectra (dots) and $\%MTR_{asym}$ (lines) for **NA^3** upon hydrazone formation with PL (20 mM, grey) or PLP (20 mM, light purple; 40 mM, purple). The **NA^3**-PL hydrazone was not soluble at 40 mM. (B) *Z*-Spectra (dots) and $\%MTR_{asym}$ (lines) for **2-HYNIC** upon hydrazone formation with PL (20 mM, grey; 40 mM, black) or PLP (20 mM, light blue; 40 mM, blue). (C) Schematic representation of the ability of **2-HYNIC** to produce substantial CEST-MRI contrast upon binding to PLP, serving as a marker of the PDXK–PDXP activity balance.

Towards the goal of accessing vitamin B_6 metabolism as an imaging biomarker and given the prognostic value of PDXK activity in lung cancer [7], we compared the capability of **NA^3** and **2-HYNIC** to detect PLP vs. PL by CEST-MRI in two human non-small cell lung cancer cell lines *in vitro*: A549 adenocarcinoma and H460 large cell carcinoma (Figure 2.4A). Compared to naïve

cells, only a modest increase in $\%MTR_{asym}$ was observed upon incubation with 20 mM **NA^3**. However, a substantial increase in contrast resulted from the incubation of both cell lines treated with 20 mM **2-HYNIC**, with the signal being greater in H460 than in A549 ($\%MTR_{asym}$ of 3.6 *vs*. 2.9). Cells were also analyzed for vitamin B_6 metabolite content by liquid chromatography– mass spectrometry (Figure 2.4B). In naïve cells, only PN, PL, and PLP were detected, with the total intracellular PL + PLP content being similar between H460 and A549 cells. Upon incubation with **2-HYNIC**, PL- and PLP-derived hydrazones were found to comprise most of the intracellular PL + PLP pool, confirming that **2-HYNIC** can enter cells and trap the reactive carbonyl metabolites of vitamin B_6. The total amount of derivatized and free intracellular PL + PLP was not substantially different between the cell lines tested, however the intracellular PLP-to-PL ratio was greater for H460 than A549, which corroborates the greater CEST signal in H460 cells following *in vitro* imaging (Figure 2.4A). **2-HYNIC** was non-toxic within the 2 h incubation time imaged (Supplementary S5).

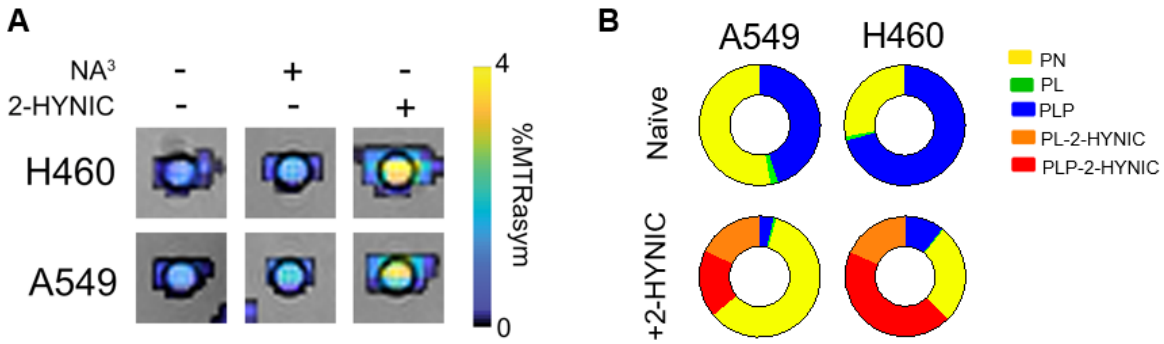

Figure 2.4 Mapping PLP by 2-HYNIC in lung cancer cells *in vitro*. (A) CEST-MRI (Δω = 6.5 ppm mapped onto a T_1-weighted phantom image) of cell pellets of H460 (top) or A549 (bottom) naïve (left) or after incubation with **NA³** (middle) or **2-HYNIC** (right). (B) Vitamin B_6 metabolism was evaluated in A549 (left) and H460 (right) cells by liquid chromatograph–mass spectrometry either naïve (top) or after incubation with **2-HYNIC** (bottom).

With the successful imaging of intracellular PLP *in vitro*, **2-HYNIC** was applied to map PLP in animals bearing heterotopic A549 or H460 tumor xenografts (Figure 2.5). Following the intravenous administration of **2-HYNIC**, an increase in CEST-MRI contrast at Δω = 6.5 ppm was observed in the tumor and in surrounding tissues (Figure 2.5A), steadily increasing in the tumor up to 60 min post-injection (Figure 2.5B and Supplementary S5). The location of the A549 tumor coincided axially with the bladder, which demonstrated similar time-dependent increase in CEST-MRI contrast (Figure 2.5Ai *vs*. iii). Similarly to the *in vitro* results, CEST-MRI contrast was significantly greater in the H460 tumors after 60 min ($p < 0.05$), even after normalizing to pre-injection tumor contrast (Figure 2.5C). Since H460 xenografts were previously found to be more sensitive to a range of chemotherapeutic agents, including cisplatin, gemcitabine, and vinorelbine [24], the difference in PLP levels between H460 and A549 mapped by **2-HYNIC** may inform

personalized therapy selection. Importantly, all of these agents are components of chemotherapeutic combinations applied clinically for lung cancer treatment [25], encouraging future studies directly investigating the value of **2-HYNIC**-mediated PLP mapping for predicting the efficacy of lung cancer chemotherapy.

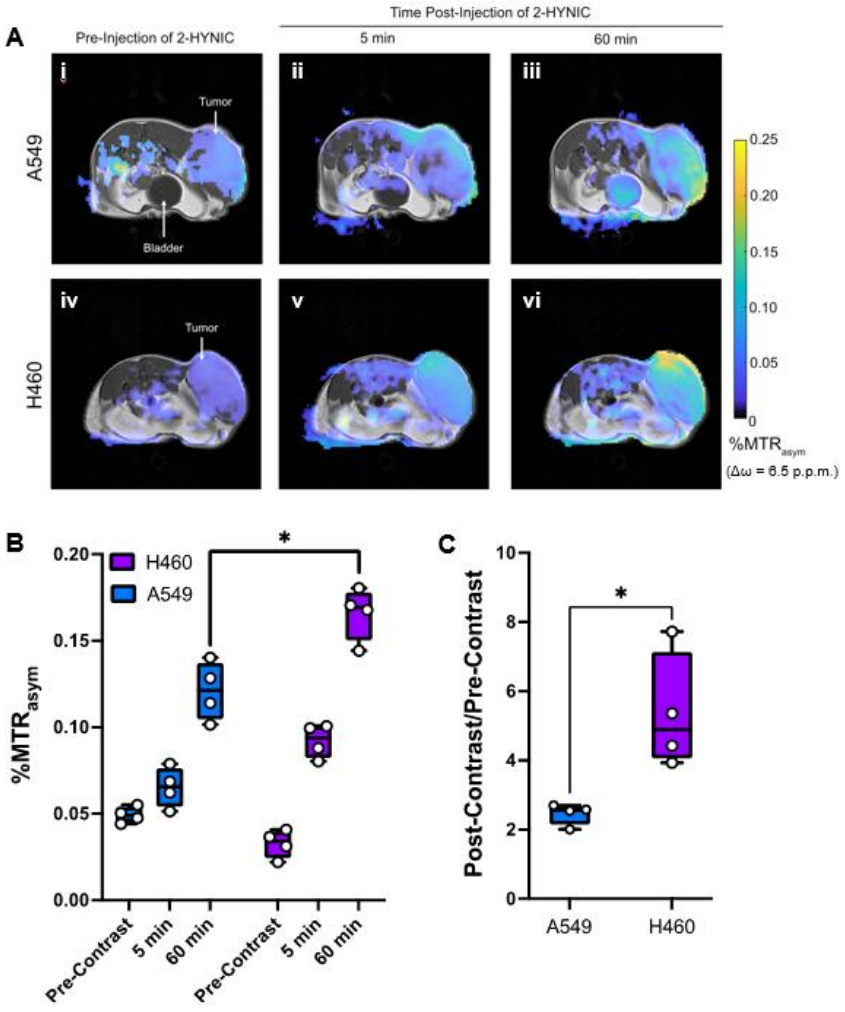

Figure 2.5 Mapping of PLP by 2-HYNIC *in vivo* in lung tumor xenografts. (A) CEST-MRI (Δω = 6.5 ppm mapped onto an axial T_1-weighted image) of mice bearing A549 (i–iii) or H460 (iv–vi) before (i and vi), 5 min (ii and v), and 60 min (iii and vi) after intravenous administration of **2-HYNIC**. Tumor xenografts of A549 and H460 human lung cancers were established in a total of n=8 (n=4 *per* tumor cell type). (B) Average $\%MTR_{asym}$ value for a tumor region of interest are plotted over time for A549 (blue) and H460 (purple) tumors. (C) Plot of the average $\%MTR_{asym}$ 60 min post-contrast injection normalized to the pre-injection signal for A549 (blue) and H460 (purple) tumors. Plots show mean (horizontal line), standard deviation (box), and min/max range (whiskers) with individual data points. * $p < 0.05$.

2.7. Conclusion

Herein we present a second generation HydrazoCEST contrast agent, **2-HYNIC**, enabling the mapping of PLP *in vitro* and *in vivo* by MRI. Unlike the first-generation contrast agent based on the **NA^3** scaffold with signalling preference for aliphatic aldehydes, the CEST-MRI contrast generated by **2-HYNIC** is substantially enhanced upon hydrazone formation with aromatic aldehydes. The importance of vitamin B_6 metabolism in health and its alteration in a variety of pathologies, coupled with the limited number of tools available to directly evaluate intracellular PLP levels and the lack of tools available for *in vivo* mapping, encouraged the application of **2-HYNIC** to map aromatic aldehyde B_6 vitamers key to many biochemical functions. Intracellular PL:PLP content was mapped *in vitro* in A549 and H460 human lung cancer cells, with confirmation of hydrazone formation by mass spectrometry. Importantly, the differences in PL:PLP content observed *in vitro* between the two cell lines were recapitulated *in vivo*, supporting the ability of **2-HYNIC** to map the PL:PLP balance by CEST-MRI. With the introduction of **2-HYNIC** as second-generation HydrazoCEST contrast agent, intracellular PL:PLP content becomes an accessible imaging biomarker with the potential to illuminate a range of diseases, opening up new avenues of translational and fundamental research surrounding this critical coenzyme sourced from our diet.

2.8. Acknowledgements

This work was supported by NSERC Discovery Grant RGPIN 2015-05796 (A. J. S.), the Canada Research Chairs Program 950-230754 (A. J. S.), and the Canadian Institutes of Health Research PJT376892 (A. J. S.), and student support from the Ontario Graduate Scholars Program (A. K.) and Queen Elizabeth II Graduate Student Scholarship in Science and Technology (N. C.).

2.9. Conflict of Interests

There are no conflicts to declare.

2.10. Supplementary Information

2.10.1. General Experimental Procedures

Reagents were commercially available or prepared as stated below. All solvents were HPLC grade except for water (18.2 MΩ cm millipore water) and diethyl ether (Et_2O). Volatiles were removed under reduced pressure in a rotary evaporator. Thin-layer chromatography (TLC) was carried out on Al backed silica gel plates with compounds visualized by 5% ninhydrin stain and UV light. Melting points (mp) were obtained on EZ-Melt apparatus and are uncorrected. NMR spectra were recorded on a 300 spectrometer for ^1H NMR spectra δ values were recorded as follows: DMSO-D_6 (2.50 ppm), D_2O containing one drop of 40% NaOD, pH > 10 (4.79 ppm); for

^{13}C (93.75 or 125 MHz) δ DMSO-D_6 (39.50 ppm). Mass spectra (MS) were obtained using electron impact (EI, compound **4**) or electrospray ionisation (ESI, compounds **3**, **5a** and **6a**); compounds **5b** and **6b** were analyzed by tandem ultra-high performance hydrophilic interaction liquid chromatography-ESI (UPLC-HILIC-Z-ESI) in negative mode using the chromatographic conditions described previously [26]. Synthetic procedures associated with this work can be found in the Supplementary Scheme S1.

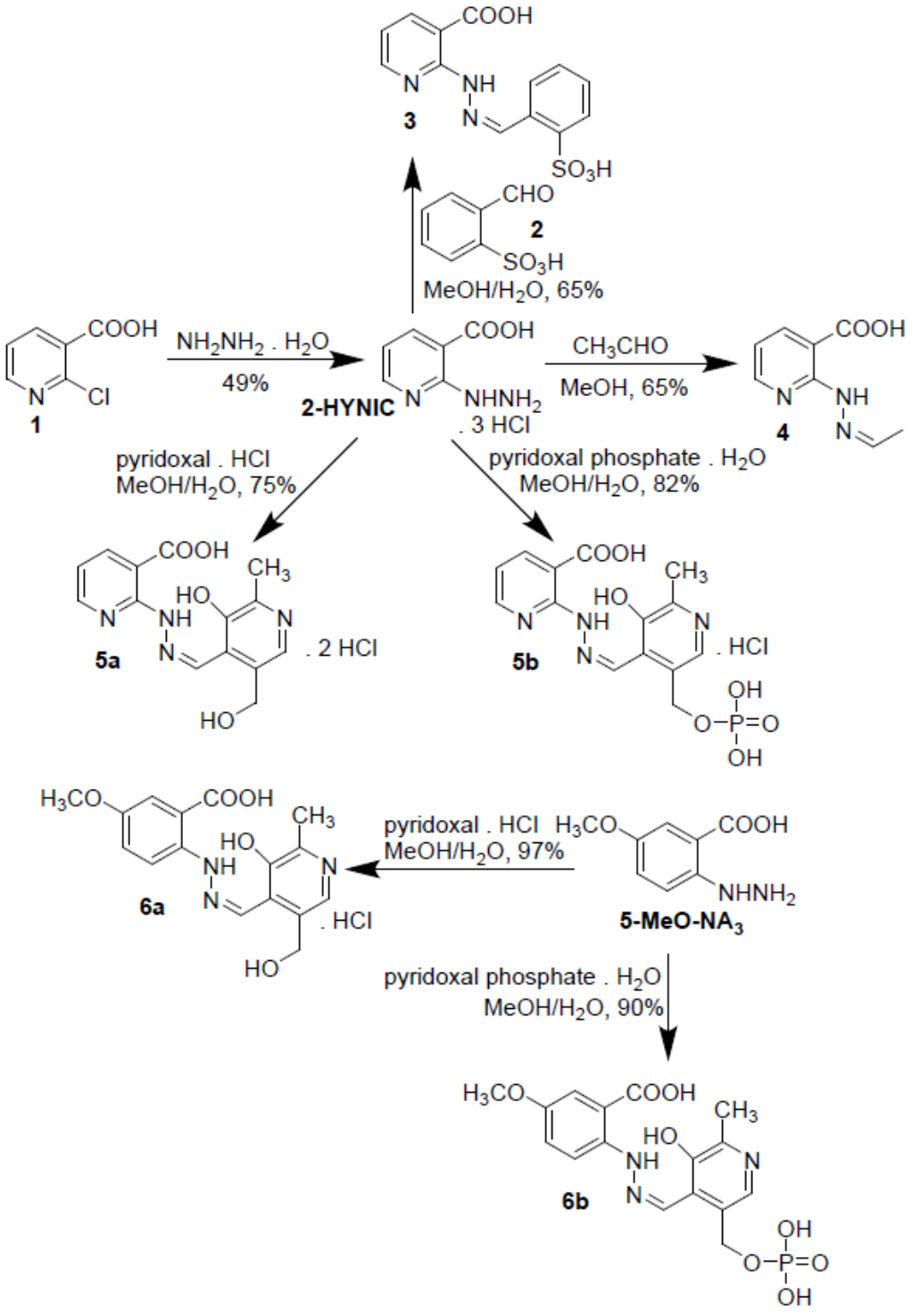

S1. General synthetic scheme.

2.10.2. Synthetic Procedure for the preparation of hydrazones **3**, **4**, **5a**, **5b**, **6a** and **6b**

Preparation of 2-hydrazinonicotinic acid trihydrochloride (2-HYNIC · 3 HCl)

This material was prepared as described previously [27]. Briefly, 2-chloronicotinic acid (**1**, 1.58 g, 10 mmol) was dissolved in hydrazine hydrate solution (7 mL) and the mixture was stirred for 2 h at 100 ˚C. The volatiles were evaporated, the residue was dissolved in water (10 mL), resulting solution was cooled in an ice bath and the pH was adjusted (pH ~ 5, conc. HCl). Separated precipitate was filtered off with suction, was washed with ice-cold water and was dried. 2-Hydrazinonicotinic acid trihydrochloride (2-HYNIC · 3 HCl), pale yellow solid, 1.29 g, 49%. Spectral characteristics of 2-HYNIC · 3 HCl were in agreement with those described previously [26].

Reaction of 2-HYNIC · 3 HCl with 2-formylbenzenesulfonic acid (2)

A suspension of 2-HYNIC · 3 HCl (263 mg, 1 mmol) in MeOH (10 mL) and water (2.5 mL) was treated with 2-formylbenzenesulfonic acid sodium salt (**2**, 208 mg, 1 mmol). The mixture was stirred for 18 h at room temperature (rt), the precipitate was filtered off with suction, was washed with ice-cold water and was dried. Hydrazone **3**, yellow solid, 208 mg, 65%. ^{1}H NMR δ (D_2O, containing 1 drop of 40% NaOH, pH > 10) 8.75 (s, 1H); 8.21 (m, 1H); 8.17 (dd, *J* = 5.0, 2.0 Hz, 1H); 8.11 (dd, *J* = 8.0, 2.0 Hz, 1H); 7.85 (ddd, *J* = 8.0, 1.5. 0.5 Hz, 1H); 7.56 (tdd, *J* = 7.0, 1.0. 0.5 Hz, 1H); 7.43 (td, *J* = 8.0, 1.5 Hz, 1H); 6.87 (dd, *J* = 7.5, 5.0 Hz, 1H). ^{13}C NMR δ (D_2O, containing 1 drop of 40% NaOH, pH > 10) 173.3, 153.9, 150.0, 141.1, 140.9, 140.0, 131.6, 131.5, 129.0,

126.8 (2 × C), 115.2, 114.3. HRMS (ESI) *m/z* found 322.0512 $[M + H]^+$ (calcd 322.0498 for $C_{13}H_{12}N_3O_5S$).

Reaction of 2-HYNIC · 3 HCl with acetaldehyde

Acetaldehyde (170 µL, 3 mmol) was added to a solution of 2-HYNIC · 3 HCl (263 mg, 1 mmol) in MeOH (2 mL). The mixture was stirred for 18 h at rt, was diluted with Et2O (10 mL) and was set aside for 2 h at -10 ˚C. A precipitate formed; it was filtered off, was washed with ice-cold Et_2O and was dried. Hydrazone **4**, yellow solid, 116 mg, 65%. ^{1}H NMR δ (DMSO-D_6) 11.96 (brs, D_2O exch., 0.35H); 11.75 (br s, D_2O exch., 0.65H); 8.47 (dd, *J* = 7.5, 1.5 Hz, 0.65H); 8.41 (dd, *J* = 7.5, 2.0 Hz, 0.35H); 8.30 (dd, *J* = 5.0, 2.0 Hz, 0.35H); 8.27 (dd, *J* = 5.5, 1.5 Hz, 0.65H); 7.86 (q, *J* = 5.0 Hz, 0.65H); 7.08 (q, *J* = 5.5 Hz, 0.35H); 7.00 (m, 1H); 2.03 (d, *J* = 5.0 Hz, 1.3H); 1.95 (d, *J* = 5.0 Hz, 0.7H). ^{13}C NMR δ (DMSO-D_6) 167.6 (minor), 166.4 (major), 152.4 (minor), 150.6 (major), 150.5 (major), 147.3 (minor), 145.3 (major + minor), 145.1 (major), 143.6 (minor), 114.2 (minor), 113.5 (major), 110.2 (major), 110.0 (minor), 18.5 (major), 13.5 (minor). HRMS (EI) *m/z*; found 179.0695 $[M^+]$ (calcd 179.0695 for $C_8H_9N_3O_2$), LRMS (EI) *m/z* (rel. abundance): 179 $[M^+]$ (10), 94 (60).

Reactions of 2-HYNIC · 3 HCl and 5-methoxy-*N*-aminoanthranilic acid dihydrochloride (5-MeO-NA3 · 2HCl) with pyridoxal and pyridoxal phosphate

Separate suspensions of 2-HYNIC · 3 HCl (132 mg, 0.5 mmol) or 5-MeO-NA[3] · 2HCl (128 mg, 0.5 mmol) in MeOH (5 mL) and water (2.5 mL) were treated with pyridoxal hydrochloride (102 mg, 0.5 mmol) or pyridoxal phosphate hydrate (, 124 mg, 0.5 mmol). The mixtures were stirred for 18 h at rt; the precipitates were filtered off with suction, were washed with ice-cold water and were dried.

Hydrazone **5a** dihydrochloride, yellow solid, 141 mg, 75%. ^{1}H NMR δ (D_2O, containing 1 drop of 40% NaOH, pH > 10) 8.47 (s, 1H); 8.16 (dd, *J* = 5.0, 2.0 Hz, 1H); 8.08 (dd, *J* = 7.5, 2.0 Hz, 1H); 7.40 (s, 1H); 6.81 (dd, *J* = 7.5, 5.0 Hz, 1H); 4.45 (s, 2H); 2.28 (s, 3H). ^{13}C NMR δ (D_2O, containing 1 drop of 40% NaOH, pH > 10) 173.3, 161.5, 154.4, 151.9, 150.6, 141.3, 140.8, 132.4, 131.1, 127.8, 115.0, 113.9, 61.3, 19.0. HRMS (ESI) *m/z* found 303.1108 $[M + H]^+$ (calcd 303.1093 for $C_{14}H_{15}N_4O_4$).

Hydrazone **5b** hydrochloride, orange solid, 172 mg, 82%. ^{1}H NMR δ (D_2O, containing 1 drop of 40% NaOH, pH > 10) 8.20 (s, 1H); 8.07 (dd, *J* = 5.0, 2.0 Hz, 1H); 7.99 (dd, *J* = 7.5, 2.0 Hz, 1H); 7.59 (s, 1H); 6.85 (dd, *J* = 7.5, 5.0 Hz, 1H); 4.86 (d, *J* = 6.0 Hz, 2H); 2.31 (s, 3H). ^{13}C NMR δ (D_2O, containing 1 drop of 40% NaOH, pH > 10) 171.0, 152.8, 151.1, 148.3, 144.7, 138.1, 130.9, 130.3 (d, *J* = 8.5 Hz), 126.1, 116.3, 114.8, 61.7 (d, *J* = 4.5 Hz), 15.4. ^{31}P NMR δ (D_2O, containing 1 drop of 40% NaOH, pH > 10) 0.8 (t, *J* = 6.0 Hz); 0.8 (s, H-decoupled). HRMS (ESI) *m/z* found 381.0613 $[M - H]^-$ (calcd 381.0606 for $C_{14}H_{14}N_4O_7P$).

Hydrazone **6a** hydrochloride, red solid, 179 mg, 97%. ^{1}H NMR δ (D_2O, containing 1 drop of 40% NaOH, pH > 10) 8.28 (s, 1H); 7.32 (s, 1H); 7.25 (d, *J* = 3.0 Hz, 1H); 7.11 (d, *J* = 9.0 Hz, 1H); 6.91 (dd, *J* = 9.0, 3.0 Hz, 1H); 4.51 (s, 2H); 3.66 (s, 3H); 2.22 (s, 3H). ^{13}C NMR δ (D_2O, containing 1 drop of 40% NaOH, pH > 10) 174.6, 161.0, 151.1, 150.9, 140.0, 138.4, 131.6, 130.2, 127.0, 119.5, 118.3, 115.1, 114.0, 61.5, 55.5, 19.0. HRMS (ESI) *m/z* found 332.1259 $[M + H]^+$ (calcd 332.1246 for $C_{16}H_{18}N_3O_5$).

Hydrazone **6b**, orange solid, 186 mg, 90%. ^{1}H NMR δ (D_2O, containing 1 drop of 40% NaOH, pH > 10) 8.38 (s, 1H); 7.79 (s, 1H); 7.56 (d, *J* = 9.0 Hz, 1H); 7.39 (d, *J* = 3.0 Hz, 1H); 7.16 (dd, *J* = 9.0, 3.0 Hz, 1H); 5.13 (d, *J* = 6.0 Hz, 2H); 3.80 (s, 3H); 2.30 (s, 3H). ^{13}C NMR δ (D_2O, containing 1 drop of 40% NaOH, pH > 10) 174.9, 160.0, 151.1, 149.1, 140.4, 139.1, 130.3 (d, *J* = 7.0 Hz), 130.5, 126.8, 119.9, 118.5, 115.3, 115.2, 63.2 (d, *J* = 4.0 Hz), 55.9, 18.9. ^{31}P NMR δ (D_2O, containing 1 drop of 40% NaOH, pH > 10) 4.1 (t, *J* = 6.0 Hz); 4.1 (s, H-decoupled). HRMS (ESI) *m/z* found 410.0765 $[M - H]^-$ (calcd 410.0759 for $C_{16}H_{17}N_3O_8P$).

2.10.3. MRI Acquisition Protocols

Z-spectra Acquisition by 300 MHz NMR

CEST spectra were acquired on a Bruker AVANCE II 300 MHz NMR spectrometer (Bruker Corp., Billerica, MA, USA) equipped with a 5 mm BBOF probe. A pseudo 2D pulse sequence was used with a variable frequency list consisting of 201 values ranging from 20 ppm to -20 ppm (water at 4.7 ppm). At each frequency, 1.15 mW of presaturation power was applied during the 3 second recycle delay followed by a hard 90° pulse (centered at 2.5 ppm). The proton 90° pulse was 12.75 μs. Four scans were averaged for each spectrum. The free induction decays were Fourier transformed and the integral of the water resonance was plotted as a function of the saturation frequency to give a CEST plot. Samples were composed of 10:1 PBS:D_2O solutions of the complexes (adjusted to pH 7.5) and were heated to 37 °C using heated forced air through a Model 1025 Small Animal Monitoring and Gating System (SA Instruments, Inc., Stony Brook, NY). Similar methodology was used to evaluate the pH (15 mM, 37 ºC, pH range range 6.0 to 12.0, increments of 0.5 pH unit) sensitivity of selected agents. Z-spectra were processed using MatLab (v. 2017b, MathWorks, Inc., MA, USA) and invoking the Interactive Peak Fitter code (v.12.1) [T. O'Haver https:/terpconnect.umd.edu/~toh/spectrum/InteractivePeakFitter.htm] to fit Lorentzian curves to the acquired data. Spectra were plotted in GraphPad Prism (v. 7.0c, GraphPad Software, Inc., CA, USA).

CEST MRI Acquisition Routine & Analysis

All CEST-MRI acquisitions were performed on a 3T pre-clinical MRI (MR Solutions, Ltd.). A single slice Single Shot Shot Rapid Imaging with Refocused Echoes (RARE) pulse sequence was implemented with the following parameters: Average=1, Matrix size=96x96, TE=7 ms, Echo Spacing=7 ms, TR=6000 ms, CEST Length=5000 ms. Field of view (FOV), slice thickness, spectral width for the Z-spectra and the sampling step size were different for *in vitro* and the *in vivo* protocol and are outlined in the sections below. In order to correct for B_0 inhomogeneity, a Water Saturation Shift Referencing (WASSR) sequence was implemented prior to any Z-spectra acquisitions [28]. For WASSR, Z-spectra were acquired from +200 to -200 Hz at 25 Hz steps, and a pre-saturation pulse B_1 amplitude $B_1 = 0.65$ μT. The total acquisition time for WASSR was 1 min 42 seconds. Images were post-processed and analyzed using the Matlab routine provided by Guanshu Liu et al., available for download here: http://godzilla.kennedykrieger.org/CEST/ [29]. Code modifications were necessary to read the vendor specific imaging files and to reorder the image data. Maps of $\%MTR_{asym}$ were generated and overlaid onto the T_1-weighted RARE images acquired in the same slice.

***In vitro* CEST MRI**

A549 and H460 cells were cultured in T125 flasks in DMEM media supplemented with 10% FBS and 1% PenStrep in a humidified CO_2 incubator until the cells reached 70% confluency. Media was replaced with media alone, media containing 20 mM NA^3, or media containing 20 mM 2-HYNIC, and cells were left to incubate overnight. Cells were then lifted by trypsinization, washed with 1 × PBS, and suspended in 200 μL 1 × PBS. The suspension was added to microcapillary

tubes sealed at one end, which were placed into Eppendorf tubes sealed-end down and centrifuged for 2 min at 1200 rpm to pellet the cells in the microcapillary. Microcapillary tubes were then inserted into a 50 mL Falcon tube containing ultrasound gel, comprising the MRI phantom. The MRI phantom was placed into a 38 mm diameter send and receive volume coil and inserted into the MRI. Z-spectra were acquired as described above, with a slice thickness of 7 mm, an FOV of 40 x 40 mm, spanning +2000 Hz to -2000 Hz centered on the water resonance, sampling in 50 Hz steps, and a pre-saturation pulse B_1 amplitude B_1 = 2.61 μT. Acquisition time was 13 min 56 seconds.

In vivo CEST MRI study

All animal studies were conducted under Animal Use Protocol SCe-3254-R1 approved by the IACUC at the University of Ottawa. Tumor xenografts of A549 and H460 human lung cancers were established in a total of n=8 (n=4 *per* tumor cell type) 6 week-old female nu/nu mice (Charles River Laboratories) through the subcutaneous injection of 2 × 10^6 cells suspended in 1 × PBS above the rear left flank. Four to six weeks after cell injection, CEST MRI imaging was performed. Prior to imaging, tail veins were cannulated with an ~1m long cannula (~100 μL dead volume), permitting *intravenous* injection in the MRI. Mice were warmed and respiration rate was monitored through the duration of the imaging experiment. Tumors were centered in the FOV using standard localizer sequences. A WASSR sequence was performed, followed by CEST MRI prior to contrast agent administration (single slice, slice thickness = 2.0 mm FOV = 35 x 35 mm, CEST frequency range from +1500 to -1500 Hz centered on the water resonance, sampled in steps of 100 Hz, a pre-saturation pulse B_1 amplitude B_1 = 2.61 μT, and acquisition time 3 minutes 6 seconds). After the completion of the initial Z-spectrum, each mouse received a bolus injection of

100 µL of 40 mM (~0.85 mg) dissolved in saline, and the line was flushed with 100 µL saline. No adverse events were noted in any of the mice receiving 2-HYNIC injections. Post-contrast Z-spectra were acquired sequentially for 60 min post-injection. Using the Matlab routine provided by Guanshu Liu et al. [29], regions of interest (ROI) were drawn over the entire tumor area of each image, and the average $\%MTR_{asym}$ for that ROI was calculated as part of the analysis routine. The $\%MTR_{asym}$ value at $\Delta\omega = 6.5$ p.p.m. was plotted for each animal before, 5 and 60 min after injection of 2-HYNIC. The ROI values of $\%MTR_{asym}$ for each mouse at 60 min post-contrast injection were normalized to pre-injection (i.e. background) levels. Time-course data were analyzed by two-way ANOVA with Šídák's multiple comparisons, and post-contrast/pre-contrast data was analyzed by two-way t-test using Prism (v. 9.1.0., GraphPad Softwae, LLC).

2.10.4. Vitamin B_6 Metabolites Quantification Protocol

Vitamin B_6 Metabolite Quantification

Pyridoxal hydrazone, pyridoxal 5'-phosphate hydrazone and related compounds were quantified in samples by liquid chromatography-mass spectrometry (LC-MS).

A549 and H460 cells were seeded in 100 mm tissue culture-treated dishes and cultured with Dulbecco's Modified Eagle Medium (DMEM) supplemented with 10 % fetal bovine serum (FBS) and 1 % penicillin-streptomycin in a humidified CO_2 incubator until the cells reached 70% confluency. Twenty-four hours after seeding, the media was replaced with fresh media alone. After another 24 hrs, the media was replaced with fresh media alone or containing 20 mM 2-HYNIC and incubated for 4 hrs. Two technical replicates for each of the three biological replicates were

performed, with biological replicates performed one week apart. Polar metabolites were liquid-liquid extracted from confluent cell cultures using LC-MS grade solvents (Optima, Fisher; OmiSolv, Sigma). Cells were rinsed with ice cold 150 mM ammonium formate, pH 7.4 and quenched with -20 °C equilibrated 50 % methanol (360 µL). The cell slurry was transferred to prechilled tubes containing 1.4 mm ceramic beads (Omni International) and 220 µL of ice-cold acetonitrile. Cells were lysed by bead beating (MagNA Lyser, Roche Diagnostics) at 2000 RPM for two rounds of one minute. Ice-cold dichloromethane (600 µL) and H_2O (300 µL) were then added, and samples were vortexed and incubated on ice for 10 minutes. Samples were centrifuged at 4,000 RPM for 10 minutes at 1°C and the supernatants collected and dried by vacuum centrifugation at -4 °C (Refrigerated Centrivap, Labconco). The resulting dried polar metabolite extract was stored at -80 °C until LC-MS analysis.

Samples were resuspended in H_2O and run on a 6470 Triple Quadruple MS equipped with a 1290 Infinity ultraperformance LC system utilizing the Metabolomics Dynamic MRM Database and Method (Agilent), which uses an ion-pairing reverse phase chromatography. This method was optimized for phosphate-containing metabolites with the addition of 5 µM InfinityLab deactivator (Agilent) to mobile phases A and B, which requires decreasing the backflush acetonitrile to 90 %. Precursor/product ion pairs for pyridoxamine, pyridoxine, pyridoxal 5-phosphate were present in the database, but ion pairs were optimized with neat standards for the novel compounds pyridoxine hydrazone and pyridoxal 5-phosphate hydrazone (Supplementary S56). Relative metabolite quantifications were calculated by interpolating external compound calibration curves in Mass Hunter Quantitative Analysis 10.0 (Agilent).

Live-Dead Flow Cytometry Assay

A549 cells were cultured in DMEM supplemented with 10 % fetal bovine serum and 1 % penicillin-streptomycin. The cells were maintained under cell culture conditions (37 °C, 5 % CO_2, and in a humidified environment). Cells were passaged into a 24-well plate and grown to confluency. At confluency, fresh phenol red-free media was added with and without 20 mM sterile-filtered 2-HYNIC, and incubated under cell culture conditions for 2 or 4 hrs. At the appropriate time point, cells were washed with sterile Dulbecco's phosphate buffered saline (DPBS) and detached from the plate by incubation with 0.25 % trypsin-EDTA. Cells were resuspended in phenol red-free DMEM and pelleted by centrifugation (5 min, 1000 xg, 4 °C). The supernatant was aspirated, and cell pellets were resuspended in LIVE/DEAD® Viability stain (ThermoFisher), consisting of 1 μM calcein-AM and 2 μM ethidium homodimer-1 in DPBS. This solution was incubated for 20 min under cell culture conditions. After performing standard compensation, cell solutions were examined using a Gallios flow cytometer using a 488 nm excitation (530/30 bandpass) for calcein- AM (live cells, green) and 530 nm excitation (610/20 bandpass) for ethidium homodimer-1 (dead cells, red).

2.10.5. ^{1}H-NMR of the Hydrazone NH Proton in Hydrazones **3** and **4**

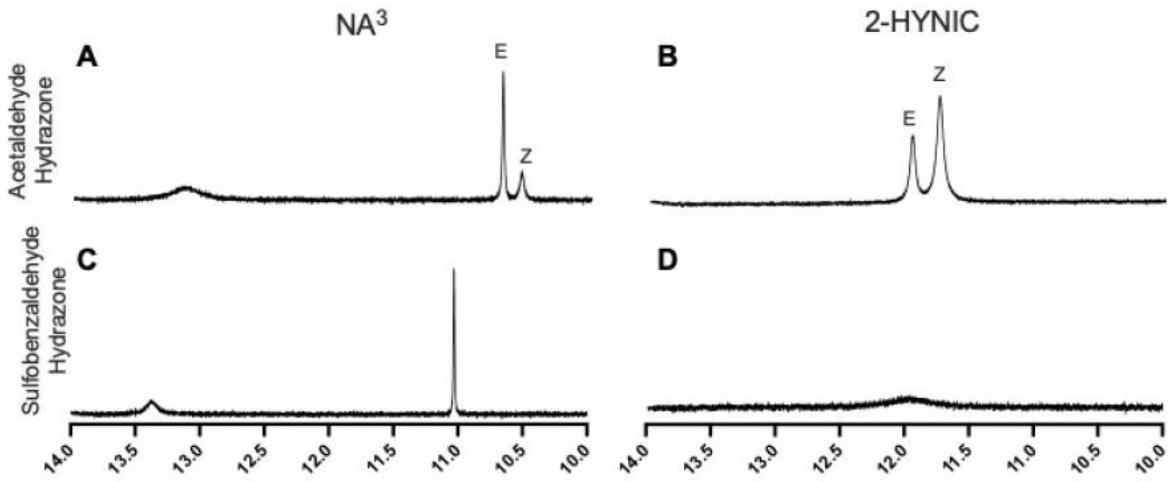

S2. ^{1}H-NMR of the hydrazone NH proton, supporting conformational assignment across tested hydrazones. Acetaldehyde-derived hydrazones of NA^3 (A) and 2-HYNIC (B), and 2-formylbenzenesulfonic acid-derived hydrazones of NA^3 (C) and 2-HYNIC (D) are shown. The *E* and *Z* conformations are indicated on the acetaldehyde-derived hydrazone spectra.

2.10.6. CEST Effect as a Function of pH and UV Spectrometry of Hydrazones **5a**, **5b**, **6a** and **6b**

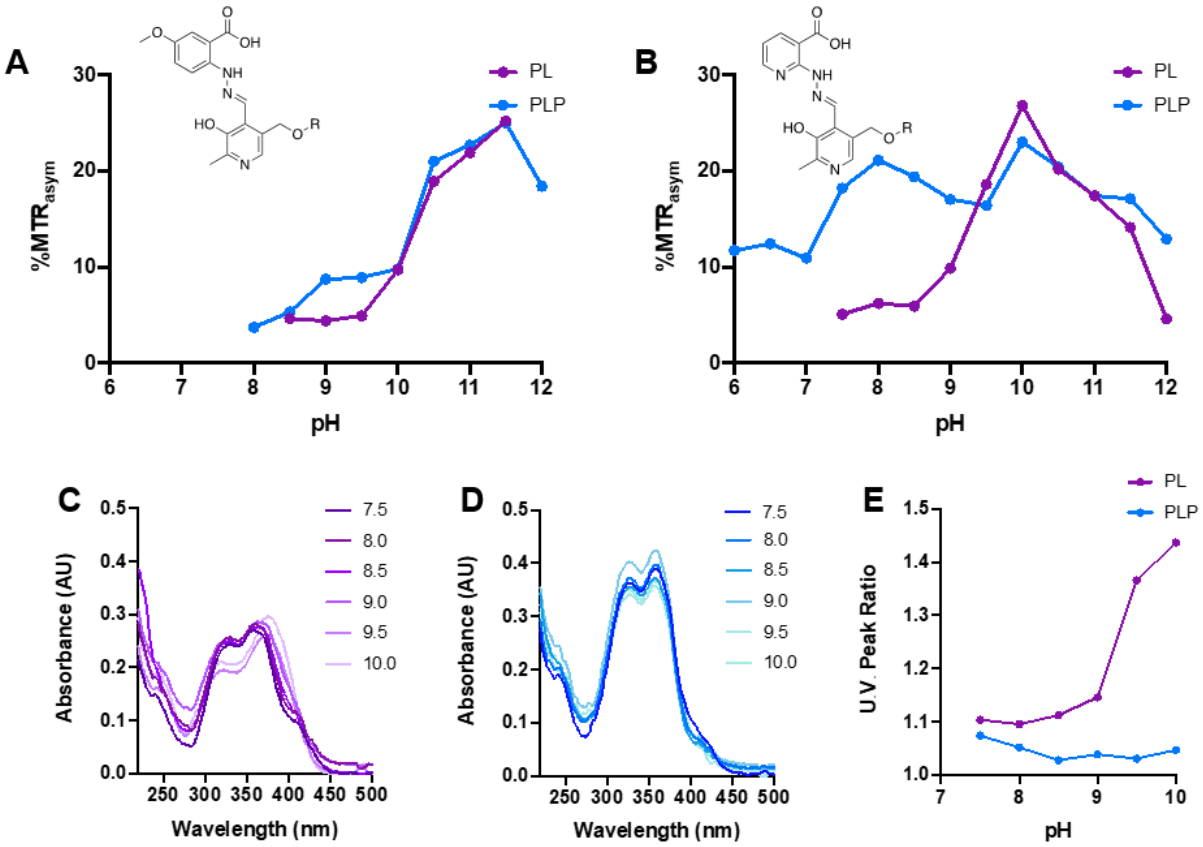

S3. The effect of pH titration on the CEST-MRI contrast generation and UV spectrophotometry of PL(P)-derived hydrazones. Solutions (40 mM) of NA[3] (A) or 2-HYNIC (B) derived hydrazones of PL (purple) or PLP (blue) were adjusted to the pH values between 6.0 and 12.0. Limited solubility at low pH prevented the full pH range to be evaluated for all compounds. The effect of pH on the absorbance spectrum of 2-HYNIC-derived hydrazones of PL (C) and PLP (D) was evaluated. (E) The ratio of the absorbance at λ_{abs} = 385/325 nm was plotted over the range of pH values tested.

2.10.7. Molecular Mechanics Simulation of the Effect of pH on Hydrazones **5a** and **5b** Conformations

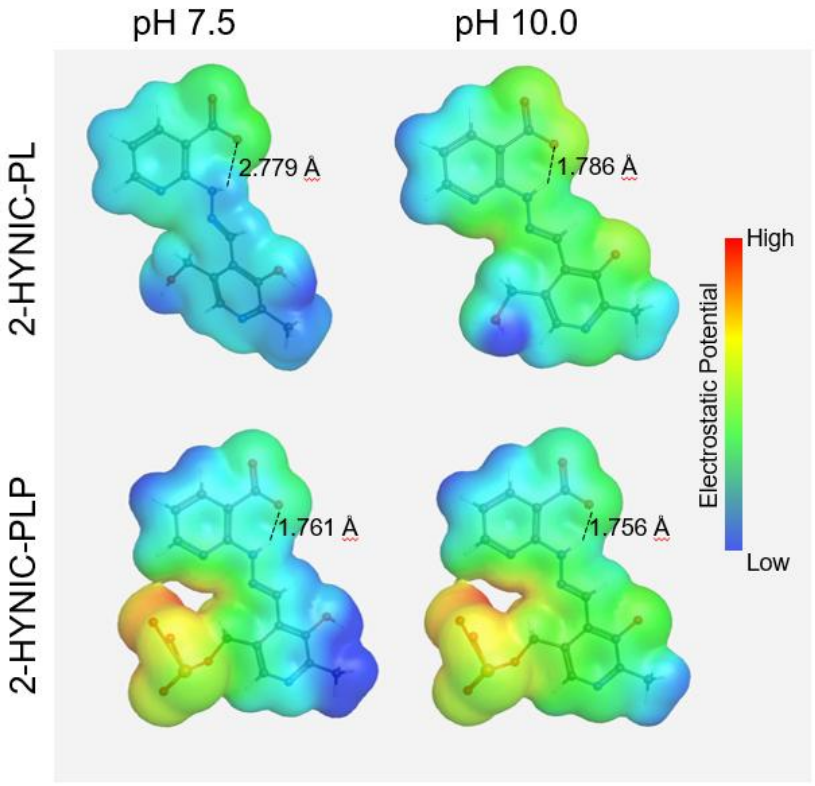

S4. Molecular mechanics simulation of the effect of pH on hydrazone conformations. Structural optimization was performed using a B3LYP routine in water as implemented by WebMO, resulting in the conformations shown**.** 2-HYNIC-PL (*top*) and 2-HYNIC-PLP (*bottom*) hydrazones were simulated in aqueous media at pH 7.5 (*left*) or pH 10.0 (*right*), and energy minimizations were performed. The hydrogen bond distance between the hydrazone proton and neighboring carboxylate were calculated and are indicated as dashed black lines.

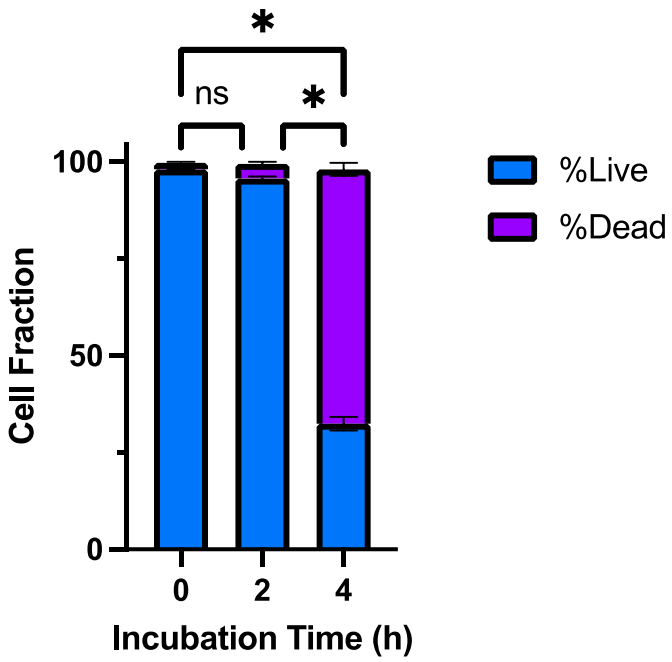

S5. *In vitro* cytotoxicity of 2-HYNIC in A549 lung cancer cells. The fraction of live (blue) and dead (purple) cells are plotted for cells prior to (0 h), and 2 and 4 h after treatment with 20 mM 2-HYNIC. Bar height represents the mean and whiskers represent the standard deviation of n=3 trials. ns = not statistically significant, * $p<0.05$.

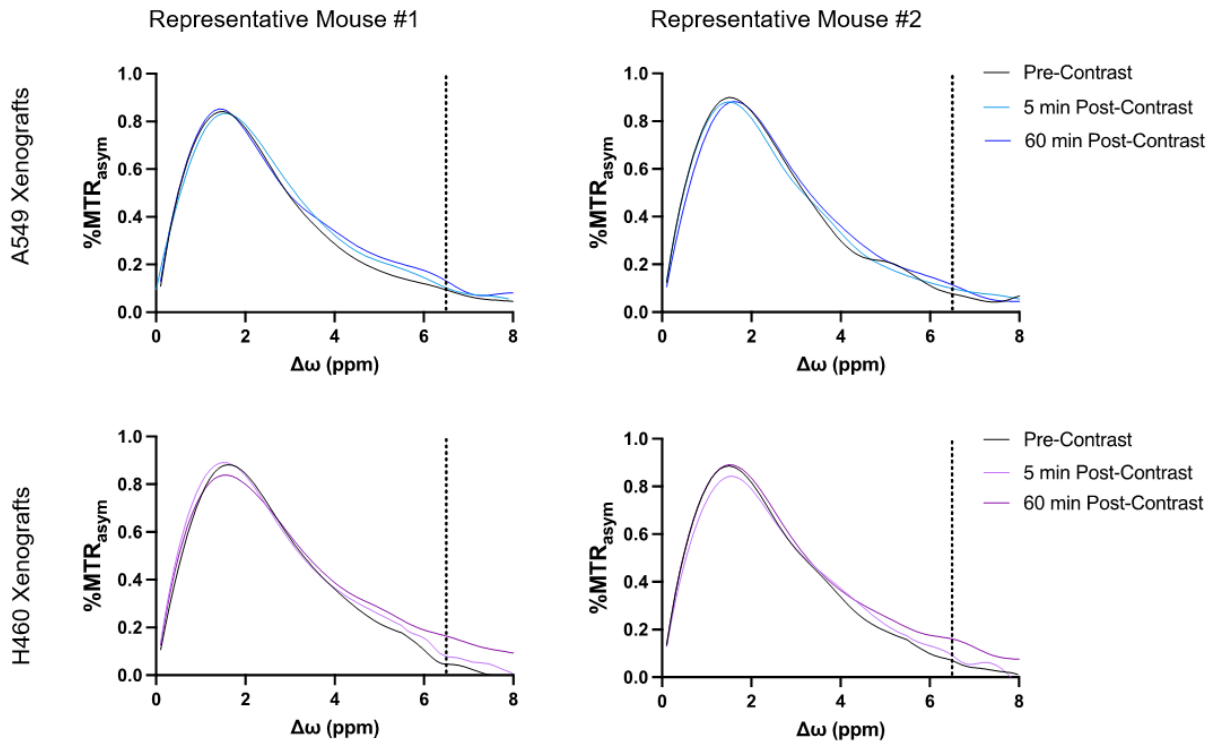

S6. %MTR$_{asym}$ Data. The %MTR$_{asym}$ plots from two representative bearing either A549 (*top*) or H460 (*bottom*) tumor xenografts are provided. Plots show pre-contrast data (black), data acquired 5 min after injection of 2-HYNIC (light blue: A549, light purple:H460), and 60 min after 2-HYNIC injection (dark blue: A549, dark purple: H460). Dashed vertical line demarcates Δω = 6.5 p.p.m.

2.10.8. Detailed Spectral Characterization of Hydrazones **3**, **4**, **5a**, **5b**, **6a** and **6b**

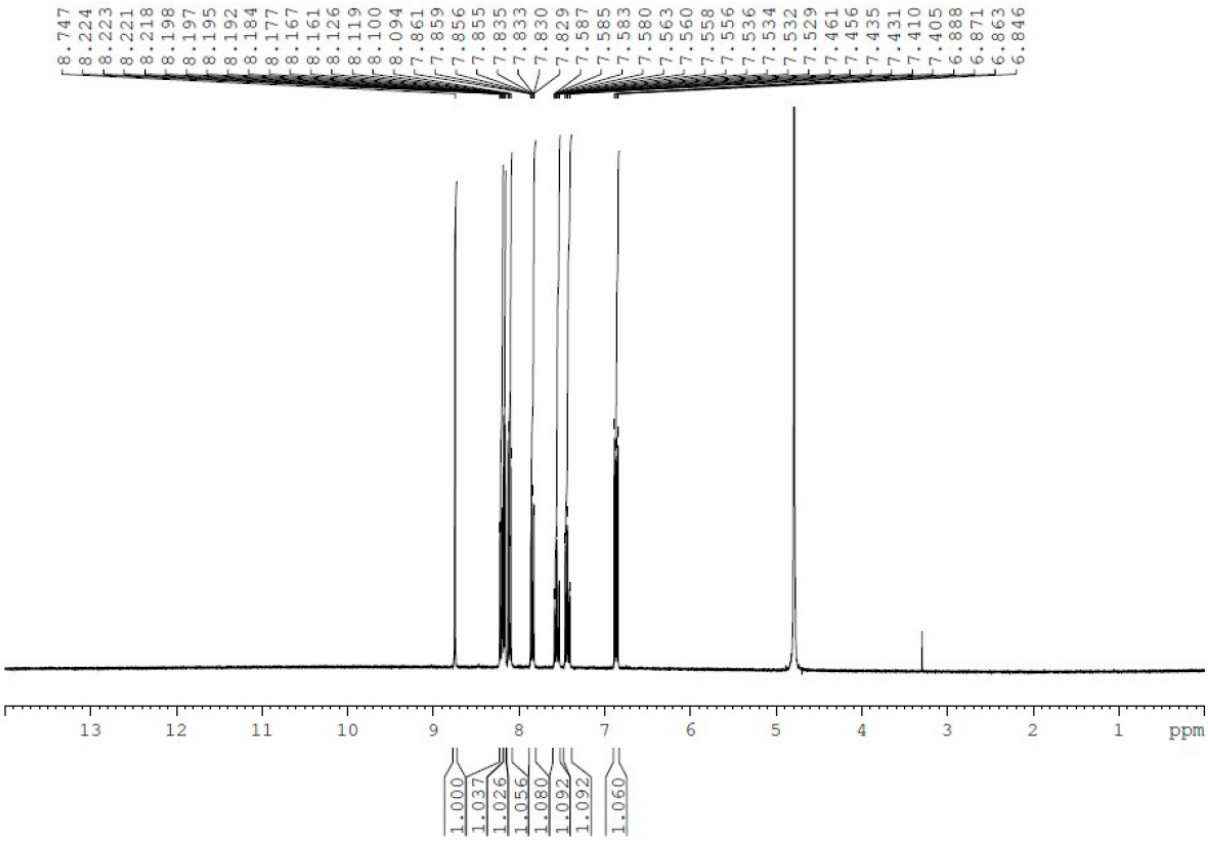

S7. ^{1}H NMR spectrum of hydrazone 3. Due to solubility problems, the spectrum was acquired in D_2O, containing 1 drop of 40 % NaOH, pH > 10.

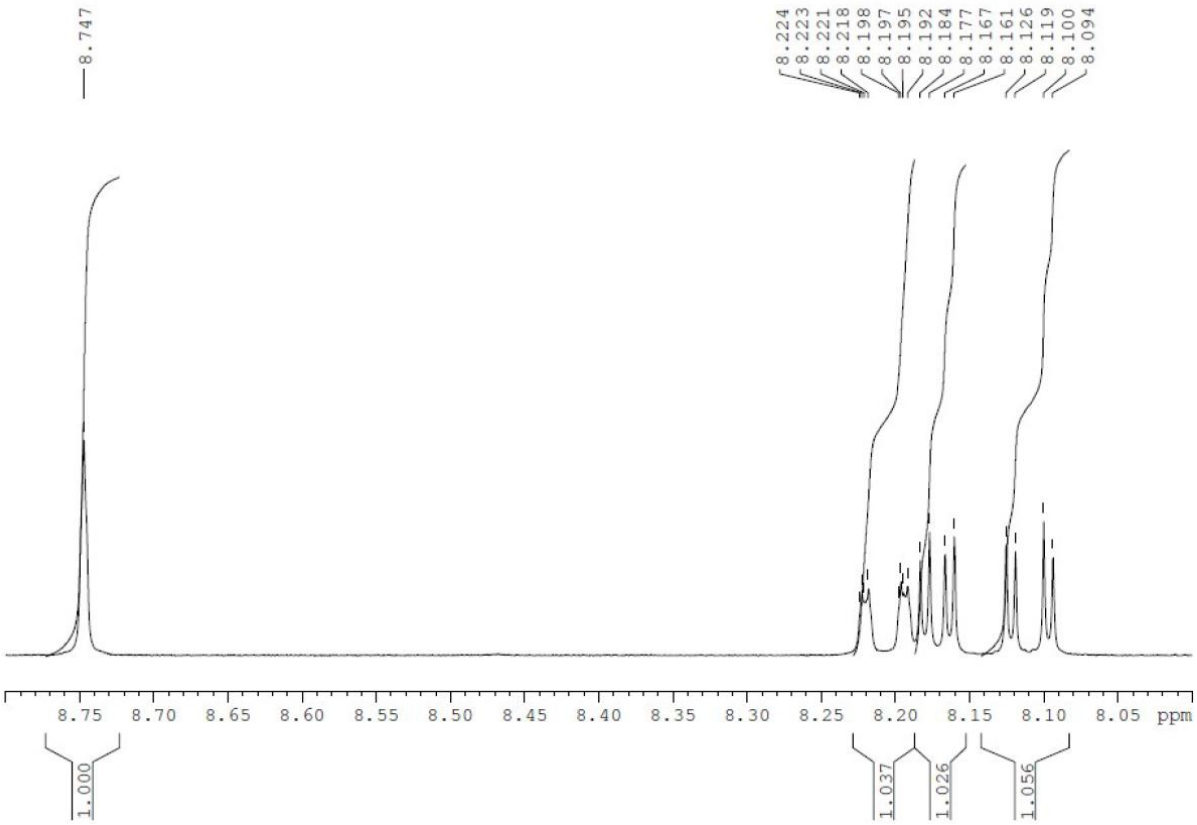

S8. ^{1}H NMR spectrum of hydrazone 3, expanded view.

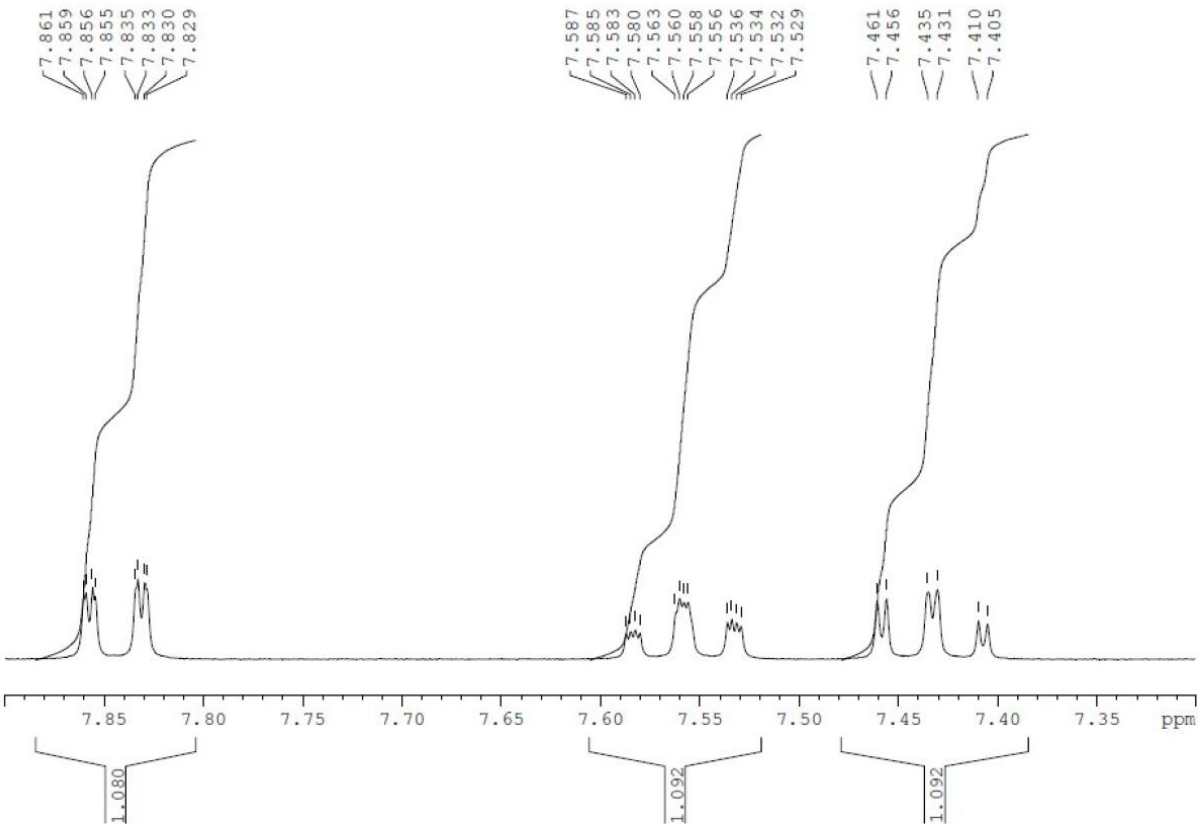

S9. ^{1}H NMR spectrum of hydrazone 3, expanded view.

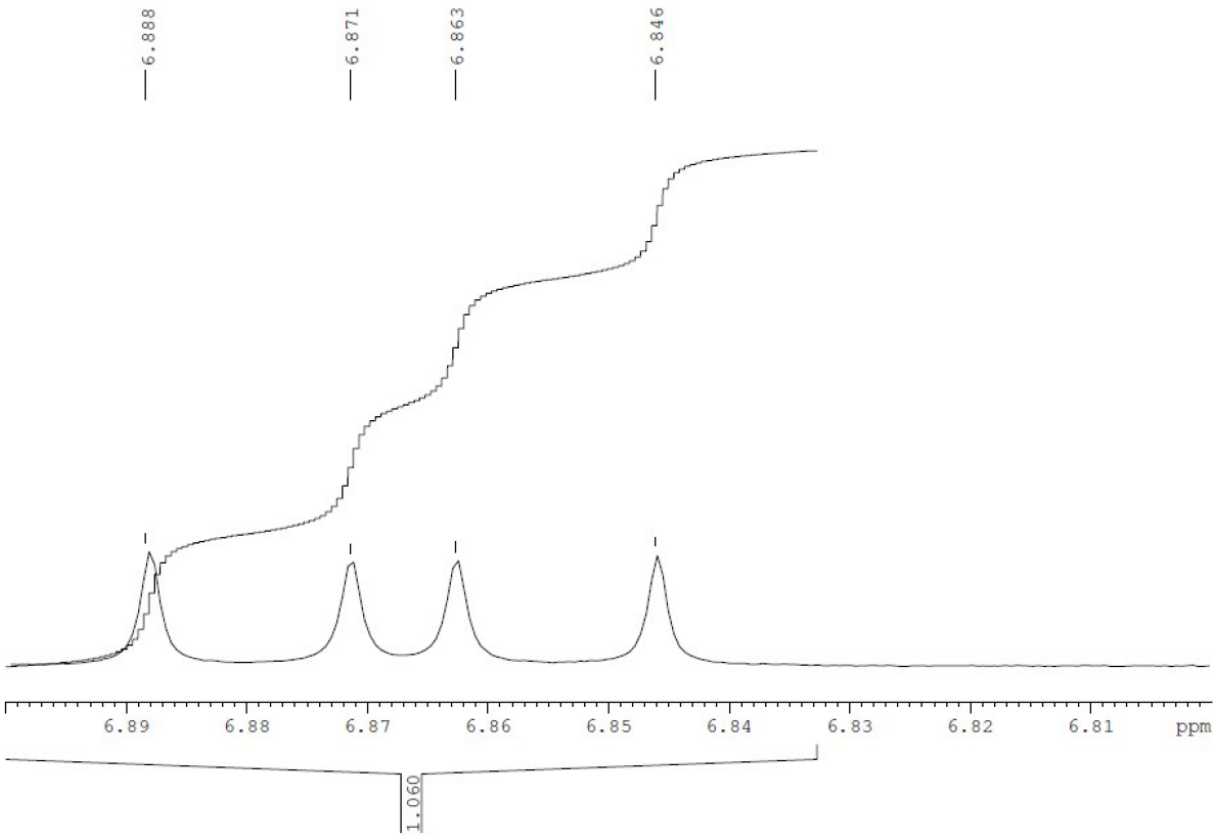

S10. ^{1}H NMR spectrum of hydrazone 3, expanded view.

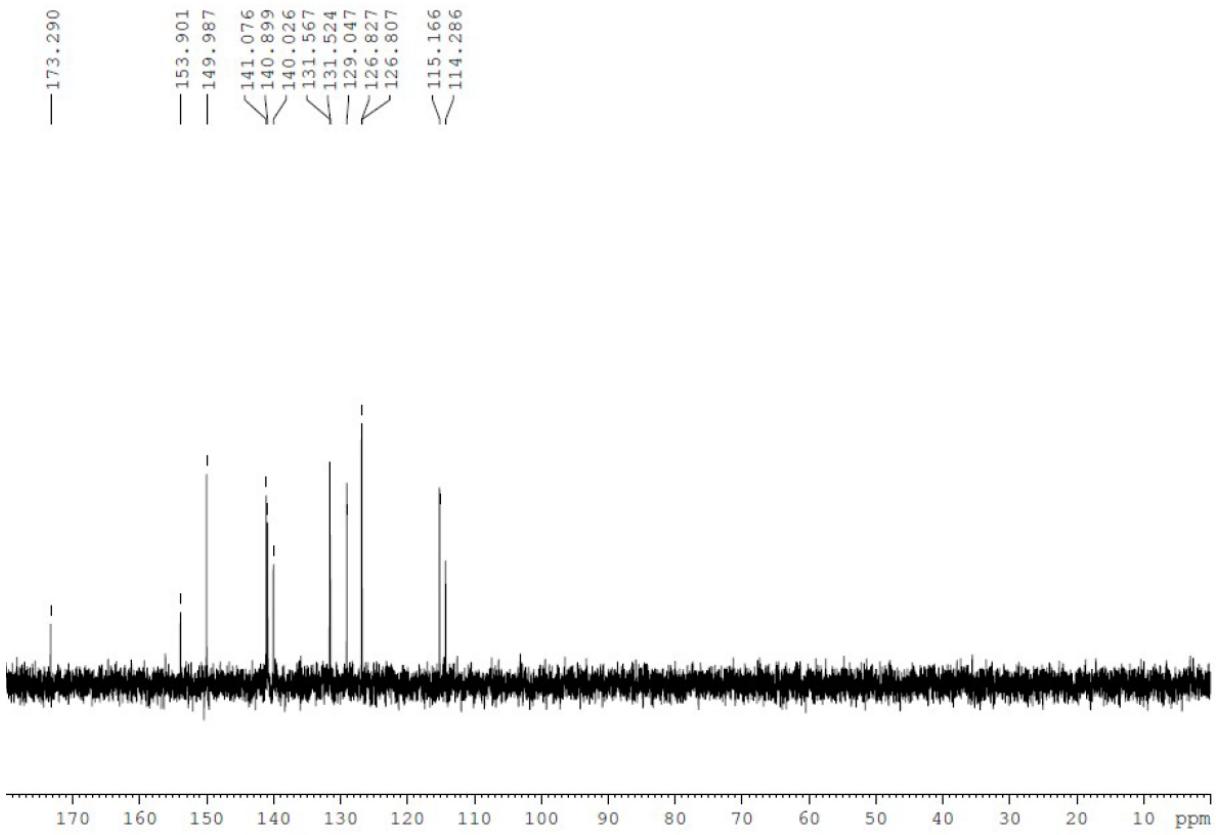

S11. ^{13}C NMR spectrum of hydrazone 3. Due to solubility problems, the spectrum was acquired in D_2O, containing 1 drop of 40 % NaOH, pH > 10.

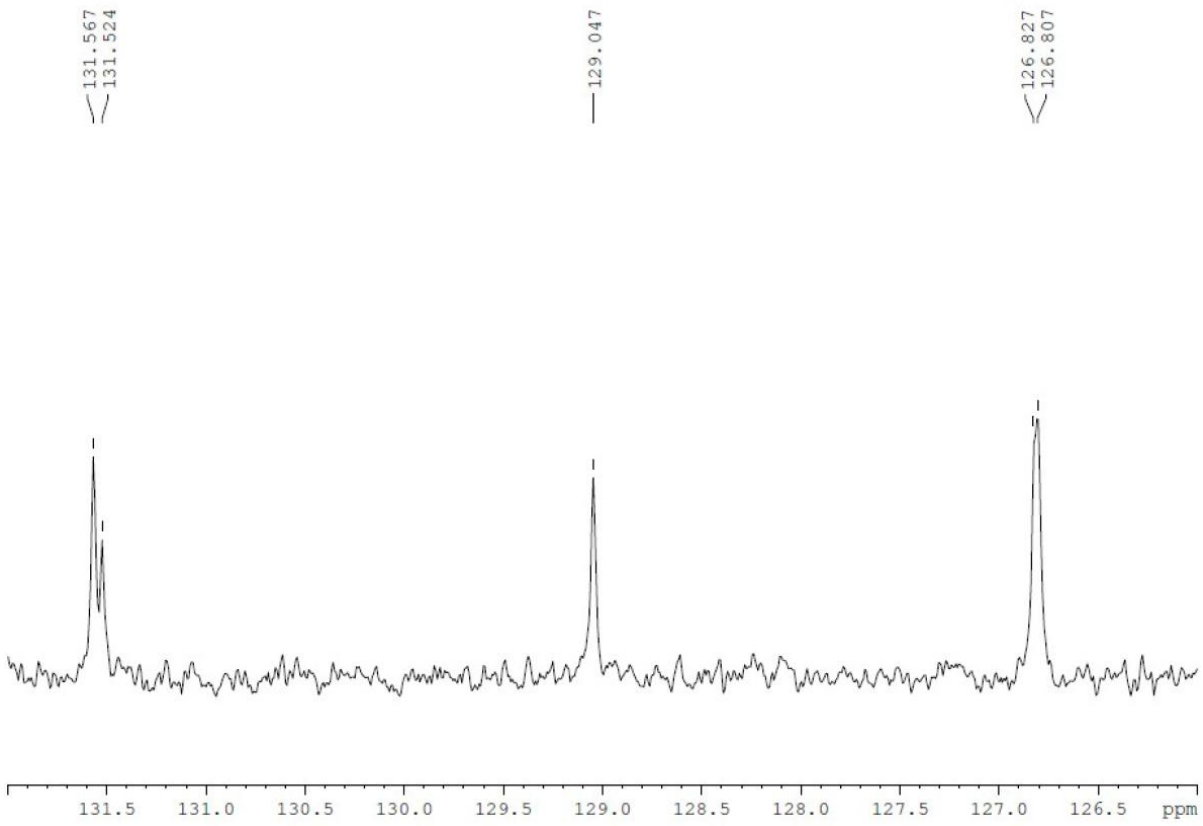

S12. ^{13}C NMR spectrum of hydrazone 3, expanded view.

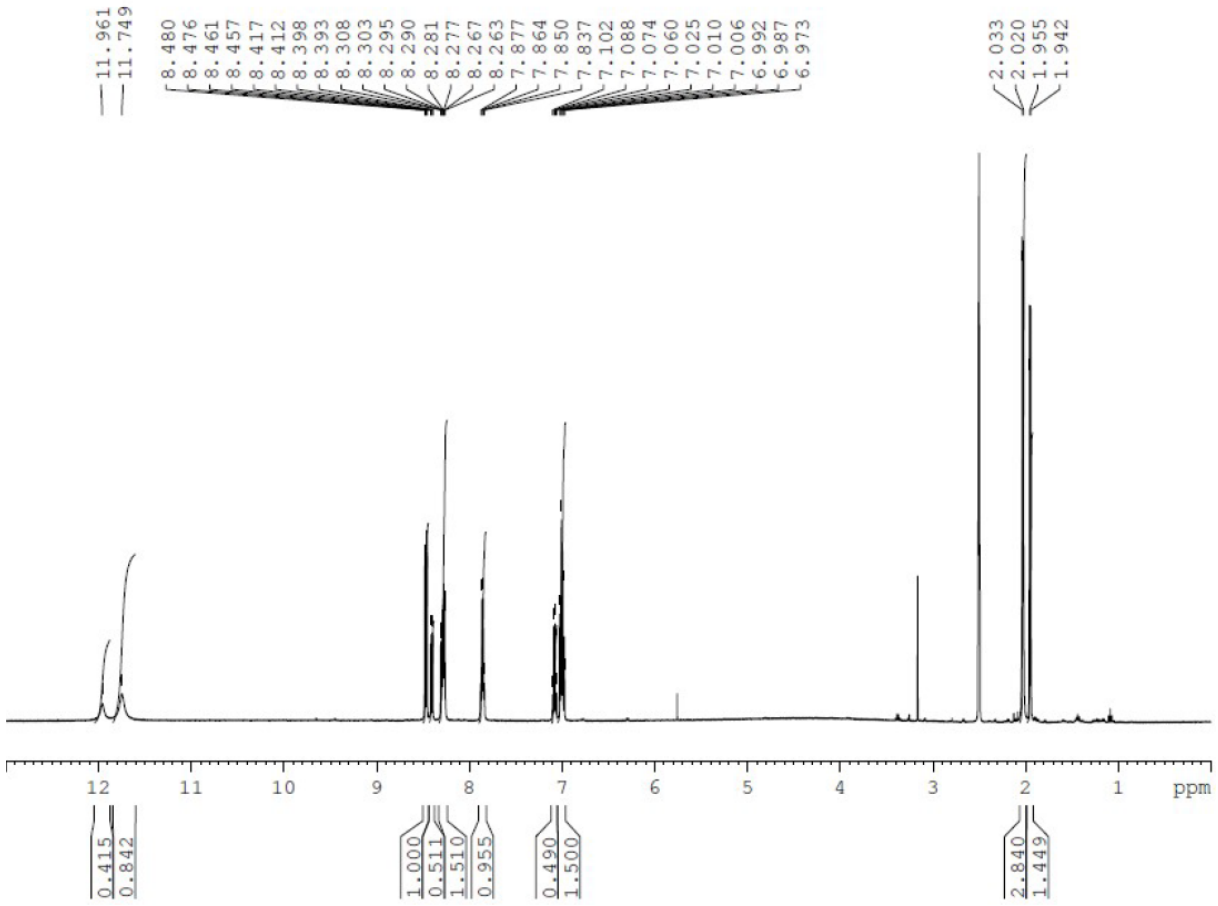

S13. ^{1}H NMR spectrum of hydrazone 4 in DMSO-D_6.

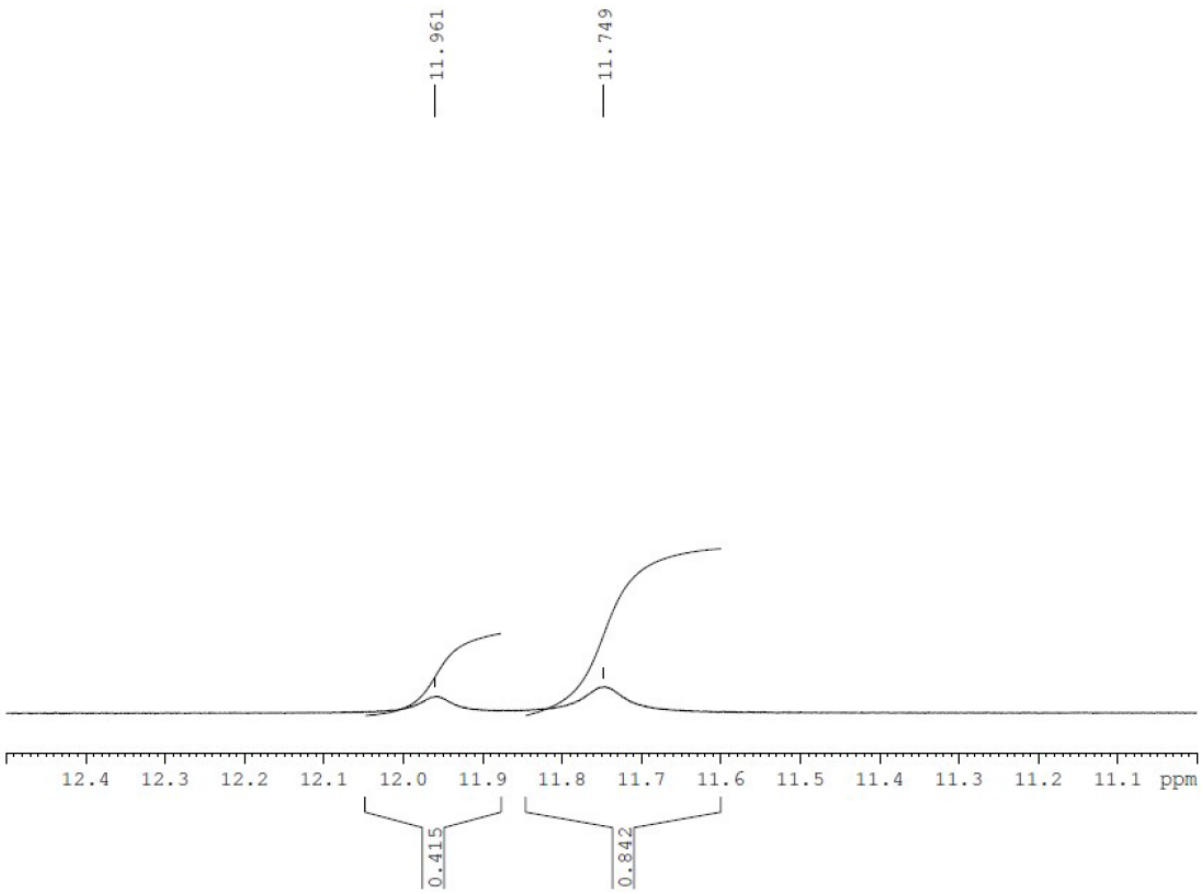

S14. ^{1}H NMR spectrum of hydrazone 4 in DMSO-D$_6$, expanded view.

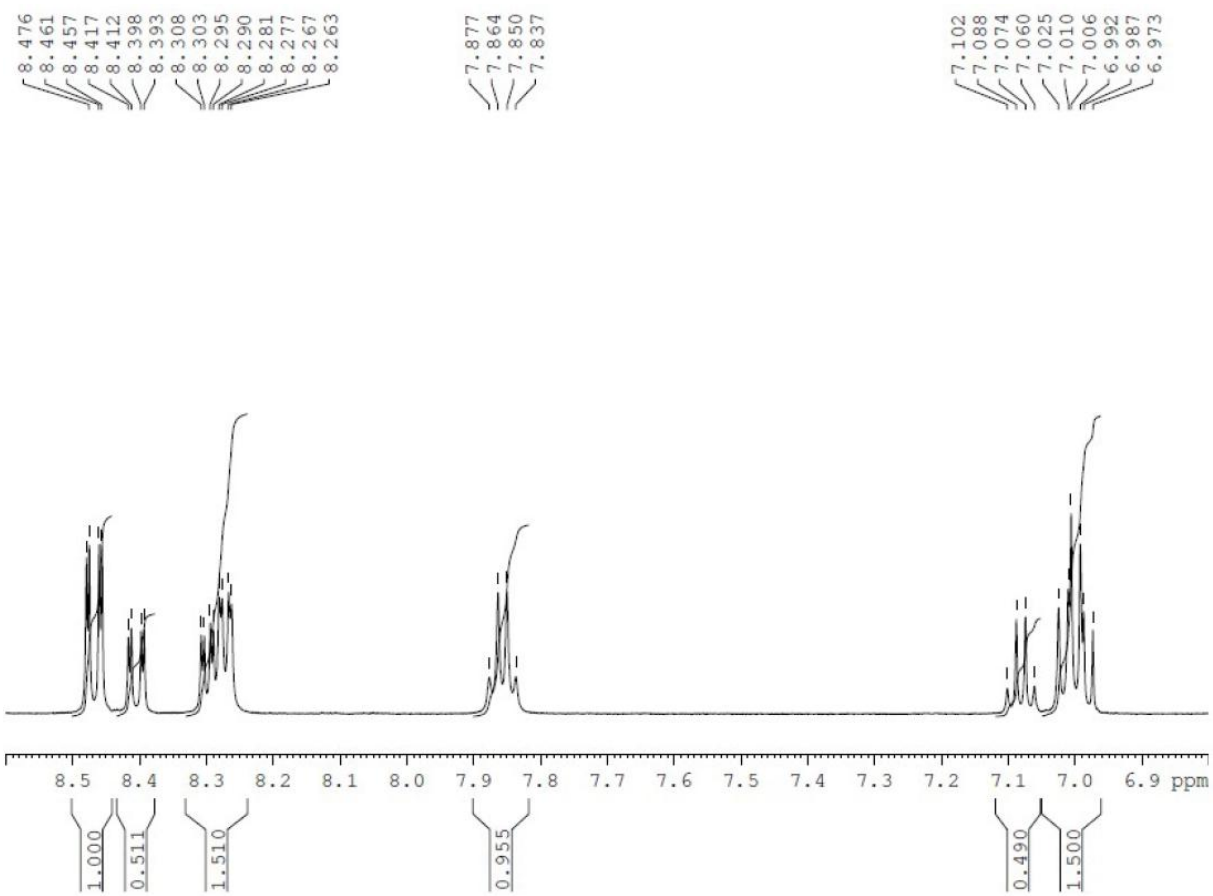

S15. ^{1}H NMR spectrum of hydrazone 4 in DMSO-D$_6$, expanded view.

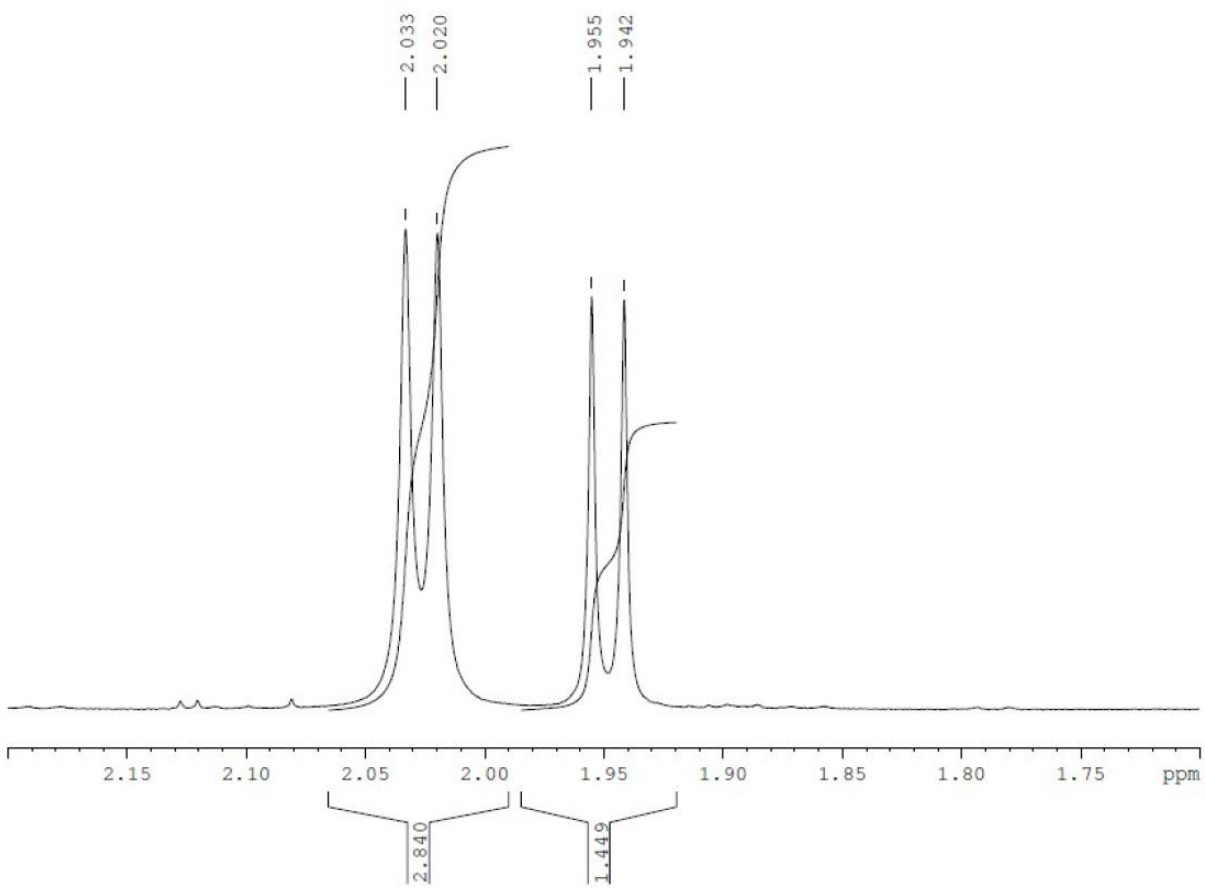

S16. ^{1}H NMR spectrum of hydrazone 4 in DMSO-D_6, expanded view.

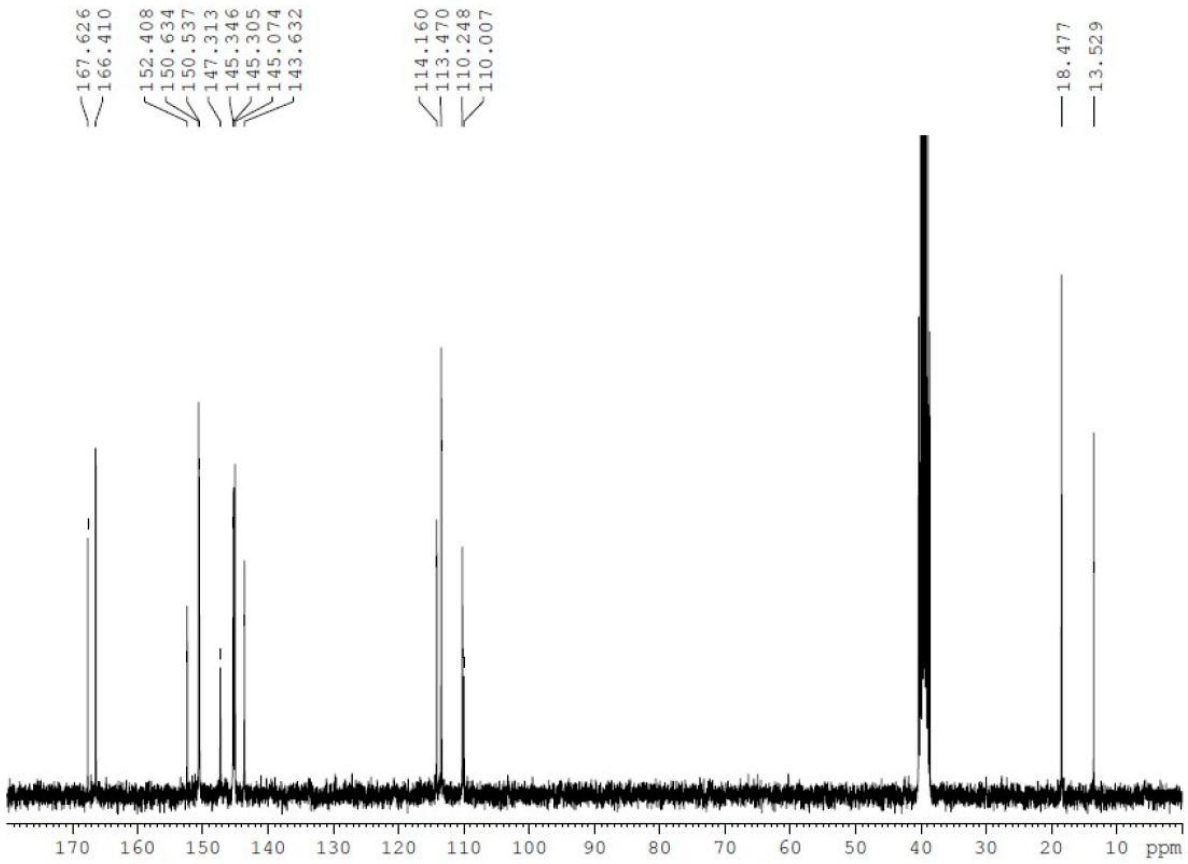

S17. ^{13}C NMR spectrum of hydrazone 4 in DMSO-D_6.

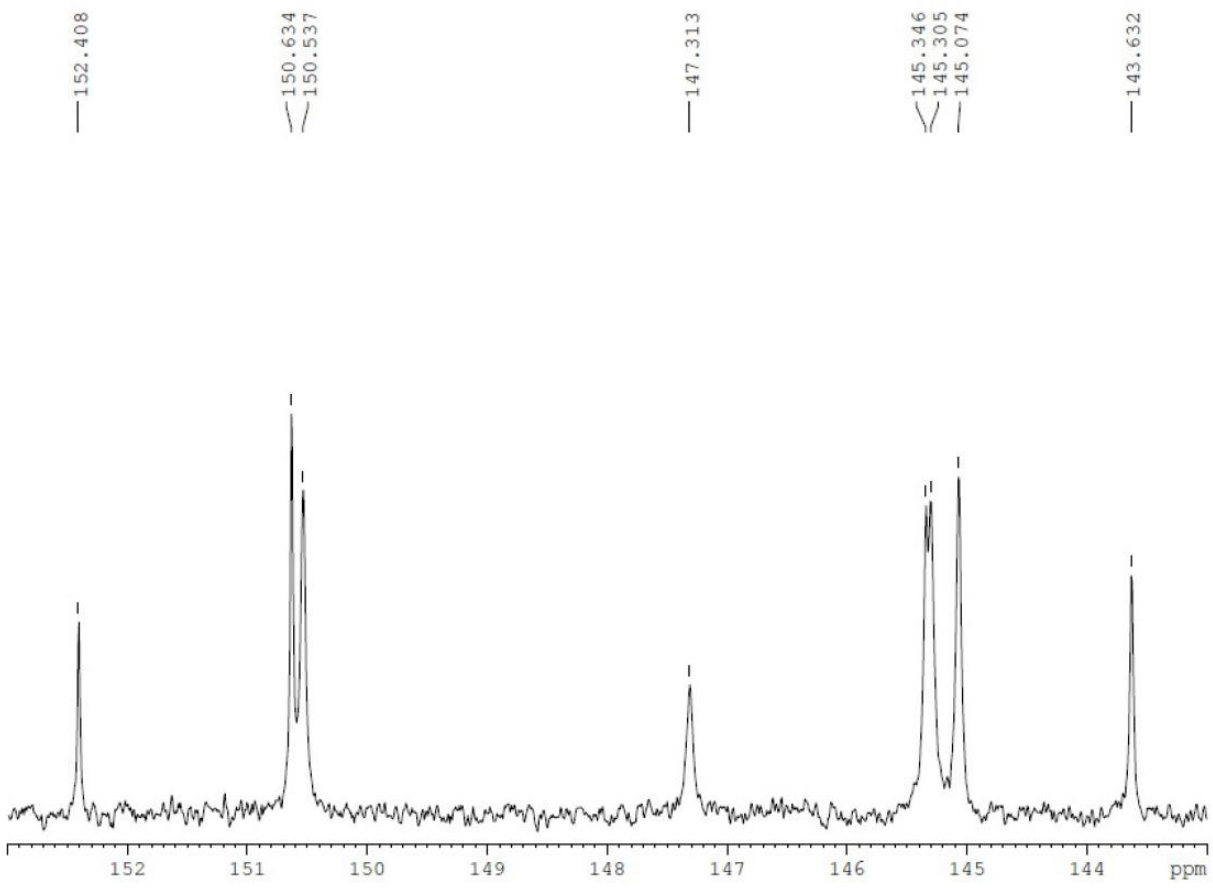

S18. ^{13}C NMR spectrum of hydrazone 4 in DMSO-D$_6$, expanded view.

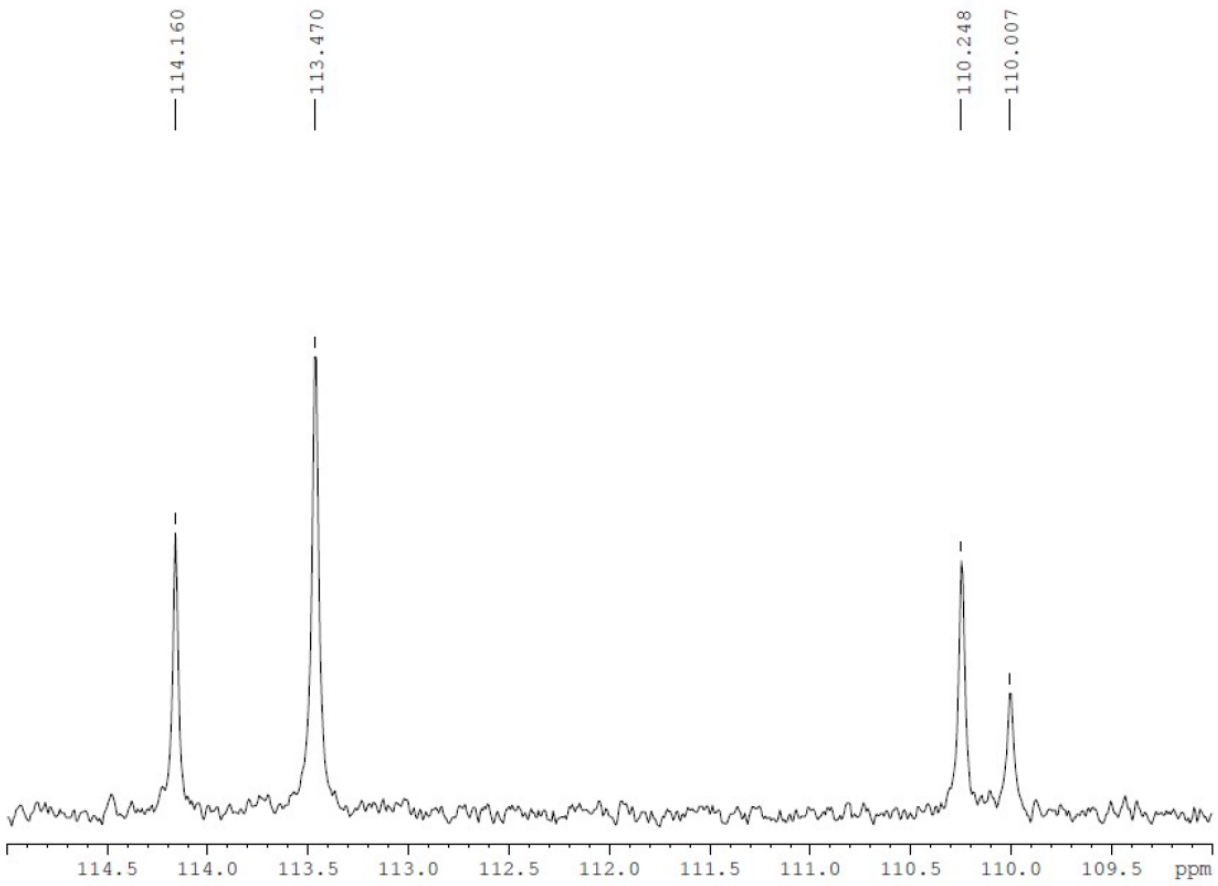

S19. ^{13}C NMR spectrum of hydrazone 4 in DMSO-D$_6$, expanded view.

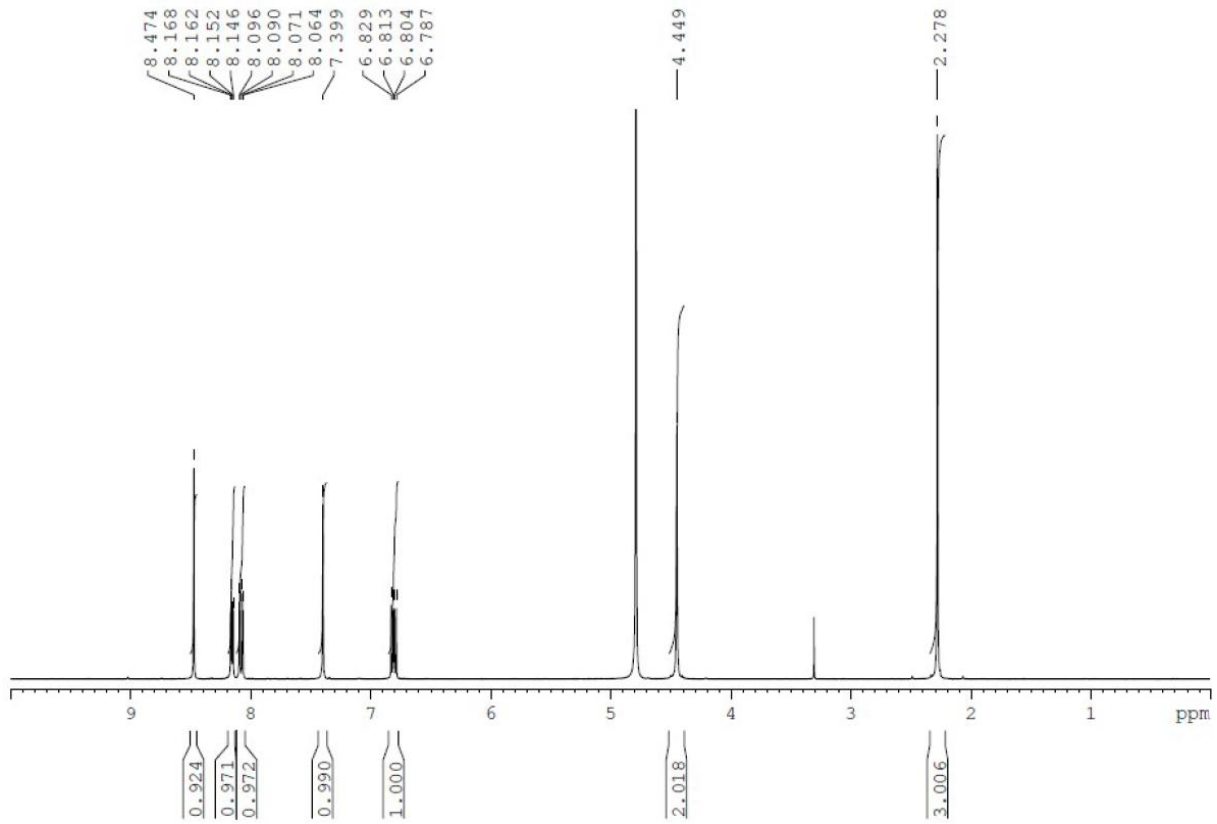

S20. ^{1}H NMR spectrum of hydrazone 5a. Due to solubility problems, the spectrum was acquired in D_2O, containing 1 drop of 40 % NaOH, pH > 10.

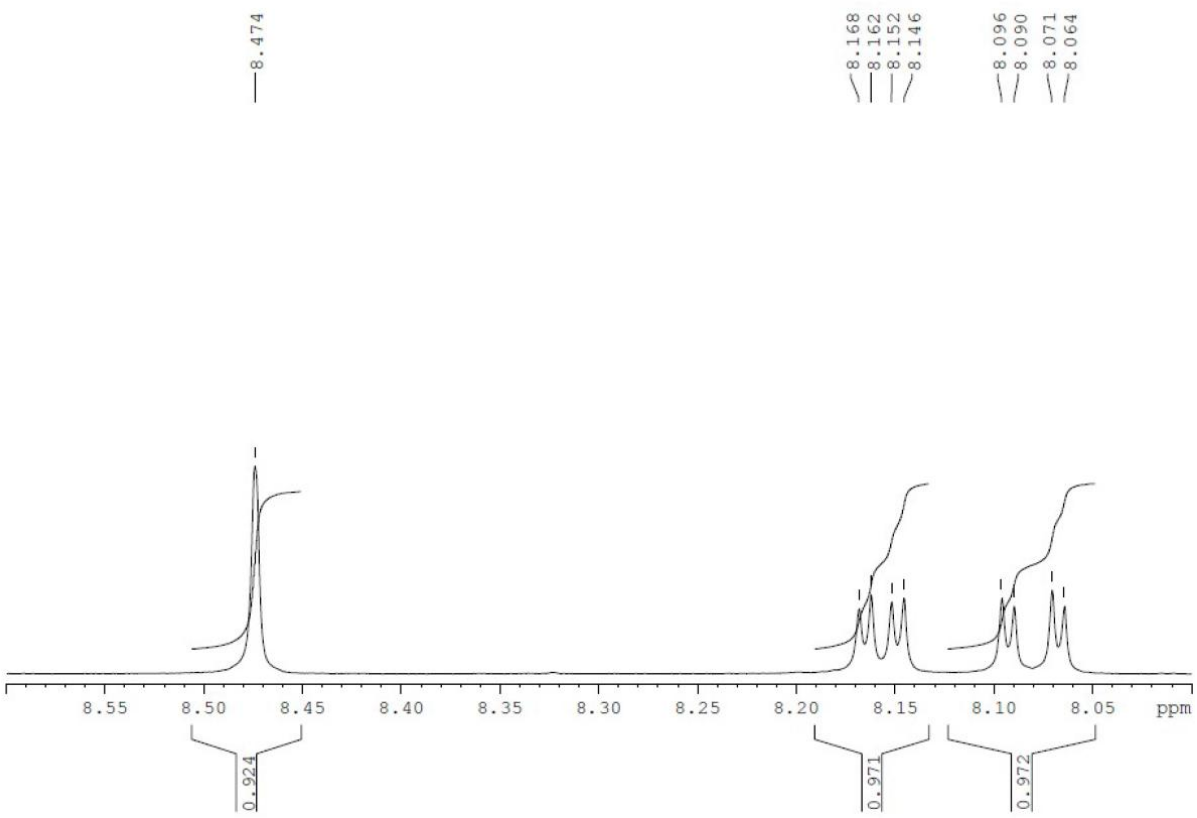

S21. ^{1}H NMR spectrum of hydrazone 5a, expanded view.

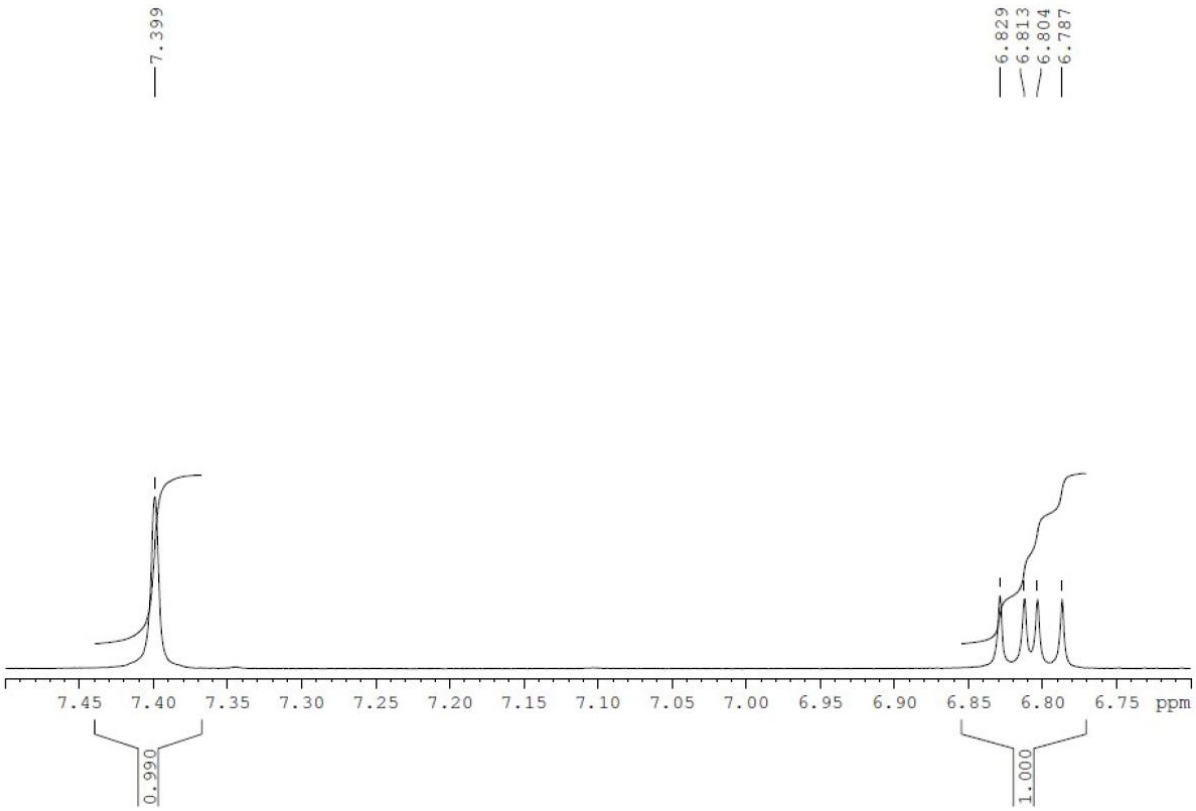

S22. ^{1}H NMR spectrum of hydrazone 5a, expanded view.

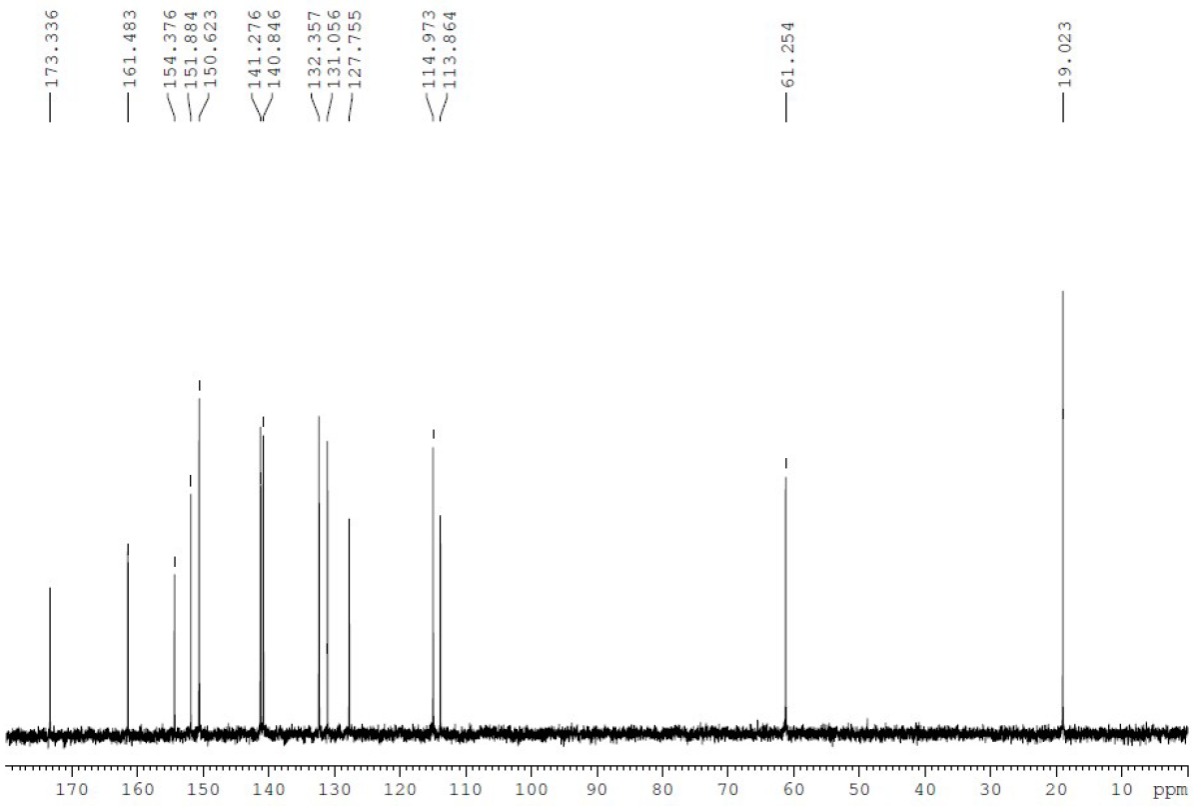

S23. ^{13}C NMR spectrum of hydrazone 5a. Due to solubility problems, the spectrum was acquired in D_2O, containing 1 drop of 40% NaOH, pH > 10.

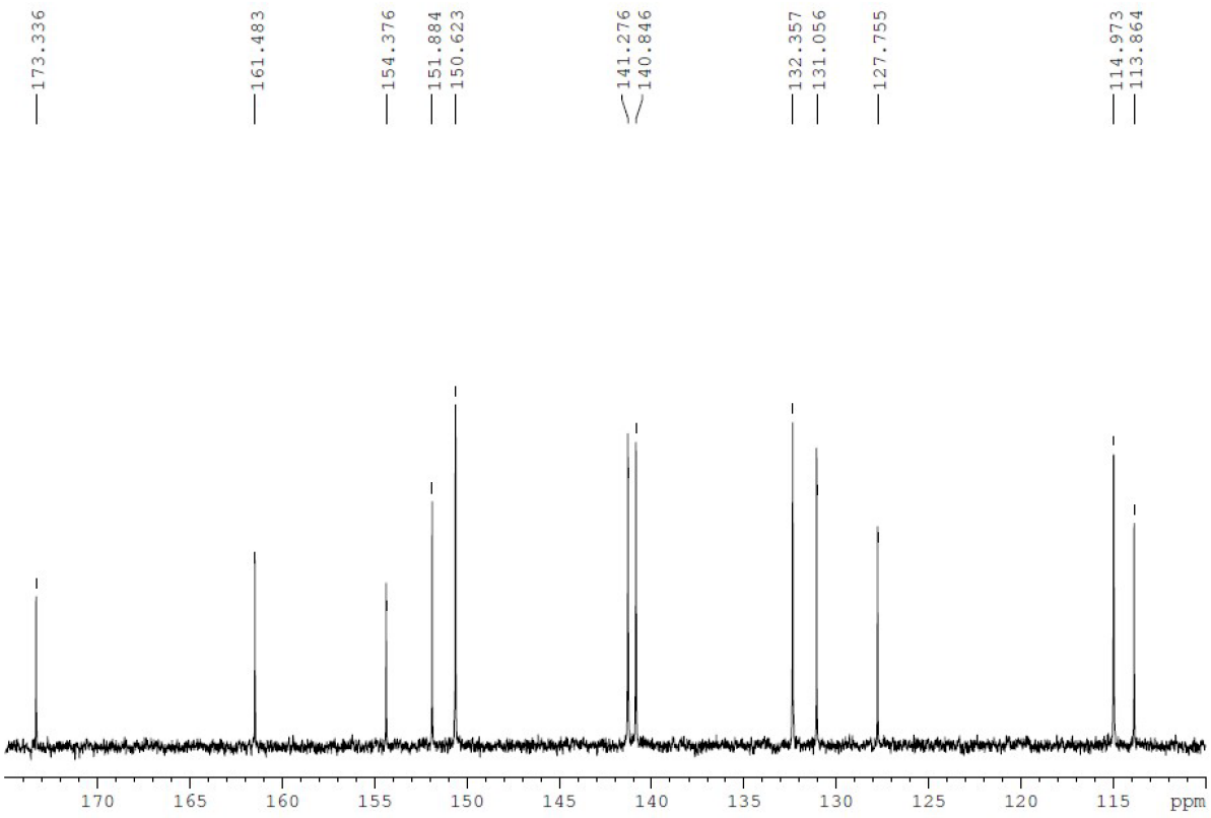

S24. ^{13}C NMR spectrum of hydrazone 5a, expanded view.

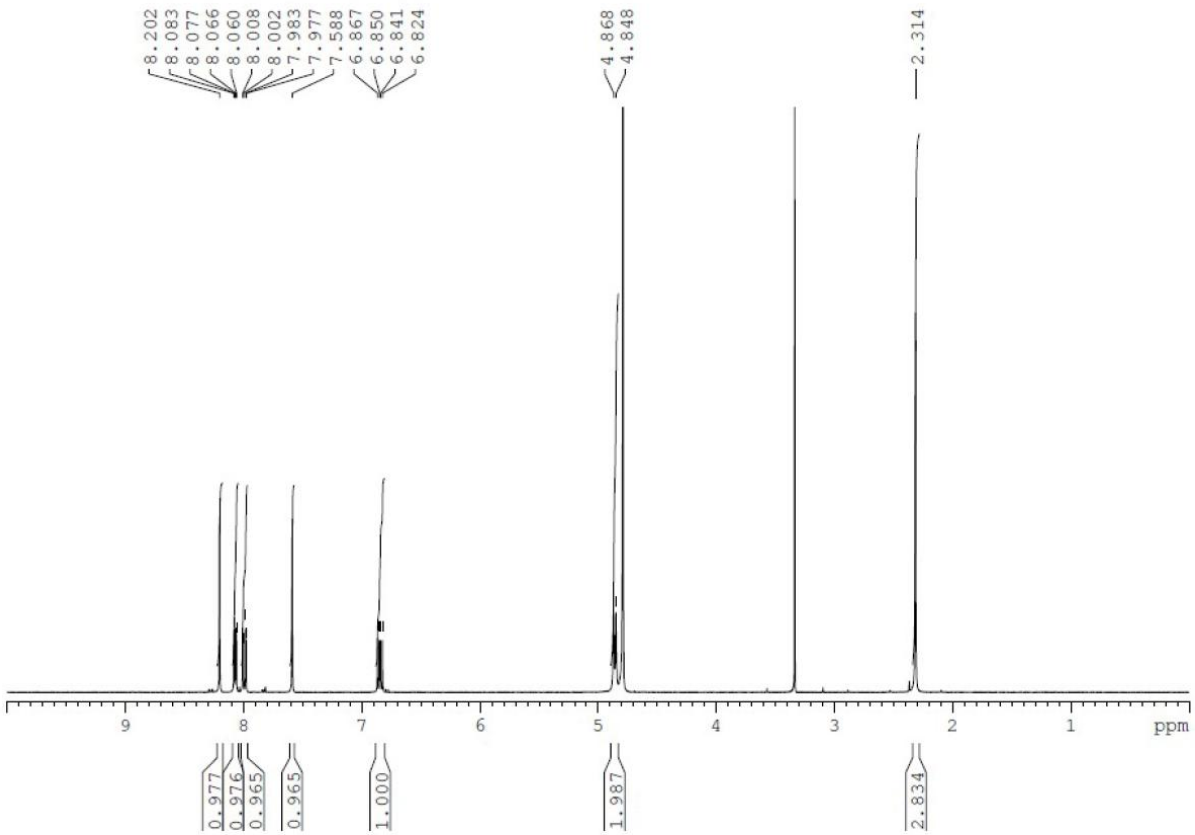

S25. ^{1}H NMR spectrum of hydrazone 5b. Due to solubility problems, the spectrum was acquired in D_2O, containing 1 drop of 40 % NaOH, pH > 10. The signal at δ 3.31 ppm is due to the presence of MeOH in the sample.

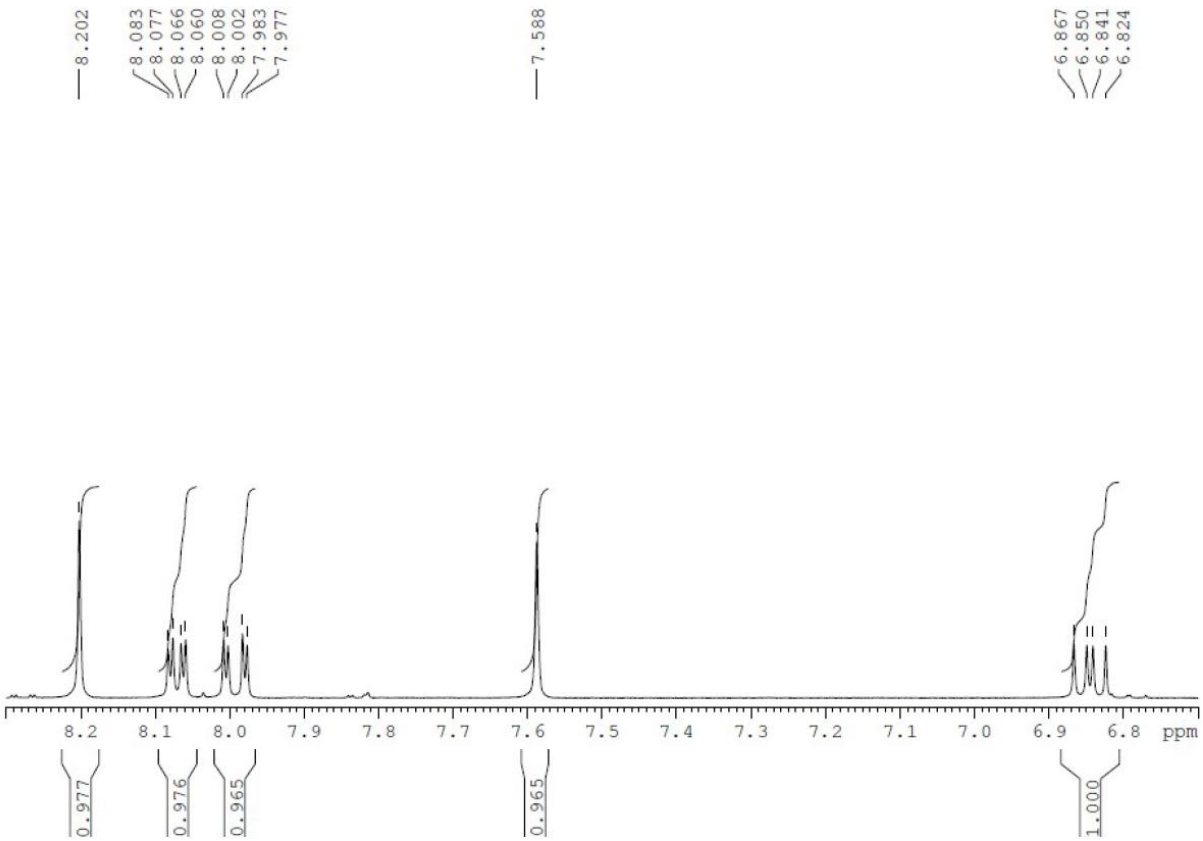

S26. ^{1}H NMR spectrum of hydrazone 5b, expanded view.

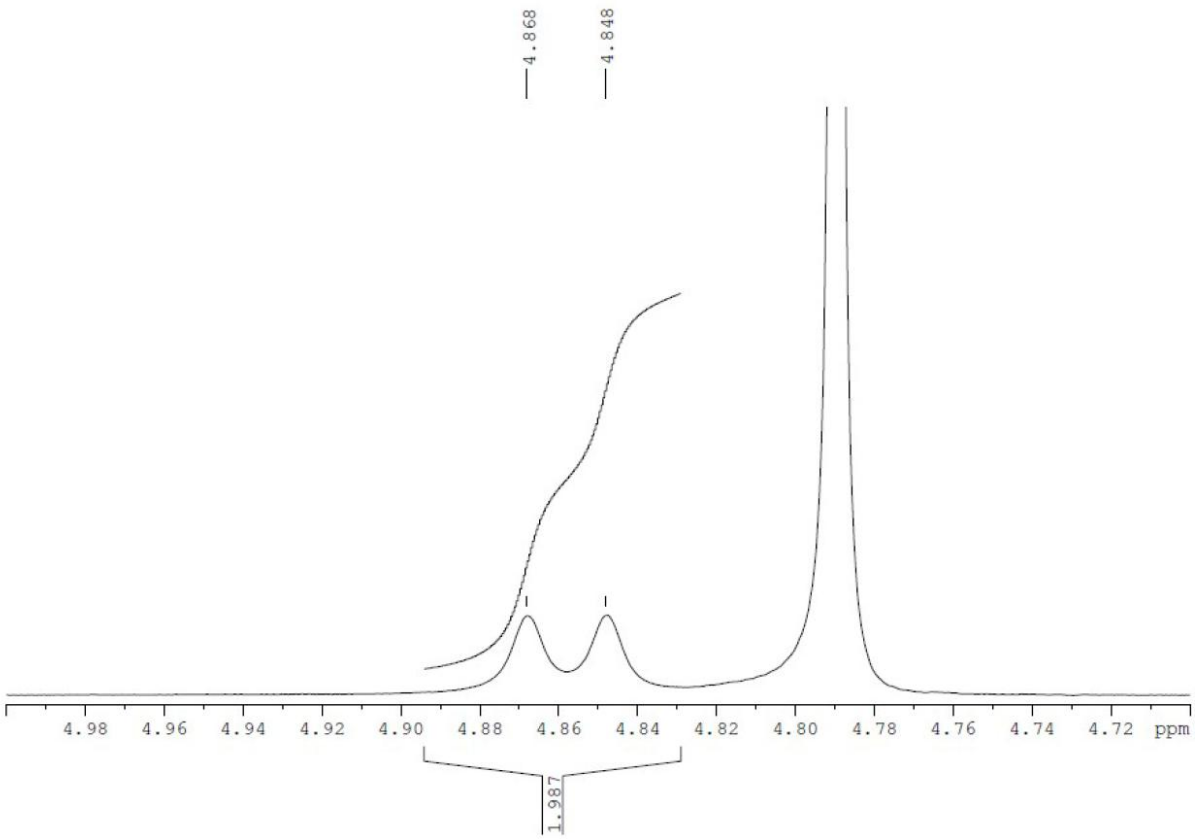

S27. ^{1}H NMR spectrum of hydrazone 5b, expanded view.

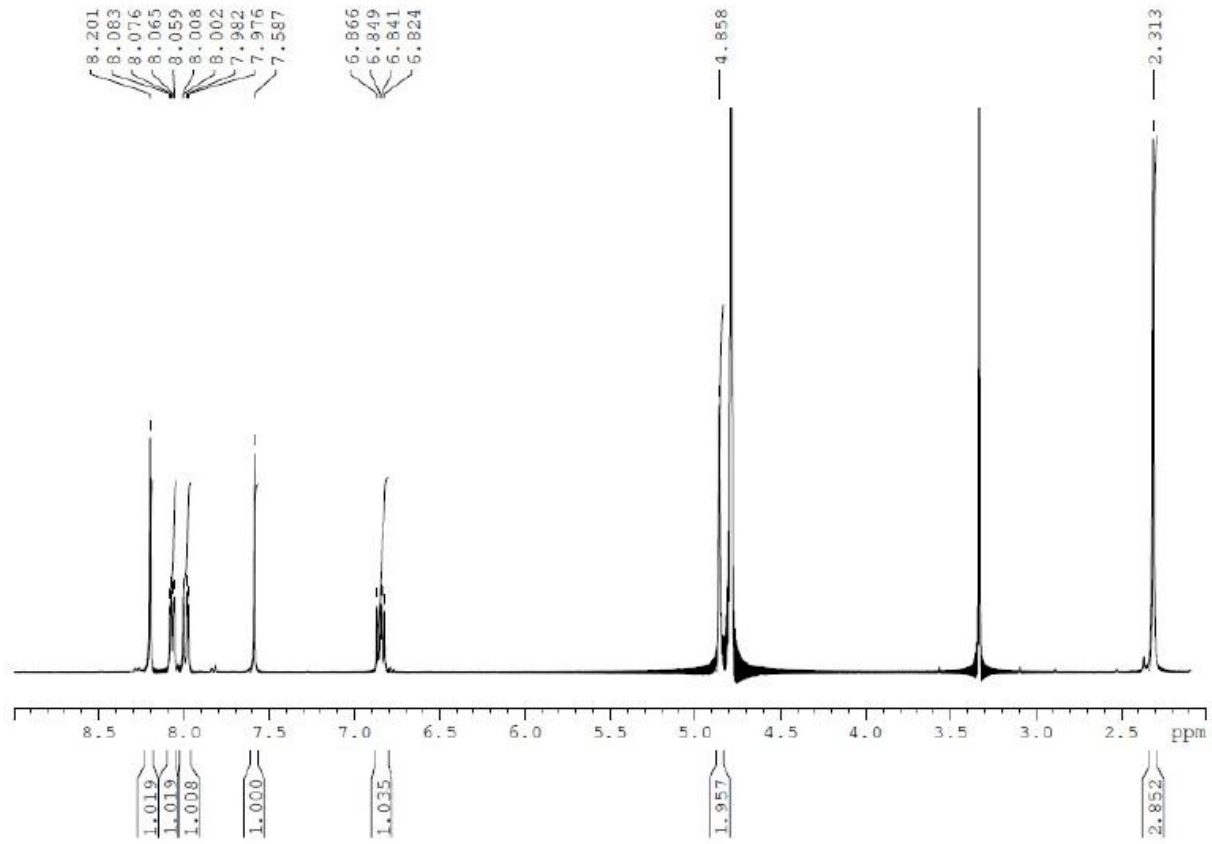

S28. Phosphorus decoupled ^{1}H NMR spectrum of hydrazone 5b. The signal at δ 3.31 ppm is due to the presence of MeOH in the sample.

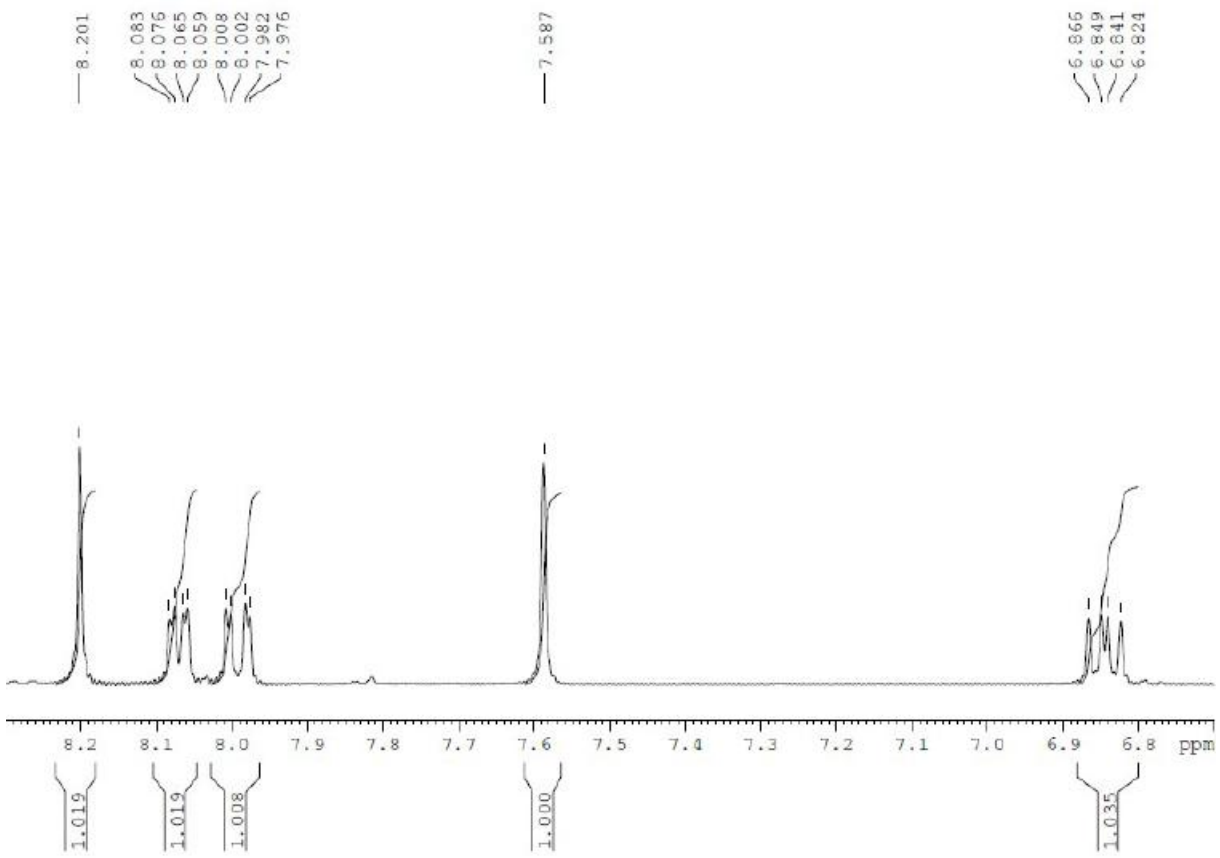

S29. Phosphorus decoupled ^{1}H NMR spectrum of hydrazone 5b, expanded view.

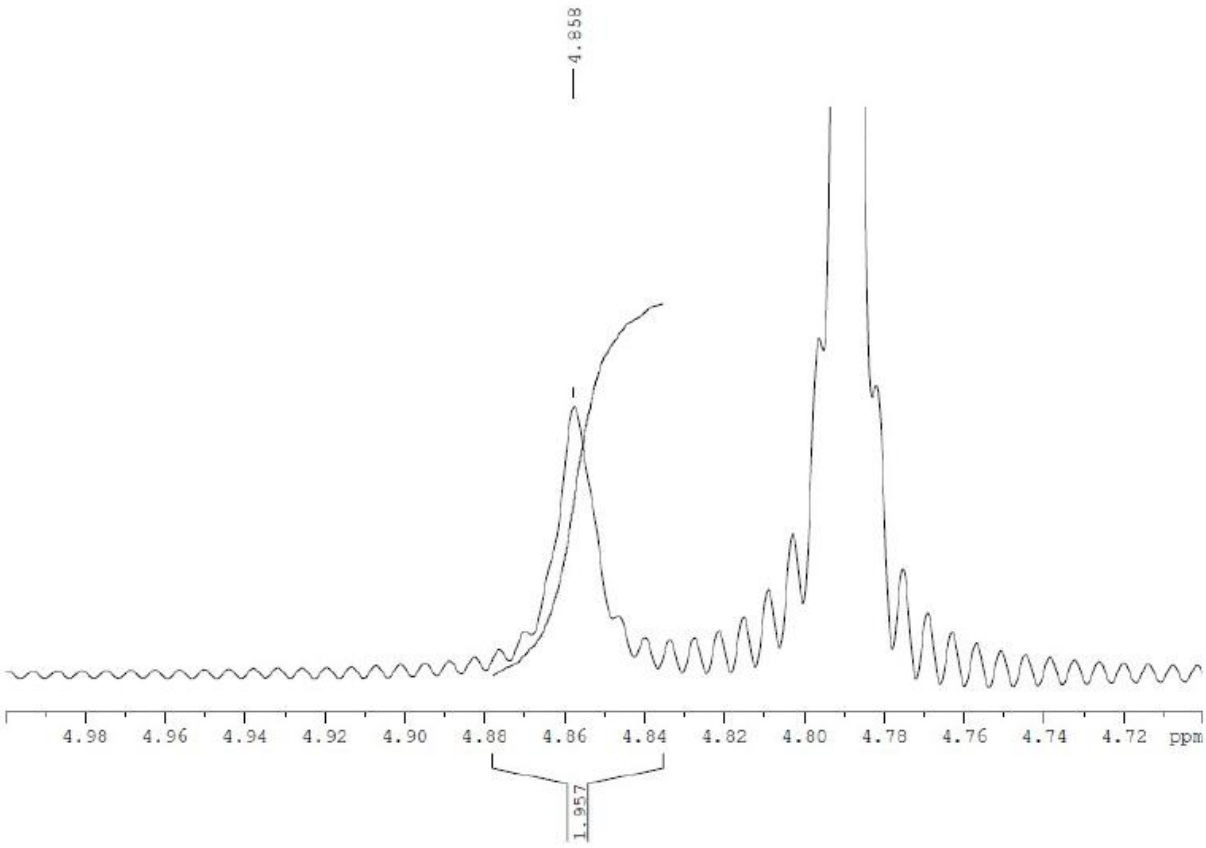

S30. Phosphorus decoupled ^{1}H NMR spectrum of hydrazone 5b, expanded view.

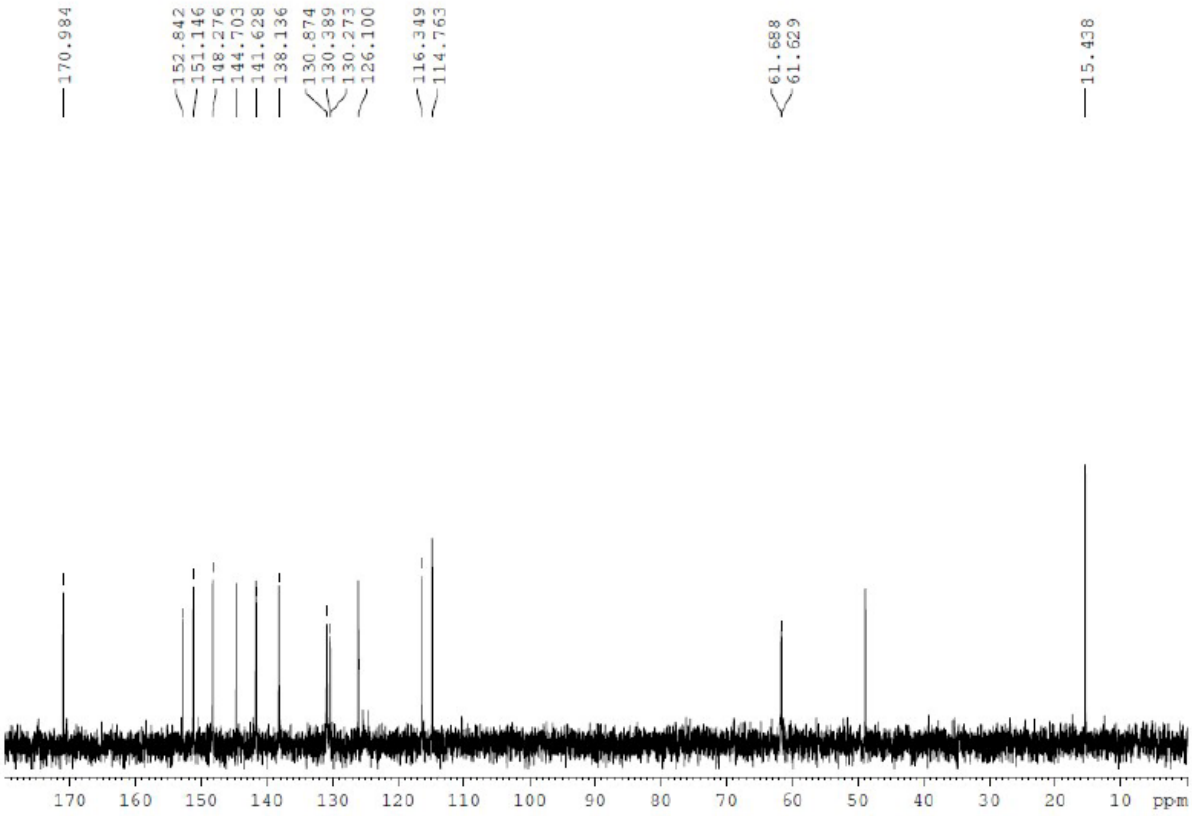

S31. ^{13}C NMR spectrum of hydrazone 5b. Due to solubility problems, the spectrum was acquired in D_2O, containing 1 drop of 40 % NaOH, pH > 10. The signal at δ 49.0 ppm is due to the presence of MeOH in the sample.

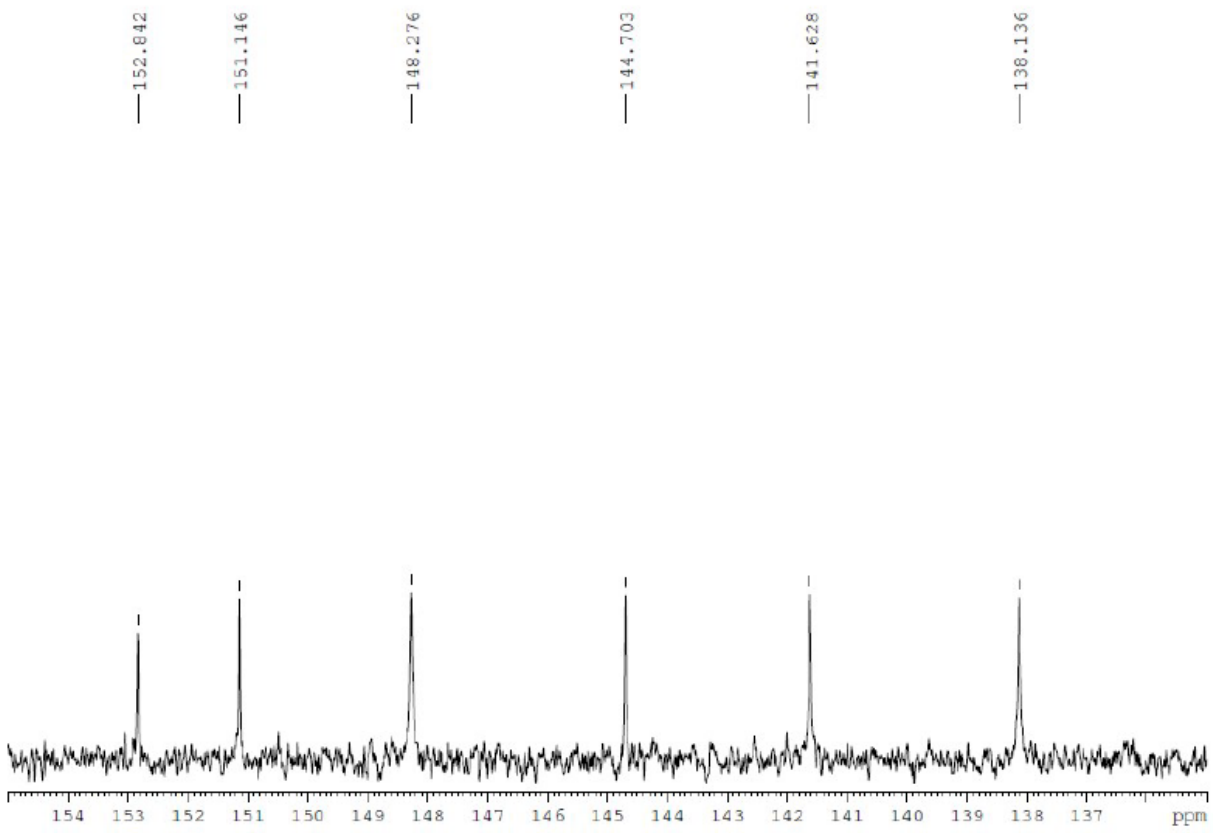

S32. ^{13}C NMR spectrum of hydrazone 5b, expanded view.

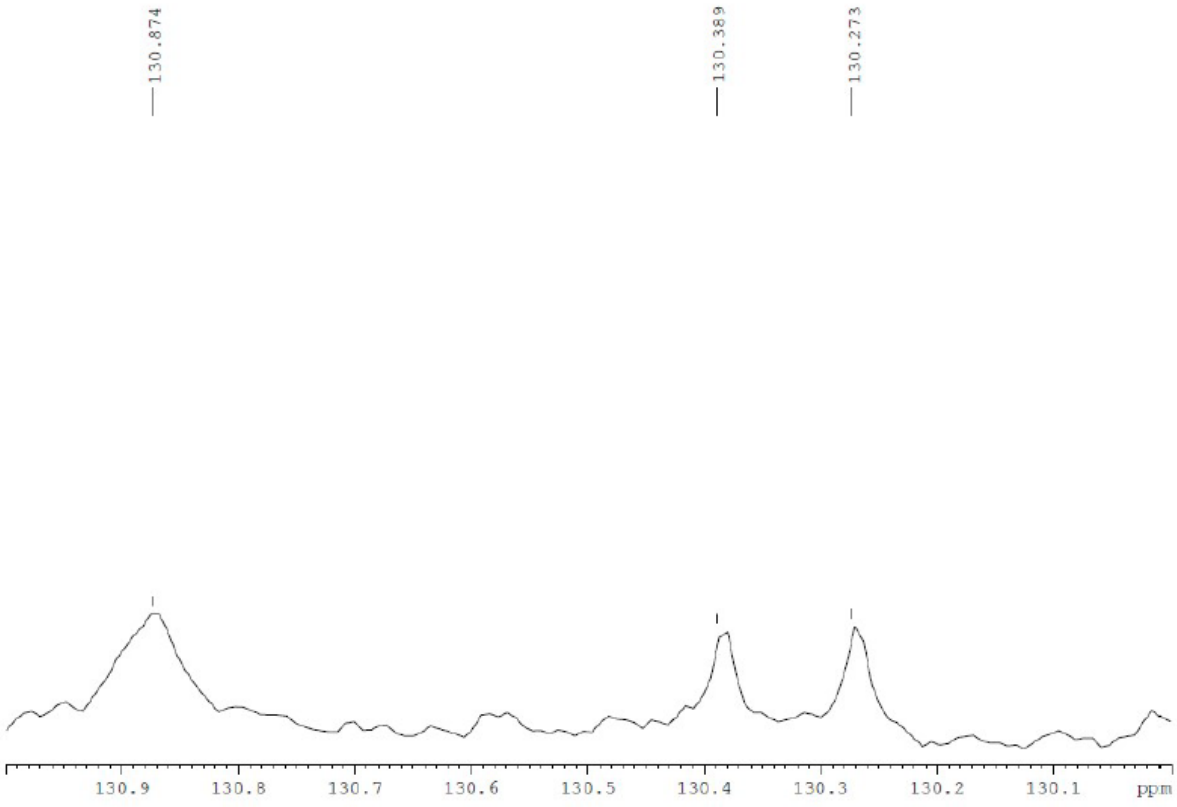

S33. ^{13}C NMR spectrum of hydrazone 5b, expanded view.

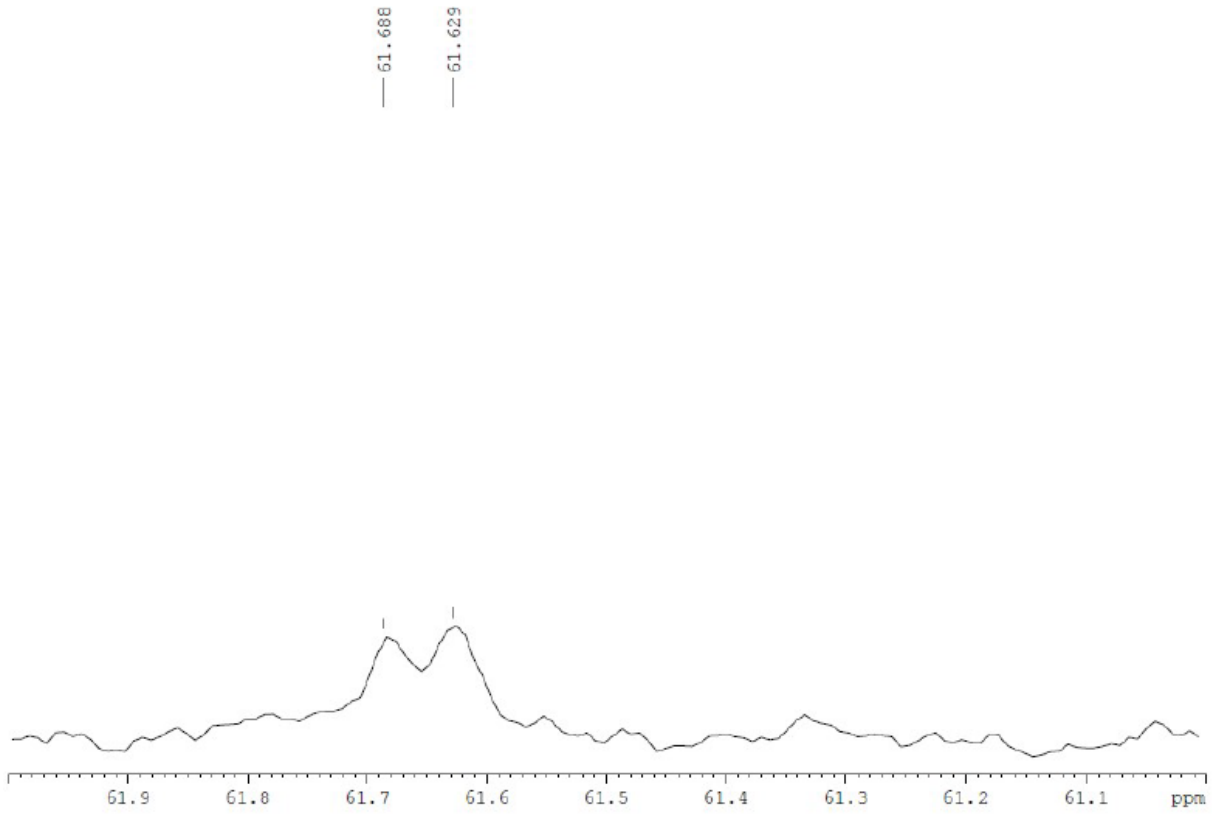

S34. ^{13}C NMR spectrum of hydrazone 5b, expanded view.

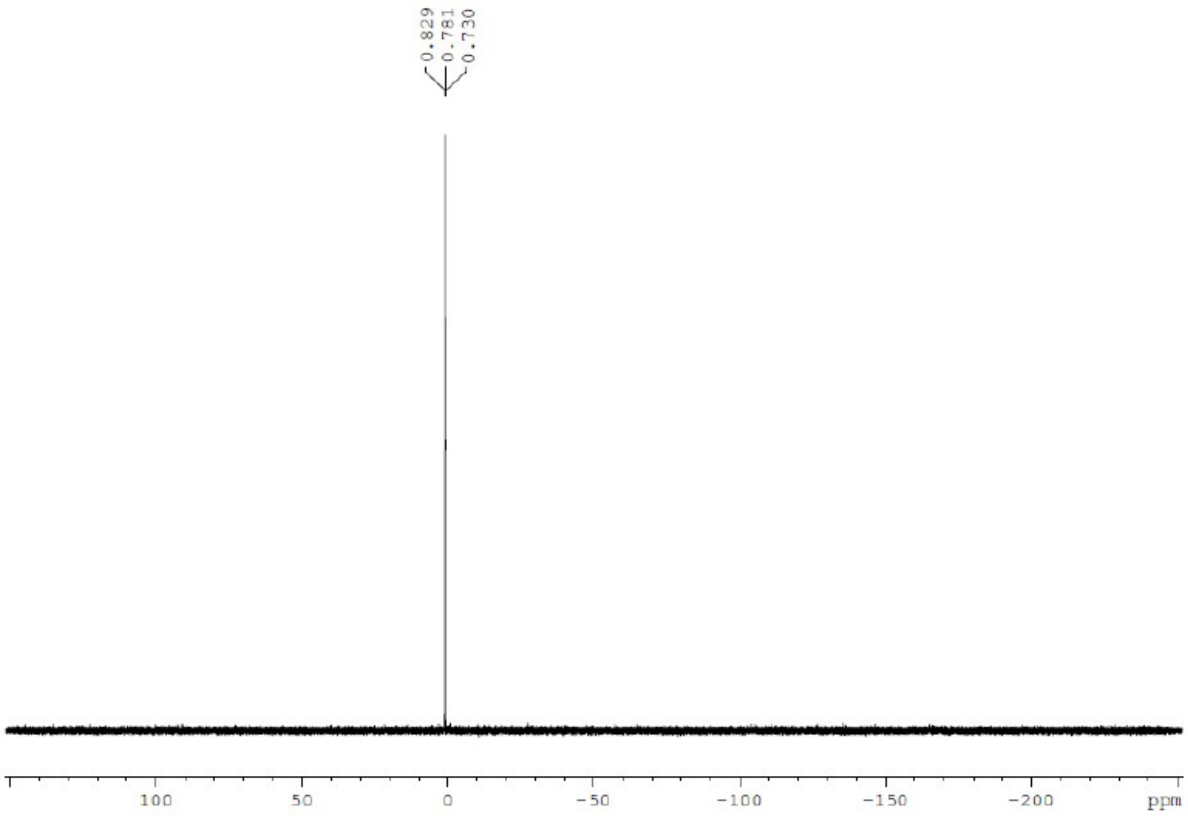

S35. ^{31}P NMR spectrum of hydrazone 5b. Due to solubility problems, the spectrum was acquired in D_2O, containing 1 drop of 40% NaOH, pH > 10.

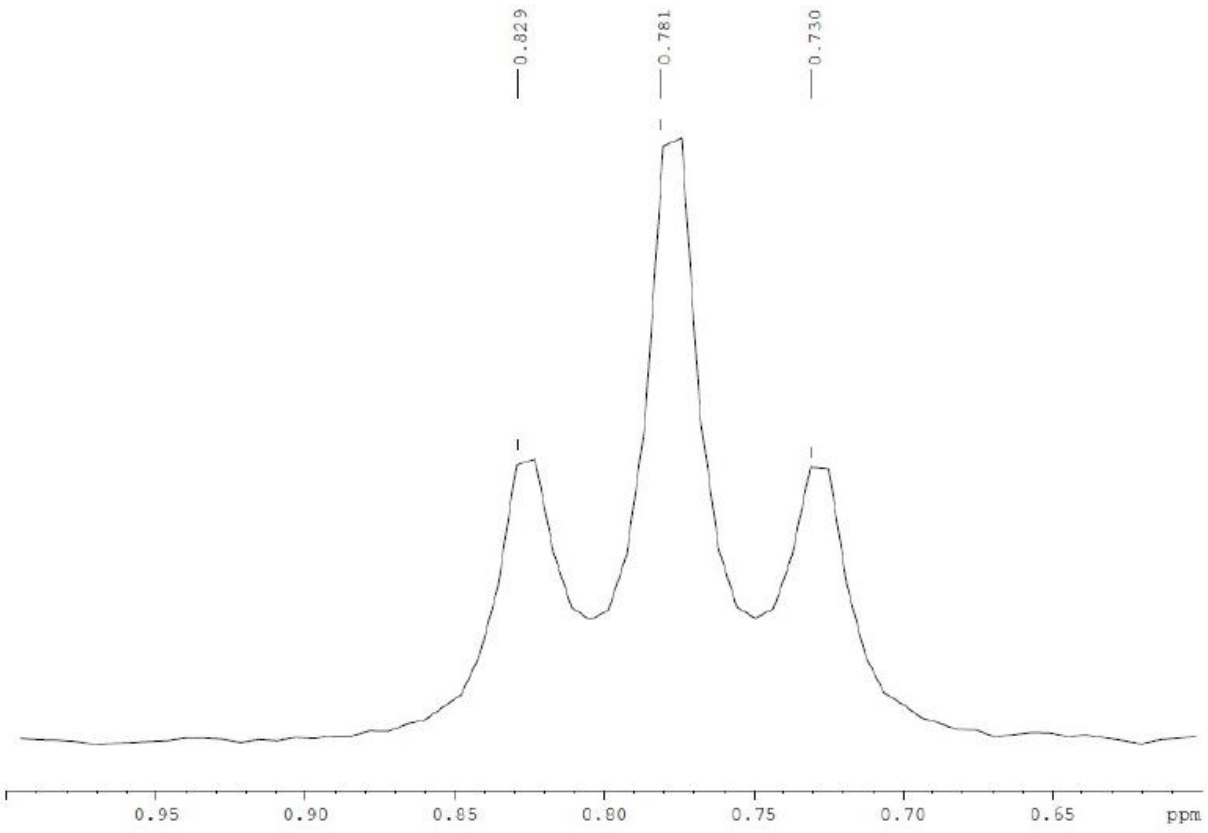

S36. ^{31}P NMR spectrum of hydrazone 5b, expanded view.

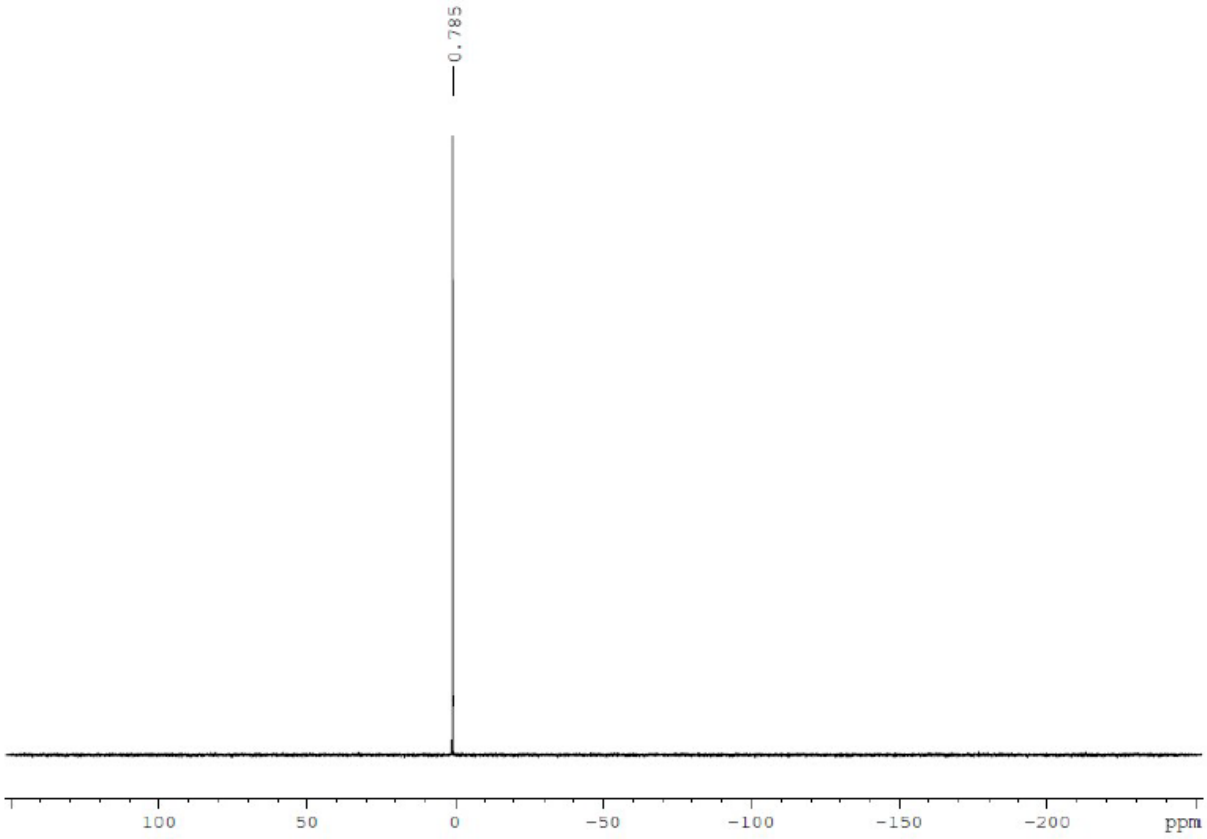

S37. Proton decoupled ^{31}P NMR spectrum of hydrazone 5b.

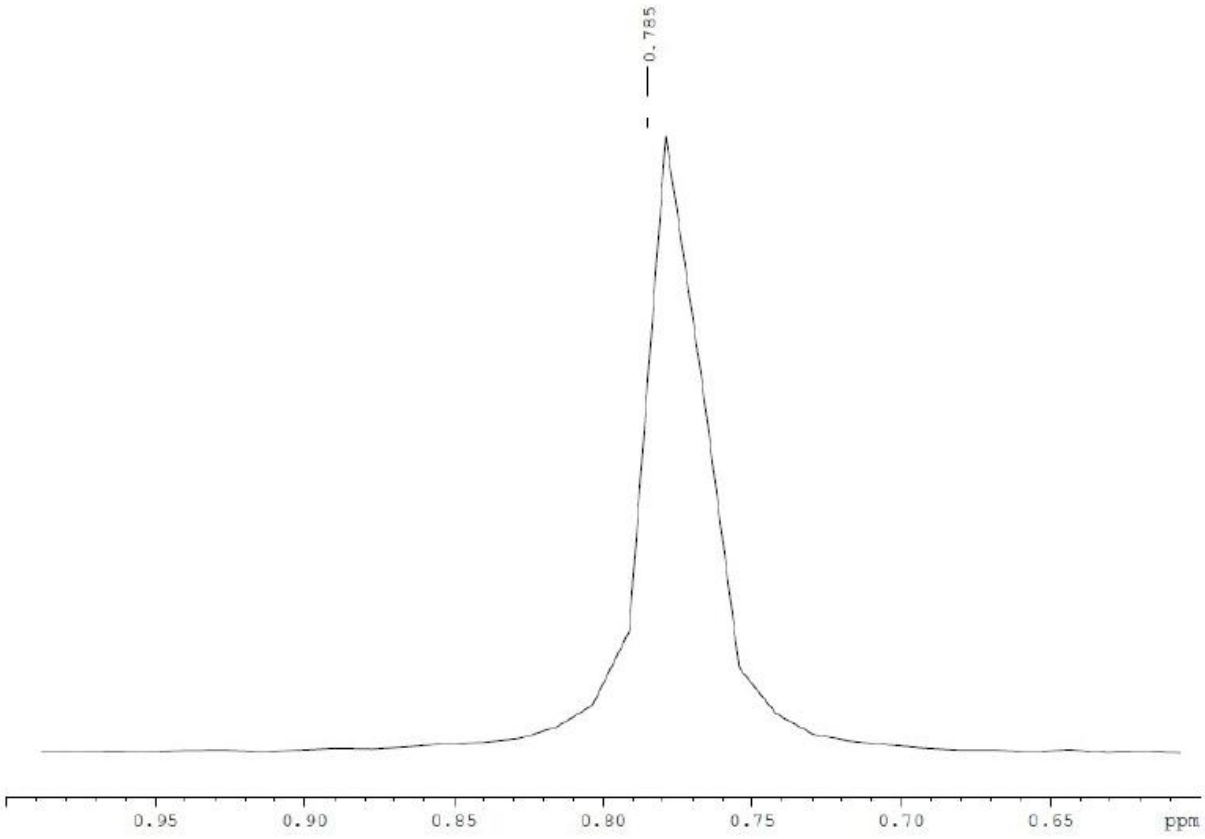

S38. Proton decoupled ^{31}P NMR spectrum of hydrazone 5b, expanded view.

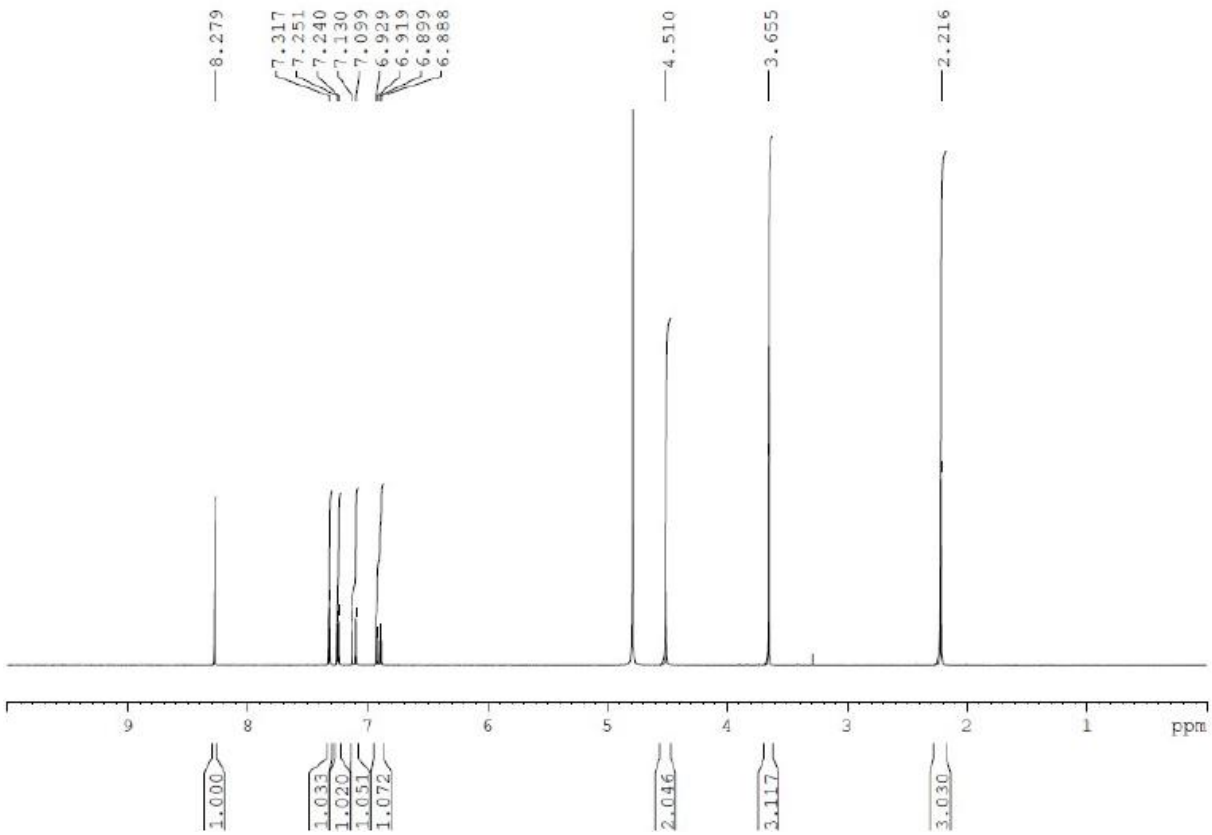

S39. ^{1}H NMR spectrum of hydrazone 6a. Due to solubility problems, the spectrum was acquired in D_2O, containing 1 drop of 40 % NaOH, pH > 10.

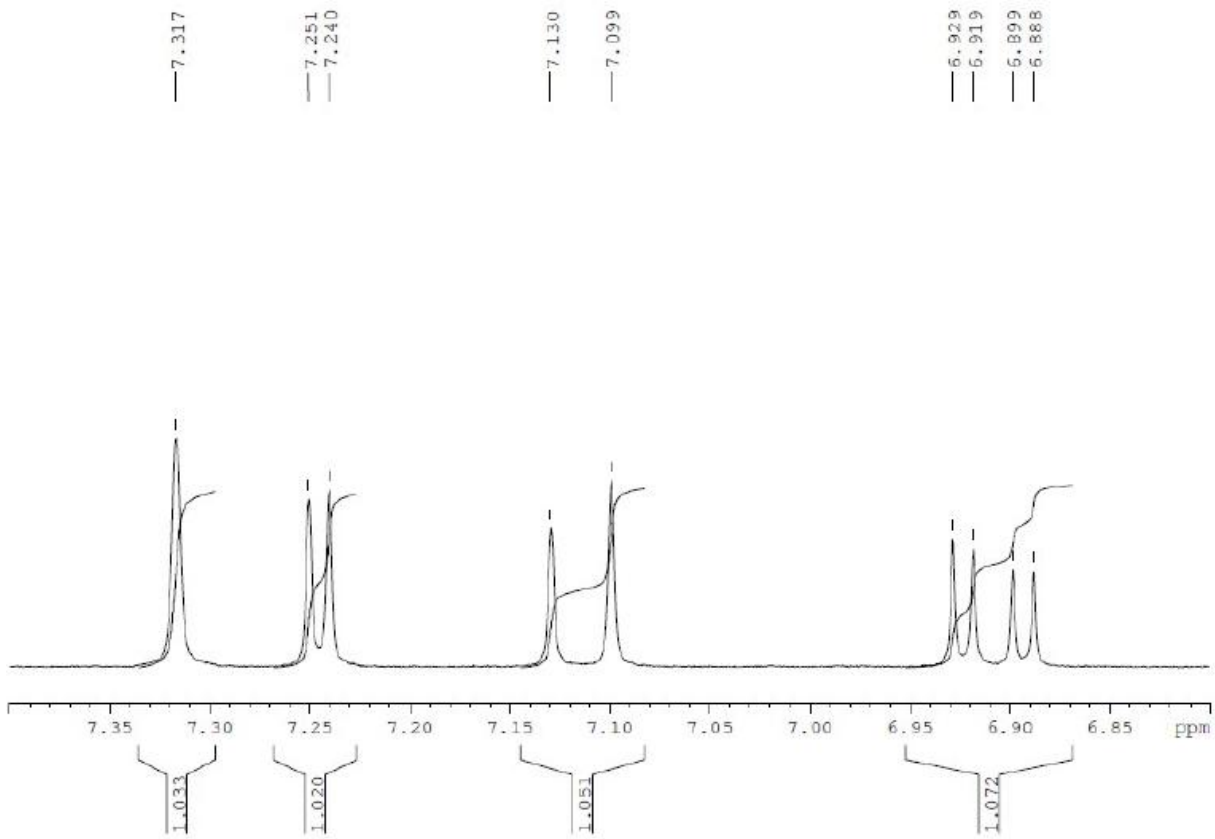

S40. ^{1}H NMR spectrum of hydrazone 6a, expanded view.

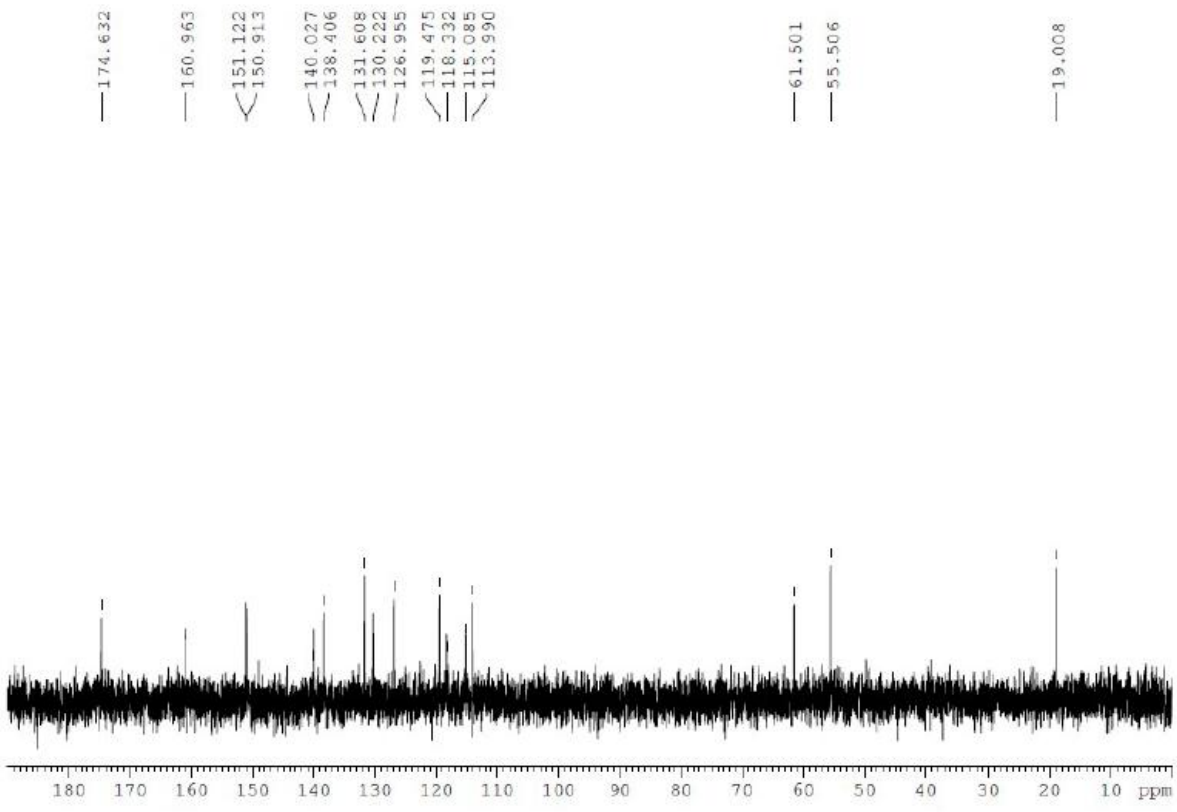

S41. ^{13}C NMR spectrum of hydrazone 6a. Due to solubility problems, the spectrum was acquired in D_2O, containing 1 drop of 40 % NaOH, pH > 10.

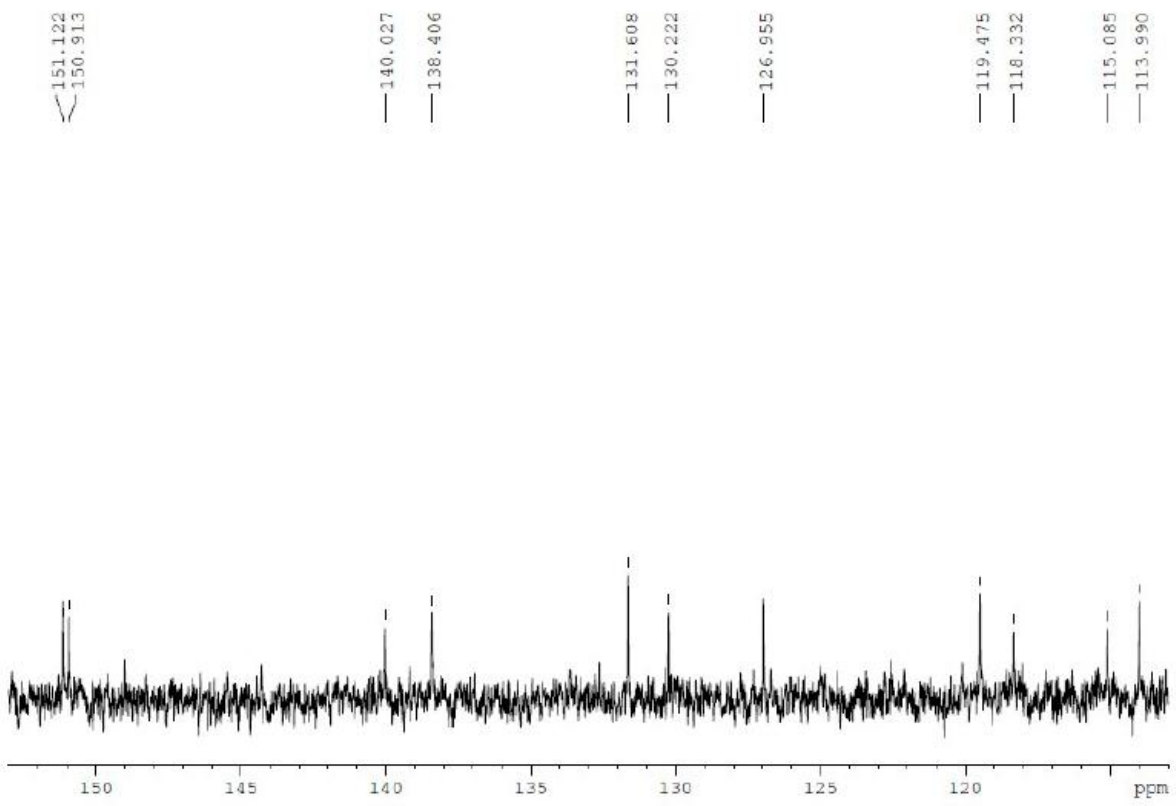

S42. ^{13}C NMR spectrum of hydrazone 6a, expanded view.

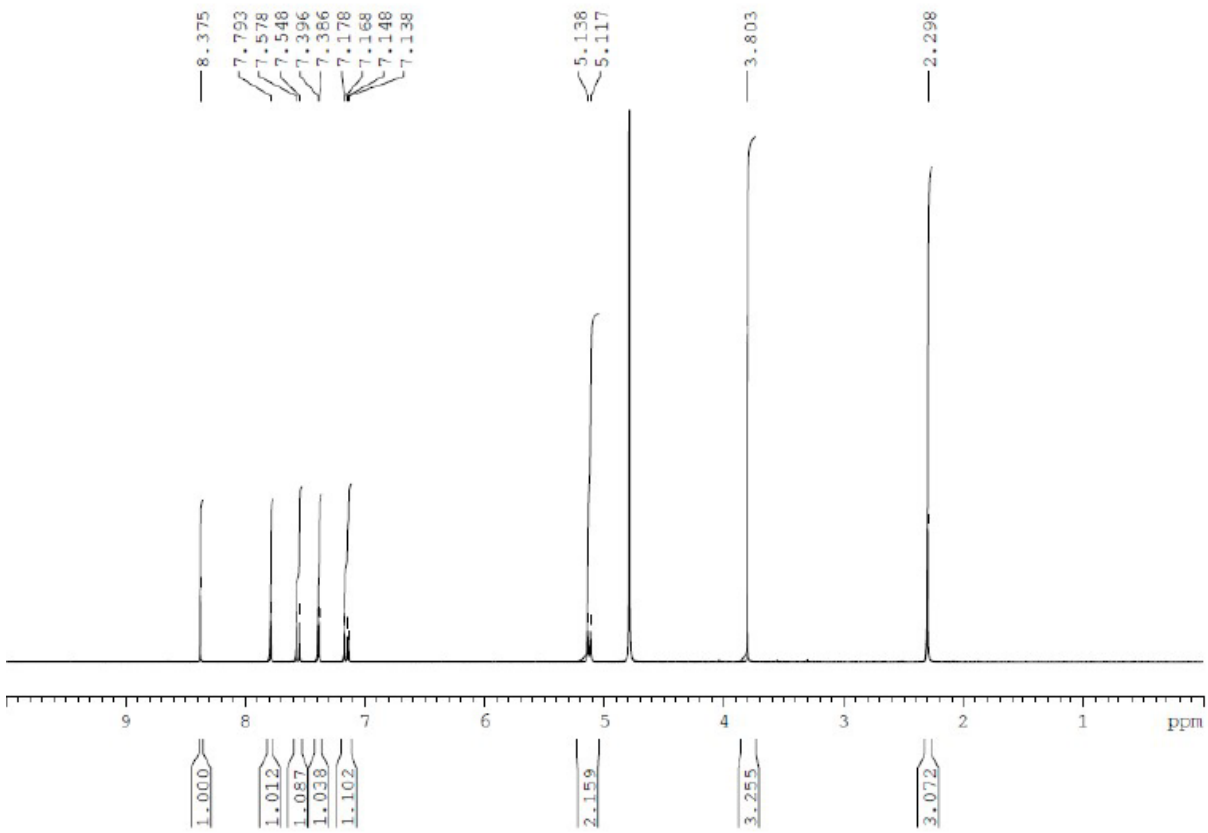

S43. ^{1}H NMR spectrum of hydrazone 6b. Due to solubility problems, the spectrum was acquired in D_2O, containing 1 drop of 40 % NaOH, pH > 10.

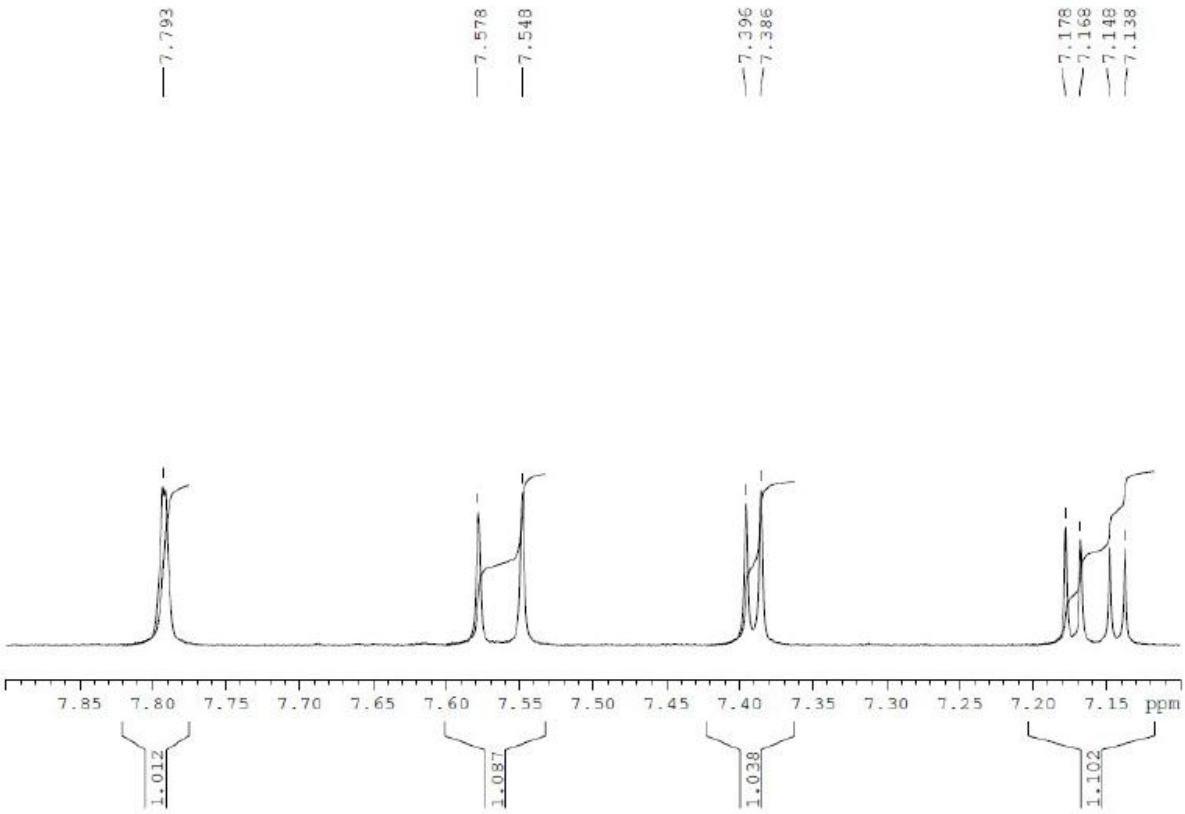

S44. ^{1}H NMR spectrum of hydrazone 6b, expanded view.

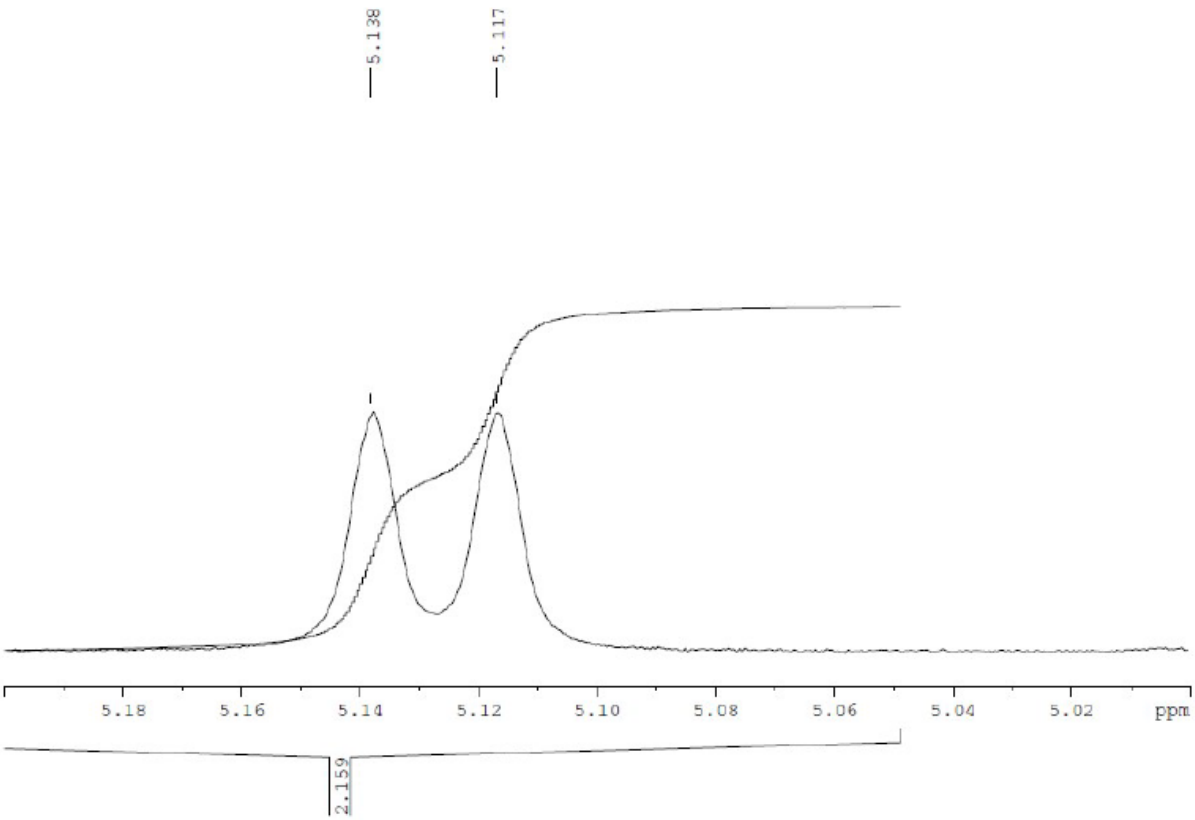

S45. ^{1}H NMR spectrum of hydrazone 6b, expanded view.

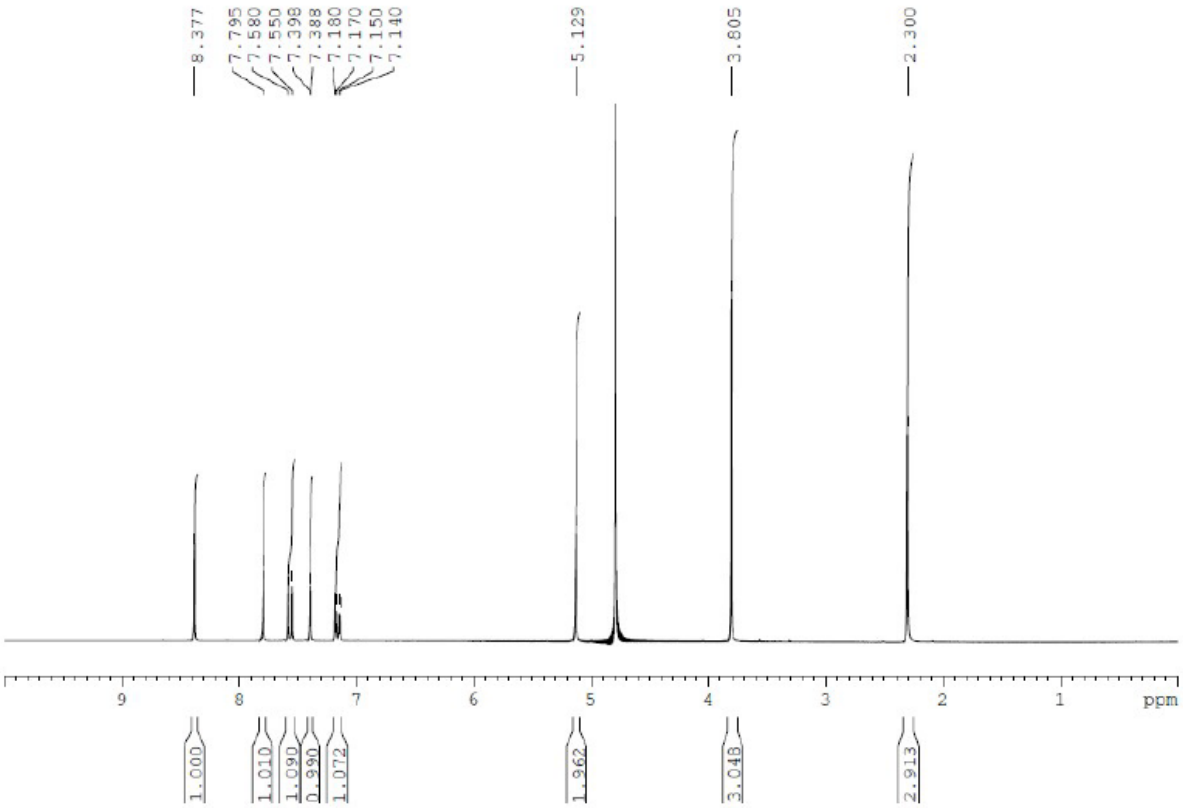

S46. Phosphorus decoupled ^{1}H NMR spectrum of hydrazone 6b.

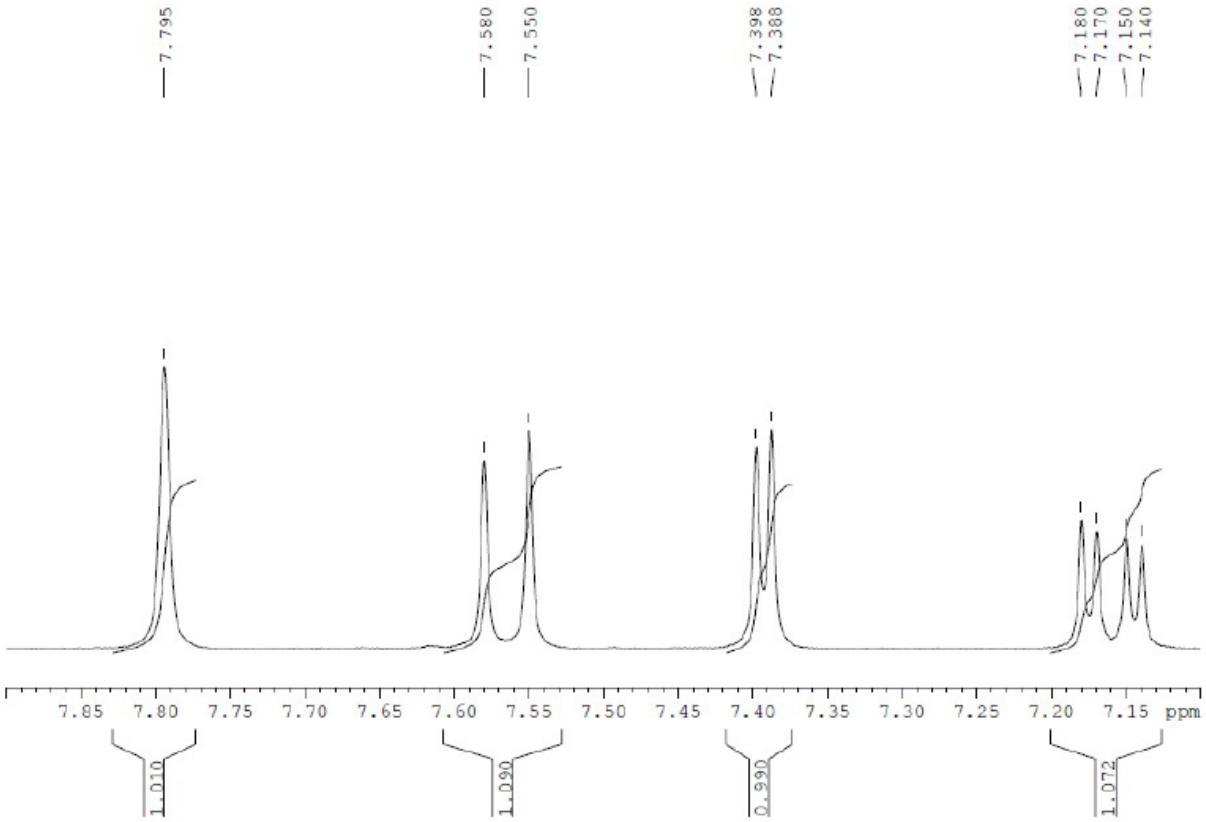

S47. Phosphorus decoupled ^{1}H NMR spectrum of hydrazone 6b, expanded view.

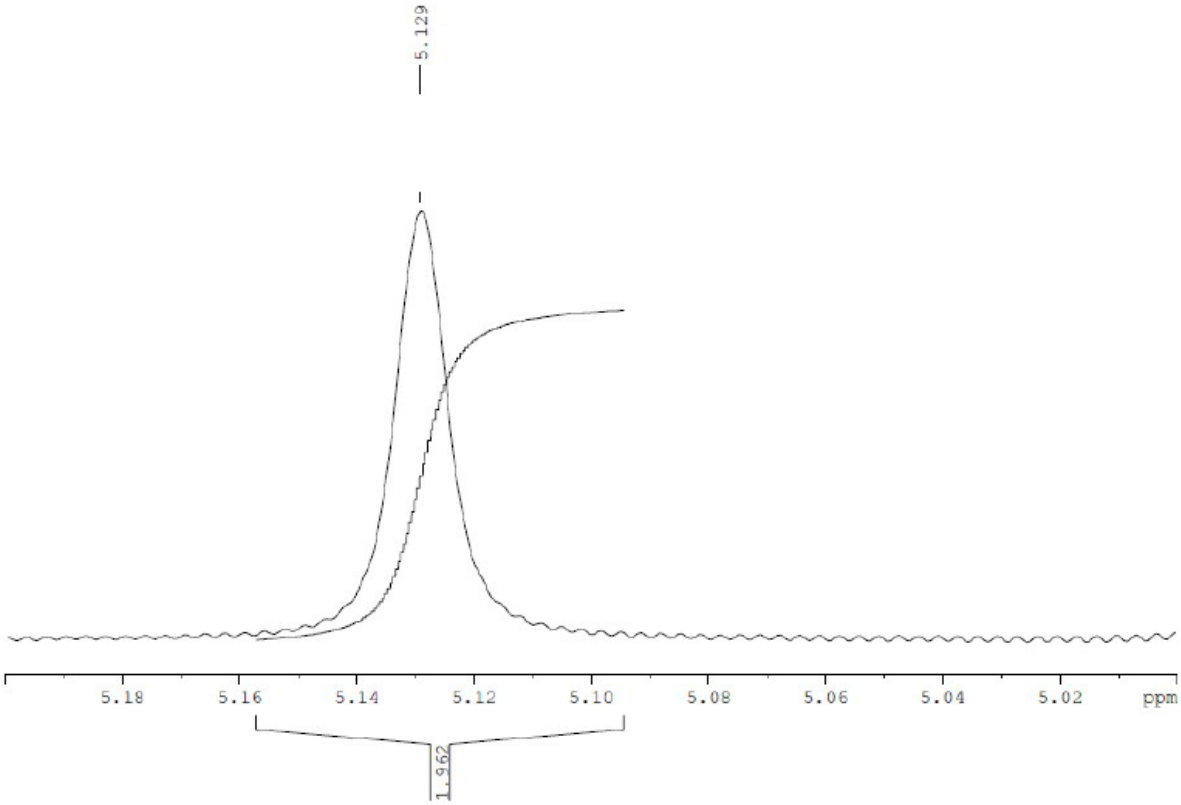

S48. Phosphorus decoupled ^{1}H NMR spectrum of hydrazone 6b, expanded view.

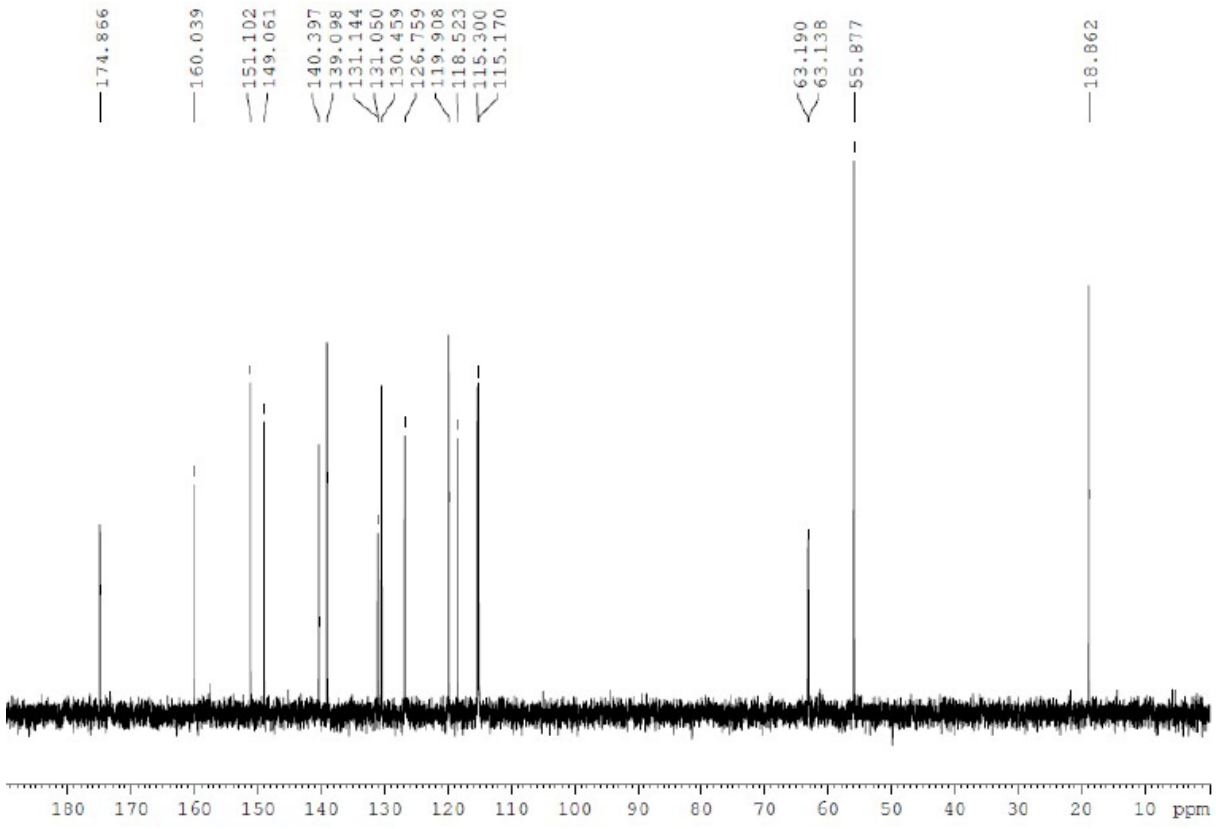

S49. ^{13}C NMR spectrum of hydrazone 6b. Due to solubility problems, the spectrum was acquired in D_2O, containing 1 drop of 40 % NaOH, pH > 10.

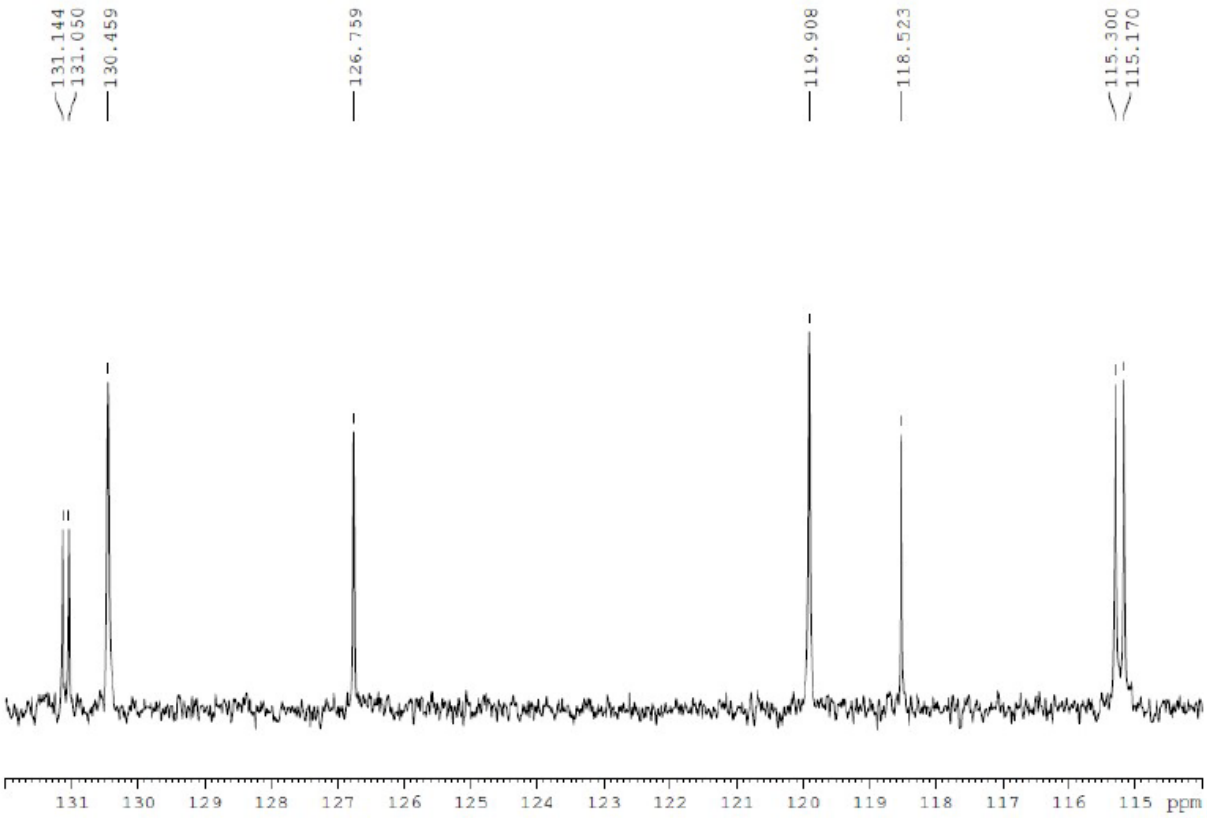

S50. ^{13}C NMR spectrum of hydrazone 6b, expanded view.

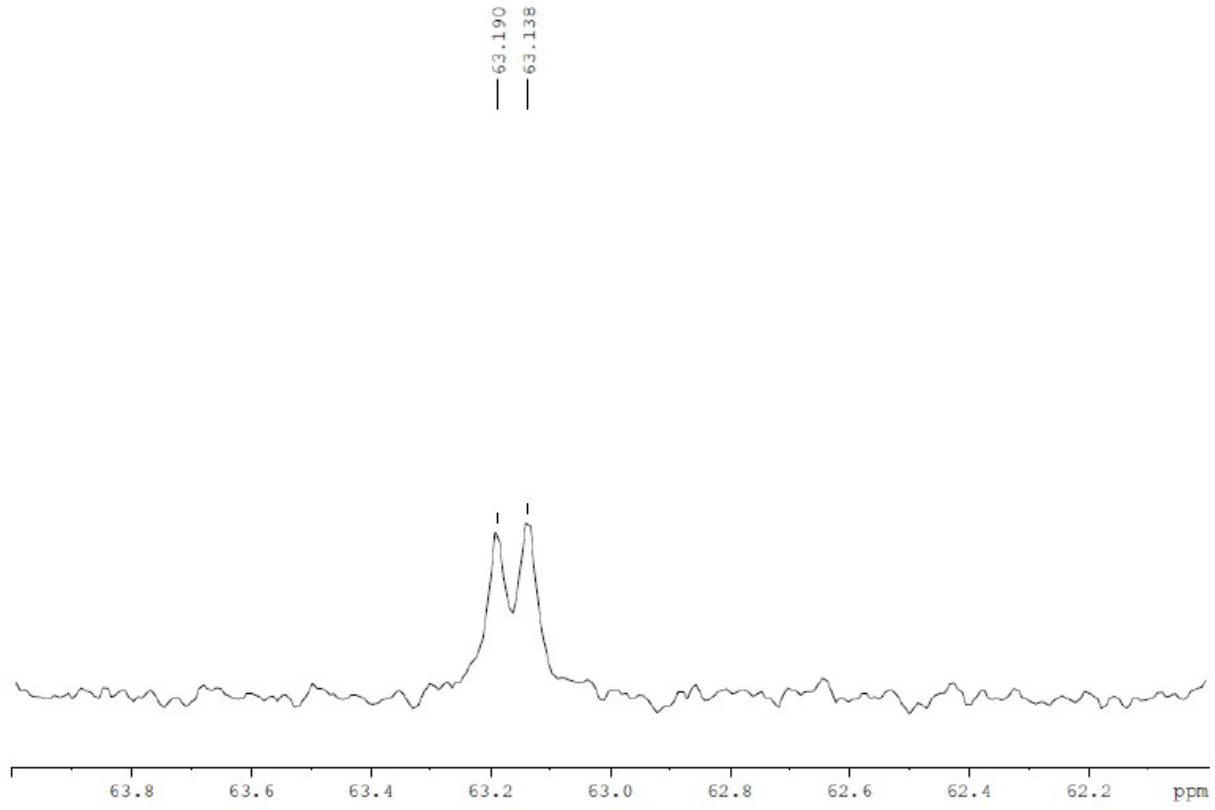

S51. ^{13}C NMR spectrum of hydrazone 6b, expanded view.

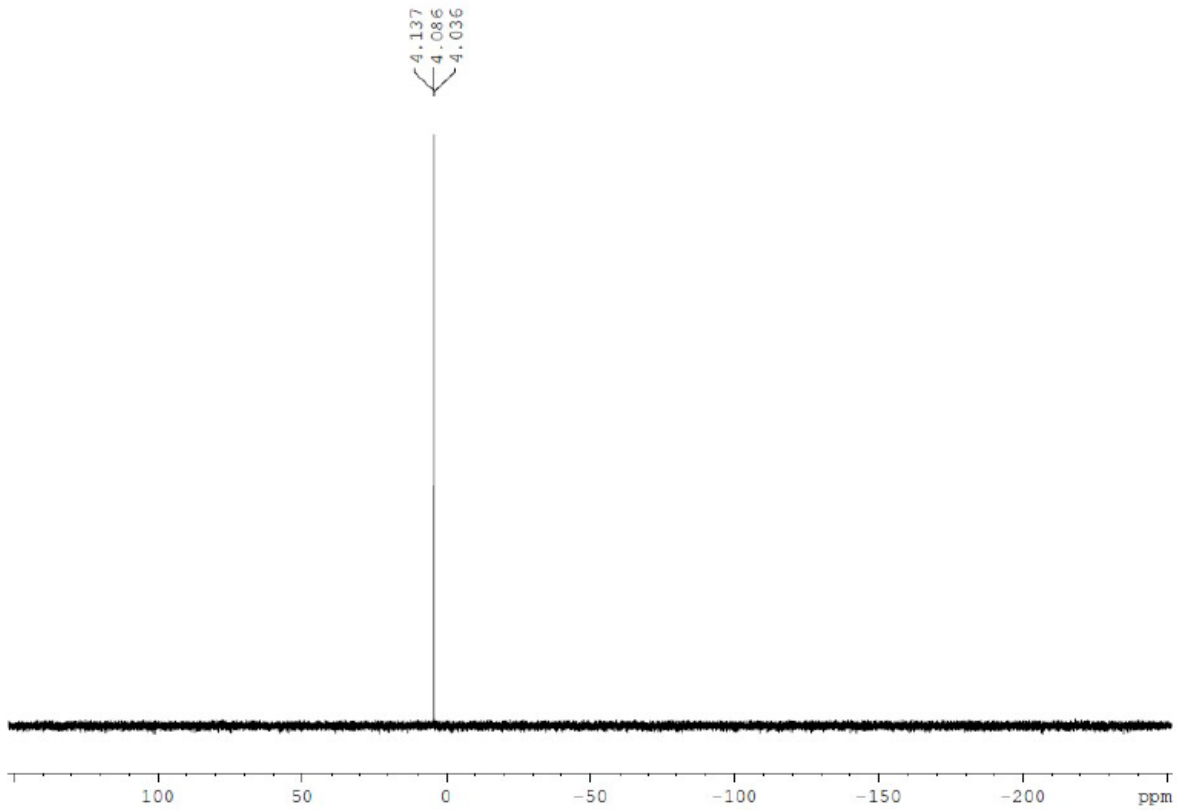

S52. ^{31}P NMR spectrum of hydrazone 6b. Due to solubility problems, the spectrum was acquired in D_2O, containing 1 drop of 40 % NaOH, pH > 10.

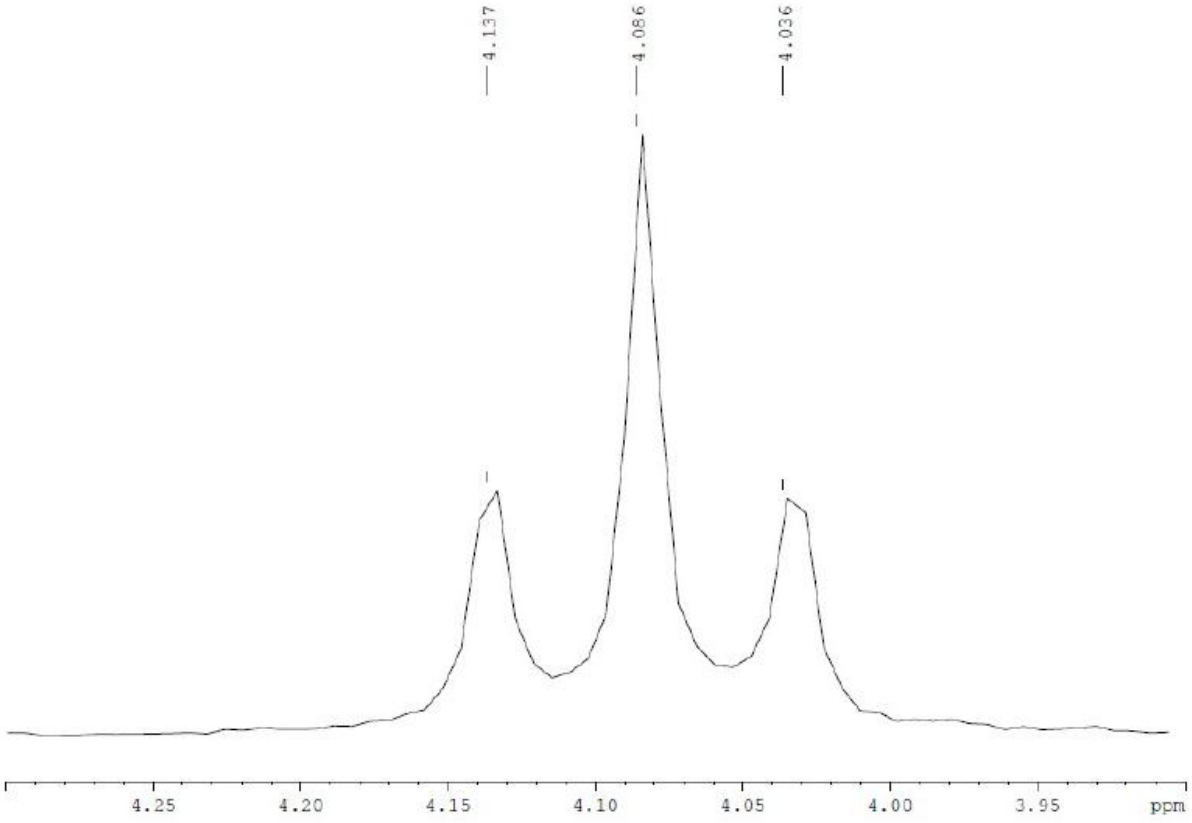

S53. ^{31}P NMR spectrum of hydrazone 6b, expanded view.

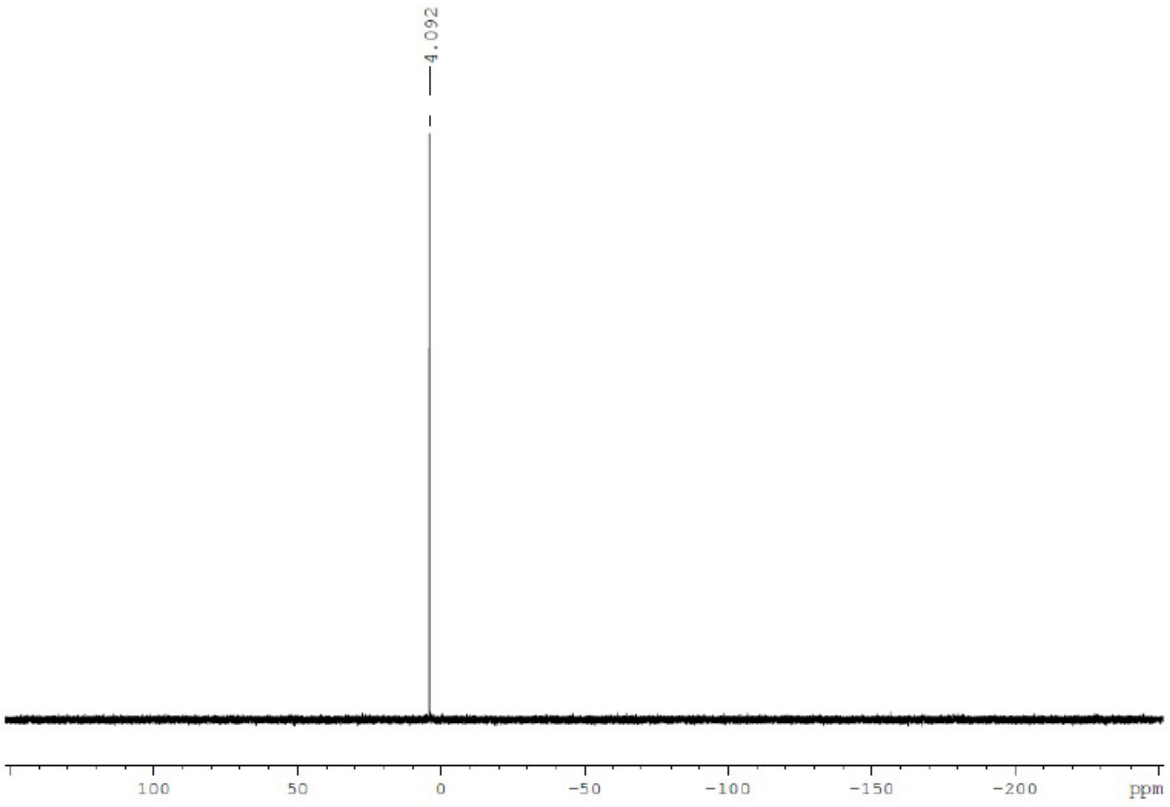

S54. Proton decoupled ^{31}P NMR spectrum of hydrazone 6b.

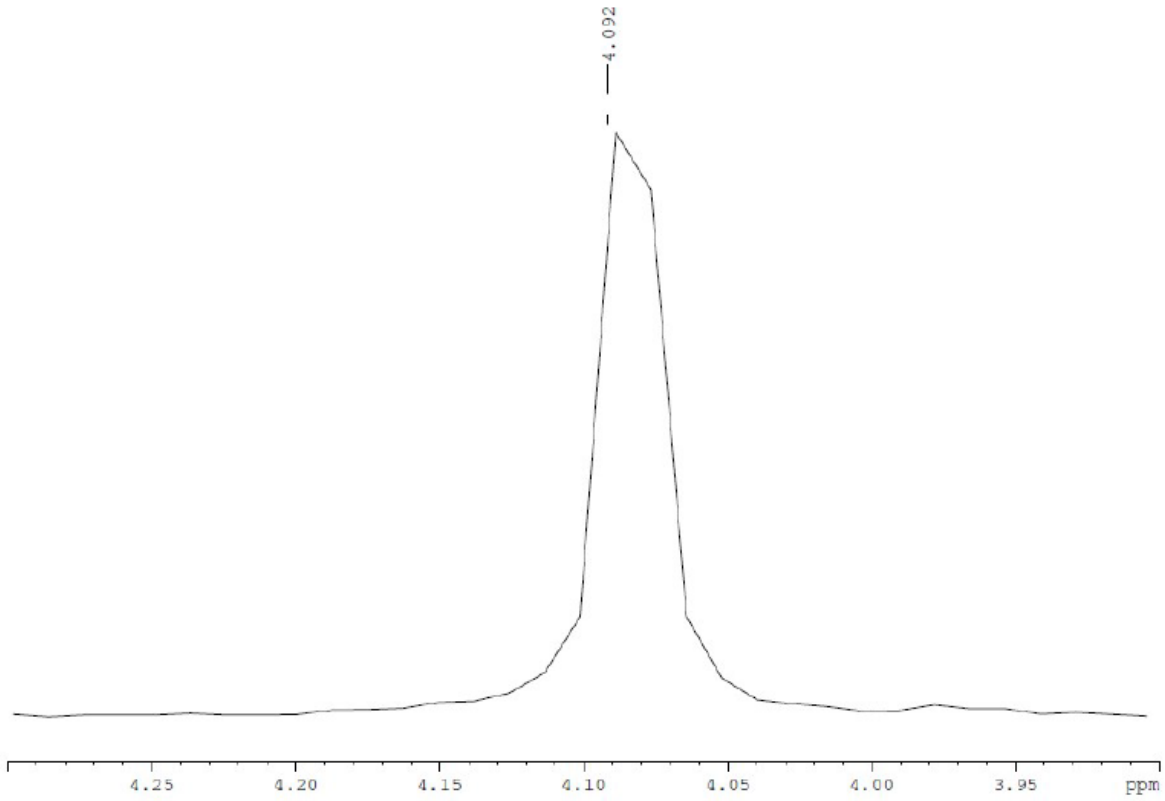

S55. Proton decoupled ^{31}P NMR spectrum of hydrazone 6b, expanded view.

2.10.9. Validation of Vitamin B_6 Metabolite Detection

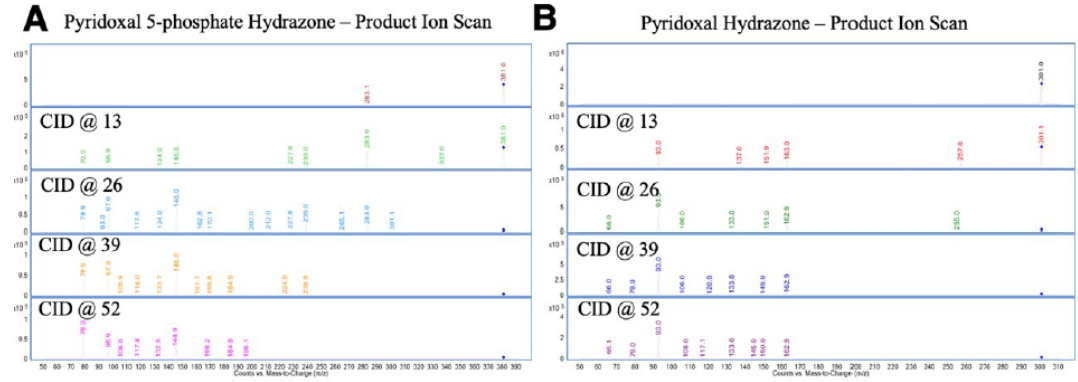

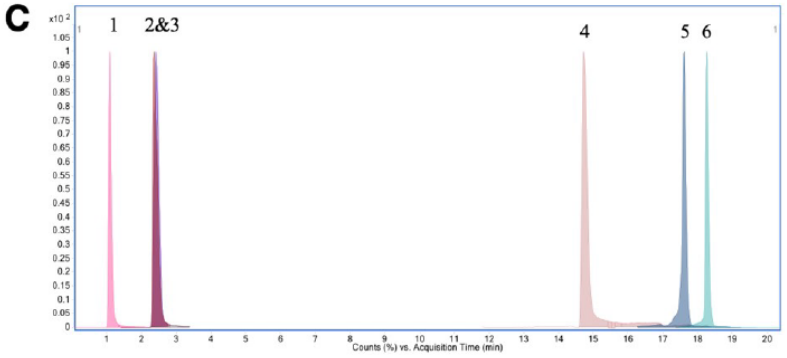

1. Pyridoxamine
2. Pyridoxine
3. Pyridoxal
4. Pyridoxal 5-phosphate
5. Pyridoxal hydrazone
6. Pyridoxal 5-phosphate Hydrazone

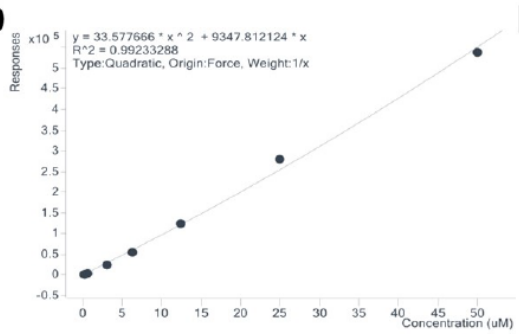

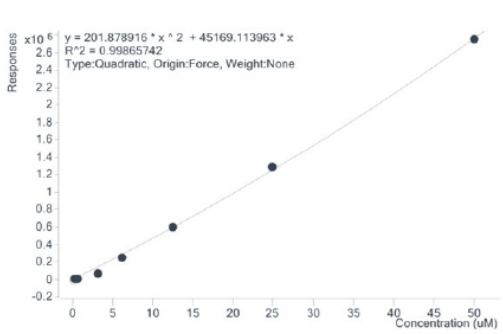

F

Compound Name	Ion Transition	Retention Time	Fragmentor	Collision Energy	Cell Accelerator Energy	Relative Response (Qual/Quant Ion)
Pyridoxal (Quantifier)	166.1 -> 138.0	2.43	76	12	4	
Pyridoxal (Qualifier)	166.1 -> 108.0	2.43	76	14	4	72
Pyridoxal 5 phosphate (Quantifier)	246.0 -> 79.0	14.87	70	30	4	
Pyridoxal 5-phosphate Hydrazone (Quantifier)	381.0 -> 79.0	18.31	116	52	4	
Pyridoxal 5-phosphate Hydrazone (Qualifier)	381.0 -> 97.0	18.31	116	16	4	71
Pyridoxamine (Quantifier)	167.1 -> 121.0	1.20	102	22	4	
Pyridoxamine (Qualifier)	167.1 -> 122.0	1.20	102	18	4	49
Pyridoxine (Quantifier)	168.1 -> 122.1	2.43	92	17	4	
Pyridoxine (Qualifier)	168.1 -> 166	2.43	92	9	4	61
Pyridoxal Hydrazone (Quantifier)	301.1 -> 93.0	17.60	110	24	4	
Pyridoxal Hydrazone (Qualifier)	301.1 -> 257.1	17.60	110	12	4	35

S56. Validation of Vitamin B_6 metabolite detection and quantification by liquid chromatography-mass spectrometry. Product ion scans are provided for the 2-HYNIC hydrazone of PLP (A) and PL (B), as well as LC-MS chromatogram (C). Standard curves for the detection of hydrazones of 2-HYNIC with PLP (D) and PL (E) are provided. (F) Detailed methodology for LCMS detection of Vitamin B_6 metabolites, including 2-HYNIC hydrazones, are tabulated.

2.11. Notes and References

(1) Percudani, R.; Peracchi, A. A Genomic Overview of Pyridoxal-Phosphate-Dependent Enzymes. *EMBO Rep* **2003**, *4* (9), 850–854.

(2) Ueland, P. M.; Ulvik, A.; Rios-Avila, L.; Midttun, Ø.; Gregory, J. F. Direct and Functional Biomarkers of Vitamin B6 Status. *Annu Rev Nutr* **2015**, *35*, 33–70.

(3) Richard, J. P.; Amyes, T. L.; Crugeiras, J.; Rios, A. Pyridoxal 5′-Phosphate: Electrophilic Catalyst Extraordinaire. *Current Opinion in Chemical Biology* **2009**, *13* (4), 475–483.

(4) di Salvo, M. L.; Safo, M. K.; Contestabile, R. Biomedical Aspects of Pyridoxal 5'-Phosphate Availability. *Front Biosci (Elite Ed)* **2012**, *4* (3), 897–913.

(5) Niculescu, A. B.; Le-Niculescu, H.; Levey, D. F.; Roseberry, K.; Soe, K. C.; Rogers, J.; Khan, F.; Jones, T.; Judd, S.; McCormick, M. A.; Wessel, A. R.; Williams, A.; Kurian, S. M.; White, F. A. Towards Precision Medicine for Pain: Diagnostic Biomarkers and Repurposed Drugs. *Mol Psychiatry* **2019**, *24* (4), 501–522.

(6) Kuypers, N. J.; Hoane, M. R. Pyridoxine Administration Improves Behavioral and Anatomical Outcome after Unilateral Contusion Injury in the Rat. *Journal of Neurotrauma* **2010**, *27* (7), 1275–1282.

(7) Galluzzi, L.; Vitale, I.; Senovilla, L.; Olaussen, K. A.; Pinna, G.; Eisenberg, T.; Goubar, A.; Martins, I.; Michels, J.; Kratassiouk, G.; Carmona-Gutierrez, D.; Scoazec, M.; Vacchelli, E.; Schlemmer, F.; Kepp, O.; Shen, S.; Tailler, M.; Niso-Santano, M.; Morselli, E.; Criollo, A.; Adjemian, S.; Jemaà, M.; Chaba, K.; Pailleret, C.; Michaud, M.; Pietrocola, F.; Tajeddine, N.; de La Motte Rouge, T.; Araujo, N.; Morozova, N.; Robert, T.; Ripoche, H.; Commo, F.; Besse, B.; Validire, P.; Fouret, P.; Robin, A.; Dorvault, N.; Girard, P.; Gouy, S.; Pautier, P.; Jägemann, N.; Nickel, A. C.; Marsili, S.; Paccard, C.; Servant, N.; Hupé, P.; Behrens, C.; Behnam-Motlagh, P.; Kohno, K.; Cremer, I.; Damotte, D.; Alifano, M.; Midttun, Ø.; Ueland, P. M.; Lazar, V.; Dessen, P.; Zischka, H.; Chatelut, E.; Castedo, M.; Madeo, F.; Barillot, E.; Thomale, J.; Wistuba, I. I.; Sautès-Fridman, C.; Zitvogel, L.; Soria, J. C.; Harel-Bellan, A.; Kroemer, G. Prognostic Impact of Vitamin B6 Metabolism in Lung Cancer. *Cell Reports* **2012**, *2* (2), 257–269.

(8) Kushnir, M. M.; Song, B.; Yang, E.; Frank, E. L. Development and Clinical Evaluation of a High-Throughput LC-MS/MS Assay for Vitamin B6 in Human Plasma and Serum. *J Appl Lab Med* **2021**, *6* (3), 702–714.

(9) Chiang, E.-P.; Smith, D. E.; Selhub, J.; Dallal, G.; Wang, Y.-C.; Roubenoff, R. Inflammation Causes Tissue-Specific Depletion of Vitamin B6. *Arthritis Research & Therapy* **2005**, *7* (6), R1254.

(10) Hansen, C. M.; Shultz, T. D.; Memon, H. S.; Kwak, H.-K.; Leklem, J. E. Assessment of Vitamin B-6 Status in Young Women Consuming a Controlled Diet Containing Four Levels of

Vitamin B-6 Provides an Estimated Average Requirement and Recommended Dietary Allowance. *The Journal of Nutrition* **2001**, *131* (6), 1777–1786.

(11) Ueland, P. M.; McCann, A.; Midttun, Ø.; Ulvik, A. Inflammation, Vitamin B6 and Related Pathways. *Mol Aspects Med* **2017**, *53*, 10–27.

(12) Clayton, P. T. B6-Responsive Disorders: A Model of Vitamin Dependency. *J Inherit Metab Dis* **2006**, *29* (2–3), 317–326.

(13) Kim, H.; Enrione, E. B.; Narayanan, V.; Li, T.; Campa, A. Associations of Vitamin B6 Intake and Plasma Pyridoxal 5′-Phosphate with Plasma Polyunsaturated Fatty Acids in US Older Adults: Findings from NHANES 2003–2004. *Nutrients* **2022**, *14* (11), 2336.

(14) Jun, Y. W.; Hebenbrock, M.; Kool, E. T. A Fluorescent Hydrazone Exchange Probe of Pyridoxal Phosphate for the Assessment of Vitamin B6 Status. *Chem. Commun.* **2019**, *56* (2), 317–320.

(15) Lazurko, C.; Radonjic, I.; Suchý, M.; Liu, G.; Rolland-Lagan, A.-G.; Shuhendler, A. Fingerprinting Biogenic Aldehydes through Pattern Recognition Analyses of Excitation–Emission Matrices. *ChemBioChem* **2019**, *20* (4), 543–554.

(16) Suchý, M.; Lazurko, C.; Kirby, A.; Dang, T.; Liu, G.; Shuhendler, A. J. Methyl 5-MeO-N-Aminoanthranilate, a Minimalist Fluorogenic Probe for Sensing Cellular Aldehydic Load. *Org. Biomol. Chem.* **2019**, *17* (7), 1843–1853.

(17) Dang, T.; Suchy, M.; Truong, Y. J.; Oakden, W.; Lam, W. W.; Lazurko, C.; Facey, G.; Stanisz, G. J.; Shuhendler, A. J. Hydrazo-CEST: Hydrazone-Dependent Chemical Exchange

Saturation Transfer Magnetic Resonance Imaging Contrast Agents. *Chemistry – A European Journal* **2018**, *24* (36), 9148–9156.

(18) Crisalli, P.; Kool, E. T. Importance of Ortho Proton Donors in Catalysis of Hydrazone Formation. *Org. Lett.* **2013**, *15* (7), 1646–1649.

(19) Kölmel, D. K.; Kool, E. T. Oximes and Hydrazones in Bioconjugation: Mechanism and Catalysis. *Chem. Rev.* **2017**, *117* (15), 10358–10376.

(20) Kool, E. T.; Park, D.-H.; Crisalli, P. Fast Hydrazone Reactants: Electronic and Acid/Base Effects Strongly Influence Rate at Biological pH. *J. Am. Chem. Soc.* **2013**, *135* (47), 17663–17666.

(21) Yang, X.; Yadav, N. N.; Song, X.; Ray Banerjee, S.; Edelman, H.; Minn, I.; van Zijl, P. C. M.; Pomper, M. G.; McMahon, M. T. Tuning Phenols with Intra-Molecular Bond Shifted HYdrogens (IM-SHY) as diaCEST MRI Contrast Agents. *Chemistry – A European Journal* **2014**, *20* (48), 15824–15832.

(22) Song, X.; Yang, X.; Ray Banerjee, S.; Pomper, M. G.; McMahon, M. T. Anthranilic Acid Analogs as Diamagnetic CEST MRI Contrast Agents That Feature an Intramolecular-Bond Shifted Hydrogen. *Contrast Media Mol Imaging* **2015**, *10* (1), 74–80.

(23) Yang, X.; Song, X.; Li, Y.; Liu, G.; Ray Banerjee, S.; Pomper, M. G.; McMahon, M. T. Salicylic Acid and Analogues as diaCEST MRI Contrast Agents with Highly Shifted Exchangeable Proton Frequencies. *Angewandte Chemie International Edition* **2013**, *52* (31), 8116–8119.

(24) Kraus-Berthier, L.; Jan, M.; Guilbaud, N.; Naze, M.; Pierré, A.; Atassi, G. Histology and Sensitivity to Anticancer Drugs of Two Human Non-Small Cell Lung Carcinomas Implanted in the Pleural Cavity of Nude Mice. *Clinical Cancer Research* **2000**, *6* (1), 297–304.

(25) Chemotherapy for lung cancer. *Canadian Cancer Society*. **2020** https://cancer.ca/en/cancer-information/cancer-types/lung/treatment/chemotherapy.

(26) Menzies, C.; Naz, S.; Patten, D.; Alquier, T.; Bennett, B. M.; Lacoste, B. Distinct Basal Metabolism in Three Mouse Models of Neurodevelopmental Disorders. *eNeuro* **2021**, *8* (2), 0292-20.

(27) Meszaros, L. K.; Dose, A.; Biagini, S. C. G.; Blower, P. J. Synthesis and Evaluation of Analogues of HYNIC as Bifunctional Chelators for Technetium. *Dalton Trans.* **2011**, *40* (23), 6260–6267.

(28) Kim, M.; Gillen, J.; Landman, B. A.; Zhou, J.; van Zijl, P. C. M. Water Saturation Shift Referencing (WASSR) for Chemical Exchange Saturation Transfer (CEST) Experiments. *Magn Reson Med* **2009**, *61* (6), 1441–1450.

(29) Liu, G.; Gilad, A. A.; Bulte, J. W. M.; van Zijl, P. C. M.; McMahon, M. T. High-Throughput Screening of Chemical Exchange Saturation Transfer MR Contrast Agents. *Contrast Media Mol Imaging* **2010**, *5* (3), 162–170.

Chapter 3: Aqueous Click Chemistry for Controlled Synthesis of Homo- and Hetero-Bislanthanide Complexes: Magnetic and Optical Characterization

Emilie Marie Sophie Patit-Tha Brun[1], Lauren Healy[1], Halimo-Kafia M. Fourreh[1], Anna Marriott[3,4], Nan Liu [1], Mojmir Suchý[1], Neerav Mullur[1], Hannah Ehler[3,4], Kimberley Brewer[4,5], Eva Hemmer [1] and Adam J. Shuhendler[1,2]

Affiliations

[1]Department of Chemistry and Biomolecular Sciences, University of Ottawa, 150 Louis Pasteur Pvt., Ottawa, Ontario, Canada, K1N 6N5

[2]University of Ottawa Heart Institute, 40 Ruskin St., Ottawa, Ontario, Canada, K1Y 4W7

[3]Department of Physics & Atmospheric Science, Dalhousie University, 1453 Lord Dalhousie Drive, Halifax, Nova Scotia, Canada, B3H 4R2

[4]Biomedical MRI Research Laboratory, IWK Health, 5850/5980 University Avenue, Halifax, Nova Scotia, Canada B3K 6R8

[5]Department of Biomedical Engineering, Dalhousie University, 5981 University Avenue, Halifax, Nova Scotia, Canada, B3H 3J5

3.1. Overview of the Research Project Presented in this Chapter

A new approach has been developed to combine two lanthanides withing the same complex by generating a 4,5-dihydrothiazoline ring. In this method, individual synthons complexed to lanthanides, ranging from europium(III) to lutetium(III), are synthesized separately. These synthons are then coupled through an uncatalyzed click reaction. The primary focus of this project was on developing the chemistry required to couple these two lanthanides within the same complex. This involved optimizing reaction conditions, ensuring the stability of the resulting complex and its characterization. Following this, their potential applications in MRI and optical imaging were explored. The unique properties of lanthanides, such as the magnetic properties of gadolinium(III), and luminescent characteristics of europium(III), make them ideal candidates for enhancing the sensitivity and specificity of imaging techniques.

3.2. Authors Contributions

E.M.S.P.B and M.S performed all the synthesis and characterization of each chemical compounds with the support of L.H., H-K.M.F., and N.M. E.M.S.P.B conducted relaxation time analysis. N.L. performed photoluminescence spectroscopy. E.M.SP.B. prepared the samples for relaxivity measurements with the support of H.E. and A.M realized the analysis of the data.

3.3. Copyright

A manuscript based on this chapter will be submitted to a journal for potential publication.

3.4. Abstract

Lanthanides have valence shell configurations that make them unique beacons for magnetic resonance imaging (MRI) and fluorescence imaging, depending on the identity of the specific chelated lanthanide. Here, a new synthetic approach for the controlled synthesis of homo- and hetero-bislanthanide complexes, from europium(III) to lutetium(III), is introduced through an aqueous, uncatalyzed "click" reaction based on the cyanohydroxyquinoline-cysteine condensation. Using this approach, a library of homo- and hetero-bislanthanide compounds was generated from single stable building blocks, and their image signalling properties were evaluated to extend this proof of concept. Both longitudinal and transverse relaxivities including T_1/T_2 ratio images were acquired on a 3T MRI scanner, with Gd-Gd-containing compounds showing the highest relaxivities when compared to other bislanthanide combinations. Optical properties of Eu-containing combinations of some of these lanthanides were also evaluated, benefiting from energy transfer between the quinoline benzothiazole chromophore product of the click reaction and the chelated lanthanide centres. The synthetic building block approach described herein affords the facile and controlled generation of bislanthanide chelates in aqueous media to support the exploration of heterobifunctional species.

3.5. Introduction

Lanthanides, a subset of rare-earth metals [1], are composed of 15 elements spanning lanthanum(III) to lutetium(III), and their utility in magnetic and luminescent probes and chemical sensors has emerged over the last century. The everyday application of lanthanide ions to diagnostic medical imaging as gadolinium-based contrast agents (GBCA) for magnetic resonance imaging (MRI) is of significant impact [2]. The development of new contrast agents for MRI is ongoing, not only to provide molecular-level diagnostics through responsive contrast agents enabling molecular imaging, but also driven by advances in image acquisition routines bringing new capabilities to translational MRI. For example, the emerging approach of MR fingerprinting, which is the ability to rapidly and simultaneously discriminate between multiple MR-active species through their unique relaxational properties [3, 4], may open new avenues for multiplexed contrast agent imaging approaches. In any iteration, lanthanide-based MRI contrast agents must form stable lanthanide chelates to be non-toxic while altering the water proton longitudinal (R_1) or transverse (R_2) relaxation rates to generate MRI contrast [5, 6].

Lanthanide ion complexes can also display fluorescence properties amenable to biologically-relevant optical imaging [7]. Europium(III) and terbium(III) are known to be emissive lanthanides that have found utility in immunoassays [8], live cell microscopy [9], and even as a bimodal luminescence-MRI contrast agent for glutathione sensing [10]. Because the *f-f* transition energies match those of visible to near-infrared wavelengths, lanthanides have also been applied to resonance energy transfer (RET) systems as the emissive components for DNA biosensing [11] or the evaluation of protein-protein interactions in living cells. [12, 13] Lanthanide-based optical probes

are also interesting choices for time-gated RET detection [11, 14] due to their large Stokes shift and long emission lifetimes [15].

Having two or more lanthanides together in the same complex has the potential to expand the functionality of the resulting molecule or material, opening new applications not accessible by monometallic species. The ongoing search for lanthanide-based compounds and materials has resulted in the exploration of multimetallic complexes with combinations of two or more lanthanide elements in a single molecule. These multimetallic complexes have been synthesized through different approaches, including the Ugi reaction [16, 17], diazotization [18] or Cu(I)-catalyzed azide-alkyne cycloaddition (CuAAC) [19]. Previously reported methods have different limitations, notably the time of the reaction, which can take from 2 [18] to as long as 6 days for chelation plus 4 days of purification by dialysis [17]. For lanthanide combinations based on CuAAC, microwave irradiation is needed, which may not be widely accessible [19]. The majority of reactions seeking to combine two lanthanides in one molecule are based on the Ugi reaction, which is a ternary reaction system culminating in the formation of α-aminoacyl amides [16, 17]. These multicomponent systems are however limited by synthetic complexity and sensitivity to acidic media [20], encouraging the search for alternative synthetic approaches to homo- and hetero-bislanthanide compounds.

Herein we report a synthetic approach for the controlled combination of two lanthanide centers, either homo or heterometallic, based on the formation of (6-hydroxyquinolin-2-yl)-4,5-dihydrothiazole (HQDT) from *L*-cysteine and 2-cyano-6-hydroxyquinoline (CHQ) [21]. This approach is predicated upon the synthesis of stable single lanthanide building blocks that combine in a rapid, 1-to-1 manner and avoids polymerization. This route is a less molecularly complex way to combine lanthanide-containing synthons in aqueous media through a 2-component, as compared to a 3- or 4-component, reaction [22]. Previous approaches to synthesize 2-thiazoline, or 4,5-

dihydrothiazole, combined a benzonitrile with *L*-cysteine, requiring organic solvent or co-solvent [23, 24, 25]. Herein, we employed a condensation reaction that is phosphate buffer-compatible [21, 26], which allowed for easy control of the covalent combination of two lanthanide centers.

In this proof-of-concept synthesis approach towards heterobimetallic agents, a library of 17 different hetero- and homo-bislanthanide complexes from europium to lutetium was created in a controlled 1:1 ratio, and the effect of bislanthanide combinations on MRI and optical signal production properties were explored.

3.6. Results and Discussion

In order to meet the objective of this work, which is a synthetic approach to homo- or hetero-bislanthanide complexes in aqueous media, the bislanthanide complex was divided into two synthons affording a rapid and reproducible conjugation: a cysteinyl-DOTA component (Figure 3.1, **12**), and a 2-cyano-6-hydroxyquinoline-DOTA (CHQ DOTA) component (Figure 3.2, **16**). The unidirectional nature of the reaction, in that covalent linkage only occurs between one cysteinyl and one quinolinyl component, ensures total control over the resulting bislanthanide combination. Importantly, this method avoids the use of metal catalysts that could displace the chelated lanthanide through transmetallation.

After protecting the free amino-group of Boc-*N*-phenylenediamine with Fmoc (**7**), the synthesis of cysteinyl-DOTA starts with an orthogonal deprotection of the *N*-Boc-*N'*-Fmoc-phenylenediamine, followed by conjugation to Boc-S-trityl-L-cysteine, resulting in Boc-Cys(Trt)-NH-(4-*N'*-Fmoc)-phenylenediamine (**8**) with a 75% yield. Following the deprotection of Fmoc to

give Boc-Cys(Trt)-phenylenediamine (**9**), and HBTU-driven amide coupling to DOTA-OtBu monoacetic acid, the fully protected cysteinyl-DOTA conjugate (**10**) was obtained in a 36% yield (Figure 3.1). In order to obtain the CHQ-DOTA synthon, 6-hydroxy-2-cyanoquinoline (**13**) was formed from 6-methoxy-2-quinolinecarbonitrile and pyridinium chloride with a 45% yield (Figure 3.2). Following the reaction with *N*-Boc-3-bromopropylamine to generate 6-*O*-(3-*N*-Boc-amino) propoxy-2-cyanoquinoline (**14,** 86% yield), Boc deprotection and HBTU-mediated coupling to DOTA-OtBu monoacetic acid yielded the fully protected quinolinyl-DOTA conjugate (**15**).

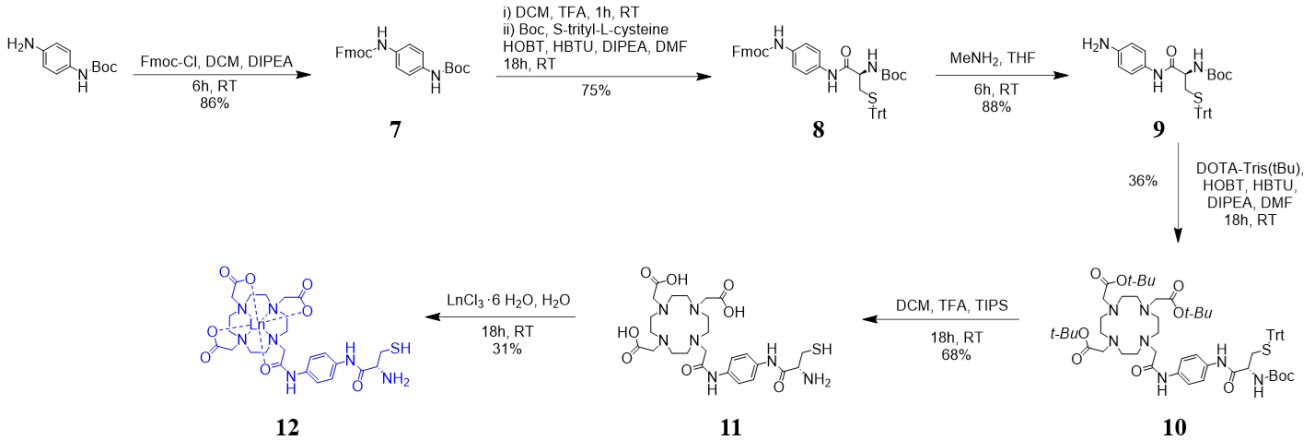

Figure 3.1 Chemical synthesis of the cysteine moiety of the complex where Ln can be Eu(III), Gd(III), Tb(III), Dy(III), Ho(III), Er(III), Tm(III), Yb(III), Lu(III) or no lanthanide. *Fmoc-Cl: 9-fluorenylmethyloxycarbonyl chloride; DCM: dicholormethane; DIPEA: N,N'-diisopropylethylamine; TFA: trifluoroacetic acid; HOBT: 1-hydroxybenzotriazole; HBTU: Hexafluorophosphate Benzotriazole Tetramethyl Uronium; DMF: N,N'-dimethylformamide; THF: tetrahydrofuran; TIPS: triisopropylsilane; RT: room temperature.*

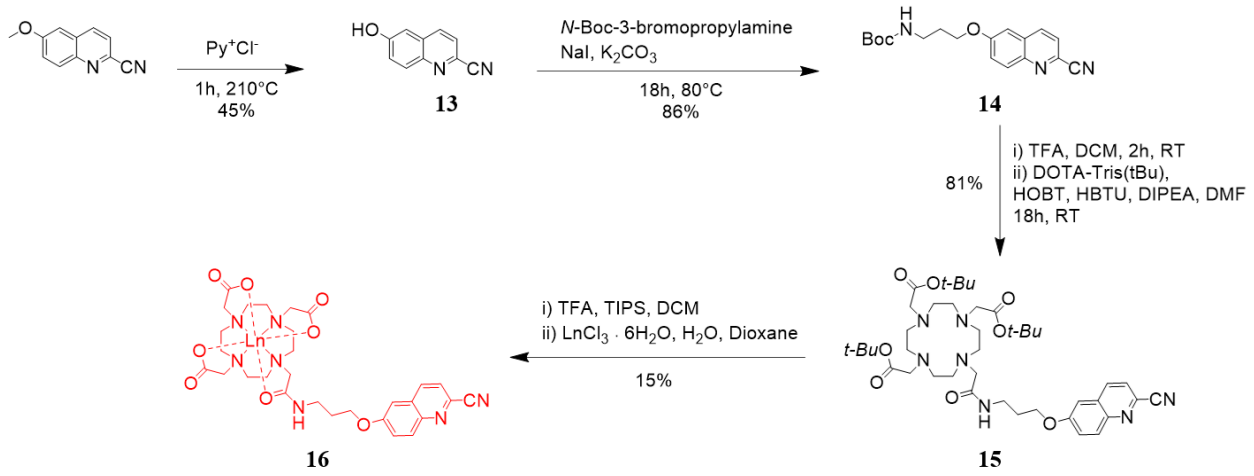

Figure 3.2 Chemical synthesis of the quinoline moiety of the complex where Ln can be Eu(III), Gd(III), Tb(III), Tm(III), Lu(III). *Py^+ Cl^-: pyridinium chloride; NaI: sodium iodide; K_2CO_3: potassium carbonate; DCM: dicholormethane; DIPEA: N,N'-diisopropylethylamine; TFA: trifluoroacetic acid; HOBT: 1-hydroxybenzotriazole; HBTU: Hexafluorophosphate Benzotriazole Tetramethyl Uronium; DMF: N,N'-dimethylformamide; TIPS: triisopropylsilane; RT: room temperature.*

With the aim to load the desired lanthanide into each synthon, each of the trityl-conjugated cysteinyl-DOTA (**10**) and CHQ-DOTA (**15**) were fully deprotected and were treated with the desired lanthanide(III) chloride hexahydrate overnight to provide lanthanide(III)-loaded cysteinyl-DOTA (**12**) (Figure 3.1) and CHQ-DOTA (**16**) (Figure 3.2) synthons. A library of nine different lanthanide chelates, from europium to lutetium, was prepared for the cysteinyl-DOTA synthon, and three different lanthanides, including europium(III), gadolinium(III) and thulium(III) were prepared for the CHQ-DOTA synthon. Each synthon was individually purified by HPLC before structural characterization by high resolution mass spectrometry (HRMS). These lanthanides ions were chosen due to the known magnetic properties of Gd(III) [2, 5, 6] and Dy(III) [27 28, 29] the known

visible and near-infrared optical properties of Eu(III), Tb(III), Dy(III), Ho(III), Er(III), Tm(III) and Yb(III) [11, 12, 13, 14, 15], and the optically and magnetically silent Lu(III) as negative control.

With the lanthanide-loaded individual synthons in hand, the catalyst-free click reaction to form the 4,5-dihydrothiazole linkage resulting in homo- or hetero-bislanthanides complex **17** could proceed (Figure 3.3). This coupling reaction is well-suited to bimetallic species on account of it being metal free, rapid (35 min at 50 °C), and performed in aqueous buffer. A combination of 17 bislanthanide complexes was synthesized, purified and characterized by HRMS (see Supplementary Information). Importantly, the chelation of lanthanide into each building block prior to click condensation prevents cross-lanthanide carboxylate coordination, preventing polymerization as supported by HRMS data. To the best of our knowledge, this is the first chemical approach to combine lanthanides at a controlled 1:1 ratio for bislanthanide complexes using an uncatalyzed aqueous click reaction. With these complexes in hand, we could begin a proof-of-concept exploration of their magnetic resonance and optical signal production properties. Although it would have been ideal to obtain single crystals of individual synthons and bislanthanide complexes to perform more in-depth characterizations, the bulkiness of the molecules makes crystallization difficult. However, our crystallization efforts are ongoing.

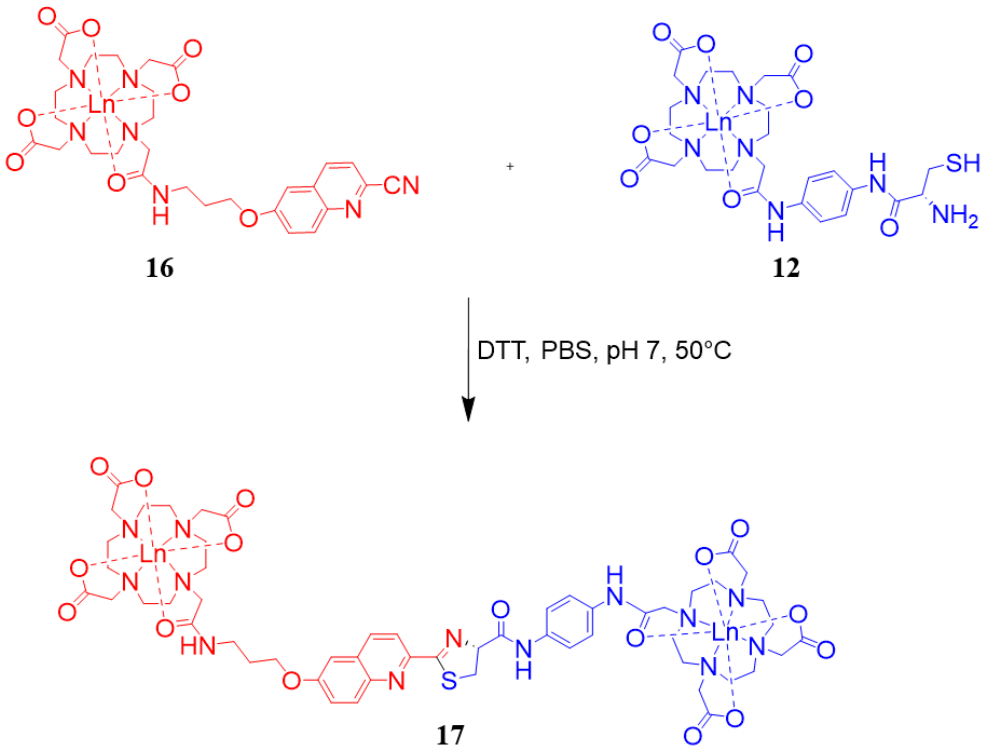

Figure 3.3 Rapid, aqueous condensation of the cysteinyl-DOTA and quinolinyl-DOTA synthons to result in a 2-dihydrothiazole linkage. *DTT: dithiothreitol; PBS: phosphate buffer saline.*

Magnetically active complexes were based on the combination of Gd(III) chelated by the CHQ-DOTA synthon with 9 different cysteinyl-DOTA chelates selected from Eu(III) to Lu(III), as well as one with an unoccupied DOTA moiety. T_1 and T_2 images of these complexes were acquired on a 3T MRI scanner to evaluate their effect on water proton relaxation (Figure 3.4). We evaluated each cysteinyl and CHQ synthon as monolanthanide agent prior to their combination into bislanthanide complexes. Gd(III)-CHQ-DOTA and Gd(III)-cysteinyl-DOTA synthons resulted in a shortening of the T_1 relaxation time. This effect was similar to the contrast production by the monolanthanide Gd(III) chelate, Gadovist, used in routine clinical contrast-enhanced MRI [30]. None of the monolanthanide synthons resulted in appreciable T_2-weighted contrast changes at

3T. When the synthons were combined into Gd-containing bislanthanide complexes and evaluated in an *in vitro* phantom, all complexes showed similar contrast enhancement effects to the monometallic Gd(III)-CHQ-DOTA: substantial T_1-weighted contrast enhancement, but limited T_2-weighted effects (Figure 3.4). While differences in T_1 and T_2-weighted effects of each bislanthanide combination were observed, the overall T_1/T_2 ratio showed limited variation (0.9 to 1.2), which may be attributable to small changes in contrast agent concentration between samples due to potential variability when working with *in vitro* samples.

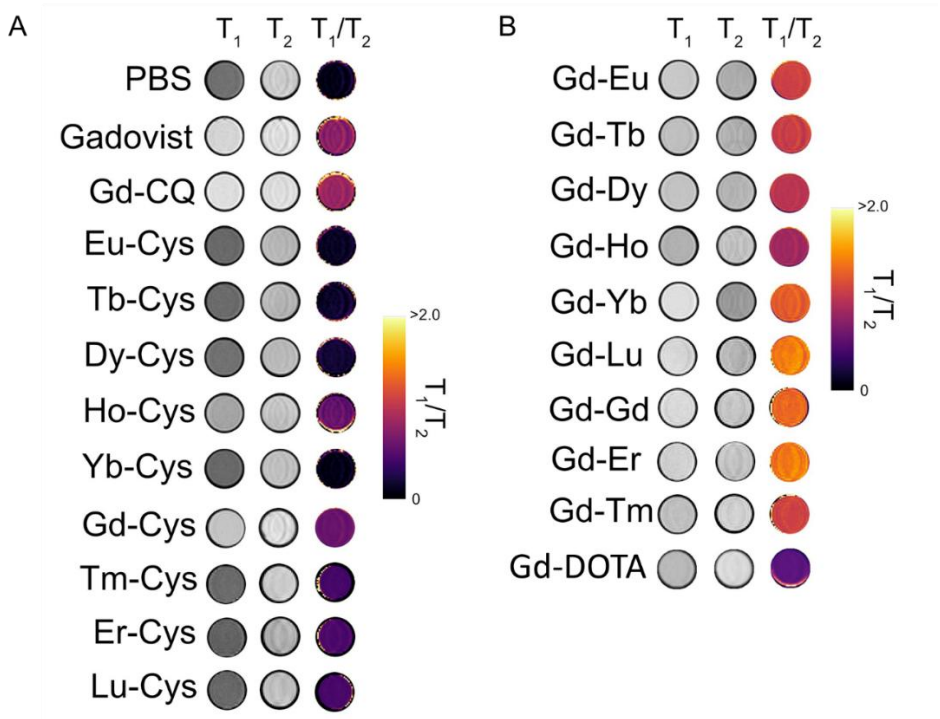

Figure 3.4 *In vitro* 0.1 mM phantom T_1-weighted, T_2-weighted, and T_1/T_2 ratio images obtained (A) for each lanthanide synthons and (B) bis-lanthanide complex, including PBS and Gadovist.

To further evaluate the MRI contrast enhancement properties of hetero-bislanthanide complexes in a concentration-independent manner, we took advantage of a newer approach to quantitative MRI called magnetic resonance fingerprinting (MRF). By simultaneously acquiring transverse and longitudinal relaxivities, MRF can generate a compound specific "fingerprint". If this fingerprint is unique from other compounds, it is possible to extract that compound's signal from a mix of multiple contrast enhancing components of an image [31]. *In vitro* phantoms were prepared at 5 concentration levels *per* bislanthanide complex, from 0.025 mM to 0.6 mM. Upon completion of the MRF measurements (Figure 3.5), only the Gd(III)-DOTA-CHQ-cysteine-DOTA-Gd(III) complex resulted in relaxivity data significantly different from the other bislanthanide complexes, with values of r_1 = 15.4 $mM^{-1}s^{-1}$ and r_2 = 22.2 $mM^{-1}s^{-1}$ (Figure 3.5A). The mean r_1 values of the hetero-bislanthanide complexes varied between 6.6.$mM^{-1}s^{-1}$ for Gd(III) -DOTA-CHQ-cysteine-DOTA and 8.2 $mM^{-1}s^{-1}$ for Gd(III) -DOTA-CHQ-cysteine-DOTA-Dy(III). The small increase of the relaxivity values of the bislanthanide complexes relative to mononuclear DOTA-chelated Gd(III) [30] can be explained by the increase of the molecular weight of the bislanthanides complexes and resulting decrease in molecular tumbling rate, enhancing the T_1-weighted relaxation effects [32, 33]. Likewise, mean r_2 values range between 9.4 $mM^{-1}s^{-1}$ for Gd(III)-DOTA-CHQ-cysteine-DOTA, to 12.9 $mM^{-1}s^{-1}$ for Gd(III) -DOTA-CHQ-cysteine-DOTA-Tb(III). By plotting r_2 *vs.* r_1 values for the bislanthanide library evaluated, the clustering of the hetero-bislanthanide complexes is apparent, with the Gd-Gd homo-bislanthanide complex being the single cluster outlier (Figure 3.5B and 3.5C). Overall, our approach to bislanthanide complex formation did not yield a diversity of relaxivity combinations, effectively resulting in two relaxivity fingerprints: one for homo- and one for hetero-bislanthanide compounds.

A

	Samples	r_1 ($mM^{-1}.s^{-1}$)	r_2 ($mM^{-1}.s^{-1}$)
1	Gd-Eu	7.8 ± 0.15	11.2 ± 0.22
2	Gd-Gd	15.4 ± 0.20	22.2 ± 0.15
3	Gd-Tb	7.9 ± 0.03	12.9 ± 0.16
4	Gd-Dy	8.2 ± 0.21	12.2 ± 0.11
5	Gd-Ho	7.1 ± 0.08	9.8 ± 0.29
6	Gd-Er	7.8 ± 0.23	10.1 ± 0.89
7	Gd-Tm	7.5 ± 0.26	10.4 ± 0.35
8	Gd-Yb	7.1 ± 0.10	9.7 ± 0.07
9	Gd-Lu	7.5 ± 0.18	10.2 ± 0.12
10	Gd-DOTA	6.6 ± 0.06	9.4 ± 0.19

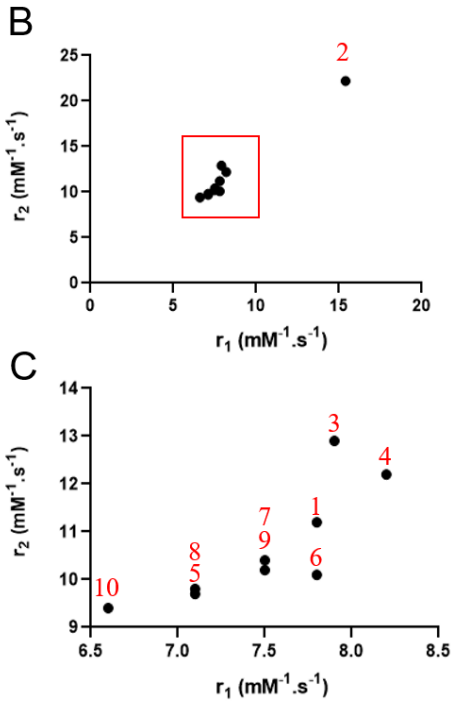

Figure 3.5 (A) Relaxivity values for 10 homo- and hetero-bis-metallic lanthanide (III) complexes obtained by MRF. Analysis was realized in triplicates (n=3). (B and C) The relationship of r_2 to r_1 values for the bis-lanthanide complexes evaluated, with (C) focusing on the region highlighted in the red box. Numbers in the plot correspond to compound identity from (A).

One of the unique properties of the (6-hydroxyquinolin-2-yl)-4,5 dihydrothiazole (HQDT) condensation approach utilized herein is the formation of a chromophore from the quinoline dihydrothiazole [34, 35]. We hypothesized that this chromophore could serve as an optical antenna to promote lanthanide-based photoluminescence from our bislanthanide complexes. Eu(III), one of the most emissive lanthanide ions [36], has found multiple applications as a fluorophore when chelated to DOTA in a variety of biological applications, including peptide conjugation [37] or live cell imaging [38]. With previous literature reporting on the fluorescent properties of some lanthanide

chelates, particularly those containing Eu(III) [39, 40], we generated a library of Eu(III) -containing bislanthanide and evaluated their optical properties.

To better understand the potential of the bis-lanthanide complexes as optical probes, the photophysical properties of the HQDT ligand was first evaluated by generating the lanthanide-free condensation product (Figure 3.6A). Both UV/Vis and excitation spectral analyses suggested that efficient ligand excitation occurs at 360 nm (Supplementary Figure S57A and S57B). Emission spectra of the clicked product resulted in a maximum at 460 nm upon excitation at 360 nm in both H_2O and D_2O solutions (Figure 3.6B and 3.6C). From this data and the evaluation of the low-temperature, solid-state emission spectrum of the lanthanide-free complex to yield the triplet state energy (Supplementary Figure S58), an energy level diagram of the HQDT ligand was constructed (Figure 3.7). The energy levels depicted in the Jablonski diagram (Figure 3.7) are derived from literature values [41]. Given that the T_1 energy level of the ligand is isoenergetic with the $^3H_3$ energy level of Eu(III) and the $^1D_2$ level Tm(III), allowing for potential ligand-to-Ln(III) energy transfer, followed by photoluminescence, the photophysical properties of bis-lanthanide complexes were evaluated, initially with chelates of Eu(III) and Tm(III) (Figure 3.8). The luminescent *f-f* transitions of Eu(III)-DOTA and Tm(III)-DOTA are well known [42] (Figure 3.7), but only the Eu(III)-DOTA moiety is expected to be emissive due to the reported quenching of Tm(III)-DOTA fluorescence upon conjugation to aryl ligand systems [42]. Indeed, a bis-lanthanide complex containing only Tm(III) showed only broad-band ligand, but no characteristic lanthanide emission (Supplementary Figure S59). Since the bis-lanthanide complex is asymmetric around the HQDT ligand product, and since each bis-lanthanide complex is comprised of one cysteinyl- to one CHQ-DOTA synthon, there is an inherent sidedness with different ligand-to-lanthanide distances, and aryl *vs.* alkyl environments (Figure 3.8). In employing chelates of Eu(III) and Tm(III), the effect of sidedness

on the bis-lanthanide emission could be isolated using a singly emissive lanthanide center while occupying both DOTA chelators with lanthanide species. Although Eu(III) can be linked to various types of chelators, the emission signals will remain unchanged, however the intensity of these signals may vary depending on the specific chelator used, without affecting the energy levels associated [43].

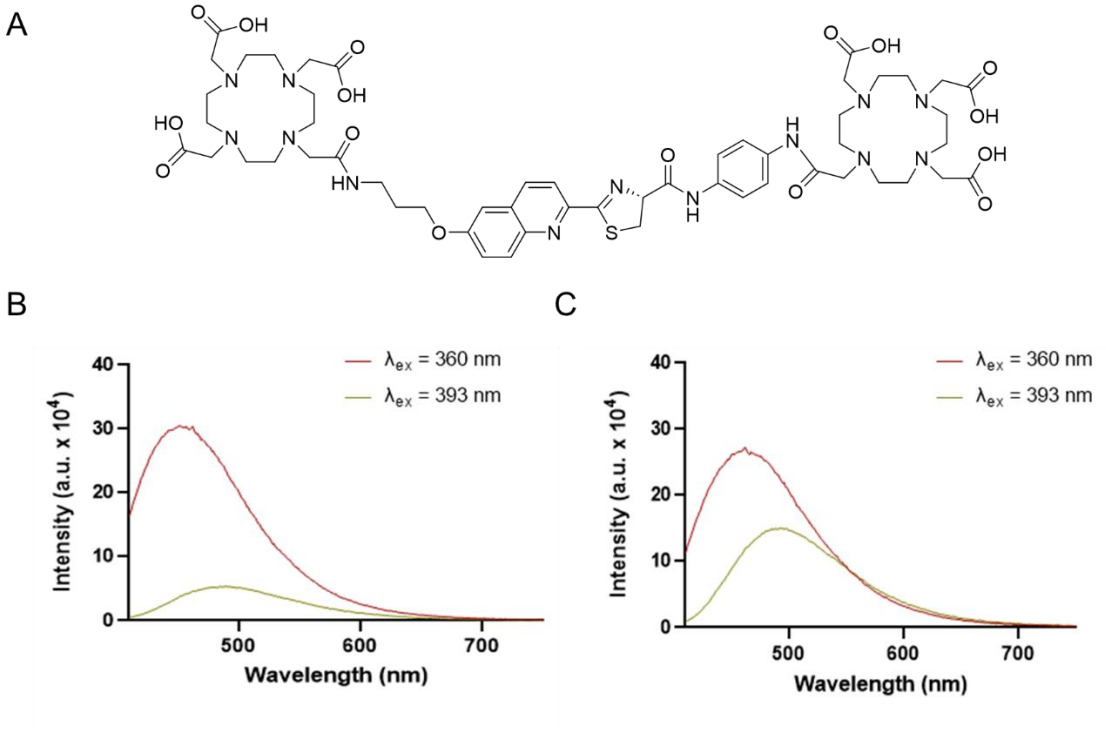

Figure 3.6 Structure of the lanthanide-free complex (A) and emission spectra of this complex in (B) H_2O and (C) D_2O at a 1 mM concentration with an excitation wavelength of 360 nm (orange) and 393 nm (green).

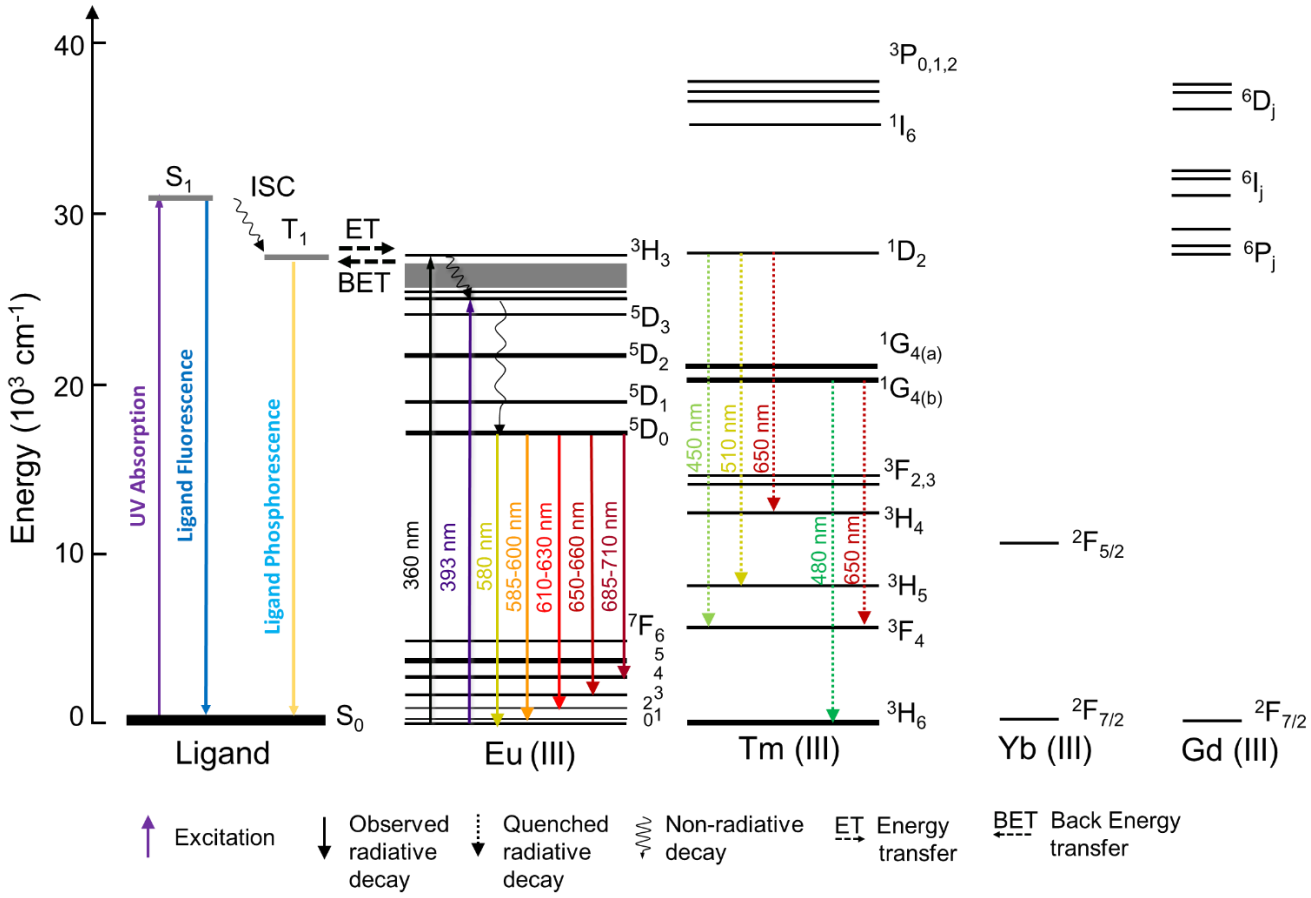

Figure 3.7 Jablonski diagram representing energy levels of the bis-lanthanide system. Energy levels of the (6-hydroxyquinolin-2-yl)-4,5 dihydrothiazole (HQDT) chromophore ligand as well as Eu(III), Tm(III), Yb(III) and Gd(III) are provided. Potential energy transfer (ET), back energy transfer (BET), radiative (both observed, solid arrow, and quenched, dashed arrow) and non-radiative decay (oscillating arrow) pathways are illustrated. Intersystem crossing (ISC) from the singlet (S1) to triplet (T1) states of the HQDT ligand is also shown.

The photophysical evaluation of the bis-lanthanide complex began with aqueous solutions of Eu(III)-DOTA-CHQ-cysteine-DOTA-Tm(III) (Eu-Tm), where the Eu(III) chelate is connected to the chromophore by a flexible propylamide linker (Figure 3.8A to 3.8D). Upon excitation of the ligand at 360 nm, a broad emission centered at 460 nm is observed due to click chromophore fluorescence (Figure 3.8A). Additional discrete emission peaks in the 550 nm to 750 nm region reveal the expected emission bands due to the $^5D_0 \rightarrow {}^7F_0$ and $^5D_0 \rightarrow {}^7F_4$ energy level transitions of Eu(III) [43] (Figure 3.8A & 3.8C, blue curves). These results also support the anticipated absence of Tm(III)-derived luminescence [42]. The presence of the Eu(III)-DOTA $^5D_0 \rightarrow {}^7F_0$ transition at 575 nm confirms the absence of mirror symmetry orthogonal to the principal symmetry axis, and degeneracy within the $^5D_0 \rightarrow {}^7F_1$ band confirms the presence of rotational symmetry in the coordination geometry [36, 43].

H_2O occupies the eighth coordination site of the DOTA-lanthanide chelate (Figure 3.8I), where overtone vibrations can attenuate luminescence by promoting non-radiative decay mechanisms [44]. Since it is also known that non-radiative decay pathways are attenuated in deuterated water (D_2O) [44], the photophysical properties of Eu-Tm were evaluated in D_2O (Figure 3.8A & 3.8C, red curves). Relative to water, the ligand peak intensity at 460 nm decreased while the Eu(III)-DOTA-associated emission peaks, especially the $^5D_0 \rightarrow {}^7F_4$ transition, increased when in D_2O. When the Eu(III)-DOTA chelate of the bis-lanthanide complex is excited directly (i.e. at 393 nm), both click chromophore and Eu(III)-DOTA emission are observed in both H_2O and D_2O (Figure 3.8B and 3.8D). In contrast to what was observed upon click chromophore excitation (360 nm), the Eu(III)-DOTA emission intensity was solvent-independent at 393 nm (Figure 3.8C *vs.* 3.8D). This data suggests that energy transfer from the ligand to the Eu(III)-DOTA moiety is susceptible to non-radiative decay pathways that can be suppressed with solvent deuteration.

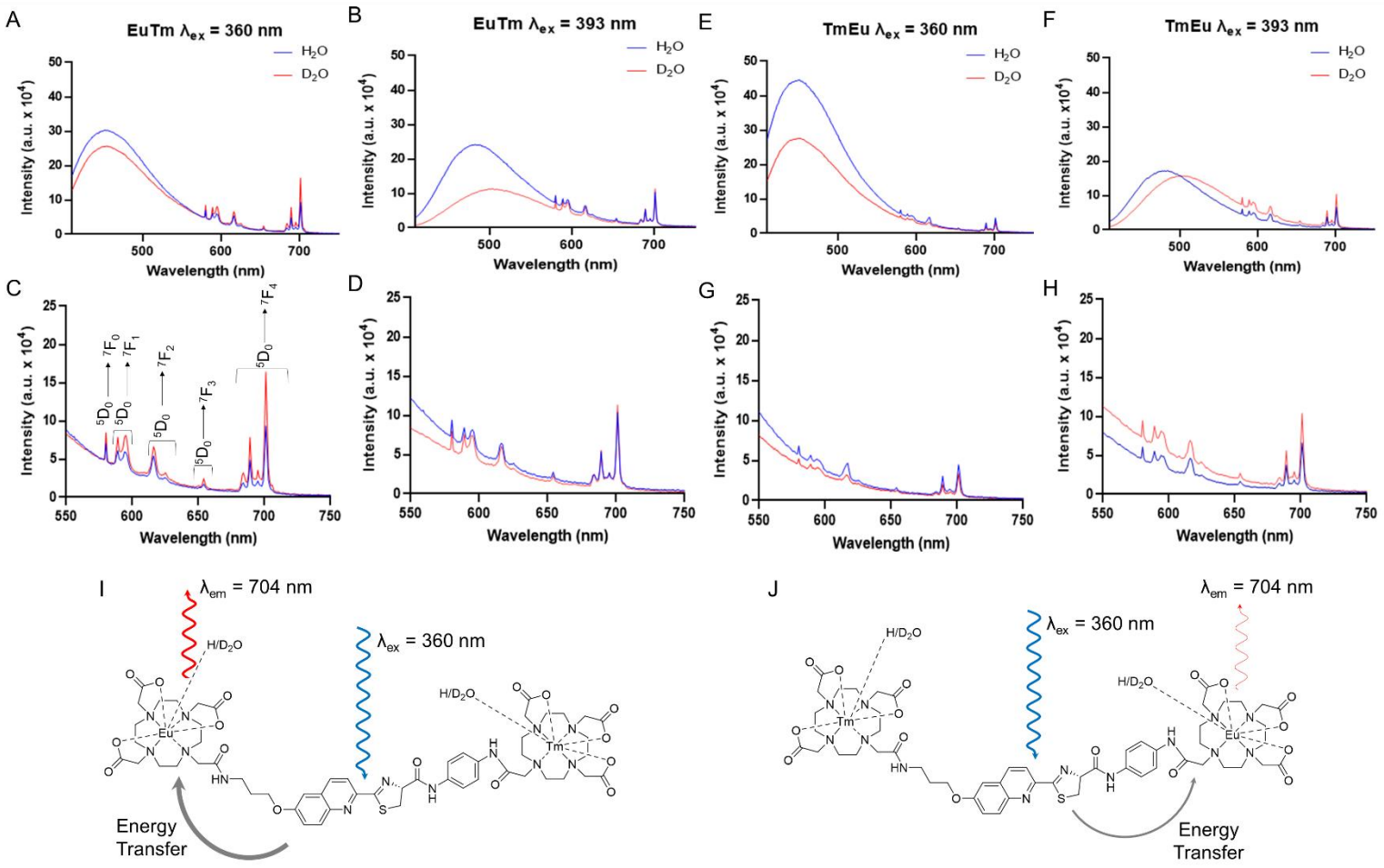

Figure 3.8 (A to D) Emission spectra obtained for 1 mM solutions of Eu(III)-DOTA-quinolinyl-cysteinyl-DOTA-Tm(III) (Eu-Tm) in water (blue line) or deuterated water (red line) at an excitation wavelength of 360 nm (A, C) and 393 nm (B, D) with a zoom in on the lanthanide-derived emission spectra (C, D). (E to H) Emission spectra obtained for 1 mM solutions of Tm(III)-DOTA-quinolinyl-cysteinyl-DOTA-Eu(III) (Tm-Eu) in water (blue line) or deuterated water (red line) at an excitation wavelength of 360 nm (E, G) and 393 nm (F, H) with a zoom in on the lanthanide-derived emission spectra (G, H). (I) Chemical representation of the Eu(III)-DOTA-quinolinyl-cysteinyl-DOTA-Tm(III) showing the effect of the resonant energy transfer when the europium(III) is on the quinolinyl moiety. (J) Chemical representation of the Tm(III)-DOTA-

quinolinyl-cysteinyl-DOTA-Eu(III) showing the effect of the resonant energy transfer when the europium(III) is on the cysteinyl moiety.

In order to determine if the same energy transfer relationship exists with Eu(III)-DOTA conjugated to the click chromophore with an aromatic linker system (i.e. *via* the cysteinyl synthon), a Tm(III)-DOTA-CHQ-cysteine-DOTA-Eu(III) (Tm-Eu) bis-lanthanide complex was investigated (Figure 3.8E to 3.8G). The ligand emission intensity increased substantially relative to the characteristic Eu(III)-DOTA-derived emission peaks upon excitation at 360 nm, with minimal change in peak intensity in the presence of deuterated solvent (Figure 3.8E & 3.8G). However, the relative Eu(III)-derived emission increased relative to the ligand peak when the complex was excited at 393 nm, with the $^5D_0 \rightarrow {}^7F_4$ emission intensity increasing in deuterated solvent (Figure 3.8F & 3.8H).The greater Eu(III)-DOTA-derived emission intensity for the Eu-Tm relative to the Tm-Eu complex suggests that Eu(III)-DOTA chelate luminescence is enhanced when connected to the click chromophore through an aliphatic as opposed to aromatic linker (Figure 3.8A *vs*. 3.8E). The increase in Eu-Tm bis-lanthanide complex emission in D_2O upon chromophore excitation at 360 nm suggests that the energy transfer pathway is susceptible to substantial non-radiative decay effects in water, as supported by the literature [43, 44, 45, 46]. The replacement of the coordinated solvent protons by deuterons alters the solvent vibration state, which results in stronger *f-f* emission bands [44]. The deuteron-enhancement of lanthanide emission also appears when the Eu(III)-DOTA center of Tm-Eu, the alternative click configuration where the lanthanide ion is linked to the chromophore by an aromatic linker, is directly excited at 393 nm (Figure 3.8F & 3.8H). These results provide evidence that the linker characteristic (i.e. aliphatic *vs.* aromatic) defines the solvent-sensitivity of the Eu(III)-DOTA emission pathways: aliphatic linkers facilitate lanthanide

ion emission upon excitation of the linked chromophore, but aromatic linkers favor emission from direct excitation of the lanthanide ion. Where there is no effect of solvent deuteration upon lanthanide emission intensity (Figure 3.8B, 3.8D *vs.* 3.8E, 3.8G), a substantial decrease in click chromophore emission is observed. While paradoxical against the known fluorescence enhancement with solvent deuteration [47], we hypothesize that the known triplet state quenching of lanthanide ion-DOTA chelates by appended aromatic groups has a larger effect than solvent-derived non-radiative decay pathways in these systems [42].

The effect of the lanthanide partner chelated by the cysteinyl-DOTA moiety on the emission of the Eu(III)-DOTA was evaluated (Figure 3.9). A combination of four different lanthanides were synthesized and their emission spectra were acquired in both H_2O and D_2O. As expected, the Eu(III)-DOTA-quinoline-cysteine-DOTA-Eu(III) complex (Eu-Eu) resulted in the highest intensity $^5D_0 \rightarrow {}^7F_4$ transition (Figure 3.9A). Fluorescence emission from Eu-Lu (Figure 3.9B) and EuYb (Figure 3.9D) complexes were similar to those observed for the Eu-Eu and Eu-Tm complexes: both increasing in intensity in D_2O relative to H_2O. While a suppression of the ligand emission is observed for the Eu-Eu (Figure 3.9A) and Eu-Gd (Figure 3.9C) complexes in D_2O, only the Eu-Eu band at 704 nm increases in D_2O. However, in both the Eu-Eu and Eu-Gd bis-lanthanide complexes, the lanthanide partner linked to the chromophore by the aromatic linker are isoenergetic with the triplet state of the chromophore, similar to Tm(III) (Figure 3.7). We hypothesize that the dominant triplet state quenching of lanthanide-DOTA chelates by aromatic systems observed with Tm(III) may apply to Eu(III) and Gd(III) as well. The ability to precisely control the ratio and sidedness of the bis-lanthanide pairings demonstrate that the photophysical outcomes of different lanthanide combinations derive from differences in the lanthanide ion energy

levels, the relative energy of the triplet state of the click chromophore, and the chemical characteristics (i.e. aliphatic *vs.* aromatic) of the linking moiety.

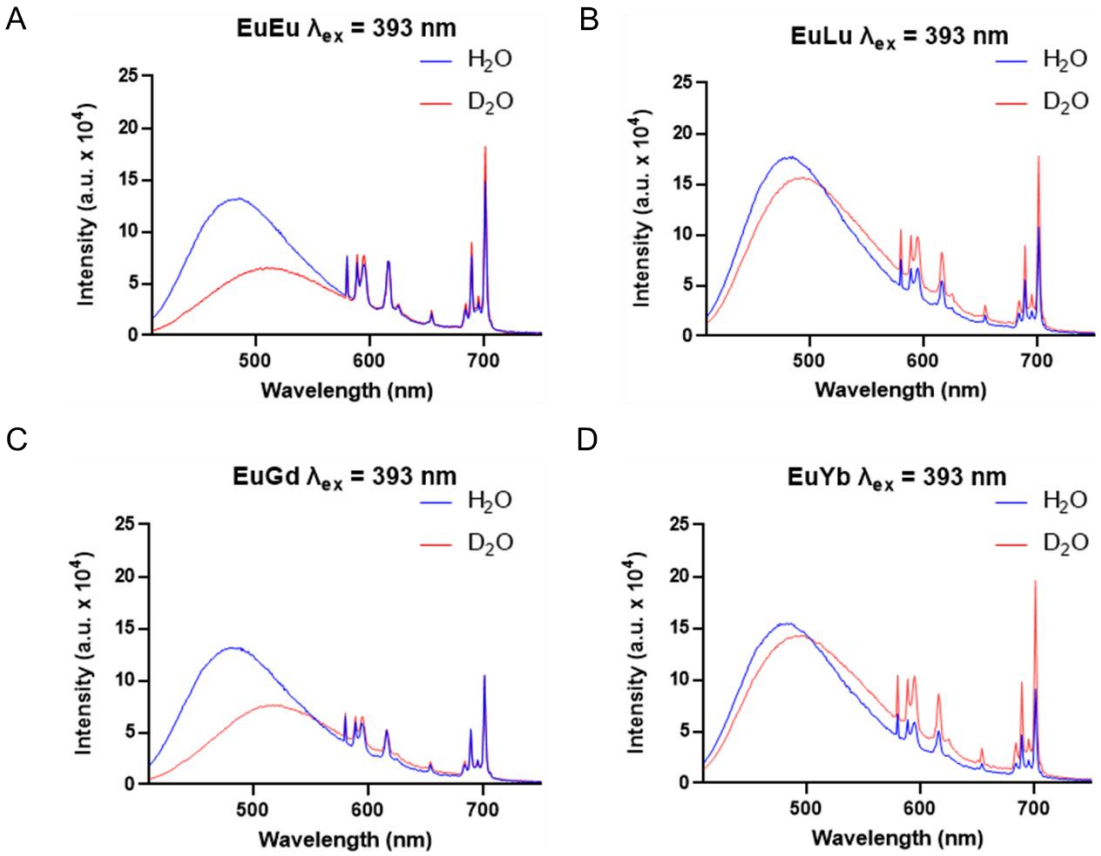

Figure 3.9 Emission spectra for (A) Eu-Eu, (B) Eu-Lu, (C) Eu-Gd, and (D) Eu-Yb obtained in water (blue line) or deuterated water (red line) at an excitation wavelength of 393 nm.

3.7. Conclusion

Herein we present the first chemical approach to the synthesis of homo- or hetero-bislanthanide complexes in a one-to-one ratio through a fast and uncatalyzed aqueous click reaction based on the formation of a 2-thiazoline ring. The library of homo- and hetero-bislanthanide compounds were subjected to preliminary evaluation of their potential contrast agents for MRI and optical imaging. Using MRF, we demonstrated that bis-gadolinium complexes resulted in relaxivities that were substantially different from those of the hetero-bis-lanthanide complexes generated. We also showed that the 4,5-dihydrothiazole that forms upon synthon condensation acts as a chromophore capable of promoting fluorescence emission of the linked Eu(III)-DOTA center. Due to molecular asymmetry of the bislanthanide product, the linker chemistry (aliphatic *vs*. aromatic) is an important modulator of lanthanide ion luminescence. The chemistry presented can be adapted to metals beyond the lanthanides by changing the type of chelator conjugated to the cysteinyl and CHQ synthons, opening up new possibility to homo- and hetero-bismetallic materials with the potential to expand on the resulting functionality for biological applications.

3.8. Conflict of Interests

There are no conflicts to declare.

3.9. Supplementary Information

3.9.1. General Experimental Procedures

All reagents were commercially available or prepared according to the procedure below. All solvents used were HPLC grade except the water that is 18.2 MΩ cm Millipore water. Compounds were visualized by using 5% ninhydrin stain and UV light on Al backed silica gel plates for the thin-layer chromatography (TLC). 300 or 400 MHz spectrometers were used for ^{1}H NMR spectra where δ values are DMSO-D_6 2.50 ppm, and for ^{13}C δ DMSO-D_6 39.50 ppm, CD_3OD 49 ppm.

3.9.2. Synthetic Procedure

Preparation of *N*-Boc-*N'*-Fmoc-phenylenediamine (7)

Fmoc-chloride (2.48 g, 10 mmol) was added to a stirred suspension of *N*-Boc-*p*-phenylenediamine (2 g, 10 mmol) in CH_2Cl_2 (120 mL) and DIPEA (8.4 mL, 50 mmol). The mixture was stirred at room temperature for 6 h, the pink solid was filtered, was washed with cold CH_2Cl_2 and was dried. *N*-Boc-*N'*-Fmoc-phenylenediamine **7**, white solid, 4.31 g, 86%. ^{1}H NMR (300 MHz, DMSO) δ 9.54 (s, 1H), 9.19 (s, 1H), 7.90 (d, *J* = 7.5, 1.1 Hz, 2H), 7.75 (d, *J* = 7.4 Hz, 2H), 7.47 – 7.28 (m, 8H), 4.45 (d, *J* = 6.7 Hz, 2H), 4.29 (t, *J* = 6.7 Hz, 1H), 1.46 (s, 9H). ^{13}C NMR (100 MHz, DMSO) δ 153.44, 152.80, 143.78, 140.76, 134.40, 133.40, 127.63, 127.07, 125.10, 120.12, 118.85, 118.61, 78.73, 65.46, 46.62, 28.12. HRMS (ESI) m/z found 453.1782 $[M + Na]^+$ (calcd 453.1790 for $C_{26}H_{26}N_2O_4SNa$).

Reaction of *N*-Boc-*N'*-Fmoc-phenylenediamine (7) with Boc-S-Trityl-L-Cysteine

TFA (1 mL) was added to a stirred suspension of *N*-Boc-*N'*-Fmoc-phenylenediamine (430 mg, 1 mmol) in CH_2Cl_2 (1 mL) which was then stirred for 1 h at room temperature. Followed by a complete evaporation, the excess of TFA was removed by evaporation with CH_2Cl_2 (3 times 35 mL). DIPEA (700 μL, 4 mmol) was added to a solution of Boc-S-Trityl-L-Cysteine (463.57 mg, 1 mmol) in dry DMF (2 mL). The mixture was cooled to 0 °C on ice, followed by the addition of HOBT (40.5 mg, 0.3 mmol) and HBTU (379 mg, 1 mmol). The mixture was stirred for 10 minutes at 0 °C followed by the addition of *N*-Fmoc-phenylenediamine (430 mg, 1 mmol). The cooling bath was removed, and the mixture was stirred for 18 hours at room temperature. The solution was then partitioned between brine (60 mL) and EtOAc (3 × 30 mL), combined organic extract was washed with brine (3 × 30 mL), was dried with Na_2SO_4 and was concentrated. The residue was subjected to FCC on 80 g SiO_2, hexane/acetone (2:1). Evaporation of the eluate afforded Boc-Cys(Trt)-NH-(4-*N'*-Fmoc)-phenylenediamine **8**, brown solid, 75%. ^{1}H NMR (300 MHz, DMSO) δ 9.88 (s, 1H), 9.64 (s, 1H), 7.90 (d, 2H), 7.75 (d, *J* = 7.3 Hz, 2H), 7.51 – 7.18 (m, 26H), 7.03 (d, *J* = 8.1 Hz, 1H), 4.47 (d, *J* = 6.7 Hz, 2H), 4.30 (t, *J* = 6.6 Hz, 1H), 4.18 (d, *J* = 7.7 Hz, 1H), 1.37 (s, 9H). ^{13}C NMR (100 MHz, DMSO) δ 168.57, 153.41, 144.20, 143.76, 140.76, 134.66, 133.47, 129.04, 128.88, 128.02, 127.63, 127.24, 127.08, 126.74, 125.09, 121.34, 120.12, 119.88, 118.69, 78.41, 65.91, 65.51, 53.92, 46.61, 34.15, 34.00, 30.91, 30.65, 28.08, 24.74, 22.02, 20.57, 13.92. HRMS (ESI) m/z found 798.2956 $[M + Na]^+$ (calcd 798.2978 for $C_{48}H_{45}N_3O_5SNa$).

Preparation of *N*-Boc-Cys(Trt)-phenylenediamine (9)

A methylamine solution in THF (7 mL, 2 M) was mixed with Boc-Cys(Trt)-NH-(4-*N'*-Fmoc)-phenylenediamine (583.2 mg, 0.78 mmol) and stirred for 1 hour at room temperature. Followed by a complete evaporation, the product was subjected to FCC on 50 g SiO_2, CH_2Cl_2/MeOH (95:5). Evaporation of the eluate afforded *N*-Boc-Cys(Trt)-phenylenediamine **9**, orange solid, 379.5 mg, 88%. ^{1}H NMR (300 MHz, DMSO) δ 9.53 (s, 1H), 7.40 – 7.14 (m, 17H), 6.95 (d, *J* = 8.3 Hz, 1H), 6.49 (d, *J* = 8.6 Hz, 2H), 4.89 (s, 2H), 4.14 (d, *J* = 7.7 Hz, 1H), 2.34 (dd, *J* = 6.9, 2.7 Hz, 2H), 1.37 (s, 9H). ^{13}C NMR (100 MHz, DMSO) δ 167.78, 145.01, 144.23, 129.04, 128.00, 127.66, 126.71, 120.98, 113.69, 78.34, 65.83, 54.85, 53.78, 34.21, 28.08. HRMS (ESI) m/z found 576.2298 $[M + Na]^+$ (calcd 576.2297 for $C_{33}H_{35}N_3O_3SNa$).

Reaction of Boc-Cys(Trt)-phenylenediamine (9) with DOTA-OtBu monoacetic acid

DIPEA (171.8 µL, 0.3 mmol) was added to a solution of DOTA-OtBu monoacetic acid (171.8 mg, 0.3 mmol) in dry DMF (2 mL) in a separate vial. The mixture was cooled to 0 °C on ice, followed by the addition of HOBT (13.4 mg, 0.1 mmol) and HBTU (113.8 mg, 0.3 mmol). The mixture was stirred for 10 minutes at 0 °C followed by the addition of Boc-Cys(Trt)-phenylenediamine (163.5 mg, 0.3 mmol). The cooling bath was removed, and the mixture was stirred for 18 hours at 60 °C. The solution was then partitioned between brine (60 mL) and EtOAc (2 × 30 mL), combined organic extract was washed with brine (3 × 30 mL), was dried with Na_2SO_4 and was concentrated. The residue was subjected to FCC on 40 g SiO_2, hexane/acetone (1:1). Evaporation of the eluate afforded a tritylated DOTA conjugate **10**, yellow solid, 332.5 mg, 36%. ^{1}H NMR (300 MHz, DMSO) δ 10.06 (s, 1H), 9.93 (s, 1H), 7.52 – 7.42 (m, 2H), 7.35 – 7.20 (m, 8H), 2.89 (s, 1H), 2.73

(d, J = 0.7 Hz, 1H), 2.08 (s, 1H), 1.51 – 1.29 (m, 21H). ^{13}C NMR (100 MHz, DMSO) δ 172.57, 172.47, 170.44, 168.71, 144.22, 134.40, 134.24, 129.08, 128.05, 126.77, 119.82, 119.41, 81.14, 81.10, 78.47, 65.95, 55.29, 33.94, 30.96, 30.69, 28.11, 27.61, 27.56, 27.53, 22.07, 13.97. HRMS (ESI) m/z found 1130.5981 $[M + Na]^+$ (calcd 1130.5976 for $C_{61}H_{85}N_7O_{10}SNa$).

Preparation of DOTA conjugate TFA salt (11)

The tritylated DOTA conjugate (120 mg, 0.2 mmol) was dissolved in CH_2Cl_2 (1 mL) and TFA (1 mL) was added with TIPS (200µL) to the mixture which was stirred for 18 hours at room temperature. The volatile is then evaporated with DCM (3 × 30 mL) and the residue triturated with hexane (3 × 10 mL, each time sonicated for 10 minutes) followed by drying in vacuum. This permits to obtain the DOTA conjugate as TFA salt **11**, pale yellow solid, 81.2 mg, 68 %. ^{1}H NMR (400 MHz, DMSO) δ 10.60 – 10.40 (m, 1H), 8.38 (s, 1H), 7.57 (d, J = 1.6 Hz, 2H), 7.34 – 7.27 (m, 1H), 7.14 – 7.08 (m, 1H), 4.18 – 2.93 (m, 49H), 2.69 (s, 4H), 1.28 (s, 1H), 1.03 (d, J = 6.8 Hz, 2H). ^{13}C NMR (100 MHz, DMSO) δ 165.57, 165.34, 165.26, 164.61, 162.33, 143.80, 129.05, 128.36, 126.26, 120.17, 120.09, 119.84, 119.32, 117.36, 115.40, 113.45, 104.77, 55.78, 52.93, 51.95, 38.25, 35.79, 30.47, 25.07, 19.24, 17.04, 17.03. HRMS (ESI) m/z found 620.2462 $[M + Na]^+$ (calcd 620.2479 for $C_{25}H_{39}N_7O_8SNa$).

Preparation of the lanthanide DOTA conjugate TFA salt (12)

The solution of DOTA conjugate TFA salt (81.2 mg, 0.14×10^{-3} mol) in water (3.6 mL) was treated with $LnCl_3$ – 6 H_2O (48 mg, 0.16×10^{-3} mol). The pH was maintained at pH 6-7 with a NaOH (1 M) solution and stirred for 18 hours at room temperature. The reaction mixture was transferred

into a Falcon tube, diluted with water (25 mL) and centrifuged (3 times 3 minutes at 3000 rpm). The supernatant was analyzed to preparative HPLC purification to then concentrate the fraction containing the product and lyophilized to provide Ln(III) DOTA cysteine complex **12**. Every Ln(III) cysteinyl DOTA complex obtained appeared as a white solid.

Table 3.1. Chromatographic retention time (minutes) and synthetic yields (%) for each Ln(III) cysteinyl DOTA component including the free lanthanide DOTA-cysteine moiety.

Compounds	Retention time t_R (min)	Yield (%)
Eu(III)-DOTA-Cysteine	12.65 – 13.83	20
Gd(III)-DOTA-Cysteine	12.21 – 13.30	27
Tb(III)-DOTA-Cysteine	12.54 – 13.61	34
Dy(III)-DOTA-Cysteine	12.57 – 13.73	31
Ho(III)-DOTA-Cysteine	12.31 – 13.76	23
Er(III)-DOTA-Cysteine	12.33 – 13.56	28
Tm(III)-DOTA-Cysteine	12.19 – 13.33	33
Yb(III)-DOTA-Cysteine	12.47 – 13.92	23
Lu(III)-DOTA-Cysteine	12.58 – 13.89	24
DOTA-Cysteine	13.93 – 15.21	19

Table 3.2. Experimental and theoretical high resolution mass spectrometry values for each Ln(III) cysteinyl DOTA component including the free lanthanide DOTA-cysteine moiety.

Compounds (dimer)	HRMS (ESI) *m/z* found	HRMS(ESI) *m/z* calcd
Eu(III)-DOTA-Cysteine	1491.3042 $[2M - H]^+$	1491.3025 for $C_{50}H_{71}N_{14}O_{16}S_2{}^{151}Eu^{153}Eu$
Gd(III)-DOTA-Cysteine	1502.3152 $[2M - H]^+$	1502.3109 for $C_{50}H_{71}N_{14}O_{16}S_2{}^{157}Gd_2$
Tb(III)-DOTA-Cysteine	1505.3088 $[2M - H]^+$	1505.3121 for $C_{50}H_{71}N_{14}O_{16}S_2{}^{159}Tb_2$
Dy(III)-DOTA-Cysteine	1512.3075 $[2M - H]^+$	1512.3110 for $C_{50}H_{71}N_{14}O_{16}S_2{}^{163}Dy_2$
Ho(III)-DOTA-Cysteine	1517.3250 $[2M - H]^+$	1517.3221 for $C_{50}H_{71}N_{14}O_{16}S_2{}^{165}Ho_2$
Er(III)-DOTA-Cysteine (monomer)	763.1746 $[M + H]^+$	763.1748 for $C_{25}H_{37}N_7O_8S^{168}Er$
Tm(III)-DOTA-Cysteine	1525.3284 $[2M - H]^+$	1525.3298 for $C_{50}H_{71}N_{14}O_{16}S_2{}^{169}Tm_2$
Yb(III)-DOTA-Cysteine	1533.3345 $[2M - H]^+$	1533.3378 for $C_{50}H_{71}N_{14}O_{16}S_2{}^{173}Yb_2$
Lu(III)-DOTA-Cysteine	1537.3472 $[2M - H]^+$	1537.3430 for $C_{50}H_{71}N_{14}O_{16}S_2{}^{175}Lu_2$
DOTA-Cysteine (monomer)	598.2633 $[M + H]^+$	598.2659 for $C_{25}H_{40}N_7O_8S$

Preparation of 6-hydroxy-2-cyanoquinoline (13)

6-methoxy-2-quinolinecarbonitrile (1.156 g, 10 mmol) was stirred with pyridinium hydrochloride (368 mg, 2 mmol) for 1 hour at 210 °C in a pressure vessel. The mixture was cooled to room temperature and partitioned between saturated $NaHCO_3$ solution (60 mL) and DCM (3 × 40 mL)

and then with CH_2Cl_2/MeOH 9:1 (2 × 40 mL). The organic extract was combined, dried and concentrated and the residue was co-evaporated with toluene (100 mL). The residue was subjected to FCC on 60 g SiO_2, CH_2Cl_2/MeOH 95:5. Evaporation of the eluate afforded 6-hydroxy-2-cyanoquinoline **13**, yellow solid, 151.2 mg, 45 %. ^{1}H NMR (400 MHz, DMSO) δ 10.68 (s, 1H), 8.40 (dd, *J* = 8.6, 0.8 Hz, 2H), 7.98 (dd, *J* = 9.2, 0.8 Hz, 2H), 7.87 (d, *J* = 8.5 Hz, 2H), 7.48 (dd, *J* = 9.2, 2.7 Hz, 2H), 7.26 (d, *J* = 2.7 Hz, 2H). ^{13}C NMR (100 MHz, CD_3OD) δ 159.88, 144.73, 137.08, 132.32, 131.91, 130.91, 125.46, 124.74, 118.83, 109.23. HRMS (ESI) m/z found 193.0372 $[M + Na]^+$ (calcd 193.0378 for $C_{10}H_6N_2ONa$).

Reaction of the 6-hydroxy-2-cyanoquinoline (13) with *N*-Boc-3-bromopropylamine

A mixture of DMF (1.7 mL) with *N*-BOC-3-bromopropylamine (173.9 mg, 0.73 mmol), 6-hydroxy-2-cyanoquinoline (133.6 mg, 0.73 mmol), K_2CO_3 (121.6 mg, 0.88 mmol) and NaI (22 mg, 0.15 mmol) was stirred for 18 hours at 80 °C. The mixture was cooled to room temperature, partitioned between brine (60 mL) and EtOAc (3 × 30 mL), and combined organic extract was washed with brine (3 × 60 mL), dried and concentrated. The residue was subjected to FCC on 60 g of SiO_2, CH_2Cl_2/MeOH (98:2) and afforded 6-*O*-(3-*N*-Boc-amino) propoxy-2-cyanoquinoline **14** after evaporation of the eluate, yellow solid, 205.6 mg, 86 %. ^{1}H NMR (400 MHz, DMSO) δ 8.48 (dd, *J* = 8.6, 0.8 Hz, 1H), 8.02 (d, *J* = 9.3 Hz, 1H), 7.95 (d, *J* = 8.5 Hz, 1H), 7.55 (d, *J* = 9.2, 2.8 Hz, 1H), 7.49 (d, *J* = 2.8 Hz, 1H), 6.98 – 6.89 (m, 1H), 4.16 (t, *J* = 6.2 Hz, 2H), 3.13 (q, *J* = 6.6 Hz, 2H), 1.92 (p, *J* = 6.5 Hz, 2H), 1.36 (s, 9H). ^{13}C NMR (100 MHz, DMSO) δ 158.75, 155.61, 143.60, 136.50, 130.66, 130.32, 129.87, 124.66, 124.09, 117.89, 106.18, 77.48, 69.74, 66.00, 36.81, 28.90, 28.19. HRMS (ESI) m/z found 350.1455 $[M + Na]^+$ (calcd 350.1481 for $C_{18}H_{21}N_3O_3Na$).

Preparation of fully protected DOTA quinoline conjugate (15)

TFA (700 µL) was added to a stirred suspension of 6-*O*-(3-*N*-Boc-amino) propoxy-2-cyanoquinoline (205.6 mg, 0.6 mmol) in CH_2Cl_2 (3.5 mL) which was then stirred for 2 hours at room temperature. Followed by a complete evaporation, the excess of TFA was removed by evaporation with CH_2Cl_2 (3 × 35 mL). DIPEA (628 µL, 3.6 mmol) was added to a solution of DOTA-OtBu monoacetic acid (343.6 mg, 0.6 mmol) in dry DMF (2 mL) in a separate vial. The mixture was cooled to 0 °C on ice, followed by the addition of HOBT (26.3 mg, 0.195 mmol) and HBTU (227.5 mg, 0.6 mmol). The mixture was stirred for 10 minutes at 0 °C followed by the addition of 6-*O*-(3-*N*-amino)propoxy-2-cyanoquinoline (205.6 mg, 0.6 mmol). The cooling bath was removed, and the mixture was stirred for 18 hours at room temperature. The solution was then partitioned between brine (60 mL) and EtOAc (3 × 40 mL), combined organic extract was washed with brine (3 × 60 mL), dried with Na_2SO_4 and concentrated. The residue was subjected to FCC on 40 g SiO_2, CH_2Cl_2/MeOH (95:5). Evaporation of the eluate afforded a fully protected DOTA quinoline conjugate **15**, yellow solid, 380.3 mg, 81 %. ^{1}H NMR (400 MHz, DMSO) δ 8.47 (d, *J* = 8.6, 0.8 Hz, 1H), 8.26 (t, *J* = 5.7 Hz, 1H), 8.08 – 7.93 (m, 2H), 7.53 (dd, *J* = 9.3, 2.8 Hz, 1H), 7.46 (d, *J* = 2.8 Hz, 1H), 4.18 (t, *J* = 6.2 Hz, 2H), 2.69 (s, 4H), 2.03 – 1.93 (m, 3H), 1.42 (d, *J* = 11.2 Hz, 30H). ^{13}C NMR (100 MHz, DMSO) δ 172.56, 172.18, 171.55, 158.67, 143.67, 136.57, 130.82, 130.33, 130.02, 124.63, 124.23, 117.91, 106.14, 81.08, 80.95, 66.10, 38.24, 35.68, 28.55, 27.57, 27.55. HRMS (ESI) m/z found 804.4628 $[M + Na]^+$ (calcd 804.4636 for $C_{41}H_{63}N_7O_8Na$)

Preparation of the Ln(III)-DOTA-quinoline conjugate (16)

A solution of fully protected DOTA quinoline conjugate (190.15 mg, 0.24 mmol) was treated in DCM (1.2 mL) with TFA (2mL) and TIPS (200 μL). The mixture was stirred for 4 hours at room temperature followed by a complete evaporation. The residue was then co-evaporated with CH_2Cl_2 (4 × 40 mL) to remove excess of TFA. The residue was dissolved in dioxane (2.4 mL) and water (6 mL) with a solution of $LnCl_3$ - $6H_2O$ (108.5 mg, 0.29 mmol). The pH of the reaction mixture was maintained at pH ~ 6 – 7 (1 M NaOH) and the mixture was stirred for 18 h at room temperature. The reaction mixture was transferred into a Falcon tube, diluted with water (15 mL) and centrifuged (3 min at 3,000 rpm). The supernatant was subjected to preparative HPLC purification. The fraction containing the product (t_R 17.5 min) was concentrated and was lyophilized to afford quinoline-decorated Ln(III) complex **16**. Every Ln(III) 2-cyano-6-hydroxyquinoline DOTA complex obtained appeared as a white solid.

Table 3.3 Chromatographic retention time (minutes) and synthetic yields (%) for each Ln(III) 2-cyano-6-hydroxyquinoline (CHQ) DOTA component including the lanthanide-free CHQ-DOTA moiety.

Compounds	Retention time t_R (min)	Yield (%)
Eu(III)-DOTA-Quinoline	16.44 – 17.37	35
Gd(III)-DOTA-Quinoline	16.72 – 17.88	42
Tm(III)-DOTA-Quinoline	16.56 – 17.63	51
DOTA-Quinoline	15.43 – 16.84	33

Table 3.4. Experimental and theoretical high resolution mass spectrometry values for each Ln(III) 2-cyano-6-hydroxyquinoline DOTA component including the free lanthanide DOTA-quinoline moiety.

Compounds	HRMS (ESI) *m/z* found	HRMS(ESI) *m/z* calcd
Eu(III)-DOTA-Quinoline	786.1738 $[M + Na]^+$	784.1722 for $C_{29}H_{36}N_7O_8{}^{151}EuNa$
Gd(III)-DOTA-Quinoline	769.1971 $[M + H]^+$	769.1945 for $C_{29}H_{37}N_7O_8{}^{158}Gd$
Tm(III)-DOTA-Quinoline	802.1853 $[M + Na]^+$	802.1865 for $C_{29}H_{36}N_7O_8{}^{169}TmNa$
DOTA-Quinoline	614.2913 $[M + H]^+$	614.2938 for $C_{29}H_{40}N_7O_8$

Preparation of the homo-/hetero-bislanthanide complexes (17)

A solution of Ln(III)-DOTA-cysteine conjugate (6 mg, 7.84 x 10^{-3} mmol) dissolved in PBS (1.5 mL) was stirred with Ln(III)-DOTA-quinoline conjugate (5.4 mg, 7.84 x 10^{-3} mmol) before adding the DTT (120.9 mg, 0.784 mmol). The pH of the reaction mixture was maintained at pH ~ 6 – 7 (1 M NaOH) and the mixture was stirred for 40min at 50°C. The reaction mixture was transferred into a Falcon tube, diluted with water (15 mL) and subjected to preparative HPLC purification. The fraction containing the product was concentrated and was lyophilized to afford quinoline-decorated Ln(III)-DOTA-quinoline-cysteine-DOTA-Ln(III) complex **17**. Every bislanthanide complexes obtained appeared as a white solid.

Table 3.5. Chromatographic retention time (minutes), synthetic yields (%) and HPLC purity (%) for each Ln(III)-DOTA-CHQ-cysteine-DOTA-Ln(III) complexes including the free lanthanide DOTA-CHQ-cysteine-DOTA complex.

Compounds	Retention time t_R (min)	Yield (%)	HPLC Purity (%)
Gd(III)-DOTA-quinoline-DOTA-cysteine-Eu(III)	16.65 – 17.47	54	82
Gd(III)-DOTA-quinoline-DOTA-cysteine-Gd(III)	16.22 – 17.12	43	86
Gd(III)-DOTA-quinoline-DOTA-cysteine-Tb(III)	16.53 – 17.53	37	91
Gd(III)-DOTA-quinoline-DOTA-cysteine-Dy(III)	16.51 – 17.14	47	92
Gd(III)-DOTA-quinoline-DOTA-cysteine-Ho(III)	16.53 – 17.49	45	94
Gd(III)-DOTA-quinoline-DOTA-cysteine-Er(III)	16.31 – 17.23	66	84
Gd(III)-DOTA-quinoline-DOTA-cysteine-Tm(III)	16.90 – 17.60	48	87
Gd(III)-DOTA-quinoline-DOTA-cysteine-Yb(III)	16.56 – 17.25	23	92
Gd(III)-DOTA-quinoline-DOTA-cysteine-Lu(III)	16.84 – 17.95	33	91
Gd(III)-DOTA-quinoline-DOTA-cysteine	16.78 – 17.66	46	89
Eu(III)-DOTA-quinoline-DOTA-cysteine-Eu(III)	16.41 – 17.26	61	89
Eu(III)-DOTA-quinoline-DOTA-cysteine-Gd(III)	16.39 – 17.18	59	80

Eu(III)-DOTA-quinoline-DOTA-cysteine-Tm(III)	16.41 – 17.19	51	88
Eu(III)-DOTA-quinoline-DOTA-cysteine-Yb(III)	16.38 – 17.15	49	87
Eu(III)-DOTA-quinoline-DOTA-cysteine-Lu(III)	16.44 – 17.13	39	78
Tm(III)-DOTA-quinoline-DOTA-cysteine-Eu(III)	16.46 – 17.15	66	61
Tm(III)-DOTA-quinoline-DOTA-cysteine-Tm(III)	16.48 – 17.20	56	70
DOTA-quinoline-DOTA-cysteine	15.42 – 16.06	54	94

Table 3.6. Experimental and theoretical high resolution mass spectrometry values for each Ln(III)-DOTA-CHQ-cysteine-DOTA-Ln(III) complexes including the free lanthanide DOTA-quinoline-DOTA-cysteine complex.

Compounds	HRMS (ESI) *m/z* found	HRMS (ESI) *m/z* calcd
Gd(III)-DOTA-quinoline-DOTA-cysteine-Eu(III)	1515.5197 $[M + H + H_2O]^+$	1515.3332 for $C_{54}H_{72}N_{13}O_{17}S^{158}Gd^{153}Eu$
Gd(III)-DOTA-quinoline-DOTA-cysteine-Gd(III)	1522.3380 $[M + H + H_2O]^+$	1522.3372 for $C_{54}H_{72}N_{13}O_{17}S^{158}Gd_2$
Gd(III)-DOTA-quinoline-DOTA-cysteine-Tb(III)	1505.3225 $[M + H]^+$	1505.3279 for $C_{54}H_{70}N_{13}O_{16}S^{158}Gd^{159}Tb$
Gd(III)-DOTA-quinoline-DOTA-cysteine-Dy(III)	1526.3311 $[M + H + H_2O]^+$	1526.3412 for $C_{54}H_{72}N_{13}O_{17}S^{158}Gd^{163}Dy$
Gd(III)-DOTA-quinoline-DOTA-cysteine-Ho(III)	1528.3354 $[M + H + H_2O]^+$	1528.3356 for $C_{54}H_{72}N_{13}O_{17}S^{158}Gd^{165}Ho$
Gd(III)-DOTA-quinoline-DOTA-cysteine-Er(III)	1512.3275 $[M + H]^+$	1512.3344 for $C_{54}H_{70}N_{13}O_{16}S^{157}Gd^{167}Er$
Gd(III)-DOTA-quinoline-DOTA-cysteine-Tm(III)	1514.3326 $[M + H]^+$	1514.3366 for $C_{54}H_{70}N_{13}O_{16}S^{157}Gd^{169}Tm$
Gd(III)-DOTA-quinoline-DOTA-cysteine-Yb(III)	1537.3492 $[M + H + H_2O]^+$	1537.351 for $C_{54}H_{72}N_{13}O_{17}S^{158}Gd^{173}Yb$
Gd(III)-DOTA-quinoline-DOTA-cysteine-Lu(III)	1520.3386 $[M + H]^+$	1520.3432 for $C_{54}H_{70}N_{13}O_{16}S^{157}Gd^{175}Lu$
Gd(III)-DOTA-quinoline-DOTA-cysteine	1368.4380 $[M + H + H_2O]^+$	1368.4444 for $C_{54}H_{76}N_{13}O_{17}S^{158}Gd$
Eu(III)-DOTA-quinoline-DOTA-cysteine-Eu(III)	768.6392 $[M + 2\ Na]^+$	768.6451 for $C_{54}H_{69}N_{13}O_{16}S^{153}Eu_2Na_2$
Eu(III)-DOTA-quinoline-DOTA-cysteine-Gd(III)	1516.3445 $[M + H + H_2O]^+$	1516.3402 for $C_{54}H_{72}N_{13}O_{17}S^{153}Eu^{156}Gd$

Eu(III)-DOTA-quinoline-DOTA-cysteine-Tm(III)	1532.3927 $[M + Na]^+$	1532.3164 for $C_{54}H_{69}N_{13}O_{17}S^{153}Eu^{169}TmNa$
Eu(III)-DOTA-quinoline-DOTA-cysteine-Yb(III)	1532.3535 $[M + H + H_2O]^+$	1532.3544 for $C_{54}H_{72}N_{13}O_{17}S^{153}Eu^{172}Yb$
Eu(III)-DOTA-quinoline-DOTA-cysteine-Lu(III)	1556.3766 $[M + Na^+ + H_2O]^+$	1556.3324 for $C_{54}H_{71}N_{13}O_{17}S^{153}Eu^{175}LuNa$
Tm(III)-DOTA-quinoline-DOTA-cysteine-Eu(III)	1550.3247 $[M + Na^+ + H_2O]^+$	1550.3258 for $C_{54}H_{71}N_{13}O_{17}S^{153}Eu^{169}TmNa$
Tm(III)-DOTA-quinoline-DOTA-cysteine-Tm(III)	1566.3167 $[M + Na^+ + H_2O]^+$	1566.3394 for $C_{54}H_{71}N_{13}O_{17}S^{169}Tm_2Na$
DOTA-quinoline-DOTA-cysteine	1217.3829 $[M + Na]^+$	1217.3761 for $C_{54}H_{75}N_{13}O_{16}SNa$

3.9.3. HPLC Analysis

Each mono lanthanides synthons and bimetallic complexes were purified on a HPLC system (Shimadzu) by preparing a 5 mg/mL solution in water. The separation was realized on a polar C18 Phenomenex Luna column (250 x 4.6 mm, particle size 5 µm, pore size 100 Å). The mobile phase is composed of water + 0.1 % TFA (mobile phase A) and acetonitrile + 0.1 % TFA (mobile phase B). Products are eluted according to a linear gradient from 0.0 to 23.00 min 0-92% B, 23.01-24.01 min 1%, followed by a 6 min column equilibration after each run. Chromatograms were detected at 254 nm and a flow rate of 10 mL/min was set up with a temperature of 25 °C.

3.9.4. Relaxation Time Analysis

All MRI acquisitions were performed on a 3T pre-clinical MRI (MR Solutions, Ltd.). Contrast agent samples were prepared in 1× PBS in standard NMR tubes, which were then inserted into a 50 mL Falcon tube containing ultrasound gel, comprising the MRI phantom. The MRI phantom was placed into a 38-mm-diameter send-receive coil and inserted into the MRI. A multislice Rapid Imaging with Refocused Echoes (RARE) pulse sequence was implemented for the evaluation of phantoms using the following parameters for T_1-weighted imaging: slice thickness of 5 mm, FOV of 40×40 mm, averages = 3, matrix size = 96×96, TE = 11 ms, echo spacing = 7 ms, TR = 720 ms, and acquisition time of 2 minutes 16 seconds. For T_2-weighted imaging, all parameters were the same as for T_1-weighted images, except TE = 68 ms and TR = 4800 ms, and acquisition time was

7 minutes 28 seconds. T_1-weighted/T_2-weighted ratiometric images were generated using ImageJ[17] by invoking the image math command and using a custom look up table.

3.9.5. Relaxivities Measurement

All MRF acquisitions were acquired on a 3T preclinical scanner (Agilent, Santa Clara, CA) with a quadrature RF coil. Bislanthanide complexes were dissolved and mixed in a PBS and 4% gelatin solution at 5 different concentrations (0.025 mM, 0.05 mM, 0.2 mM, 0.4 mM and 0.6 mM) and placed in an NMR tube. The NMR tubes were then placed in the quadrature coil. The MRF sequence was based off a Steady State Free Precession paradigm, with varied TR, TE and flip angle (FA) for 1000 imaging frames. TR, TE, and FA initially remain constant to enable conventional steady-state recovery for 200 frames. A 1D Perlin variation of TR ranging from 16 to 20 ms was then introduced, alongside a Perlin noise pattern for FA ranging from 20 to 60°, with two intervals where FA is omitted. For the final 400 frames, FA was kept constant while TE changes sinusoidally, gradually increasing from 5 to 10 ms. The acquisition utilized a variable density trajectory, each interleaf sampling 923 points with a 5 μs dwell time, resulting in a 5 ms acquisition window. Total acquisition of 8 interleaves per imaging slice resulted in a total scan time of 2 mins per slice. Reconstruction and parameter matching of the images was performed in MATLAB (The MathWorks; Natick, MA), on a virtual machine with 200GB memory and 24 CPUS running on a Linux enterprise cluster.

3.9.6. Photoluminescence Spectroscopy

Steady-state photoluminescence spectroscopy of the bislanthanide complexes in solution (1 mM concentration in H_2O or D_2O) was carried out in a quartz cuvette (suitable spectral range from 200 to 2500 nm, 1 cm optical path) inserted into the Peltier temperature sample holder of a QuantaMaster 8075-21 spectrofluorometer from HORIBA, equipped with a double additive excitation monochromator with triple gratings, a single emission monochromator with triple gratings, and a red-extended photomultiplier detector R13456 PMT (185 to 980 nm). A 75 W continuous Xenon lamp was used as the excitation source for the recording of steady-state excitation and emission spectra. A long-pass 400 nm filter was placed in front of the detector. Excitation spectra were corrected in real time according to the response of the excitation monochromators and the lamp intensity. Emission spectra were corrected according to the sensitivity of the photomultiplier detector and response of the monochromator gratings.

3.9.7. Supplementary data

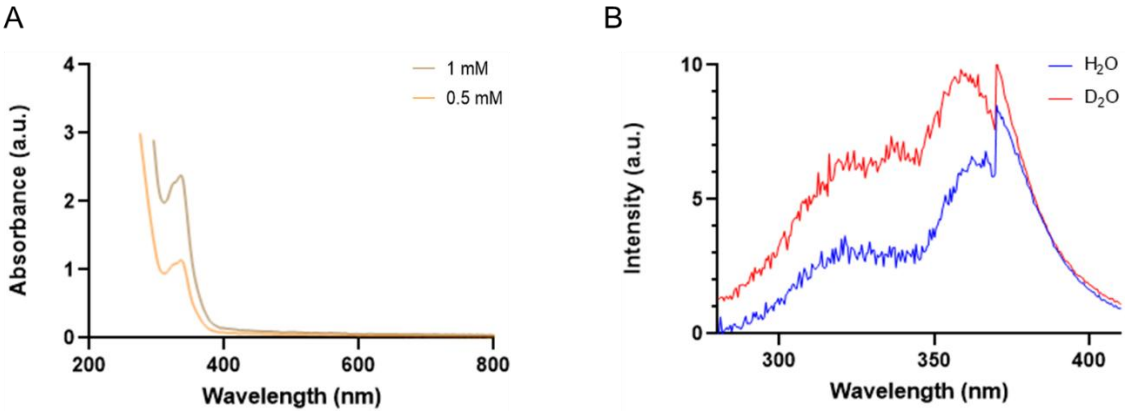

S57. (A) UV-visible spectrum of the lanthanide-free complex in H_2O at 1 mM and 0.5 mM concentration obtained on a range from 200 nm to 800 nm. (B) Excitation spectra of the free lanthanide complex obtained in H_2O and D_2O at 1 mM concentration, monitoring the 460 nm emission.

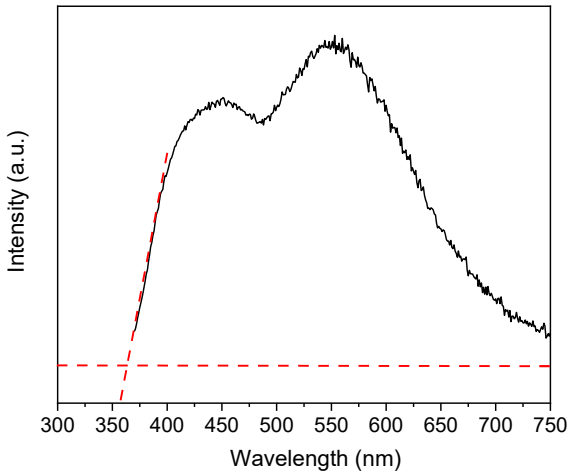

S58. Solid state emission spectrum (λ_{ex} = 320 nm) of the lanthanide-free complex collected at 77 K to determine the position of the triplet excited state (T_1), returning a value of 27473 cm^{-1}.

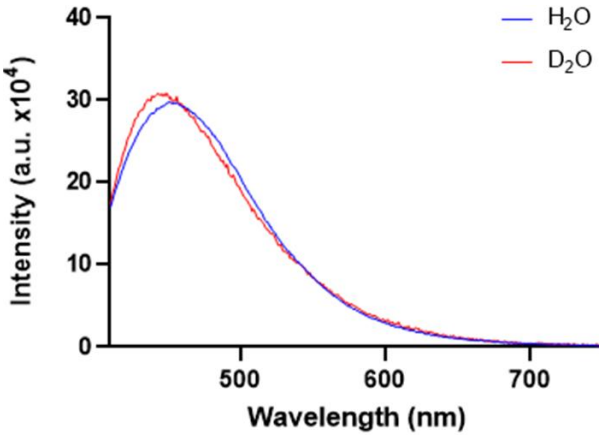

S59. Emission spectrum of Tm(III)-DOTA-quinolinyl-cysteinyl-DOTA-Tm(III) (Tm-Tm) in water (blue line) and deuterated water (red line) under 360 nm excitation. The solution was made in a concentration of 1 mM.

3.9.8. NMR Spectral Characterization

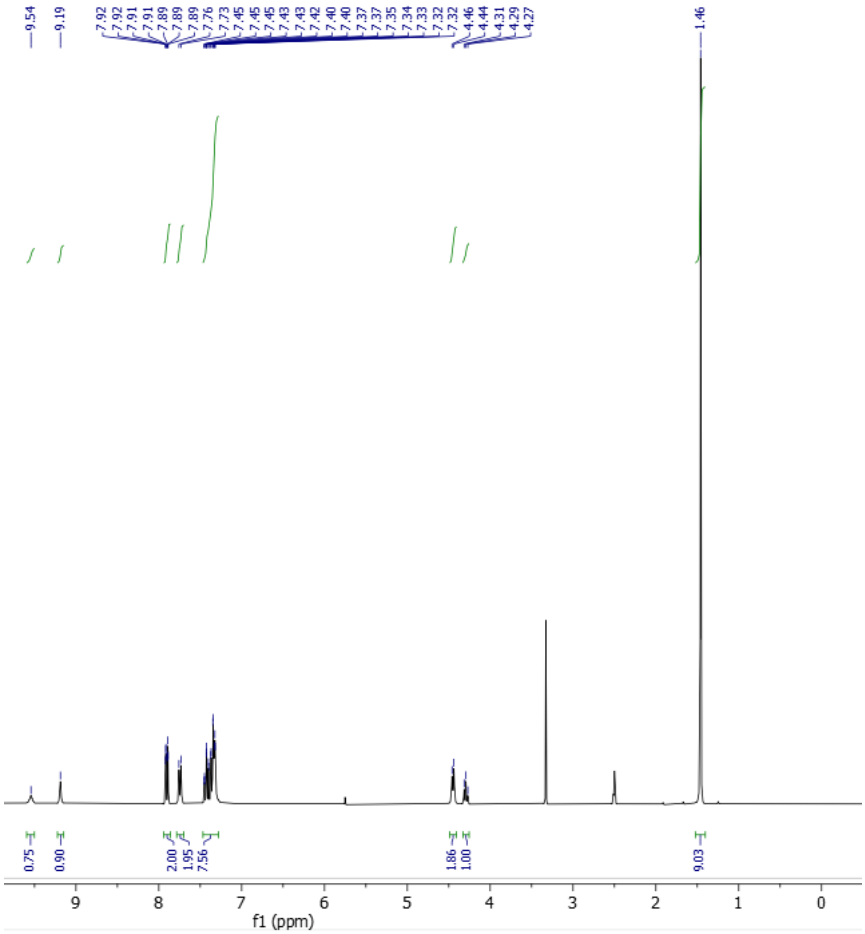

S60. ^{1}H NMR spectrum of compound **7** in DMSO-D_6.

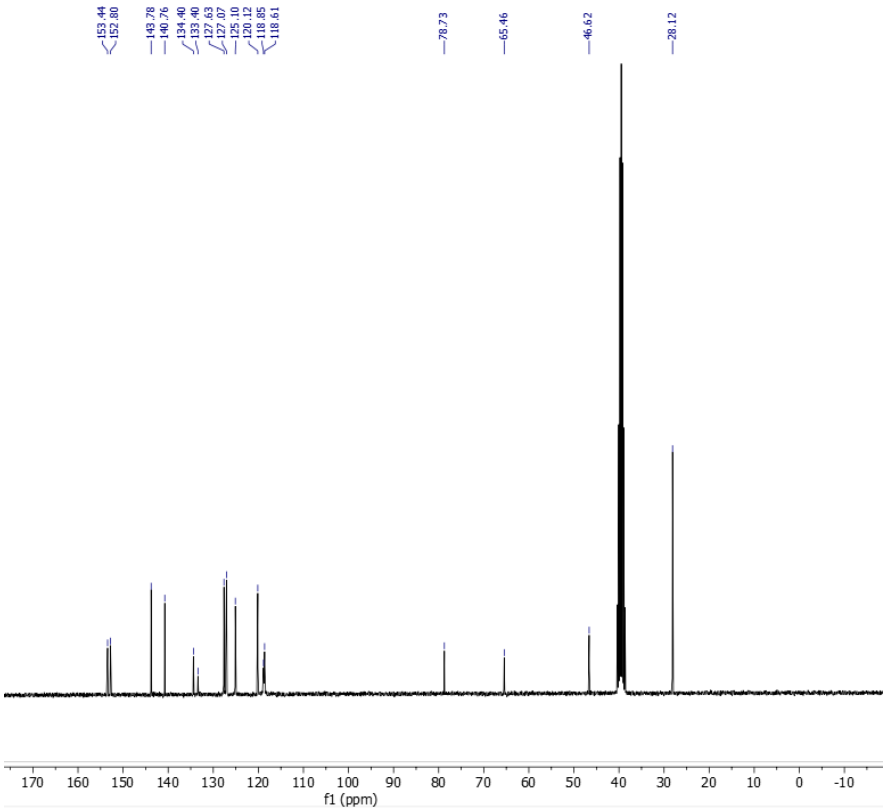

S61. ^{13}C NMR spectrum of compound **7** in DMSO-D_6.

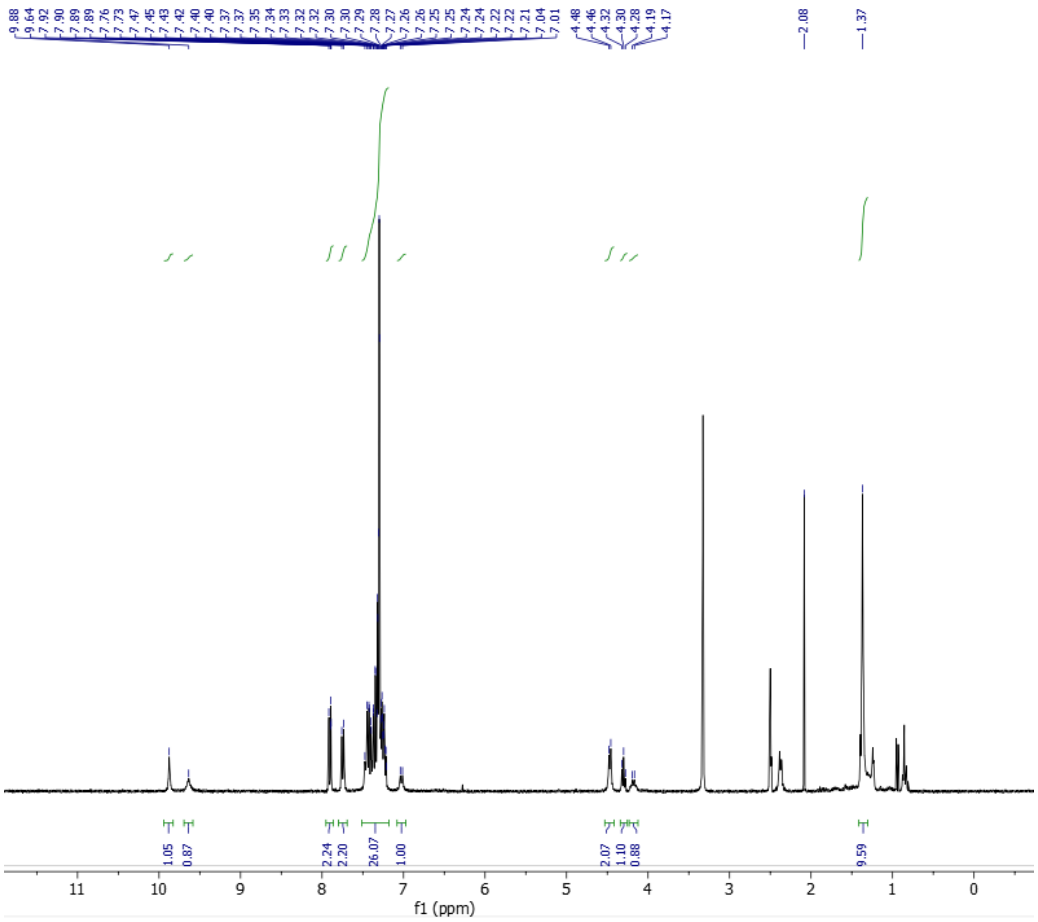

S62. ^{1}H NMR spectrum of compound **8** in DMSO-D_6.

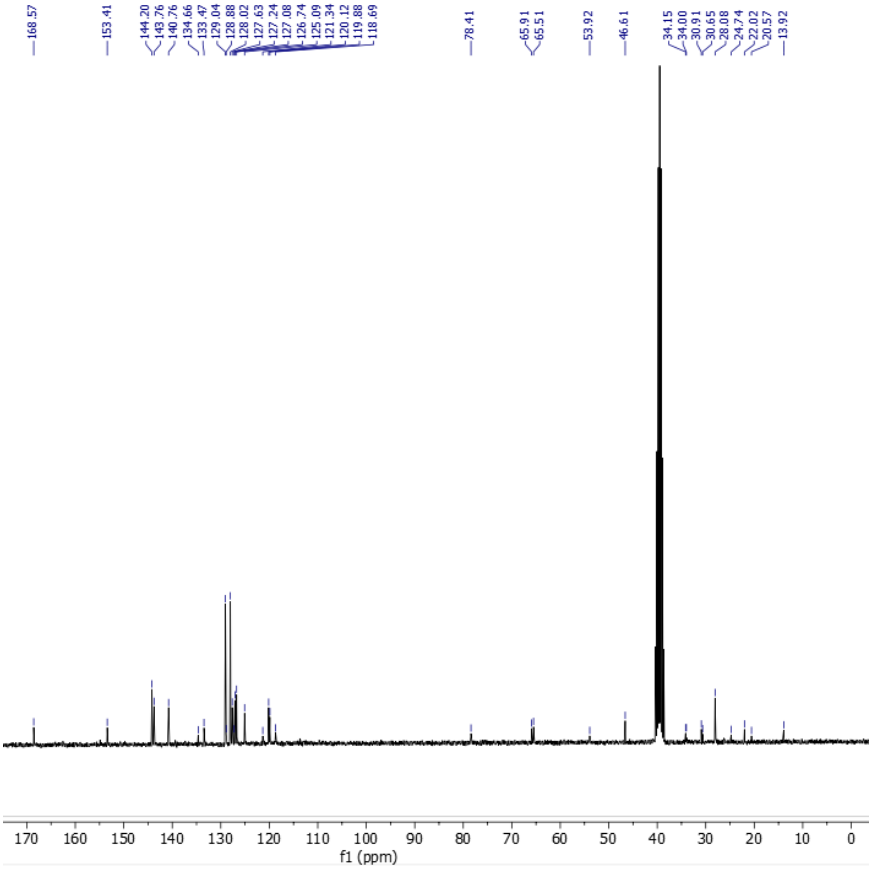

S63. ^{13}C NMR spectrum of compound **8** in DMSO-D_6.

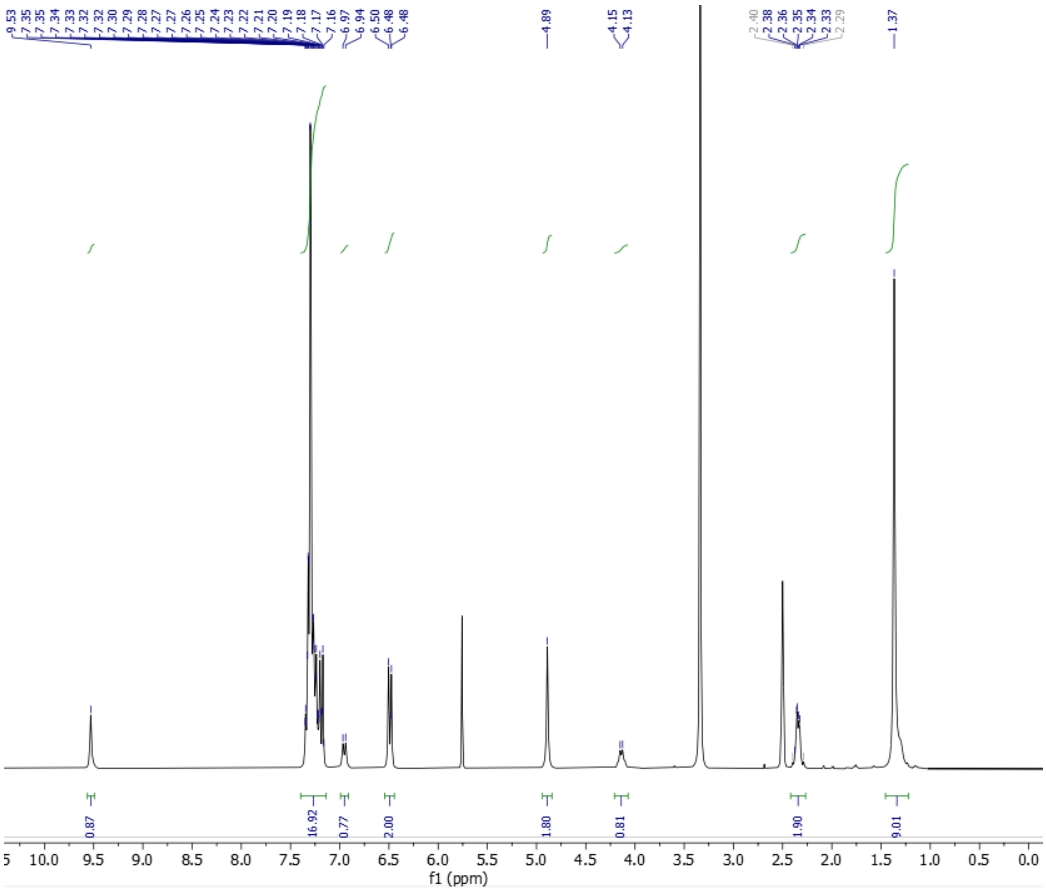

S64. ^{1}H NMR spectrum of compound **9** in DMSO-D_6.

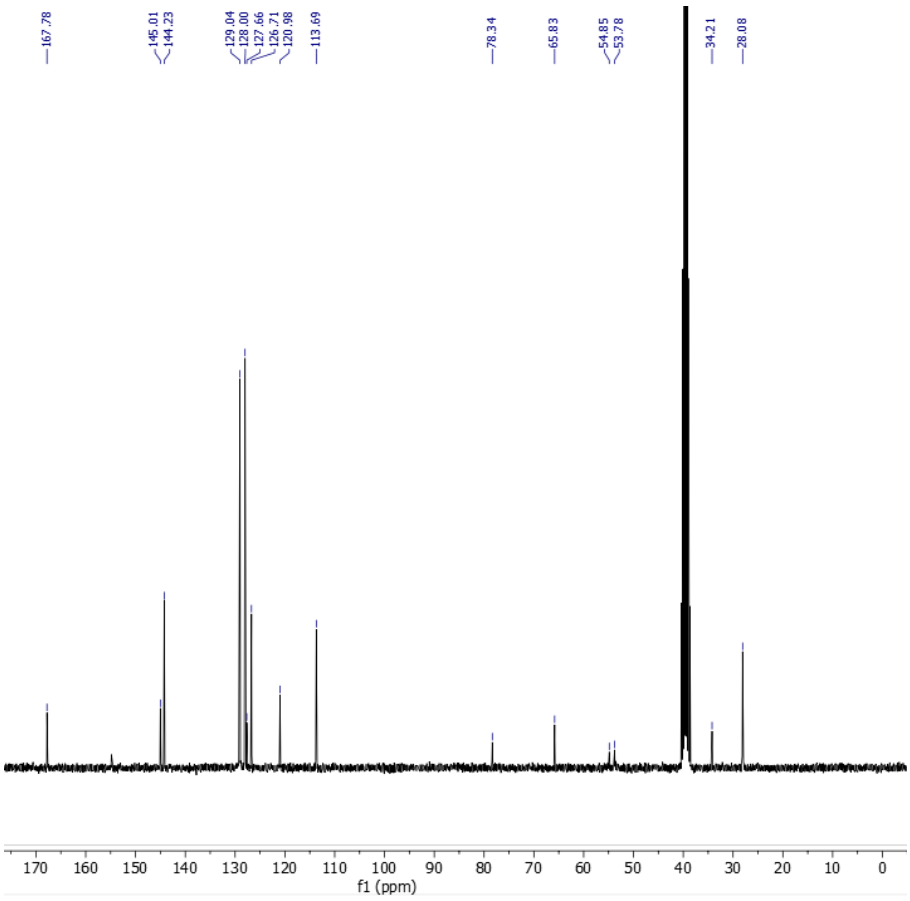

S65. ^{13}C NMR spectrum of compound **9** in DMSO-D_6.

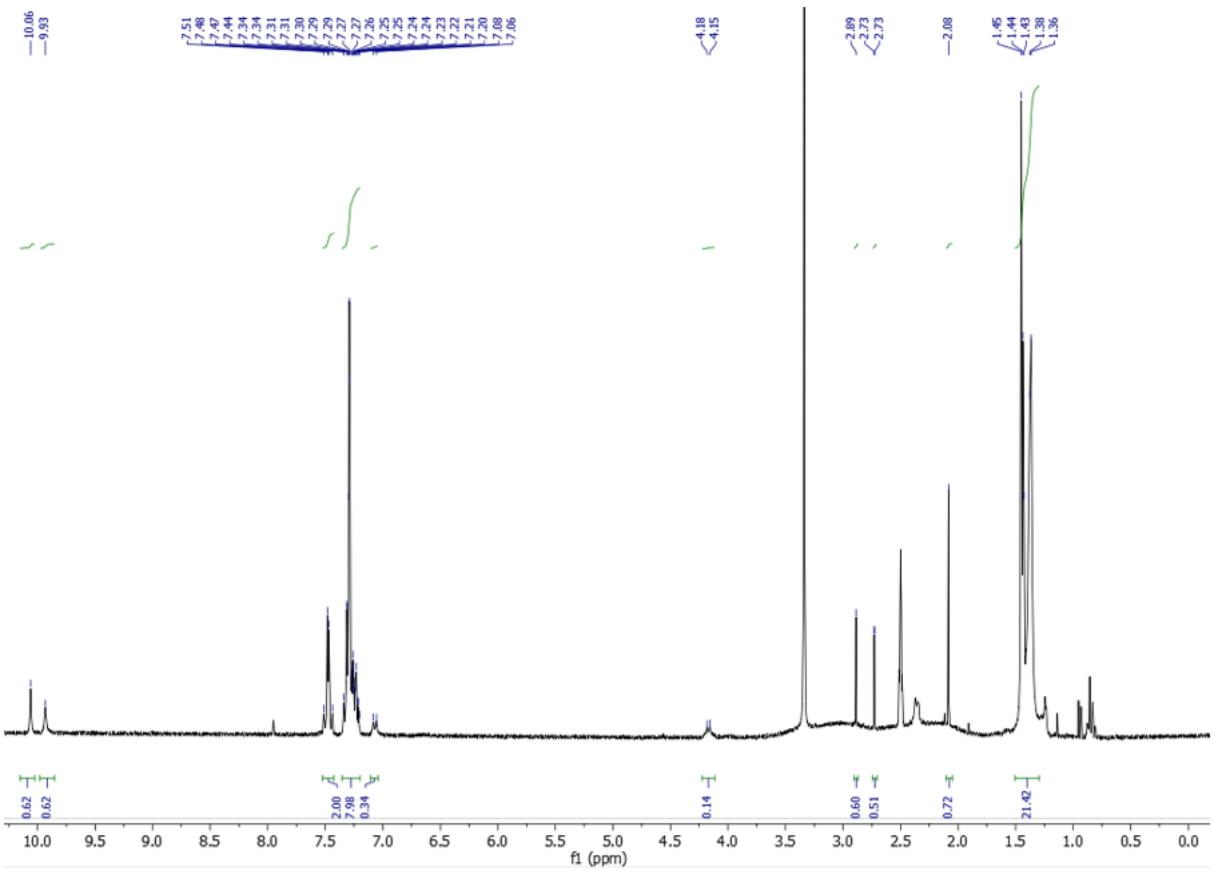

S66. ^{1}H NMR spectrum of compound **10** in DMSO-D_6.

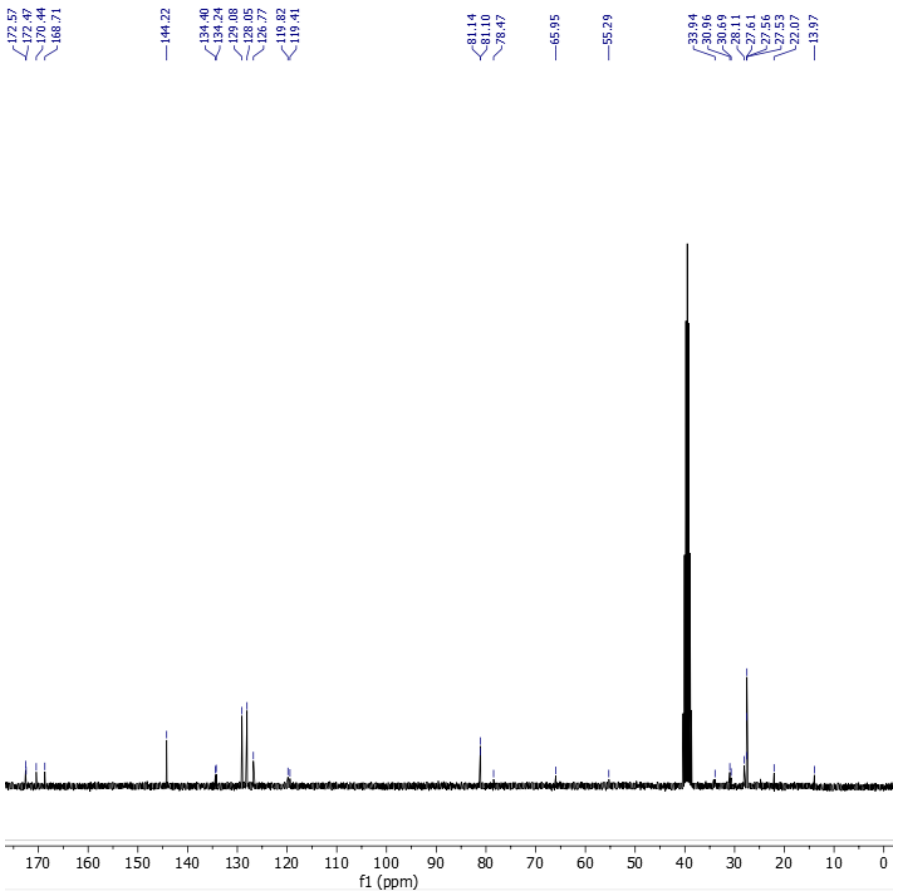

S67. ^{13}C NMR spectrum of compound **10** in DMSO-D_6.

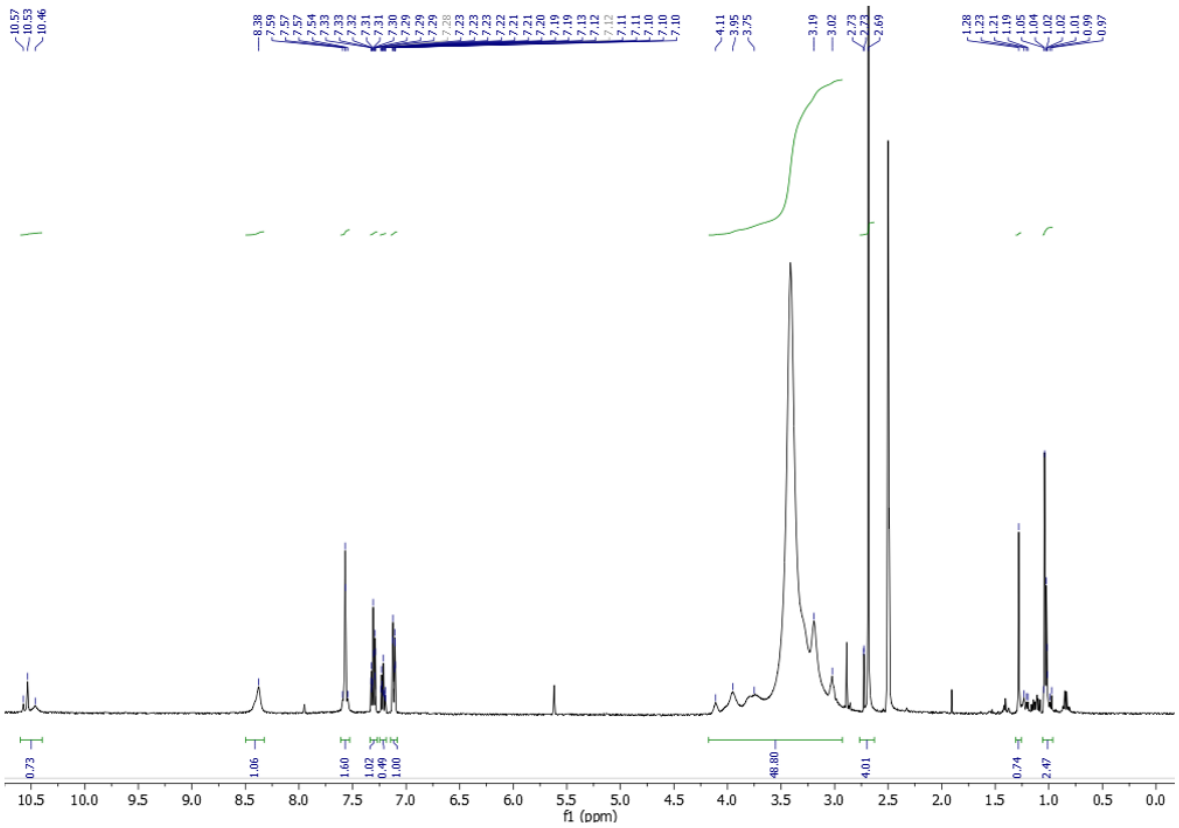

S68. ^{1}H NMR spectrum of compound **11** in DMSO-D_6.

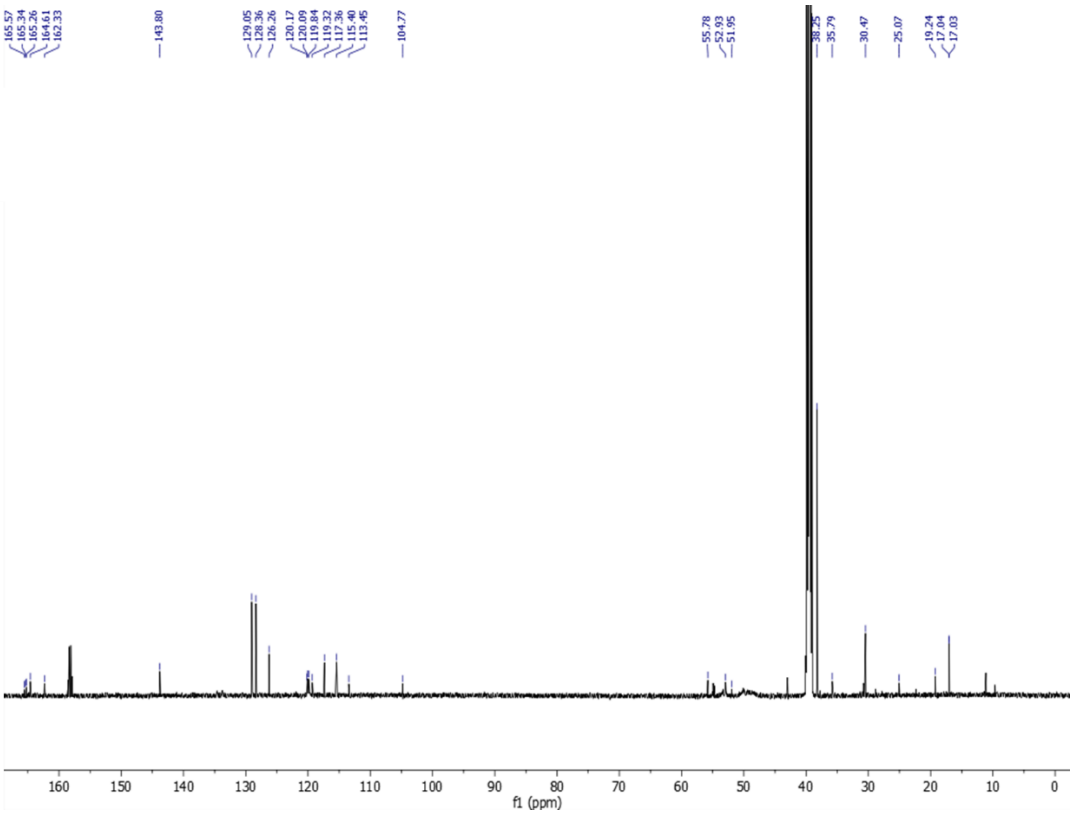

S69. ^{13}C NMR spectrum of compound **11** in DMSO-D_6.

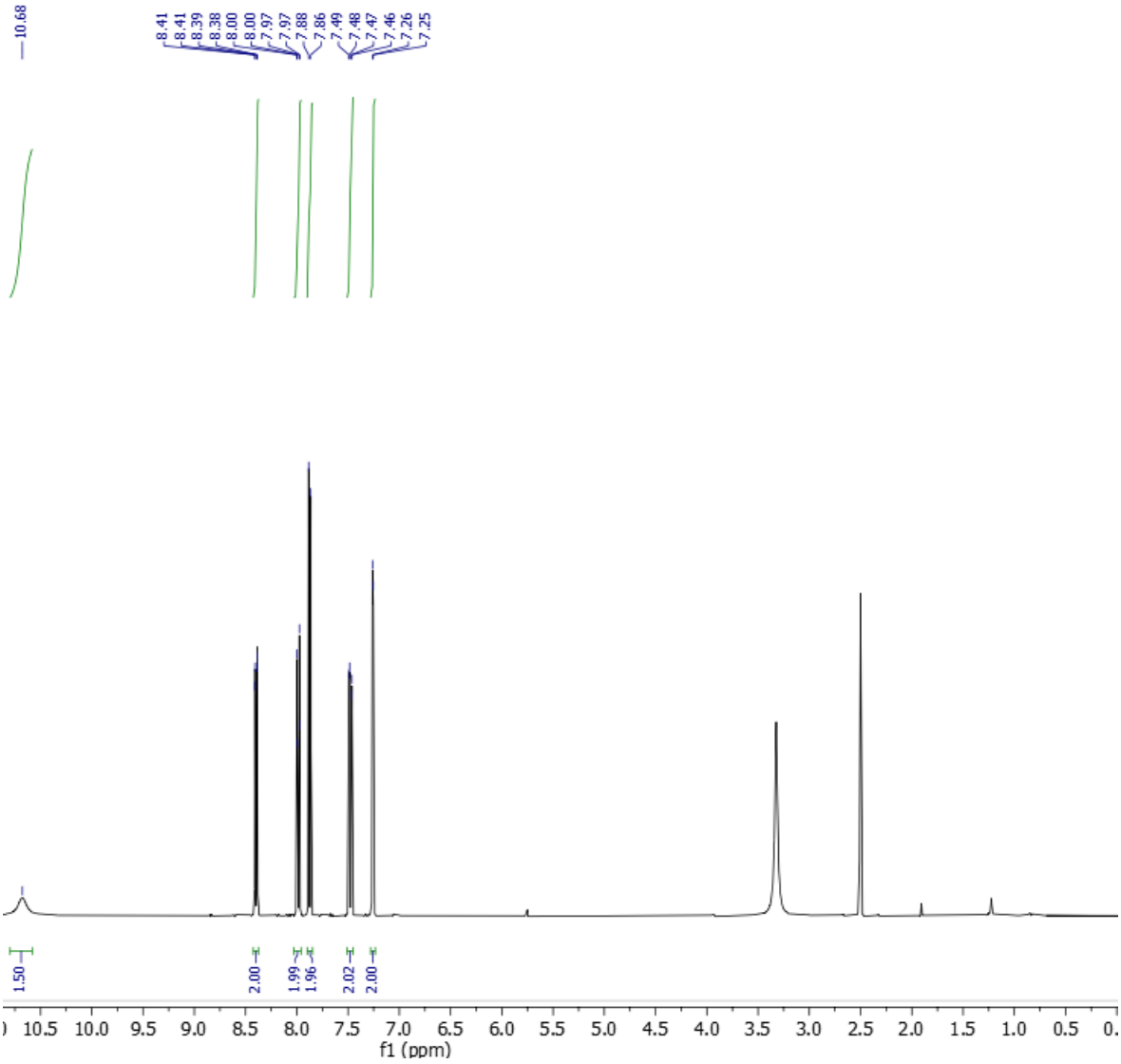

S70. ^{1}H NMR spectrum of compound **13** in DMSO-D_6.

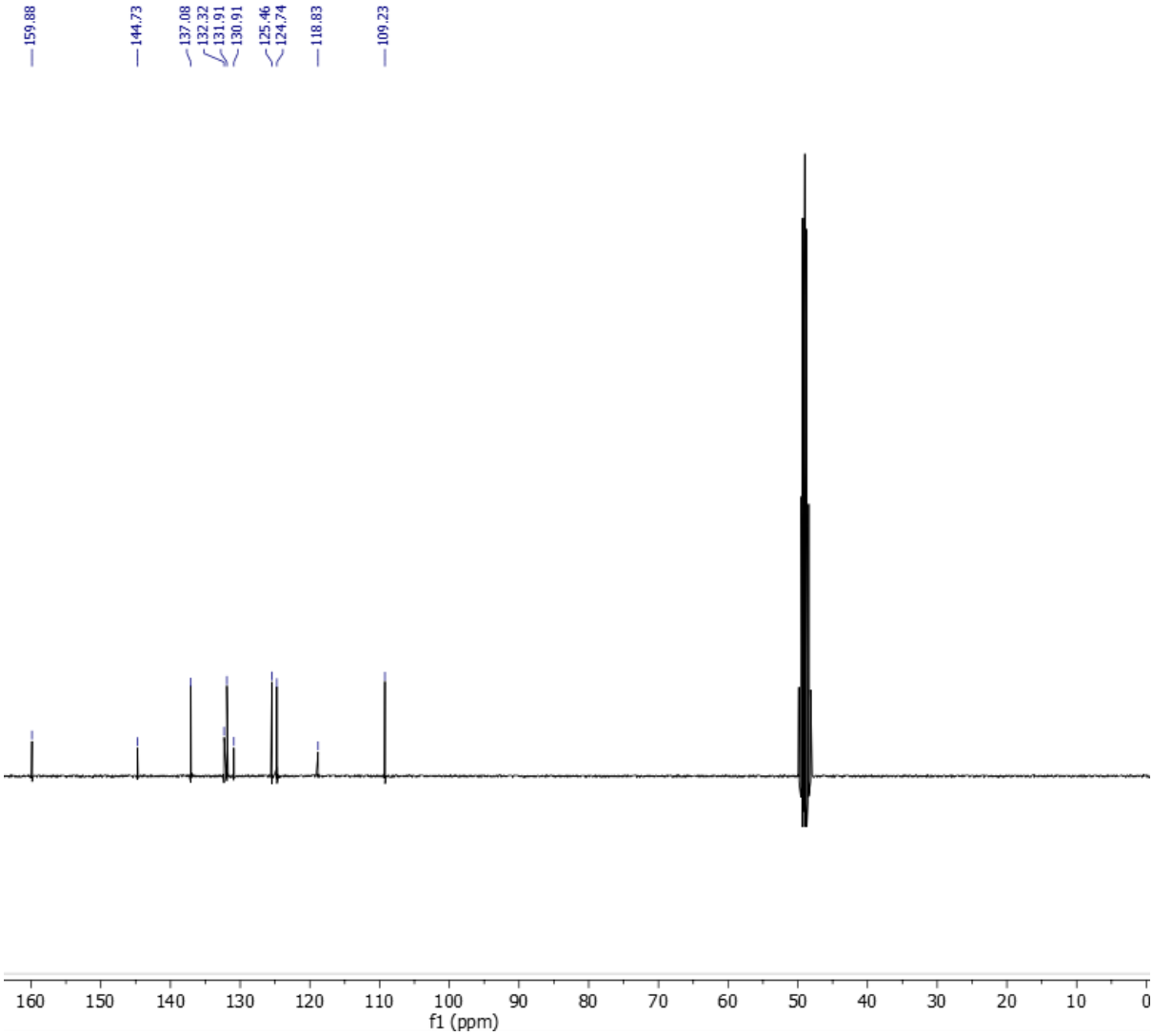

S71. ^{13}C NMR spectrum of compound **13** in CD_3OD.

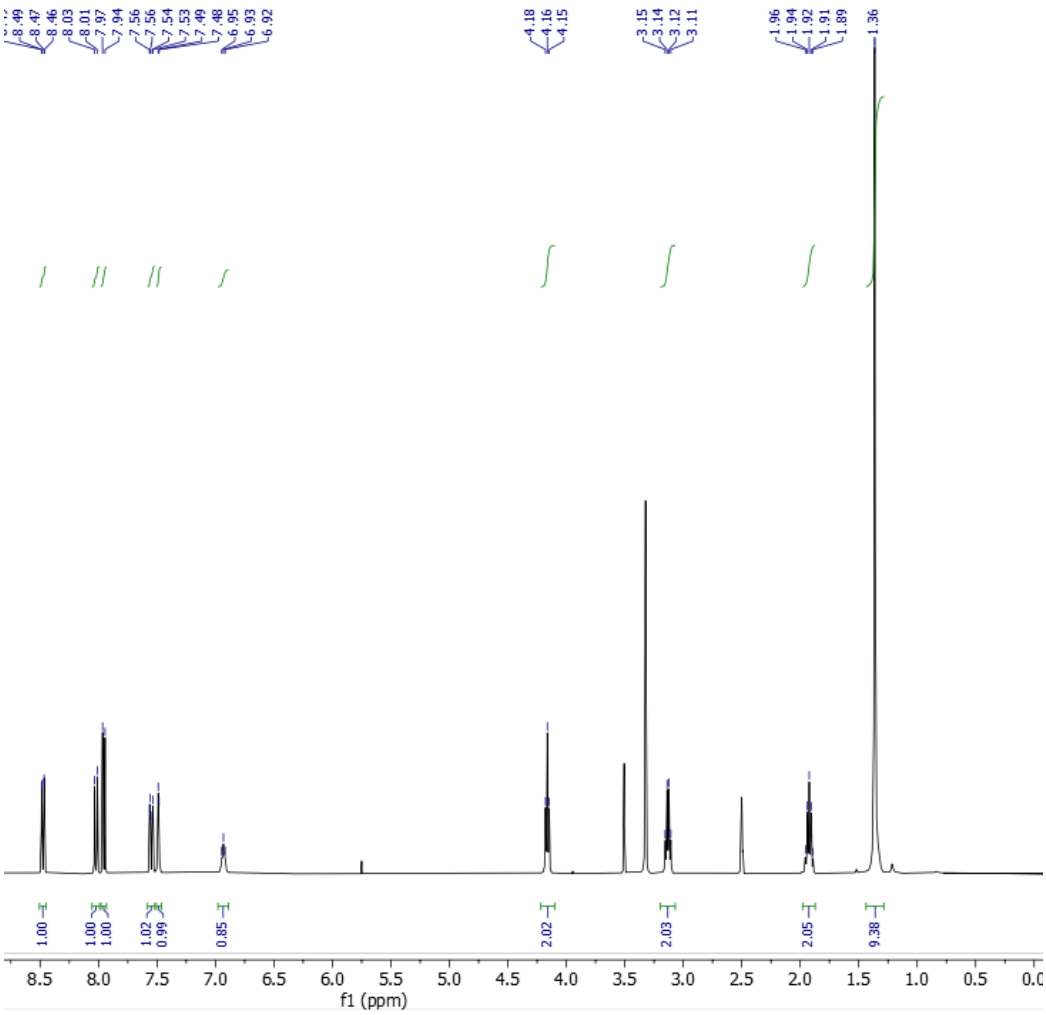

S72. ^{1}H NMR spectrum of compound **14** in DMSO-D_6.

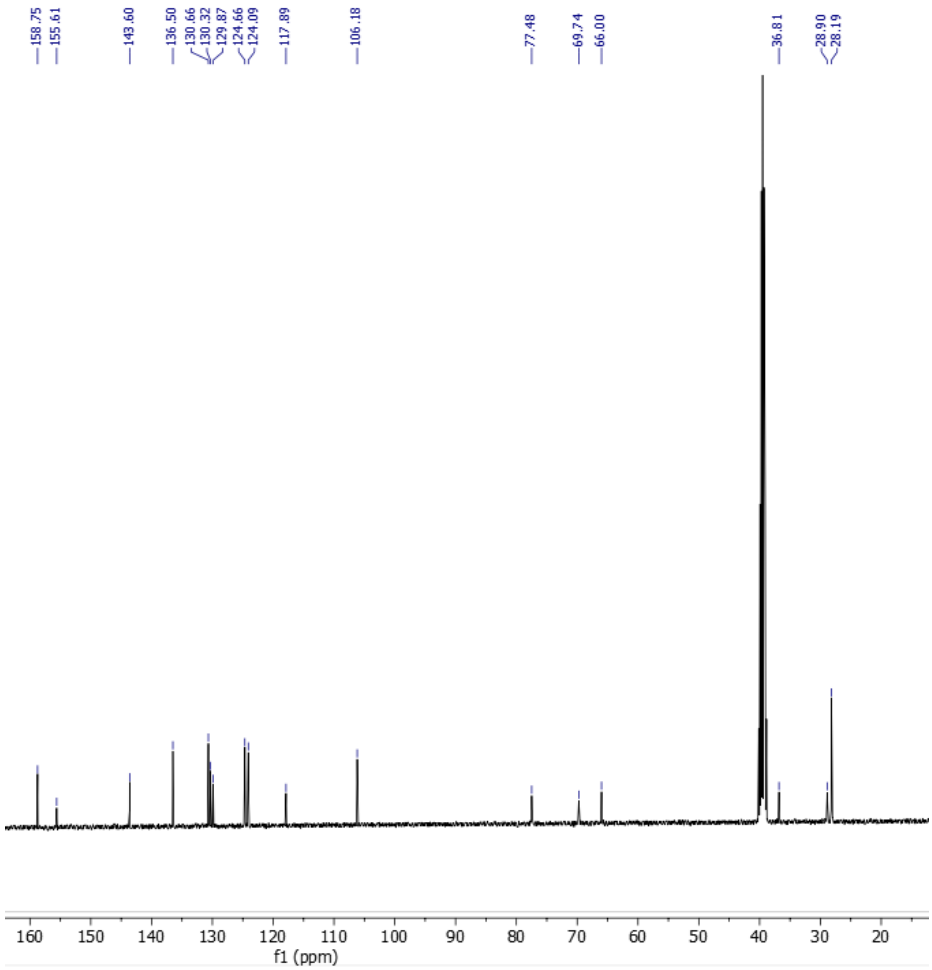

S73. ^{13}C NMR spectrum of compound **14** in DMSO-D_6.

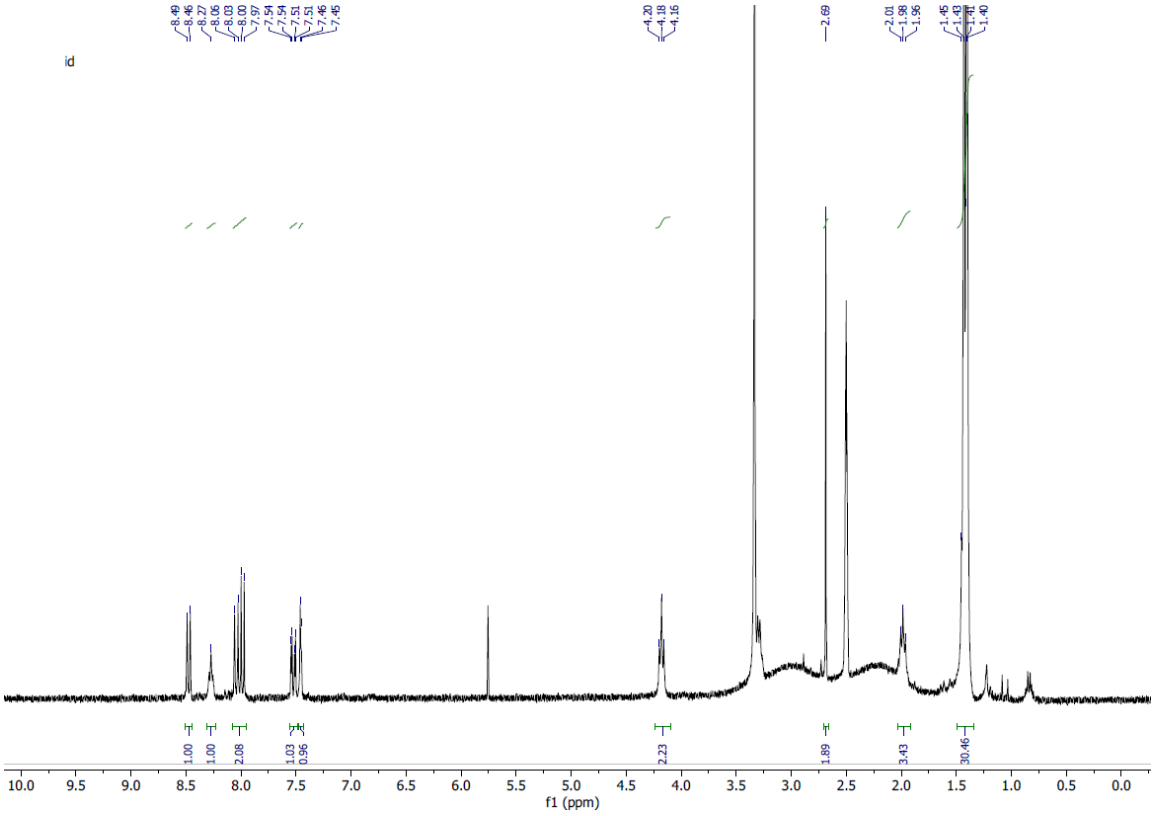

S74. ^{1}H NMR spectrum of compound **15** in DMSO-D_6.

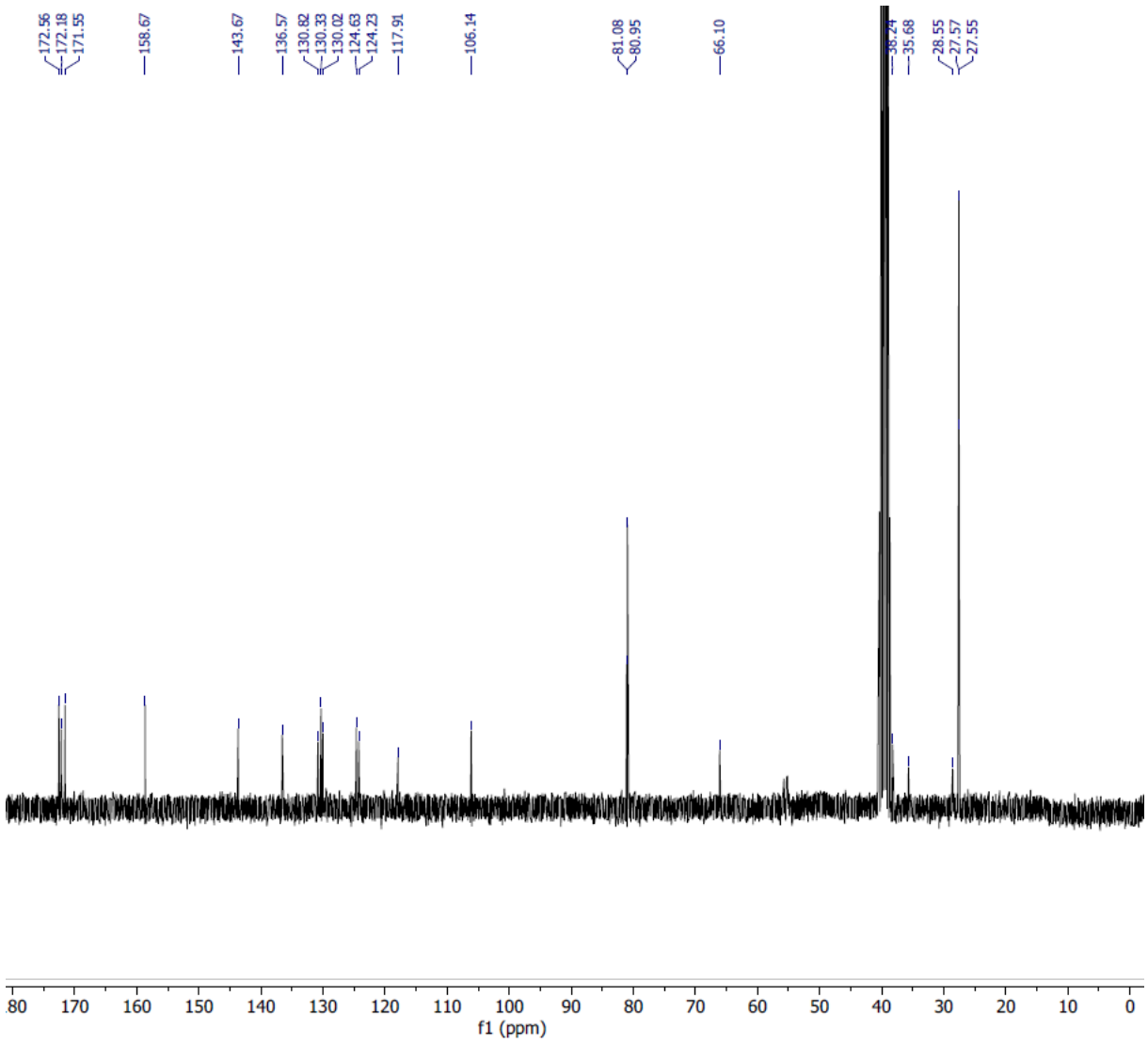

S75. ^{13}C NMR spectrum of compound **15** in DMSO-D_6.

3.10. Notes and References

1. da Rocha, J. D. G.; Cechinel, M. A. P; Rocha, L. F.; Riella, H. G.; Padoin, N.; Soares, C. Exploring the Potential of Rare Earth Doped Carbon Dots: Concepts and Applications. *Chem. Eng. J. Adv.* **2024**, *17*, 100583.

2. Caravan, P. Strategies for increasing the sensitivity of gadolinium based MRI contrast agents. *Chem. Soc. Rev.* **2006**, *35*, 512–523.

3. Panda, A.; Mehta, B. B.; Coppo, S.; Jiang, Y.; Ma, D.; Seiberlich, N.; Griswold, M. A.; Gulani, V. Magnetic resonance fingerprinting – An overview. *Curr. Opin. Biomed. Eng.* **2017**, *3*, 56–66.

4. Bipin Mehta, B.; Coppo, S.; McGivney, D. F.; Hamilton, J. I.; Chen, Y.; Jiang, Y.; Ma, D.; Seiberlich, N.; Gulani, V.; Griswold, M. A. Magnetic resonance fingerprinting: a technical review. *Magn. Reson. Med.* **2019**, *81*, 25–46.

5. Li, H.; Meade, T. J. Molecular Magnetic Resonance Imaging with Gd(III)-Based Contrast Agents: Challenges and Key Advances. *J. Am. Chem. Soc.*, **2019**, *141*, 17025–17041.

6. Morrow, J. M.; Tóth, E. Next-Generation Magnetic Resonance Imaging Contrast Agents. *Inorg. Chem.* **2017**, *56* (11), 6029–6034.

7. Cho, U.; Chen, J. K. Lanthanide-Based Optical Probes of Biological Systems. *Cell Chem. Biol.* **2020**, *27* (8), 921–936.

8. Wang, Y.; Ma, B.; Liu, M.; Chen, E.; Xu, Y.; Zhang, M. Europium Fluorescent Nanoparticles-Based Multiplex Lateral Flow Immunoassay for Simultaneous Detection of Three Antibiotic Families Residue. *Front. Chem.* **2021**, *9*, 793355.

9. Chen, T.; Pham, H.; Mohamadi, A.; Miller, L. W. Single-Chain Lanthanide Luminescence Biosensors for Cell-Based Imaging and Screening of Protein-Protein Interactions. *iScience* **2020**, *23* (9), 101533.

10. Song, B.; Shi, W.; Shi, W.; Ma, H.; Tan, M.; Zhang, W.; Guo, L.; Yuan, J. A dual-modal nanoprobe based on Eu(III) complex–MnO2 nanosheet nanocomposites for time-gated luminescence–magnetic resonance imaging of glutathione *in vitro* and *in vivo*. *Nanoscale* **2019**, *14*, 6784–6793.

11. Dekaliuk, M.; Hildebrandt, N. Lanthanide-FRET Molecular Beacons for microRNA Biosensing, Logic Operations, and Physical Unclonable Functions. *Eur. J. Inorg. Chem.* **2023**, *26* (36), e202300288.

12. Rajapakse, H. E.; Gahlaut, N.; Mohandessi, S.; Yu, D.; Turner, J. R.; Miller, L. M. Time-resolved luminescence resonance energy transfer imaging of protein–protein interactions in living cells. *Proc. Natl. Acad. Sci.* **2010**, *107* (31), 13582–13587.

13. Bhattacharya, K.; Bernasconi, L.; Picard, D. Luminescence resonance energy transfer between genetically encoded donor and acceptor for protein-protein interaction studies in the molecular chaperone HSP70/HSP90 complexes. *Sci. Rep.* **2018**, *8*, 2801.

14. Afsari, H. S.; Dos Santos, M. C.; Lindén, S.; Chen, T.; Qiu, X.; van Bergen En Henegouwen, P. M. P.; Jennings, T. L.; Susumu, K.; Medintz, I. L.; Hildebrandt, N.; Miller, L. W.

Time-gated FRET nanoassemblies for rapid and sensitive intra- and extracellular fluorescence imaging. *Sci. Adv.* **2016**, *2* (6), e1600265.

15. Wheeler, S.; Butler, S. J. Exploiting the Unique Properties of Lanthanide Complexes as FRET Probes: from Quantitation to Protein Dynamics. *Anal. Sens.* **2023**, *3*, e202200036.

16. Sørensen, T. J.; Kenwright, A. M.; Faulkner, S. Bimetallic lanthanide complexes that display a ratiometric response to oxygen concentrations. *Chem. Sci.* **2015**, *6* (3), 2054–2059.

17. Sørensen, T. J.; Tropiano, M.; Kenwright, A. M.; Faulkner, S. Triheterometallic Lanthanide Complexes Prepared from Kinetically Inert Lanthanide Building Blocks. *Eur. J. Inorg. Chem.* **2017**, *15*, 2165–2172.

18. Placidi, M. P.; Villaraza, A. J. L.; Natrajan, L. S.; Sykes, D.; Kenwright, A. M.; Faulkner, S. Synthesis and Spectroscopic Studies on Azo-Dye Derivatives of Polymetallic Lanthanide Complexes: Using Diazotization to Link Metal Complexes Together. *J. Am. Chem. Soc.* **2009**, *131* (29), 9916–9917.

19. Szíjjártó, C.; Pershagen, E.; Borbas, K. E. Functionalisation of lanthanide complexes via microwave-enhanced Cu(I)-catalysed azide–alkyne cycloaddition. *Dalton Trans.* **2012**, *41* (25), 7660–7669.

20. Ahmed Fouad, M.; Abdel-Hamid, H.; Salah Ayoup, M. Two decades of recent advances of Ugi reactions: synthetic and pharmaceutical applications. *RSC Adv.* **2020**, *10*, 42644–42681.

21. Ye, D.; Shuhendler, A. J.; Cui, L.; Tong, L.; Tee, S. S.; Tikhomirov, G.; Felsher, D. W.; Rao, J. Bioorthogonal cyclization-mediated in situ self-assembly of small-molecule probes for imaging caspase activity *in vivo*. *Nat. Chem.* **2014**, *6* (6), 519–526.

22. Main, M.; Snaith, J. S.; Meloni, M. M.; Jauregui, M.; Sykes, D.; Faulkner, S.; Kenwright, A. M. Using the Ugi multicomponent condensation reaction to prepare families of chromophore appended azamacrocycles and their complexes. *Chem. Commun.* **2008**, *41*, 5212–5214.

23. Liu, J.; Li, Y.; Chen, Y.; Hua, X.; Wan, Y.; Wei, W.; Song, H.; Yu, S.; Zhang, X.; Li, Z. Design, Synthesis, Antifungal Activities and SARs of (R)-2-Aryl-4,5-dihydrothiazole-4-carboxylic Acid Derivatives. *Chin. J. Chem.* **2015**, *33* (11), 1269–1275.

24. Lu, Y.; Li, C.-M.; Wang, Z.; Chen, J.; Mohler, M. L.; Li, W.; Dalton, J. T.; Miller, D. D. Design, Synthesis, and SAR Studies of 4-Substituted Methoxylbenzoyl-aryl-thiazoles Analogues as Potent and Orally Bioavailable Anticancer Agents. *J. Med. Chem.* **2011**, *54* (13), 4678–4693.

25. Liu, J.; Li, F.; Wang, Y.; Zhang, H.; Dong, J.; Sun, P.; Li, Y.; Li, Z. Synthesis, biological activities and 3D-QSAR studies of (R)-2-phenyl-4,5-dihydrothiazole-4-carboxamide derivatives containing a sulfur ether moiety. *Chin. Chem. Lett.* **2019**, *30* (3), 668–671.

26. Shuhendler, A. J.; Ye, D.; Brewer, K. D.; Bazalova-Carter, M.; Lee, K.-H.; Kempen, P.; Wittrup, K. D.; Graves, E. E.; Rutt, B.; Rao, J. Molecular Magnetic Resonance Imaging of Tumor Response to Therapy. *Sci. Rep.* **2015**, *5*, 14759.

27. Gómez-González, E.; Caro, C.; García-Martín, M. L.; Becerro, A. I.; Ocaña, M. Outstanding MRI contrast with dysprosium phosphate nanoparticles of tuneable size. *Nanoscale* **2022**, *14* (31), 11461–11470.

28. Aime, S.; Botta, M.; Barbero, L.; Uggeri, F.; Fedeli, F. Water signal suppression by T2-relaxation enhancement promoted by Dy(III) complexes. *Magn. Reson. Chem.* **1991**, *29* (13), S85–S88.

29. Harris, M.; Henoumont, C.; Peeters, W.; Toyouchi, S.; Vander Elst, L.; Parac-Vogt, T. N. Amphiphilic complexes of Ho(III), Dy(III), Tb(III) and Eu(III) for optical and high field magnetic resonance imaging. *Dalton Trans.* **2018**, *47* (31), 10646–10653.

30. Shen, Y.; Goerner, F. L.; Snyder, C.; Morelli, J. N.; Hao, D.; Hu, D.; Li, X.; Runge, V. M. T1 relaxivities of gadolinium-based magnetic resonance contrast agents in human whole blood at 1.5, 3, and 7 T. *Invest. Radiol.* **2015**, *50* (5), 330–338.

31. Mehta, B.; Coppo, S.; McGivney, D. F.; Hamilton, J. I.; Chen, Y.; Jiang, Y.; Ma, D.; Seiberlich, N.; Gulani, V.; Griswold, M. A. Magnetic resonance fingergrinting: a technical review. *Magn Reson Med.* **2019**, *81* (1), 25-46.

32. Zhang, J.; Dai, L.; He, L.; Bhattarai, A.; Chan, C.-M.; Tai, W. C.-S.; Vardhanabhuti, V.; Law, G.-L. Design and synthesis of chiral DOTA-based MRI contrast agents with remarkable relaxivities. *Commun. Chem.* **2023**, *6* (251), 1–10.

33. Caravan, P.; Esteban-Gómez, D.; Rodríguez-Rodríguez, A.; Platas-Iglesias, C. Water exchange in lanthanide complexes for MRI applications. Lessons learned over the last 25 years. *Dalton Trans.* **2019**, *48* (30), 11161–11180.

34. Ibrahim Mohamed Allaoui, Z.; le Gall, E.; Fihey, A.; Plaza-Pedroche, R.; Katan, C.; le Guen, F. R.; Rodríguez-López, J.; Achelle, S. Push–Pull (Iso)quinoline Chromophores: Synthesis, Photophysical Properties, and Use for White-Light Emission. *Chem. – Eur. J.* **2020**, *26* (36), 8153–8161.

35. Lee, H.; Landgraf, R.; Wilson, J. N. Synthesis and photophysical properties of a fluorescent cyanoquinoline probe for profiling ERBB2 kinase inhibitor response. *Bioorg. Med. Chem.* **2017**, *25* (21), 6016–6023.

36. Binnemans, K. Interpretation of europium(III) spectra. *Coord. Chem. Rev.* **2015**, *295*, 1–45.

37. Fremy, G.; Raibaut, L.; Cepeda, C.; Sanson, M.; Boujut, M.; Sénèque, O. A novel DOTA-like building block with a picolinate arm for the synthesis of lanthanide complex-peptide conjugates with improved luminescence properties. *J. Inorg. Biochem.* **2020**, *213*, 111257.

38. Smith, D. G.; McMahon, B. K.; Pal, R.; Parker, D. Live cell imaging of lysosomal pH changes with pH responsive ratiometric lanthanide probes. *Chem. Commun.* **2012**, *48* (68), 8520–8522.

39. Liu, C.; Li, P.; Yan, X.; Yang, L.; Liu, P.; Wang, Q. Design of a dual Ir-Eu tag for fluorescent visualization and ICP-MS quantification of SIRPα and its host cells. *Anal. Bioanal. Chem.* **2024**, *416* (11), 2691-2697.

40. Josan, J. S.; De Silva, C. R.; Yoo, B.; Lynch, R. M.; Pagel, M. D.; Vagner, J.; Hruby, V. J. Fluorescent and Lanthanide Labeling for Ligand Screens, Assays, and Imaging. *Methods Mol. Biol. Clifton Nj* **2011**, *716*, 89–126.

41. Carnall, W. T.; Goodman, G. L.; Rajnak, K.; Rana, R. S. A systematic analysis of the spectra of the lanthanides doped into single crystal LaF3. *J. Chem. Phys.* **1989**, *90*, 3443–3457.

42. Blackburn, O. A.; Tropiano, M.; Sørensen, T. J.; Thom, J.; Beeby, A.; Bushby, L. M.; Parker, D.; Natrajan, L. S.; Faulkner, S. Luminescence and upconversion from thulium(III) species in solution. *Phys. Chem. Chem. Phys.* **2012**, *14* (38), 13378–13384.

43. Thomsen, M. S.; Nawrocki, P. R.; Kofod, N.; Sørensen, T. J. Seven Europium(III) Complexes in Solution – The Importance of Reporting Data When Investigating Luminescence Spectra and Electronic Structure. *Eur. J. Inorg. Chem.* **2022**, *27*, e202200334.

44. Hasegawa, M.; Ohmagari, H.; Tanaka, H.; Machida, K. Luminescence of lanthanide complexes: From fundamental to prospective approaches related to water- and molecular-stimuli. *J. Photochem. Photobiol. C Photochem. Rev.* **2022**, *50*, 100484.

45. Muller, G. Luminescent chiral lanthanide(III) complexes as potential molecular probes. *Dalton Trans.* **2009**, *44*, 9692–9707.

46. Xiao, X., Haushalter, J. P., Weiss, M. & Faris, G. W. Optical response measurements of a new class of upconverting luminescent reporters. *Genetically Engineered and Optical Probes for Biomedical Applications II*, **2004**, *5329*, 229–238.

47. Maillard, J.; Klehs, K.; Rumble, C.; Vauthey, E.; Heilemann, M.; Fürstenberg, A. Universal quenching of common fluorescent probes by water and alcohols. *Chem. Sci.* **2021**, *12* (4), 1352–1362.

Chapter 4: Second Generation Probes of Homo-Bislanthanide Complexes – Potential Application for Glioblastoma Treatment

Emilie Marie Sophie Patit-Tha Brun [1, 2], Halimo-Kafia M. Fourreh [1, 2] and Adam J. Shuhendler [1, 2, 3]

[1]Dept. Chemistry & Biomolecular Sciences, University of Ottawa, Ottawa, Ontario, Canada. E-mail: adam.shuhendler@uottawa.ca

[2]University of Ottawa Heart Institute, Ottawa, Ontario, Canada

[3]Dept. Biology, University of Ottawa, Ottawa, Ontario, Canada

4.1. Overview of the Research Project Presented in this Chapter

A second generation probe, Lu(III) DOTA-quinoline-lysine-DOTA-Lu(III), has been synthesized as a potential targeted radionuclide therapy agent against glioblastoma. A previous study reported a first generation probe based on the condensation of two individually synthesized components to form a 2-thiazioline ring. Based on this same chemistry, an azide modified lysine is added as a linker on one side of the complex, to bind two peptides, D-VAP and RI-VAP, for glioblastoma targeting. In this project, the primary focus was on the synthesis of the homo-bimetallic complex with efforts to optimize the yield and identifying the most effective method for Fmoc deprotection in the presence of a DOTA component. This process led to a redesigning of the synthetic scheme

4.2. Authors Contributions

E.M.S.P.B. performed all synthesis and characterization for every chemical compounds with support from H-K.M.F.

4.3. Abstract

Glioblastoma multiforme, a grade IV tumor in the central nervous system, can be regulated by the glucose-regulated protein 78 kDa (GRP78), which is considered as a potential biomarker due to its role in regulating high-grade gliomas. A novel synthetic approach is introduced to bind D-VAP and RI-VAP, peptides that target GRP78, specifically to glioblastoma cells. Based on the previously reported condensation method between a cyanohydroxyquinoline and cysteine moieties to form a 2-thiazoline ring, a second-generation probe based on lutetium(III) has been synthesized. This probe includes a linker through an azide-modified lysine amino acid. With the azide-functionalized Lu(III) DOTA-quinoline-lysine-DOTA-Lu(III) complex, the strain promoted azide-alkyne cycloaddition (SPAAC) will be performed using DBCO-maleimide to attach desired peptides to the homo-bimetallic complex. After evaluating the complex as a cold standard, the radioactive isotope ^{177}Lu will be incorporated into both complexes to test their potential as targeted radionuclide therapy agent against glioblastoma.

4.4. Introduction

Gliomas, which are tumors that originate from glial cells, the supportive cells in the brain, account for 80% of all brain tumors and tumors in the central nervous system (CNS) [1]. Classified as grade IV CNS tumors, glioblastoma, also known as glioblastoma multiforme (GBM), is a highly aggressive and malignant type of brain tumor. Even if this disease occurs almost exclusively in the brain, it can also be detected in the brain stem, cerebellum and spinal cord [2, 3]. Glioblastoma frequently presents varying grades of cell-differentiation within a single tumor, suggesting the existence of diverse cell populations with differing responses to treatment. Targeted diagnostics and therapies concentrate on various genetic mutations and alterations in important molecular pathways that are associated with the development and prognosis of GBM. Among the various mutations associated with it, notable examples include the loss of genetic material in the chromosome 10q [4], amplification of epidermal growth factor receptor (EGFR) [2, 5], mutations in neurofibromatosis type 1 (NF1), tumor protein p53 (TP53) [6, 7], telomerase reverse transcriptase (TERT) promoter region [8],and deletions in the phosphatase and tensin homolog (PTEN) [4], among others [1, 9].

Although multiple mutations are associated with glioblastoma, the glucose-regulated protein 78 kDa (GRP78) can be considered as a biomarker for high-grade gliomas due to its role in regulating this type of cancer [10]. GRP78, a member of the heat shock protein HSP70 family that is overexpressed in GBM, functions as a key chaperone protein located in the lumen of the endoplasmic reticulum. It is activated by stress and plays a role in the unfolded protein response (UPR), helping to ensure proper protein folding [11]. This specific protein plays a significant role in various tumor processes, including growth, metastasis, immune regulation and tumor progression

[12, 13]. Its overexpression in tumor microenvironments is a response to conditions such as glucose starvation and hypoxia which make its localization on the membrane of specific cancer cell types [14, 15]. GRP78 was found to specifically bind a 7-amino acids peptide, L-VAP (SNTRVAP), which targets metastatic androgen-independent prostate cancer [16]. Since GRP78 is overexpressed in both glioma cells and glioma stem cells [17], and the stability of peptides can be enhanced using D-amino acids [18], the efficiency of the D-VAP and the RI-VAP (PAVRTNS) peptides was tested for glioma targeting. These peptides were considered effective in accomplishing glioma-targeted drug delivery [10].

With the application of gadolinium-based contrast agents (GBCA), magnetic resonance imaging (MRI) has been considered one of the primary methods in the diagnosis and evaluation of the treatment efficacy in glioblastomas. However, due to an inaccurate reflection of tumor progression in around 28 to 30% of glioma patients in the first three months of chemoradiation [19], positron emission tomography-computed tomography (PET-CT) or single photon emission computed tomography (SPECT) have become more relevant for glioblastomas detection [1]. In addition to these imaging methods has emerged new techniques for cancer treatment such as targeted radionuclide therapy (TRT). TRT uses a biochemical vector linked to a radionuclide, which can be employed for diagnosis, therapy, or both, makes it then a radiotheranostic agent [20]. Lutetium(III), specifically isotope ^{177}Lu, is a metal radionuclide that can be combined with a targeting biomolecule, such as a peptide, to diagnose, monitor or treat disease. Due to its theranostic properties, this isotope emits simultaneously gamma photons in addition to its β particle emission [21]. Its long half-life of 6.734 days, is compatible with pharmacodynamics and pharmacokinetics properties of monoclonal antibodies and proteins [22]. Even though this radioactive isotope has been applied mostly as [^{177}Lu]PSMA-617 or [^{177}Lu]DOTA-TATE for

gastroenteropancreatic tumors [20], different TRT have been developed for GBM cases like [^{177}Lu]Lu-DOTAGA-SP [23] or ^{177}Lu-NeoBOMB1 [24].

To enhance the multifunctional properties of ^{177}Lu, one approach involves integrating two lanthanides within a single molecular complex. This strategy could potentially leverage the unique advantages of each lanthanide, creating a system that improves both diagnostic accuracy and therapeutic efficacy. Among the various methods to combine lanthanides, which include diazotization [25], Ugi reaction [26, 27], or Cu(I)-catalyzed azide-alkyne cycloaddition [28], a novel approach has been developed. This method combines two lanthanide in a 1:1 ratio through a fast and uncatalyzed aqueous click reaction, based on the formation of a 2-thiazoline ring (Chapter 3). In the case of this research project, we reported a synthetic approach to bind D-VAP (^{D}S^{D}N^{D}T^{D}R^{D}V^{D}A^{D}P) and RI-VAP (^{D}P^{D}A^{D}V^{D}R^{D}T^{D}N^{D}S) peptides with a ^{177}Lu based homo-bismetallic complex as a potential TRT agent against glioblastomas. This is achieved by the formation of (6-hydroxyquinolin-2-yl)-4,5-dihydrothiazole (HQDT) from an azide-modified-*L*-lysine linked to *L*-cysteine with 2-cyano-6-hydroxyquinoline (CHQ) [29].

4.5. Results and Discussion

Optimization of *N*-(azido-lysyl)-*N′*-(DOTA-OtBu-phenyl) amide deprotecting group chemistry

To achieve the goal of this project, based on developing a synthetic approach of a potential theranostic contrast agent in the treatment of glioblastoma, the final bimetallic complex was separated into two synthons: a lysyl-DOTA component (Figure 4.1 & 4.2, **26**) and a 2-cyano-6-hydroxyquinoline-DOTA (CHQ DOTA) component, based on the previous chapter (Figure 4.3, **30**). Like our first generation bimetallic complexes, the one-way nature of the reaction, where a covalent bond forms exclusively between one lysyl and one quinolinyl component, allows for precise control over the resulting bislanthanide combination without the need of a metal catalyst.

The initial synthesis scheme, depicted in Figure 4.1, began with the conjugation of Fmoc-azido-lysine with Boc-phenylenediamine, resulting in *N*-Fmoc-azido-lysine-*N'*-Boc-phenylenediamine amide (**18**) with a 70 % yield after purification. A selective deprotection was successfully carried out on the doubly protected phenylenediamine compound (**18**), effectively removing the Boc group under acidic conditions. This allowed for an HBTU-driven amide coupling with DOTA-OtBu monoacetic acid, leading to the desired product, *N*-Fmoc-azido-lysine-(*N'*-DOTA-OtBu-phenylenediamine) amide (**19**), with a 35 % yield.

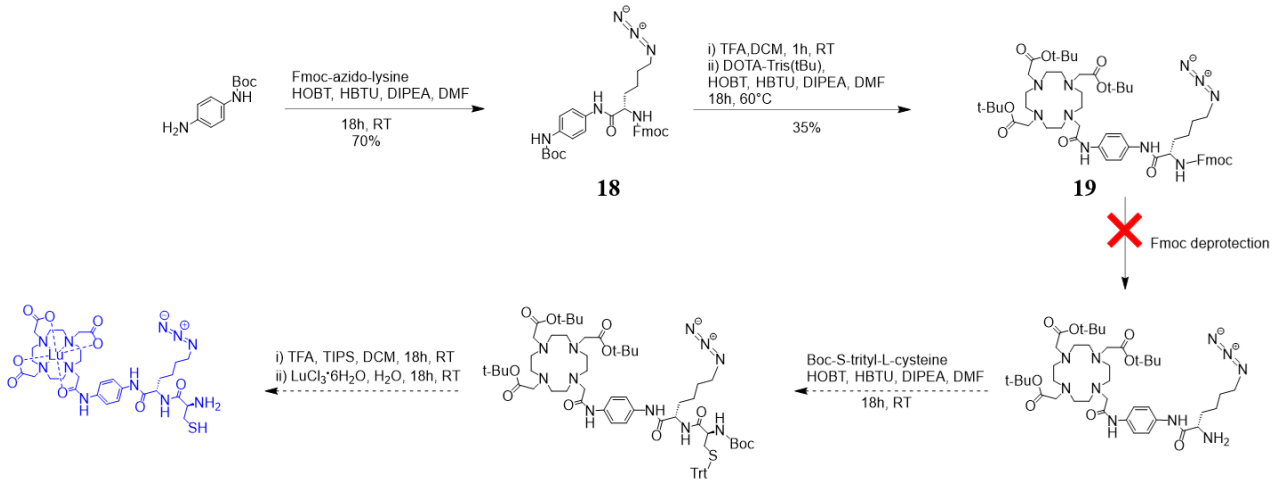

Figure 4.1 Initial synthetic scheme for Lu(III) lysine moiety complex using Boc-phenylenediamine as a precursor. *DIPEA: N,N'-diisopropylethylamine; HOBT: 1-hydroxybenzotriazole; HBTU: Hexafluorophosphate Benzotriazole Tetramethyl Uronium; DMF: N,N'-dimethylformamide; TFA: trifluoroacetic acid; DCM: dicholormethane; TIPS: triisopropylsilane; RT: room temperature.*

To obtain the final product, the lysyl-DOTA component, the next step involved Fmoc deprotection, which was necessary before performing the coupling reaction with Boc-S-trityl-L-cysteine. However, several methodologies were realized to achieve Fmoc deprotection, as presented in Table 4.1., but none were successful.

The presence of an acidic proton on the fluorenyl ring system can be extracted by a base, leading to the removal of the Fmoc group and the formation of carbon dioxide and dibenzofulvene intermediate. As a highly reactive electrophile, dibenzofulvene will react with primary or

secondary amines to prevent unwanted side reactions. Therefore, to scavenge the dibenzofulvene by-product and remove the Fmoc group, amine reagents are commonly used [30, 31].

To remove any traces of impurities, including the dibenzofulvene-amine adduct, each attempt was purified by flash column chromatography using an appropriate ratio of DCM to methanol. Known to work for the first-generation probe, the initial attempt was conducted with methylamine in tetrahydrofuran (THF) for 1 hour at room temperature. After purification, a yield of 33 % was obtained, which did not provide enough pure material to perform the next step, the coupling reaction with Boc-S-trityl-L-cysteine. Upon examining the ^{1}H NMR spectrum, residual traces of the Fmoc group were observed in the aromatic region, leading to the conclusion that this method was ineffective.

Following this, alternative conditions were investigated, including varying the reaction time, as well as exploring different solvents and secondary amines to enhance the deprotection efficiency. This is the case of diethylamine in dichloromethane (DCM), a polar solvent, as a potential solution. Experiments with varying reaction times to assess the impact on the deprotection process were conducted. This method was chosen to evaluate whether changes in solvent and reaction duration could improve the efficiency and purity of the desired product. The first attempt was realized with a 3-hour reaction time resulting in an 11 % yield, which was insufficient for the next synthesis step. Consequently, the reaction was repeated with a longer duration of 4 hours leading to no conversion. Another attempt with a 6-hour reaction time yielded 56 % providing enough product to proceed with the coupling reaction. However, after multiple purifications, the final product yield remained insufficient. Numerous side products, formed during Fmoc deprotection, were observed beyond the expected dibenzofulvene-amine adduct, unreacted starting material and the desired free amine product.

To optimize the reaction, a different approach was realized by changing the solvent, to see if it would enhance the reaction efficiency and yield. Due to the polar nature of dichloromethane, we switched to a more polar solvent, dimethylformamide (DMF), which is known to promote faster reactions [30]. Some studies have also shown that this type of reaction works better in a more polar, electron-donating solvent like DMF compared to a less polar solvent like DCM [32]. With the same secondary amine, diethylamine, the reaction was conducted from 1 hour to 18 hours and monitored by LC-MS to determine if the desired product had formed. According to the LC-MS results, the desired free amine mass (*m*/*z*), corresponding to azido-lysine-(*N'*-DOTA-OtBu-phenylenediamine) amide, was not observed. Instead, only the mass (*m*/*z*) of the starting material, *N*-Fmoc-azido-lysine-(*N'*-DOTA-OtBu-phenylenediamine) amide (**19**), was detected, indicating that the reaction did not proceed under those conditions.

Multiple reported methods have presented piperidine as one of the best methods to remove Fmoc protecting group [31, 32, 33]. Due to the nature of the amino acid used in this second-generation probe, Fmoc-azido-lysine, a new procedure with piperidine in the presence of ethyl acetate was tested according to a publish procedure [34]. The reaction was conducted for 3 hours at room temperature. Unfortunately, this new procedure was unsuccessful and failed to produce the desired product. Other studies reported that the best method involves using piperidine in the presence of DMF [35, 36], which is why this procedure was tested 1 hour and 2 hours at room temperature. Both methods resulted in the production of multiple spots on thin-layer chromatography (TLC), which were all isolated and analyzed by LC-MS. None of the spots matched the desired product mass (*m*/*z*).

In the effort to remove the Fmoc protecting group from *N*-Fmoc-azido-lysine-(*N'*-DOTA-OtBu-phenylenediamine) amide, various methods and procedures with different parameters were

explored. Despite multiple attempts, the deprotection remain unsuccessful, and there are several potentials reasons for this outcome. The reactions conditions, such as temperature or reaction time, might not have been optimal, or the base used might not have been strong enough for Fmoc removal. The choice of solvent might not have been suitable for solvating the reagents or stabilizing the intermediates formed during deprotection. Another alternative could have been tried using *N*-methyl-2-pyrrolidone, a different polar aprotic solvent [37]. The conditions used for Fmoc removal might have led to side reactions, such as decomposition or modification of other functional groups in the molecule. Without the right procedure, the reaction might not have gone to completion, or the intermediates might have been unstable. Indeed, the intermediates formed during the deprotection process might have been unstable under the reaction conditions, leading to degradation or rearrangement. Among these reasons, we believe that the primary factor for the inefficient Fmoc removal might be the presence of the DOTA moiety on the molecule. The presence of bulky groups, such as DOTA-OtBu, near the Fmoc protected amine could block the approach of the base or other reagents, making deprotection more difficult. Additionally, the DOTA moiety might be sensitive to pH changes occurring during Fmoc deprotection, potentially leading to unwanted reactions or degradation.

Table 4.1 Overview of experimental efforts to synthesize *N*-(azido-lysyl)-*N′*-(DOTA-OtBu-phenyl) amide. All reactions were performed at room temperature and followed by LC-MS. The asterisk (*) indicates the yield values achieved following purification, which included the presence of various side products.

Amine reagents	Solvent	Reaction time	Yield
Methylamine	THF	1 h	33 % *
Diethylamine	DCM	3 h	11 % *
Diethylamine	DCM	4 h	N/A
Diethylamine	DCM	6 h	56 % *
Diethylamine	DMF	1 h	N/A
Diethylamine	DMF	18 h	N/A
Piperidine	EtOAc	3 h	N/A
Piperidine	DMF	1 h	N/A
Piperidine	DMF	2 h	N/A

Design and synthesis of a novel molecular conjugate

Given our inability to identify an effective procedure for Fmoc removal on *N*-Fmoc-azido-lysine-(*N'*-DOTA-OtBu-phenylenediamine) amide, the entire synthetic scheme was revised. This decision was driven by the challenges encountered in achieving the desire deprotection without forming unwanted by-products or compromising yield. By redesigning the synthetic route, we aimed to improve the overall efficiency and purity of the same final product, Lu(III)-DOTA-lysine-cysteine complex (**26**) (Figure 4.2).

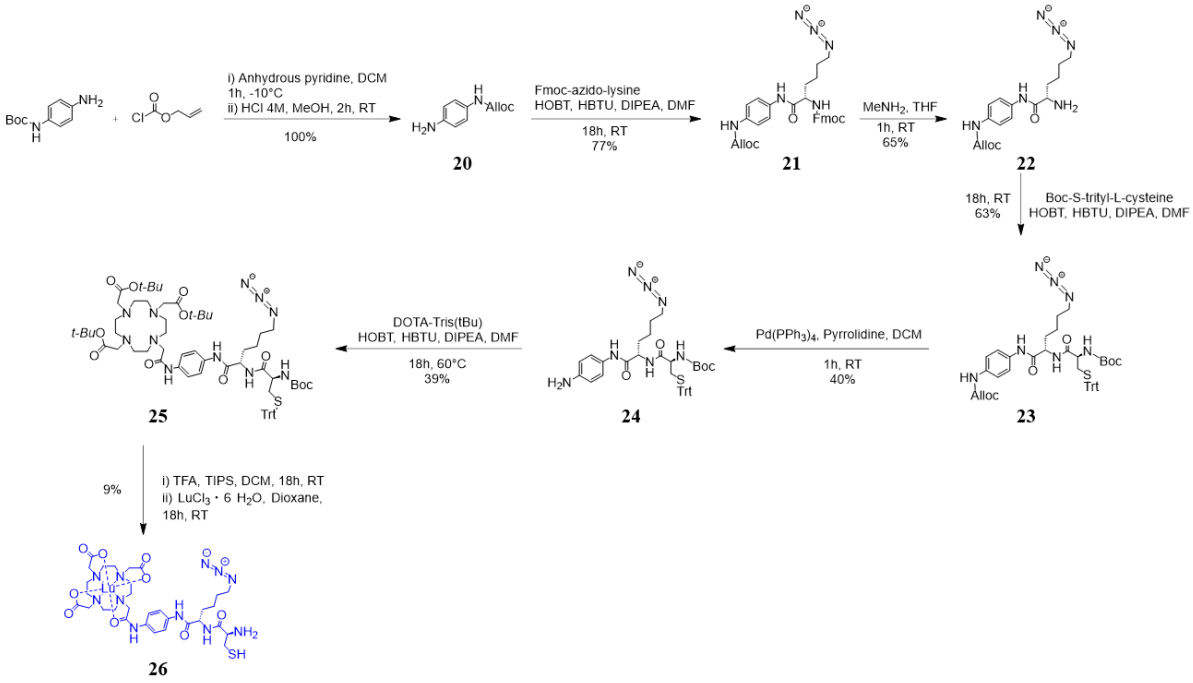

Figure 4.2 Chemical synthesis of Lu(III) lysine moiety complex. *DCM: dicholormethane; HCl: hydrochloric acid; MeOH: methanol; DIPEA: N,N'-diisopropylethylamine; HOBT: 1-hydroxybenzotriazole; HBTU: Hexafluorophosphate Benzotriazole Tetramethyl Uronium; DMF:*

N,N'-dimethylformamide; THF: tetrahydrofuran; $Pd(PPh_3)_4$: tetrakis(triphenylphosphine) palladium; TFA: trifluoroacetic acid; TIPS: triisopropylsilane; RT: room temperature.

Protection of the free amino group of Boc-*N*-phenylenediamine with Alloc, in order to generate allyl (4-aminophenyl) carbamate (**20**) after an orthogonal Boc deprotection, led to the synthesis of the first synthon, the lysyl-DOTA component. This was followed by conjugation to Fmoc-azido-lysine, resulting in *N*-Fmoc-azido-lysine-Alloc-phenylenediamine amide (**21**) with 77 % yield. Subsequent deprotection of Fmoc in presence of methylamine gave azido-lysine-Alloc-phenylenediamine amide (**22**). An HBTU-driven amide coupling with Boc-S-trityl-L-cysteine generated S-tert-butyl-cysteine-azido-lysine-(*N*-Alloc-phenylenediamine) amide (**23**) with a 63 % yield. The next step of the synthesis involved a palladium-catalyzed reaction to induce Alloc deprotection. After two purification steps, including HPLC, the desired product, S-tert-butyl-cysteine-azido-lysine-(phenylenediamine) amide (**24**) was isolated. This was followed by an HBTU-mediated coupling to DOTA-OtBu monoacetic acid, providing the fully protected S-tert-butyl-cysteine-azido-lysine-(*N'*-DOTA-OtBu-phenylenediamine) amide (**25**) with a 39 % yield. On the other hand, the CHQ-DOTA synthon was acquired according to the previous synthesis (Chapter 3) offering a fully protected quinolinyl-DOTA conjugate (**29**). Both the trityl-conjugated lysyl-DOTA (**25**) and CHQ-DOTA underwent complete deprotection and were subsequently reacted with the desired lutetium(III) chloride hexahydrate overnight. This process yielded the Lu(III)-loaded lysyl-DOTA (**26**) and CHQ DOTA synthons (**30**). Both, Lu(III)-DOTA-lysine-cysteine complex (**26**) and Lu(III)-CHQ-DOTA complex (**30**), were purified by HPLC and characterized by high resolution mass spectrometry (HRMS).

By demonstrating that the 4,5-dihydrothiazole linkage can be achieved through a catalyst-free aqueous click reaction with first-generation bimetallic complexes, the prepared lutetium(III)-loaded individual synthons were reacted together in PBS, resulting in homo-bislanthanide complex (**31**) (Figure 4.4).

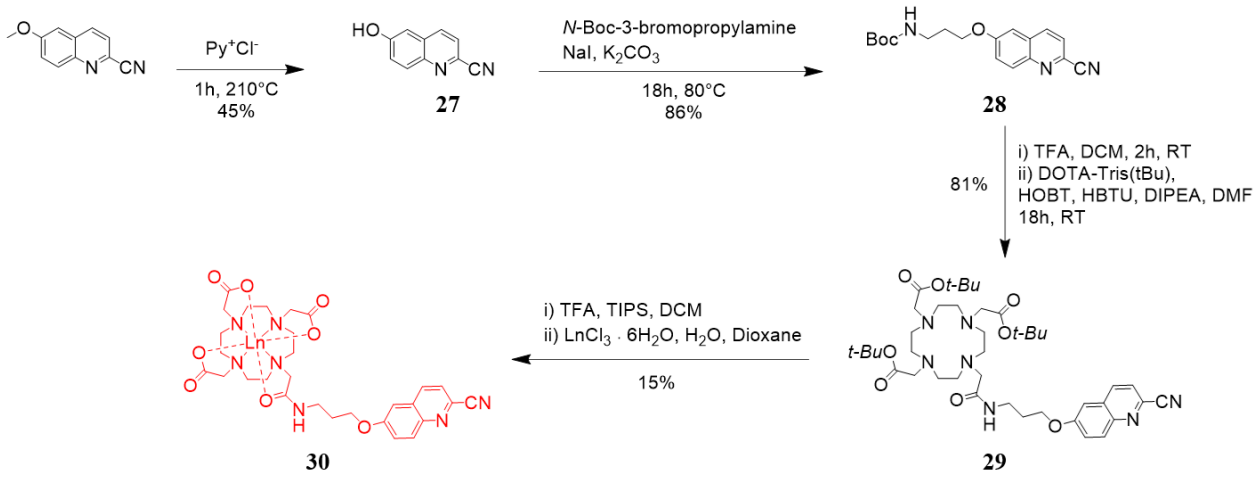

Figure 4.3 Chemical synthesis of Lu (III) quinoline moiety complex. *Py^+ Cl^-: pyridinium chloride; NaI: sodium iodide; K2CO3: potassium carbonate; DCM: dicholormethane; DIPEA: N,N'-diisopropylethylamine; TFA: trifluoroacetic acid; HOBT: 1-hydroxybenzotriazole; HBTU: Hexafluorophosphate Benzotriazole Tetramethyl Uronium; DMF: N,N'-dimethylformamide; TIPS: triisopropylsilane; RT: room temperature.*

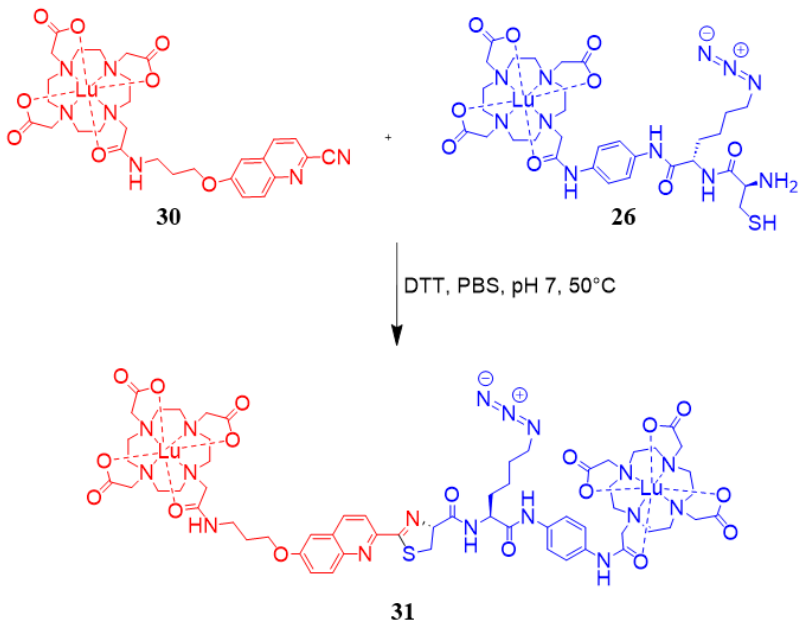

Figure 4.4 Fast and aqueous condensation of the lysyl-DOTA and quinolinyl-DOTA synthons to result in a 4,5-dihydrothiazole linkage. *DTT: dithiothreitol; PBS: phosphate buffer saline.*

Future application of the homo-bismetallic complex

After successfully synthesizing the targeted complexes, the next phase of the project involves investigating the chemical properties of the complex to understand their potential applications and interactions. Additionally, plans include evaluating the efficacy of the complex by testing them in glioblastoma cell lines. This approach will allow for an assessment of both the chemical and biological aspects of the synthesized complexes, contributing to the understanding of their potential therapeutic value against this form of brain cancer.

In order to combine our targeted peptides to GRP78, overexpressed and present on the cell surface of glioblastoma cells [17], on the homo-metallic complexes **31**, a linker between those two parts need to be synthesized (Figure 4.5). By performing a standard amide bond coupling reaction between *N*-aminoethylmaleimide and DBCO-acid, the DBCO-maleimide conjugate **32** will be obtained, resulting in a thiol-reactive maleimide group suitable for bioconjugation applications.

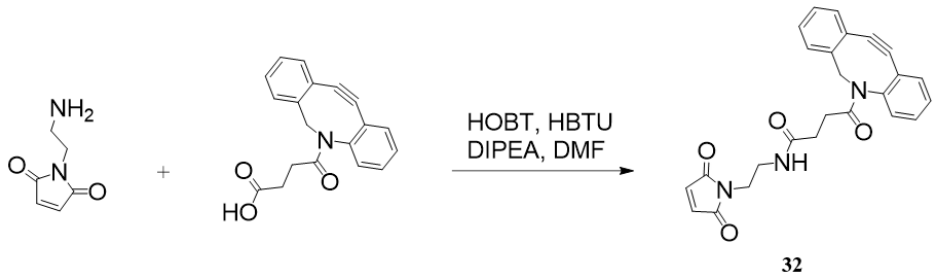

Figure 4.5 Chemical synthesis of DBCO-Maleimide conjugate. *HOBT: 1-hydroxybenzotriazole; HBTU: Hexafluorophosphate Benzotriazole Tetramethyl Uronium; DIPEA: N,N'-diisopropylethylamine; DMF: N,N'-dimethylformamide.*

On the other hand, the two peptides, D-VAP and RI-VAP, will be synthesized using a peptide synthesizer to achieve the desired sequences, each featuring a cysteine residue at the C-terminus. This cysteine will facilitate the attachment of the peptides to the resin, 2-chlorotrityl resin, ensuring efficient and stable linkage [10]. Additionally, the cysteine residue on both peptides will enable their coupling to the DBCO-maleimide conjugate **32** through the thiol-reactive maleimide group, facilitating a covalent sulfhydryl-maleimide conjugation [38], to form the final DBCO-maleimide conjugated D-VAP **33** and conjugated RI-VAP **34** (Figure 4.6).

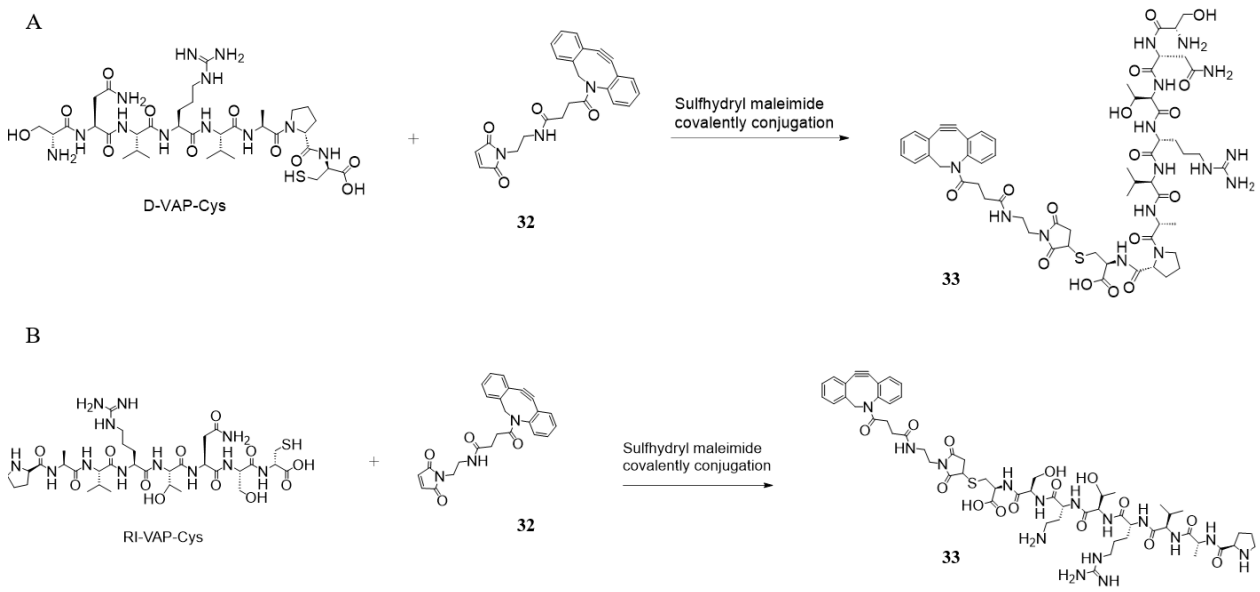

Figure 4.6 Chemical synthesis of peptide conjugates with DBCO-Maleimide. (A) Structure of D-VAP peptide with C-terminal cysteine, which reacts with the maleimide group on molecule **32** to form DBCO-Maleimide conjugated D-VAP **33**. (B) Structure of RI-VAP peptide with C-terminal cysteine, which reacts with the maleimide group on molecule **32** to form DBCO-Maleimide conjugated RI-VAP **33**.

Once the DBCO-maleimide conjugated D-VAP **33** and conjugated RI-VAP **34** are synthesized, they can both react with Lu(III)-DOTA-quinoline-lysine-DOTA-Lu(III) complex **31** to form the different complexes **35** and **36** (Figure 4.7). The lysyl-DOTA-component **26** of the homo-bismetallic complex presents an azide on the side chain of the lysine, allowing the complexation with an alkyne, here dibenzocyclooctyne (DBCO) maleimide, through a strain-promoted azide alkyne cycloaddition (SPAAC). As an alternative to copper(I)-catalysed alkyne-azide cycloaddition (CuAAC), which is limited by the toxicity of free copper ions in cellular assays and *in vivo* environments [39], SPAAC reactions are bioorthogonal. This means that they can proceed in living systems without interfering with native biological processes and without requiring a catalyst [40]. These properties makes SPAAC suitable for *in vivo* applications such as live-cell imaging and drug delivery [41]. Compared to the first generation of cyclooctynes, which have a reaction rate constant of $k = 0.12\ M^{-1}.s^{-1}$, the presence of an endocyclic sp^2 nitrogen in the DBCO ring structure enhances reactivity, resulting in improved kinetics with a rate constant of $k = 0.31\ M^{-1}.s^{-1}$ [42]. Due to its stability and versatility in functionalizing various molecules, such as biomolecules, polymer and nanoparticles [43], DBCO was selected for this project. Its properties make it ideal for conjugation with homo-bimetallic complexes to generate D-VAP and RI-VAP peptides conjugates for glioblastoma targeting.

Once the azide functionalized Lu(III)-DOTA-quinoline-cysteine-DOTA-Lu(III) DBCO-Maleimide-D-VAP conjugate **35** and RI-VAP conjugate **36** are obtained, the next step is to test these complexes in U87MG, glioblastoma cell lines, and HEK 293, serving as a negative control [10]. This will involve conducting a live/dead assay followed by flow cytometry analysis to assess the efficacy and cellular impact of the conjugates. Too evaluate their potential as therapeutic agents, the live/dead assay will determine the viability of glioblastoma cells after exposure to both

complexes, providing insights into their cytotoxic effects. This will also help identify the specificity and efficacy of the targeting strategy by analyzing whether the homo-bimetallic complexes can effectively target glioblastoma cells, particularly GRP78. Additionally, flow cytometry experiments will provides quantitative data on cell population, allowing for precise measurement of the proportion of live and dead cells [44].

After evaluating the Lu(III)-DOTA-quinoline-cysteine-DOTA-Lu(III) DBCO-Maleimide-D-VAP conjugate **35** and RI-VAP conjugate **36** complexes as cold standard on glioblastoma cell lines, the next step will be to test them as a hot standard using ^{177}Lu radioisotope. This involves assessing their potential as targeted radionuclide therapy agents by performing hot chemistry experiments and analyzing the results to determine their efficacy on U87MG cell lines as a potential treatment for glioblastoma.

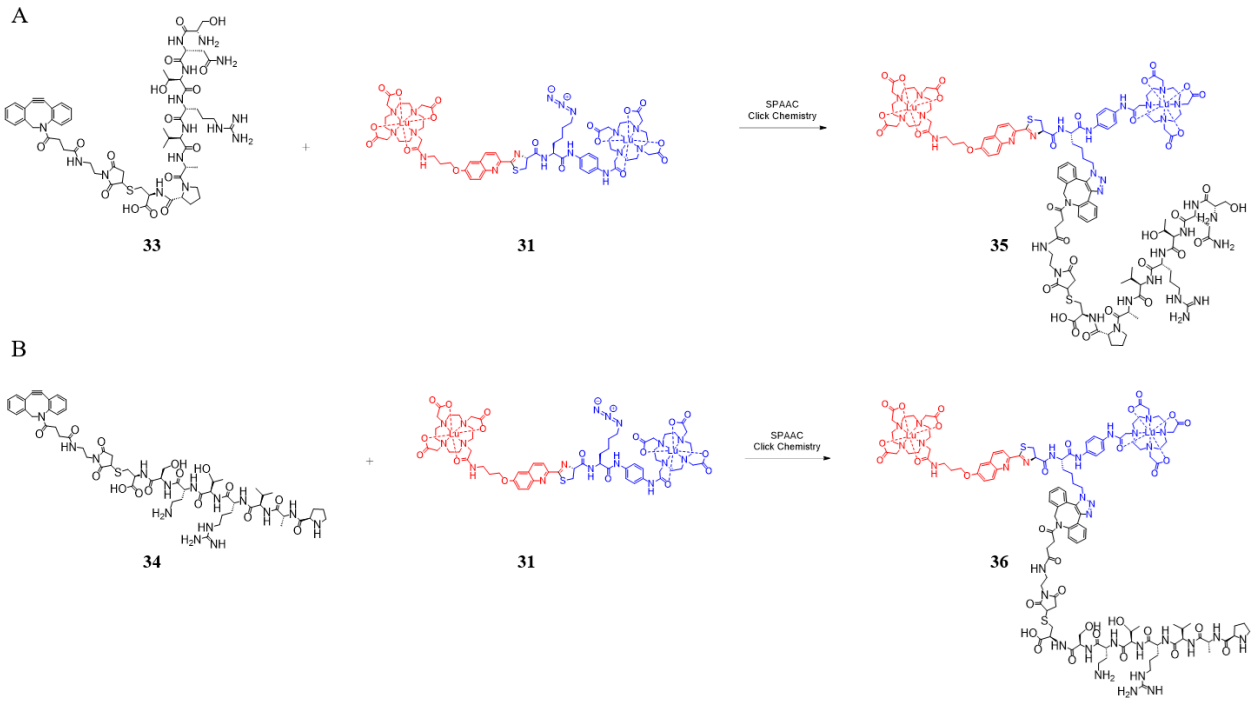

Figure 4.7 Chemical synthesis of peptide conjugates with homo-bismetallic complex. (A) Structure of DBCO-Maleimide conjugated D-VAP **33** which reacts with the azide group on the Lu(III)-DOTA-quinoline-lysine-DOTA-Lu(III) complex **31** to form, through a SPAAC chemistry, an azide functionalized Lu(III)-DOTA-quinoline-cysteine-DOTA-Lu(III) DBCO-Maleimide-D-VAP conjugate **35**. (B) Structure of DBCO-Maleimide conjugated RI-VAP **34** which reacts with the azide group on the Lu(III)-DOTA-quinoline-cysteine-DOTA-Lu(III) complex **31** to form, through a SPAAC chemistry, an azide functionalized Lu(III)-DOTA-quinoline-cysteine-DOTA-Lu(III) DBCO-Maleimide-RI-VAP conjugate **36**.

4.6. Conclusion

In this project, we present a second generation probe, Lu(III) DOTA-quinoline-lysine-DOTA-Lu(III) complex, that will be functionalized with DBCO-maleimide D-VAP and RI-VAP conjugates for targeted glioblastoma therapy. After multiple attempts to optimize or find an effective procedure to Fmoc deprotection in the presence of a DOTA component on the lysyl-DOTA, the synthetic scheme was redesigned. Based on the aqueous and uncatalyzed click reaction to form a 2-thiazoline ring between the lysyl-DOTA and quinolinyl-DOTA synthons, the functionalized azide-lysyl DOTA moiety will be attached to the DBCO-maleimide peptide conjugates through a strain-promoted azide-alkyne cycloaddition (SPAAC). While the evaluation of these complexes in glioblastoma cell lines is still ongoing at this stage of the project, the synthesis of these targeted probes has been successfully achieved up to the homo-bimetallic complexes. Incorporating the radioactive isotope ^{177}Lu into these complexes shows promise for targeted radionuclide therapy. Future testing will validate their efficacy and specificity in targeting glioblastoma cell, particularly U87MG cell line.

4.7. Conflicts of Interest

There are no conflicts to declare.

4.8. Supplementary Information

4.8.1. General Experimental Procedures

All reagents were either commercially obtained or synthesized following the procedures described below. Solvents used were HPLC grade, except for water (18.2 MΩ cm Millipore-grade). A rotary evaporator was used to remove any volatiles under reduced pressure. Thin-layer chromatography (TLC) was performed on aluminum-backed silica gel plates, with compounds visualization using 5 % ninhydrin stain and UV light. For nuclear magnetic resonance (NMR) spectroscopy, ^{1}H NMR spectra were recorded on 400 or 600 MHz spectrometers, with δ values of 2.50 ppm for DMSO-D_6 and 7.26 ppm for $CDCl_3$. For ^{13}C NMR, δ values were 39.50 ppm for DMSO-D_6 and 49.0 ppm for $CDCl_3$. High resolution mass spectrometry (HRMS) data were obtained were obtained using electrospray ionization (ESI). Preparation of the Lu(III)-DOTA-quinoline conjugate was realized according to the synthetic procedure developed in chapter 3.

4.8.2. Synthetic Procedure

Preparation of *N*-Fmoc-azido-lysine-*N'*-Boc-phenylenediamine amide (18)

A solution was prepared by dissolving Fmoc-azido-lysine (394.4 mg, 1 mmol) in dry DMF (2 mL) within a separate vial, along with DIPEA (522 µL, 3 mmol). The mixture was cooled to 0 °C using an ice bath. Subsequently, HOBt (40.5 mg, 0.3 mmol) and HBTU (379.24 mg, 1 mmol) were introduced. After stirring at 0 °C for 10 minutes, BOC-phenylenediamine (208.26 mg, 1 mmol) was added to the reaction. The cooling was then removed, and the reaction proceeded at room temperature for 18 hours. The resulting solution was extracted with brine (45 mL) and EtOAc (3 × 30 mL). The combined organic layers were washed with brine (3 × 45 mL), dried over Na_2SO_4, and concentrated under reduced pressure. The crude product was purified using flash column chromatography (FCC) on 50 g of silica gel with a hexane/acetone 2:1 eluent. Evaporation of the collected fractions yielded the *N*-Fmoc-azido-lysine-*N'*-Boc-phenylenediamine amide **18** as a light yellow solid, 483.2 mg, 83%. ^{1}H NMR (300 MHz, DMSO) δ 9.92 (s, 1H), 9.26 (s, 1H), 7.89 (d, *J* = 7.5 Hz, 2H), 7.74 (dd, *J* = 7.5, 3.9 Hz, 2H), 7.65 (d, *J* = 8.0 Hz, 1H), 7.52 – 7.27 (m, 8H), 4.31 – 4.18 (m, 3H), 4.12 (q, *J* = 8.3 Hz, 1H), 1.46 (s, 16H). ^{13}C NMR (100 MHz, DMSO) δ 170.57, 156.08, 152.81, 143.89, 143.79, 140.72, 135.06, 133.42, 127.64, 127.05, 125.33, 120.11, 119.70, 118.42, 78.85, 65.65, 55.11, 50.52, 46.67, 31.41, 28.15, 27.91, 22.84. HRMS (ESI) m/z found 607.2631 $[M + Na]^+$ (calcd 607.2645 for $C_{32}H_{36}N_6O_5Na$).

Reaction of *N*-Fmoc-azido-lysine-*N'*-Boc-phenylenediamine amide with DOTA-OtBu monoacetic acid

TFA (800 µL) was introduced to a stirred suspension of *N*-Fmoc-azido-lysine-*N'*-Boc-phenylenediamine amide (477.6 mg, 0.8 mmol) in CH_2Cl_2 (2.7 mL), and the mixture was stirred for 1 hour at room temperature. After complete evaporation, excess TFA was removed by co-evaporation with CH_2Cl_2 (3 × 60 mL) and afforded the BOC deprotected compound. In a separate vial, DIPEA (279 µL, 1.6 mmol) was added to a solution of DOTA-OtBu monoacetic acid (458.2 mg, 0.8 mmol) in dry DMF (2 mL). The mixture was cooled to 0 °C on ice, followed by the addition of HOBt (35.1 mg, 0.26 mmol) and HBTU (303.4 mg, 0.8 mmol). After stirring for 10 minutes at 0 °C, *N*-Fmoc-azido-lysine-phenylenediamine (477.6 mg, 0.8 mmol) was added. The cooling bath was removed, and the mixture was stirred for 18 hours at 60 °C. The solution was then partitioned between brine (60 mL) and EtOAc (3 × 35 mL). The combined organic extracts were washed with brine (3 × 60 mL), dried over Na_2SO_4, and concentrated. The residue was purified by flash column chromatography on 50 g of silica gel using hexane/acetone (1:1) as the eluent. Evaporation of the eluate yielded the fully protected DOTA lysine conjugate **19** as a light yellow solid, 217.4 mg, 26 %. ^{1}H NMR (400 MHz, DMSO) δ 10.05 (s, 1H), 9.99 (s, 1H), 7.89 (d, *J* = 7.7 Hz, 2H), 7.73 (t, *J* = 6.4 Hz, 2H), 7.67 (d, *J* = 7.7 Hz, 1H), 7.49 (s, 4H), 7.41 (td, *J* = 7.5, 4.4 Hz, 2H), 7.32 (td, *J* = 7.4, 4.5 Hz, 2H), 4.24 (dq, *J* = 13.3, 7.1 Hz, 3H), 4.17 – 4.05 (m, 1H), 3.24 – 1.94 (m, 32H), 1.75 – 1.27 (m, 37H). ^{13}C NMR (100 MHz, DMSO) δ 174.65, 172.65, 172.58, 170.74, 164.62, 156.12, 143.86, 143.79, 140.73, 134.57, 134.23, 129.28, 127.66, 127.63, 127.06, 125.34, 124.19, 121.11, 120.94, 120.12, 119.77, 119.58, 119.20, 113.79, 113.53, 104.51, 81.33, 81.23, 81.15, 81.13, 81.09, 73.96, 68.53, 65.67, 60.77, 59.77, 56.27, 55.83, 55.62, 55.30,

55.23, 55.19, 55.04, 54.69, 50.54, 46.68, 38.26, 29.61, 27.91, 27.61, 27.53, 24.92, 14.10. HRMS (ESI) m/z found 1039.6021 $[M + H]^+$ (calcd 1039.5981 for $C_{55}H_{79}N_{10}O_{10}$).

Preparation of allyl (4-aminophenyl) carbamate (20)

Synthesis of allyl (4-aminophenyl) carbamate was realized according to the publish patent [45], affording a pink solid, 330 mg, 100%. ^{1}H NMR (400 MHz, DMSO) δ 9.85 (s, 1H), 9.61 (s, 2H), 7.49 (d, *J* = 8.3 Hz, 2H), 7.19 (d, *J* = 6.7 Hz, 2H), 5.97 (ddt, *J* = 17.2, 10.7, 5.4 Hz, 1H), 5.35 (dq, *J* = 17.2, 1.7 Hz, 1H), 5.23 (dq, *J* = 10.4, 1.4 Hz, 1H), 4.60 (dt, *J* = 5.5, 1.5 Hz, 2H). ^{13}C NMR (100 MHz, DMSO) δ 153.24, 138.78, 133.19, 133.03, 126.14, 123.63, 120.49, 119.05, 117.69, 72.17, 70.54, 70.48, 66.37, 64.80, 60.19, 43.65.

Preparation of *N*-Fmoc-azido-lysine-Alloc-phenylenediamine amide (21)

A solution of Fmoc-azido-lysine (500 mg, 1.27 mmol) was prepared in a separate vial with dry DMF (3 mL) and DIPEA (662 μL, 3.8 mmol). The reaction mixture was cooled on ice at 0 °C, after which HOBt (51.4 mg, 0.38 mmol) and HBTU (481 mg, 1.27 mmol) were added. The mixture was stirred at 0°C for 10 minutes before the addition of allyl (4-aminophenyl) carbamate (244 mg, 1.27 mmol) to the reaction. After removal of the cooling bath, the reaction was stirred 18 hours at room temperature. The solution was then extracted with brine (45 mL) and EtOAc (3 × 30 mL). The organic layers were combined, washed with brine (3 × 45 mL), dried with Na_2SO_4 and concentrated under reduced pressure. The crude product was purified by FCC on 50 g of silica gel using hexane/acetone (1:1). Evaporation of the collected fractions afforded the *N*-Fmoc-azido-lysine-Alloc-phenylenediamine amide **21**, light yellow solid, 559.2 mg, 77%. ^{1}H NMR (600 MHz,

DMSO) δ 9.94 (s, 1H), 9.63 (s, 1H), 7.89 (d, *J* = 7.6 Hz, 2H), 7.74 (t, *J* = 7.6 Hz, 2H), 7.64 (d, *J* = 8.1 Hz, 1H), 7.50 (d, *J* = 8.5 Hz, 2H), 7.44 – 7.35 (m, 5H), 7.32 (q, *J* = 7.0 Hz, 3H), 5.97 (ddt, *J* = 16.2, 10.6, 5.4 Hz, 1H), 5.35 (dd, *J* = 17.2, 2.2 Hz, 1H), 5.23 (dd, *J* = 10.5, 1.9 Hz, 1H), 4.59 (d, *J* = 5.4 Hz, 2H), 4.34 – 4.08 (m, 5H), 2.69 (s, 2H), 1.75 – 1.30 (m, 8H). ^{13}C NMR (100 MHz, DMSO) δ 170.63, 156.08, 153.24, 143.89, 143.79, 140.72, 140.71, 134.56, 133.81, 133.38, 127.64, 127.05, 125.33, 120.12, 120.10, 119.78, 118.56, 117.51, 104.58, 65.64, 64.56, 55.11, 50.51, 46.67, 40.06, 31.39, 27.90, 22.83. HRMS (ESI) m/z found 591.2352 $[M + Na]^+$ (calcd 591.2332 for $C_{31}H_{32}N_6O_5Na$).

Preparation of azido-lysine-Alloc-phenylenediamine amide (22)

A solution of methylamine in THF (9 mL, 2 M) was combined with *N*-Fmoc-azido-lysine-Alloc-phenylenediamine amide (513.5 mg, 0.90 mmol) and stirred at room temperature for 1 hour. After a complete evaporation of the solvent, the crude product was purified by FCC on 40 g of silica with CH_2Cl_2/MeOH (95:5). Evaporation of the collected fractions afforded azido-lysine-Alloc-phenylenediamine amide **22**, light yellow solid, 202.61 mg, 65%. ^{1}H NMR (600 MHz, DMSO) δ 9.62 (s, 1H), 7.55 – 7.47 (m, 2H), 7.37 (d, *J* = 8.5 Hz, 2H), 5.97 (ddt, *J* = 17.3, 10.7, 5.4 Hz, 1H), 5.35 (dq, *J* = 17.2, 1.7 Hz, 1H), 5.23 (dq, *J* = 10.5, 1.5 Hz, 1H), 4.59 (dt, *J* = 5.4, 1.5 Hz, 2H), 3.26 (dd, *J* = 7.4, 5.4 Hz, 2H), 1.68 – 1.30 (m, 8H). ^{13}C NMR (100 MHz, DMSO) δ 173.95, 153.26, 134.44, 133.82, 133.39, 119.71, 118.58, 117.51, 104.54, 64.56, 55.25, 50.62, 40.06, 34.55, 28.21, 22.67. HRMS (ESI) m/z found 369.1664 $[M + Na]^+$ (calcd 369.1651 for $C_{16}H_{22}N_6O_3Na$).

Preparation of S-tert-butyl-cysteine-azido-lysine-(*N*-Alloc-phenylenediamine) amide (23)

A solution of Boc-S-Trityl-L-cysteine (267.7 mg, 0.58 mmol) was prepared in a separate vial with dry DMF (2 mL) and DIPEA (301 µL, 1.73 mmol). The reaction mixture was cooled on ice at 0 °C, after which HOBt (23.4 mg, 0.17 mmol) and HBTU (219 mg, 0.58 mmol) were added. The mixture was stirred at 0°C for 10 minutes before the addition of azido-lysine-Alloc-phenylenediamine amide (200 mg, 0.58 mmol) to the reaction. After removal of the cooling bath, the reaction was stirred 18 hours at room temperature. The solution was then extracted with brine (40 mL) and EtOAc (3 × 25 mL). The organic layers were combined, washed with brine (3 × 40 mL), dried with Na_2SO_4 and concentrated under reduced pressure. The crude product was purified by FCC on 30 g of silica gel using hexane/acetone (2:1). Evaporation of the collected fractions afforded the S-tert-butyl-cysteine-azido-lysine-(*N*-Alloc-phenylenediamine) amide **23**, white solid, 288.1 mg, 63%. ^{1}H NMR (400 MHz, DMSO) δ 9.89 (s, 1H), 9.65 (s, 1H), 7.80 (d, *J* = 8.1 Hz, 1H), 7.45 (d, *J* = 8.5 Hz, 2H), 7.39 – 7.20 (m, 20H), 7.07 (d, *J* = 8.2 Hz, 1H), 5.97 (td, *J* = 10.9, 5.3 Hz, 1H), 5.35 (d, *J* = 17.2 Hz, 1H), 5.23 (d, *J* = 10.5 Hz, 1H), 4.59 (d, *J* = 5.5 Hz, 2H), 4.36 (s, 1H), 3.93 (d, *J* = 7.2 Hz, 1H), 3.24 (t, *J* = 7.0 Hz, 2H), 2.35 (t, *J* = 7.5 Hz, 2H), 1.75 – 1.42 (m, 5H), 1.38 (s, 13H). ^{13}C NMR (151 MHz, DMSO) δ 169.92, 169.61, 154.99, 153.23, 144.26, 134.75, 133.48, 133.37, 129.06, 128.03, 126.78, 126.74, 119.93, 117.52, 104.55, 78.58, 65.87, 64.57, 53.57, 52.77, 50.48, 40.06, 33.61, 31.78, 30.96, 28.10, 27.80, 22.24, 13.97. HRMS (ESI) m/z found 814.3383 $[M + Na]^+$ (calcd 814.3363 for $C_{43}H_{49}N_7O_6SNa$).

Preparation of S-tert-butyl-cysteine-azido-lysine-(phenylenediamine) amide (24)

The S-tert-butyl-cysteine-azido-lysine-(*N*-Alloc-phenylenediamine) amide (258.8 mg, 0.33 mmol) was dissolved in dichloromethane (3.5 mL) followed by the addition of palladium-tetrakis(triphenylphosphine) (19.6 mg, 0.017 mmol) and pyrrolidine (65 µL, 0.79 mmol). The reaction mixture was stirred for 1 hour at room temperature under an inert atmosphere. After a complete evaporation of the solvent, the crude product was subjected to FCC on 30 g of silica with CH_2Cl_2/MeOH (95:5) to remove traces of palladium. A second purification was carried out using preparative HPLC. The fraction containing the final product (t_R 13 – 15min) was collected, concentrated and lyophilized to provide S-tert-butyl-cysteine-azido-lysine-(phenylenediamine) amide **24**, light yellow solid, 92.5 mg, 40%. ^{1}H NMR (600 MHz, DMSO) δ 9.89 (s, 1H), 7.80 (d, J = 8.2 Hz, 1H), 7.45 (d, J = 8.5 Hz, 2H), 7.30 (p, J = 8.0 Hz, 14H), 7.25 – 7.21 (m, 3H), 7.05 (d, J = 8.3 Hz, 1H), 6.93 (d, J = 8.3 Hz, 2H), 4.36 (td, J = 8.4, 5.2 Hz, 1H), 3.93 (td, J = 8.1, 5.6 Hz, 1H), 3.24 (t, J = 6.9 Hz, 3H), 2.36 (qd, J = 11.9, 6.9 Hz, 2H), 1.68 (ddt, J = 13.5, 9.8, 5.9 Hz, 1H), 1.58 (dtd, J = 13.7, 9.2, 4.9 Hz, 1H), 1.54 – 1.45 (m, 2H), 1.38 (s, 8H), 1.35 – 1.21 (m, 5H). ^{13}C NMR (100 MHz, DMSO) δ 169.95, 169.69, 157.99, 157.78, 155.00, 144.26, 129.07, 128.04, 126.75, 120.64, 78.59, 65.88, 53.56, 52.82, 50.49, 40.06, 33.60, 31.73, 28.10, 27.80, 22.25. HRMS (ESI) m/z found 730.3173 $[M + Na]^+$ (calcd 730.3151 for $C_{39}H_{45}N_7O_4SNa$).

Reaction of S-tert-butyl-cysteine-azido-lysine-(phenylenediamine)amide (24) with DOTA-OtBu monoacetic acid

A solution of DOTA-OtBu monoacetic acid (217 mg, 0.38 mmol) was prepared in a separate vial with dry DMF (3 mL) and DIPEA (103 µL, 0.63 mmol). The reaction mixture was cooled on ice at 0 °C, after which HOBt (12.8 mg, 0.09 mmol) and HBTU (120 mg, 0.32 mmol) were added. The mixture was stirred at 0°C for 10 minutes before the addition of S-tert-butyl-cysteine-azido-lysine-(phenylenediamine) amide (224 mg, 0.32 mmol) to the reaction. After removal of the cooling bath, the reaction was stirred 18 hours at 60 °C. The solution was then extracted with brine (45 mL) and EtOAc (3 × 30 mL). The organic layers were combined, washed with brine (3 × 45 mL), dried with Na_2SO_4 and concentrated under reduced pressure. The crude product was purified by FCC on 30 g of silica gel using hexane/acetone (1:1). Evaporation of the collected fractions afforded the S-tert-butyl-cysteine-azido-lysine-(N'-DOTA-OtBu-phenylenediamine) amide **25**, white solid, 158 mg, 39%. ^{1}H NMR (400 MHz, DMSO) δ 10.05 (s, 1H), 9.92 (s, 1H), 7.82 (d, *J* = 8.2 Hz, 1H), 7.52 – 7.43 (m, 4H), 7.37 – 7.18 (m, 17H), 7.07 (d, *J* = 8.2 Hz, 1H), 4.36 (s, 1H), 3.92 (q, *J* = 7.5 Hz, 1H), 3.55 – 1.90 (m, 86H), 1.74 – 1.20 (m, 48H). 13C NMR (100 MHz, DMSO) δ 172.56, 170.37, 169.95, 169.68, 164.59, 162.31, 155.01, 144.25, 134.38, 134.26, 129.06, 128.01, 126.72, 119.72, 119.31, 104.47, 81.13, 81.09, 78.57, 65.87, 56.28, 55.83, 55.61, 55.30, 55.23, 55.04, 53.64, 52.80, 50.49, 38.25, 35.78, 31.70, 30.77, 29.60, 28.09, 27.79, 27.61, 27.55, 27.53, 22.27. HRMS (ESI) m/z found 1262.6974 $[M + H]^+$ (calcd 1262.7012 for $C_{67}H_{96}N_{11}O_{11}S$).

Preparation of Lu(III)-DOTA conjugate TFA salt (26)

The tritylated DOTA conjugate (140 mg, 0.11 mmol) was dissolved in CH_2Cl_2 (2 mL) and TFA (1.2 mL) was added with TIPS (103 μL) to the mixture which was stirred for 18 hours at room temperature. The volatile is then evaporated with DCM (3 × 30 mL) and the residue triturated with hexane (3 × 10 mL, each time sonicated for 10 minutes) followed by drying in vacuum. The obtained solution of DOTA conjugate TFA salts (60 mg, 0.08 mmol) was combined in water (2.5 mL) with $LuCl_3$ – 6 H_2O (31.2 mg, 0.08 mmol). The pH was adjusted and maintained between 6 and 7 using a 1 M NaOH solution, and the mixture was stirred at room temperature for 18 hours. The reaction mixture was transferred to a Falcon tube, diluted with water (20 mL), and centrifuged three times (3 minutes at 3000 rpm each). The supernatant was purified using preparative HPLC, and the fraction containing the product (t_R = 15.53 – 16.56 minutes) was concentrated and lyophilized to provide the Lu(III)-DOTA-lysine-cysteine complex **26**, colorless solid, 6.8 mg, 9%. HRMS (ESI) m/z found 923.2626 $[M + H]^+$ (calcd 923.2608 for $C_{31}H_{46}LuN_{11}O_9S$).

Preparation of the homo-bislanthanide complex

A solution of Lu(III)-DOTA-lysine conjugate (6 mg, 6.5 × 10^{-3} mmol) in PBS (1.5 mL) was combined with Lu(III)-DOTA-quinoline conjugate (4.6 mg, 5.8× 10^{-3} mmol) and stirred. DTT (100.2 mg, 0.65 mmol) was then added to the mixture. The pH of the reaction was maintained at pH ~ 6-7 using 1 M NaOH, and the mixture was stirred 40 minutes at 50 °C. The reaction mixture was transferred to Falcon tubes, diluted with water (15 mL), and purified using preparative HPLC. The fraction containing the product (t_R = 18.31 – 19.35 minutes) was concentrated and lyophilized

to afford quinoline-decorated Lu(III)-DOTA-quinoline-lysine-DOTA-Lu(III) complex **31** as a white solid, 4 mg, 38 %.

HPLC analysis

Both lutetium (III) synthons and the homo-bislanthanide complex were purified through an HPLC system (Shimadzu) by dissolving them in water to obtain a 5 mg/mL concentration. The separation process was conducted on a polar C18 Phenomenex Luna column (250 × 4.6 mm, particle size 5 μm, pore size 100 Å). The mobile phase is composed of water with 0.1 % TFA (mobile phase A) and acetonitrile with 0.1 % TFA (mobile phase B). The elution followed a linear gradient, increasing from 0 % to 92 % B over 23 minutes, then reducing to 1 % B from 23.01 to 24.01 minutes, followed by a 6-minute equilibration period for the column. Chromatograms were monitored at 254 nm, with a flow rate of 10 mL/min and a temperature maintained at 25 °C.

4.8.3. NMR Spectral Characterization

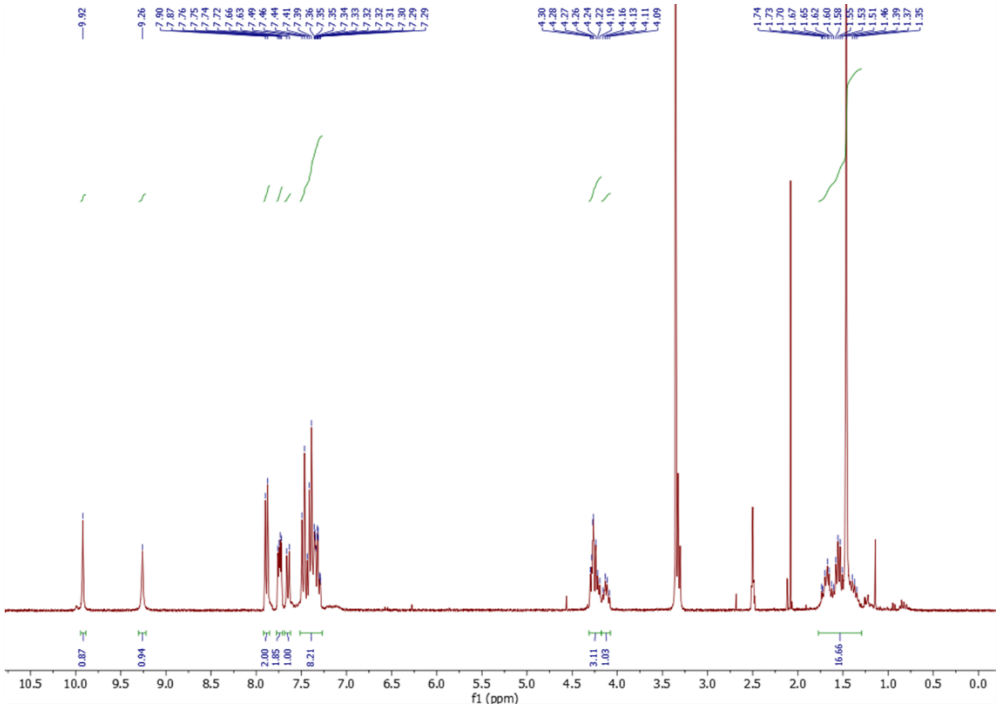

S76. ^{1}H NMR spectrum of compound 18 in DMSO-D_6. The signal at δ 2.09 ppm is due to the presence of acetone in the sample.

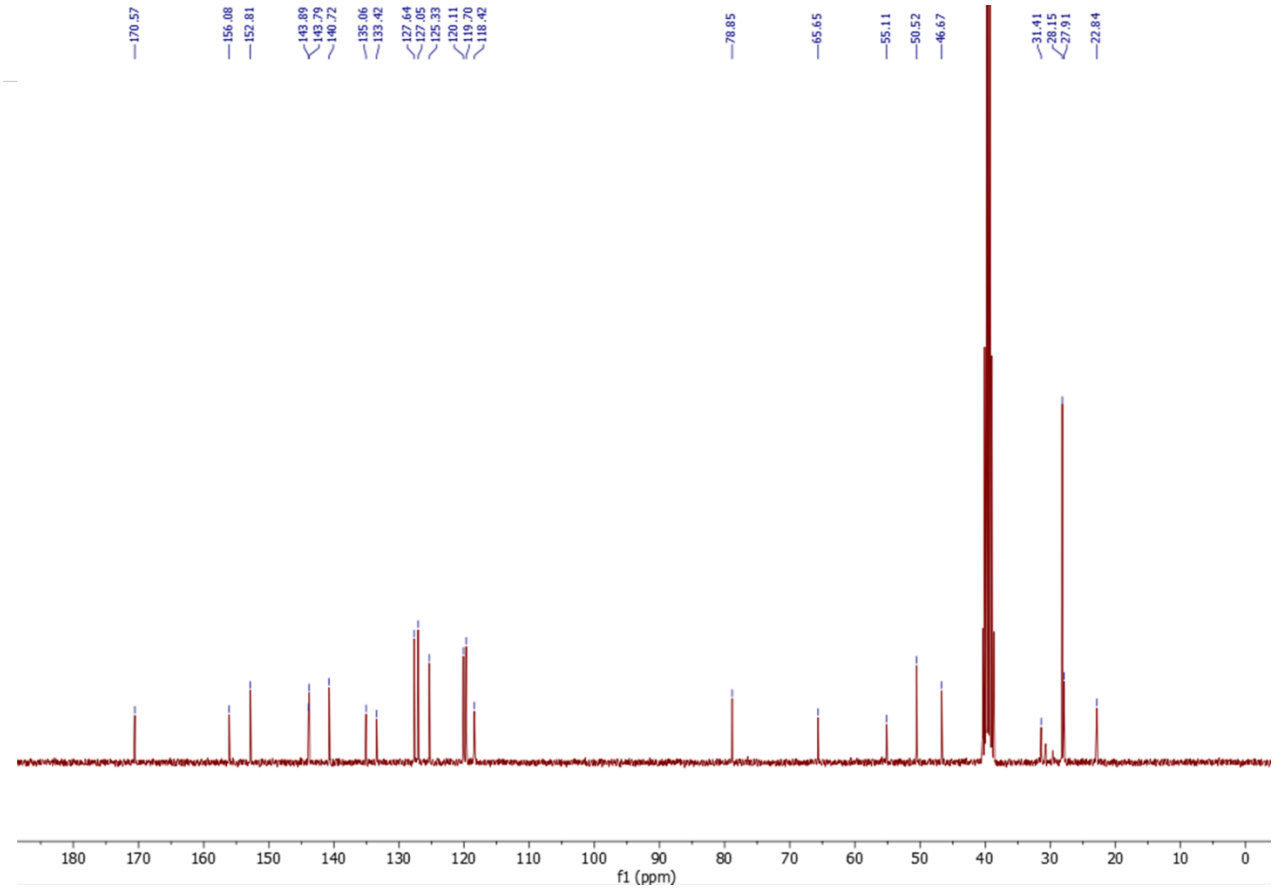

S77. ^{13}C NMR spectrum of compound 18 in DMSO-D_6.

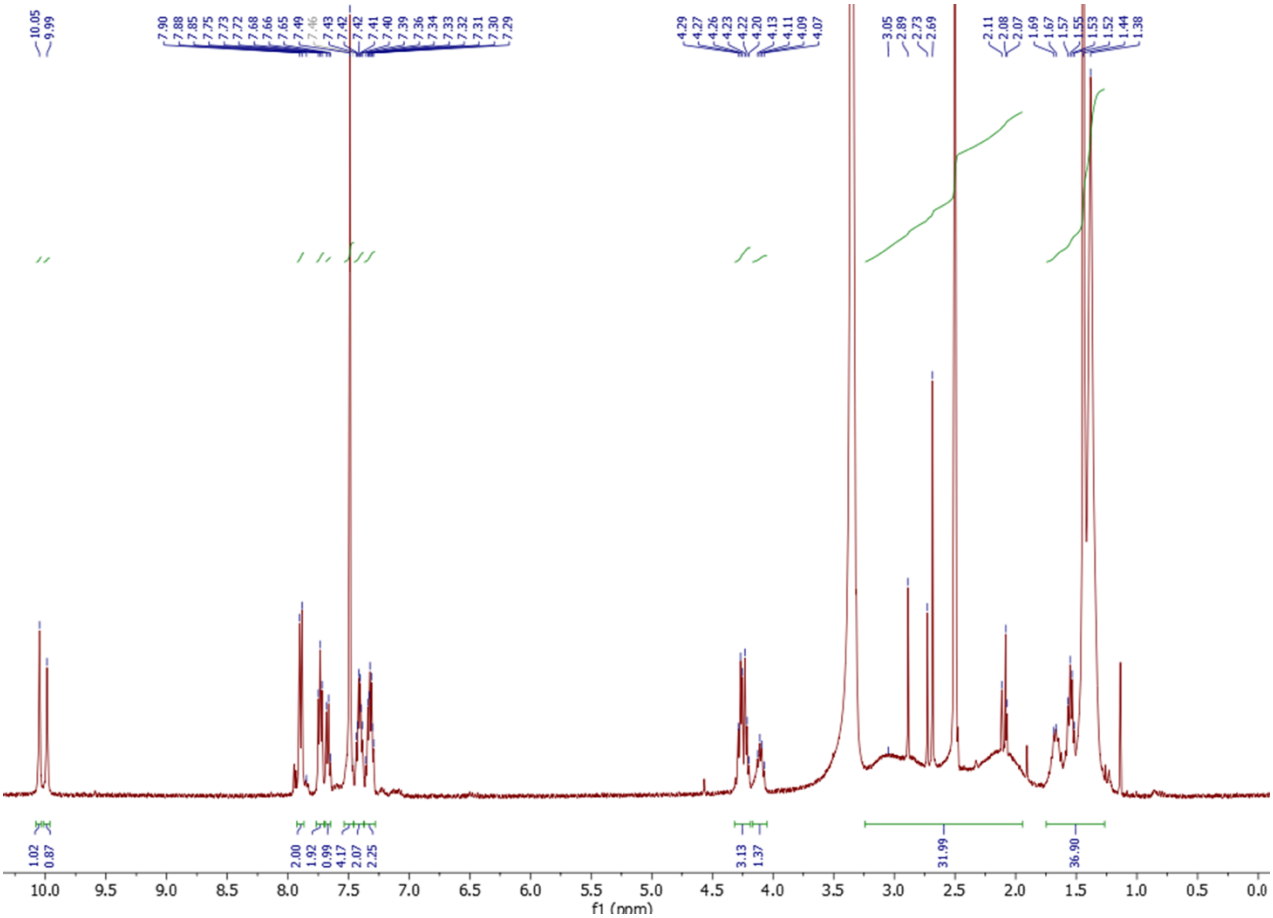

S78. ^{1}H NMR spectrum of compound 19 in DMSO-D_6.

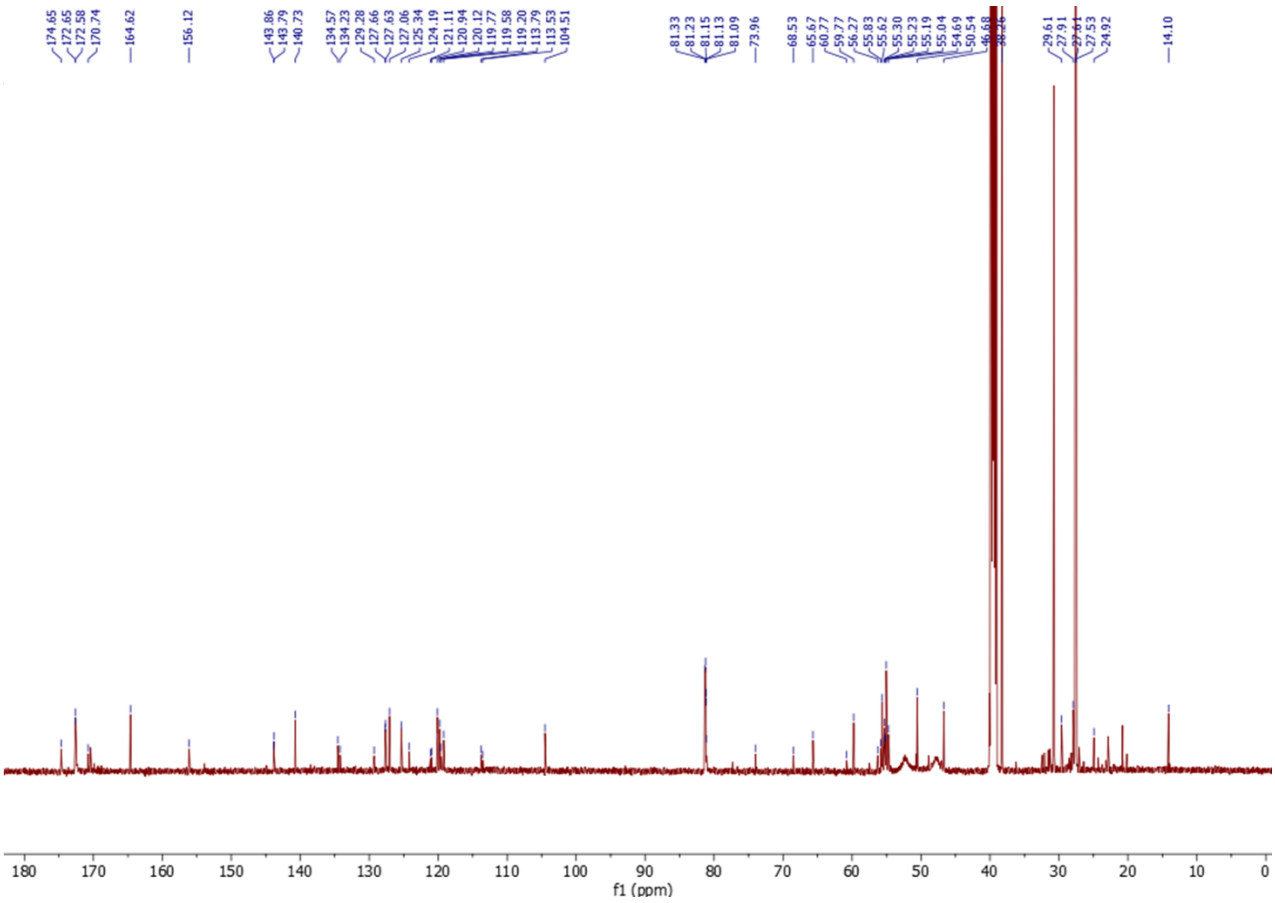

S79. ^{13}C NMR spectrum of compound 19 in DMSO-D_6. Presence of multiple peaks indicated an impure compound.

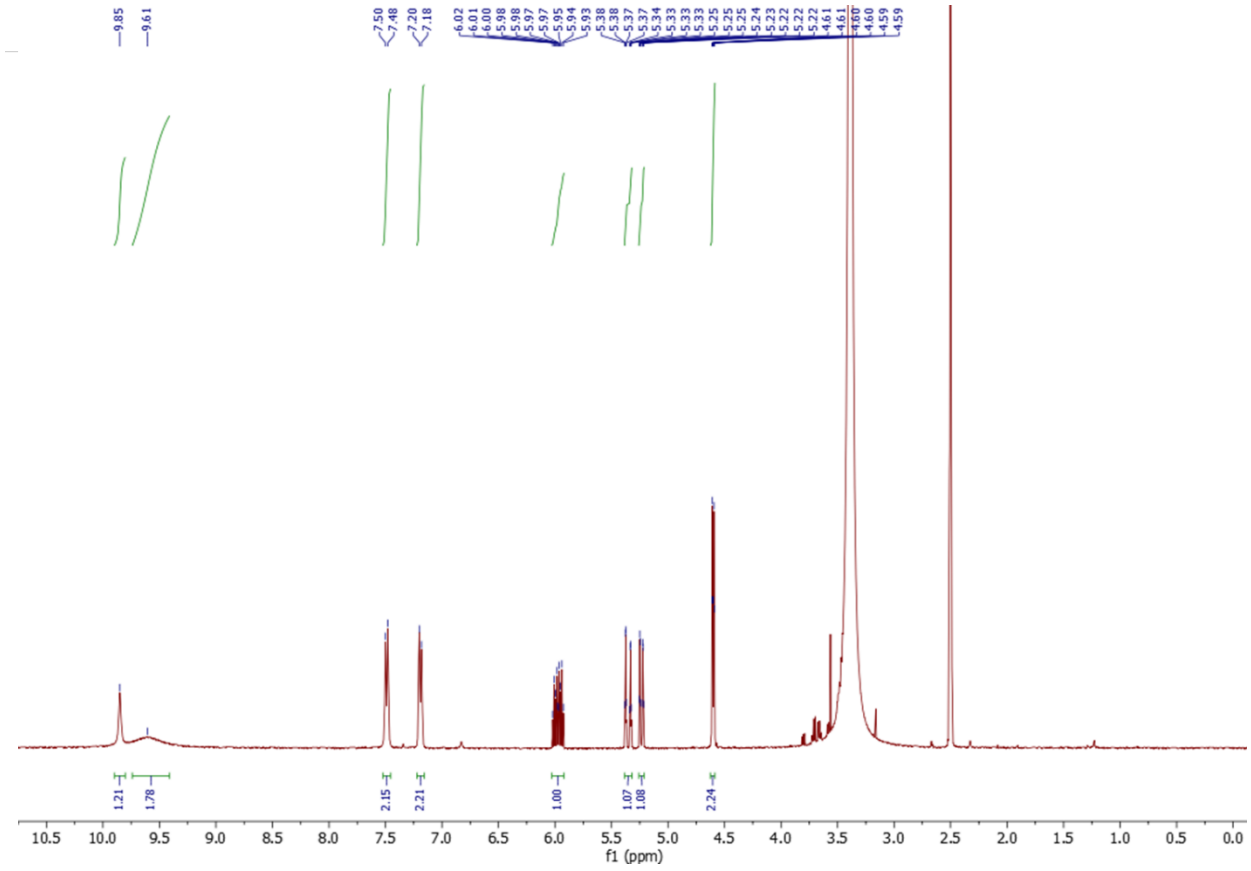

S80. ^{1}H NMR spectrum of compound 20 in DMSO-D_6.

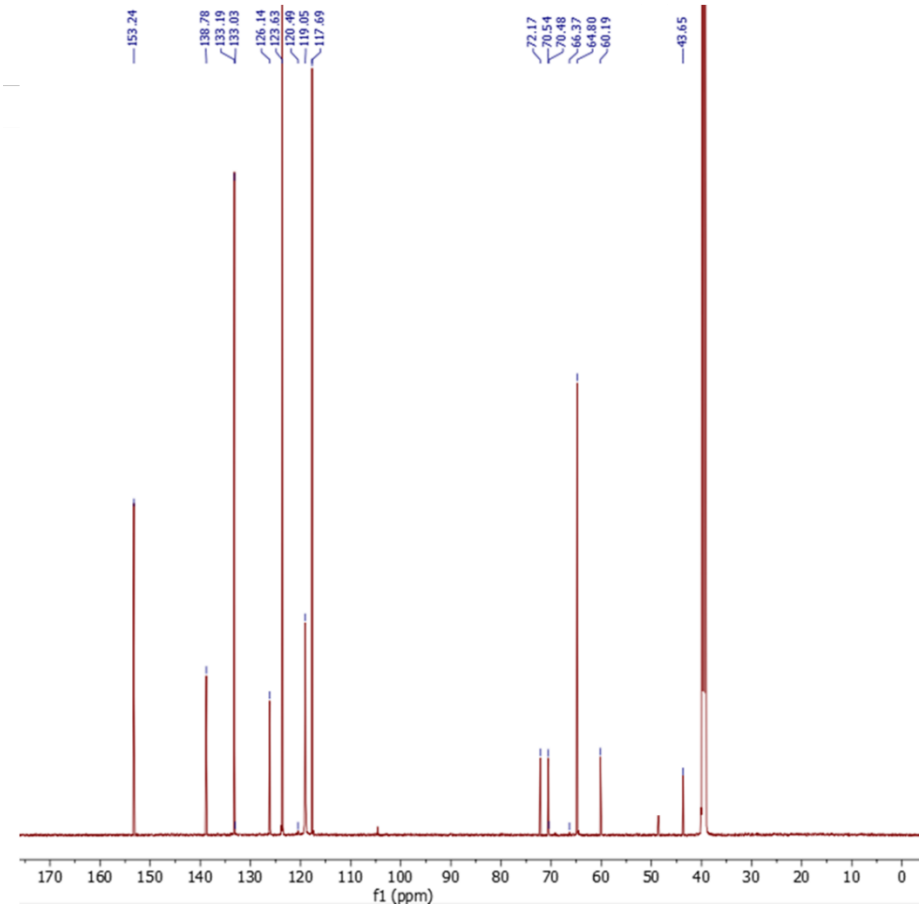

S81. ^{13}C NMR spectrum of compound 20 in DMSO-D_6. The signal at δ 48.59 ppm is due to the presence of methanol in the sample.

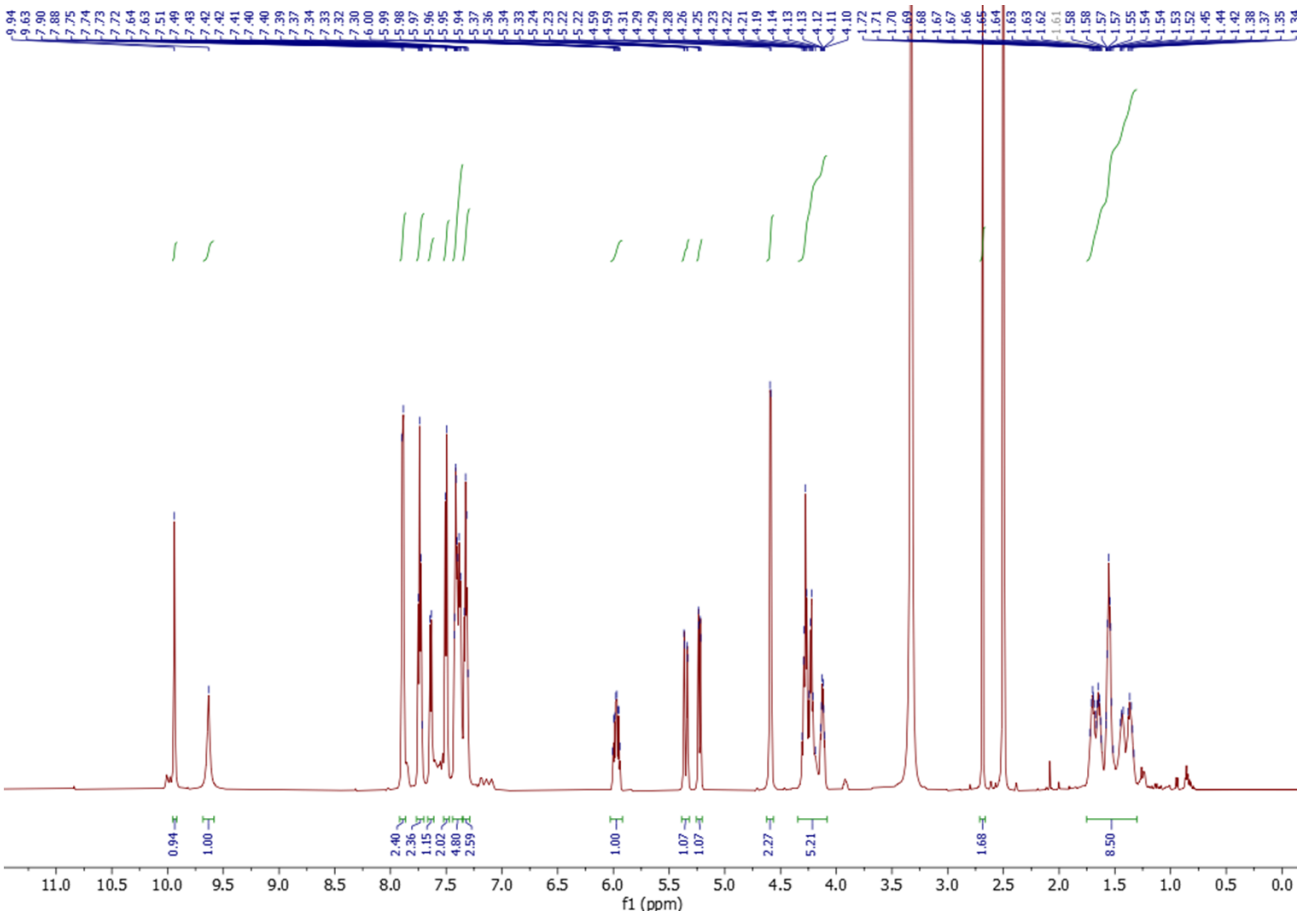

S82. ^{1}H NMR spectrum of compound 21 in DMSO-D_6.

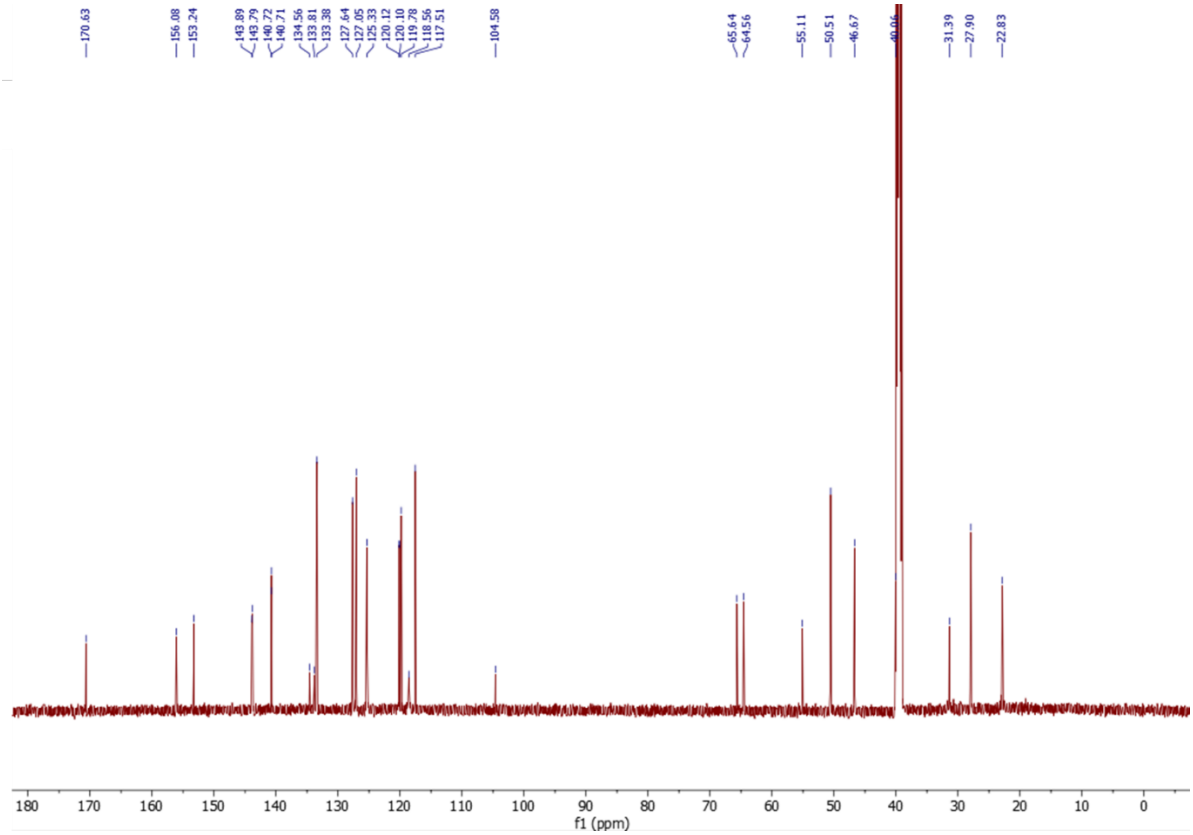

S83. ^{13}C NMR spectrum of compound 21 in DMSO-D_6.

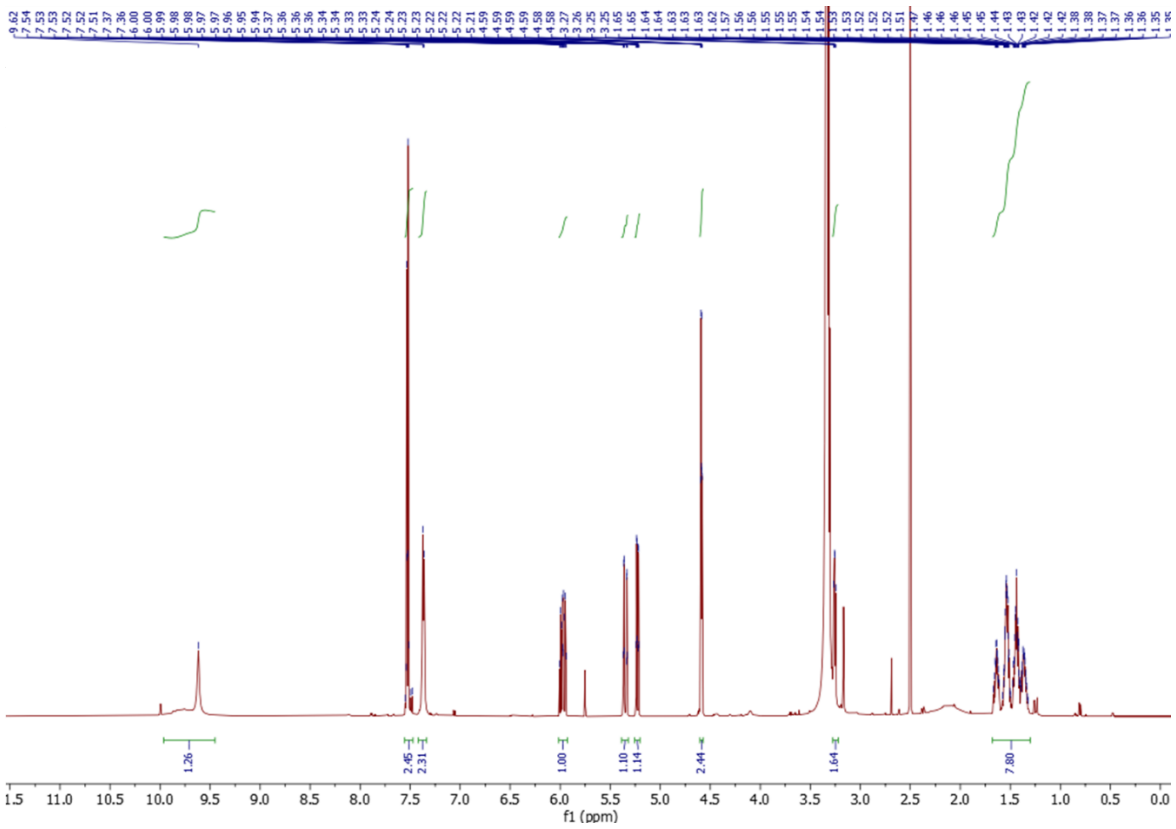

S85. ^{1}H NMR spectrum of compound 22 in DMSO-D_6.

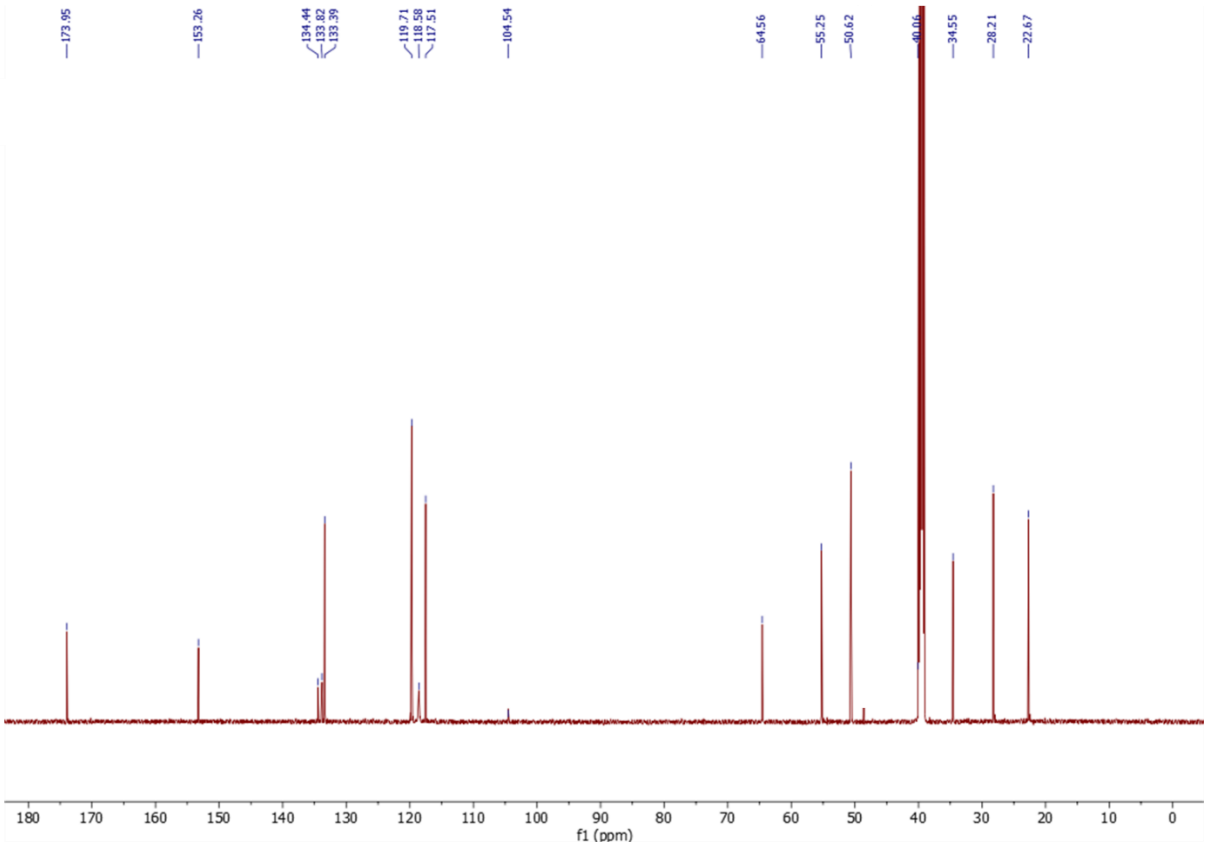

S86. ^{13}C NMR spectrum of compound 22 in DMSO-D_6. The signal at δ 48.59 ppm is due to the presence of methanol in the sample.

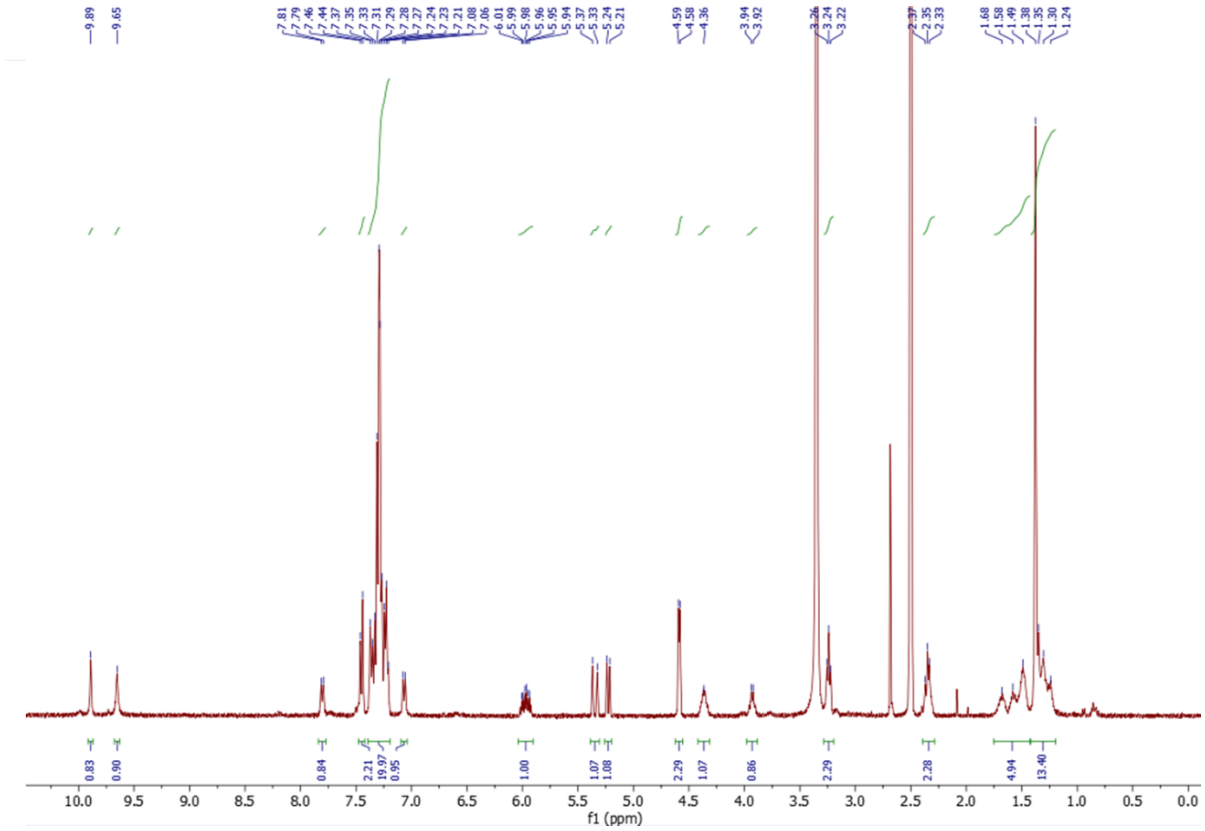

S87. ^{1}H NMR spectrum of compound 23 in DMSO-D_6.

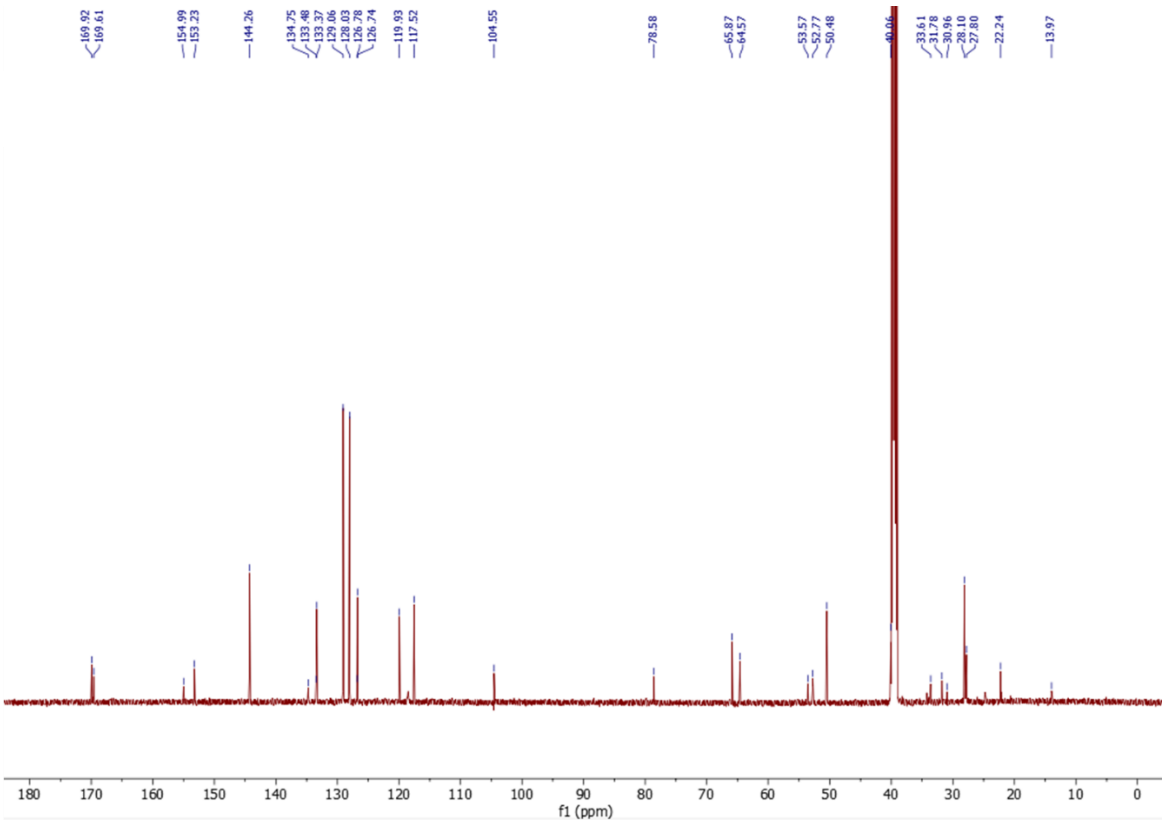

S88. ^{13}C NMR spectrum of compound 23 in DMSO-D_6.

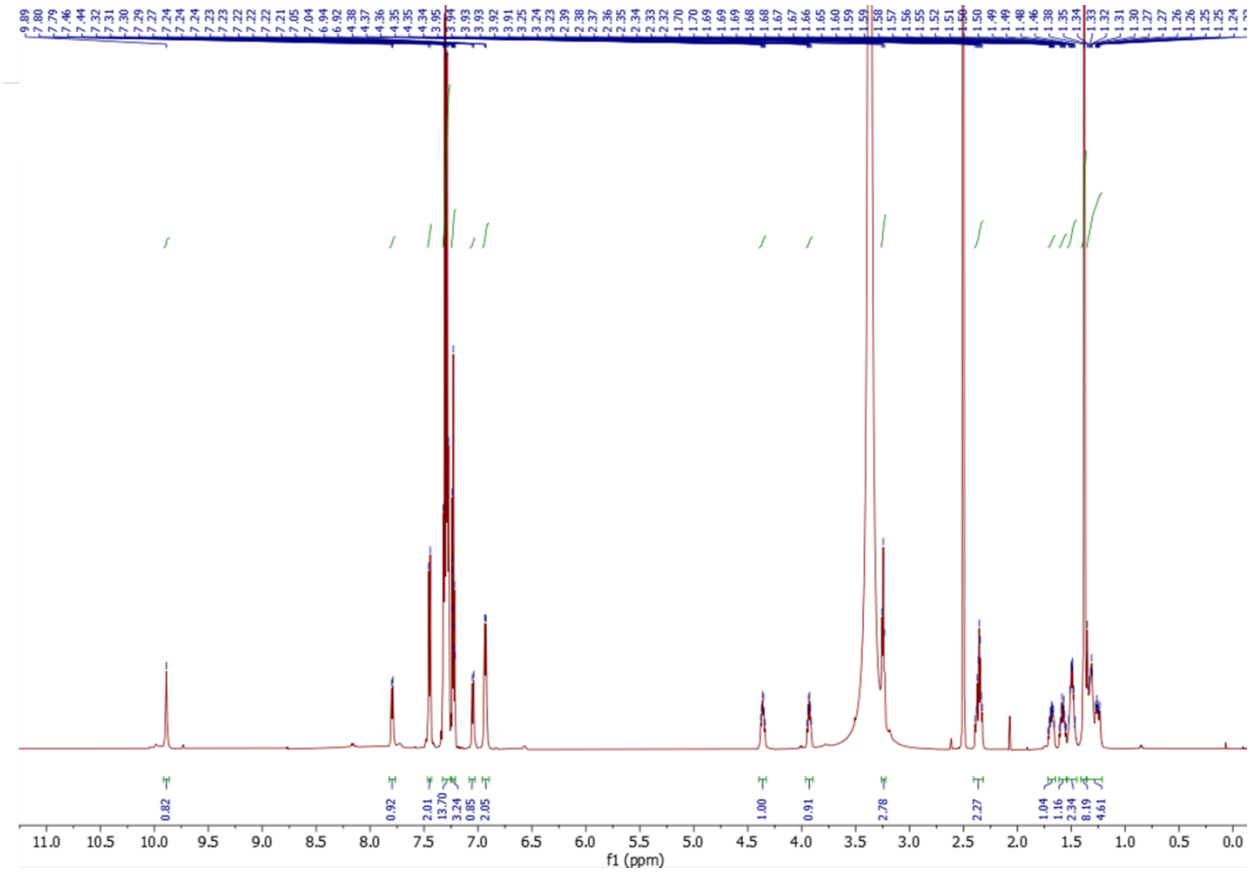

S89. ^{1}H NMR spectrum of compound 24 in DMSO-D_6.

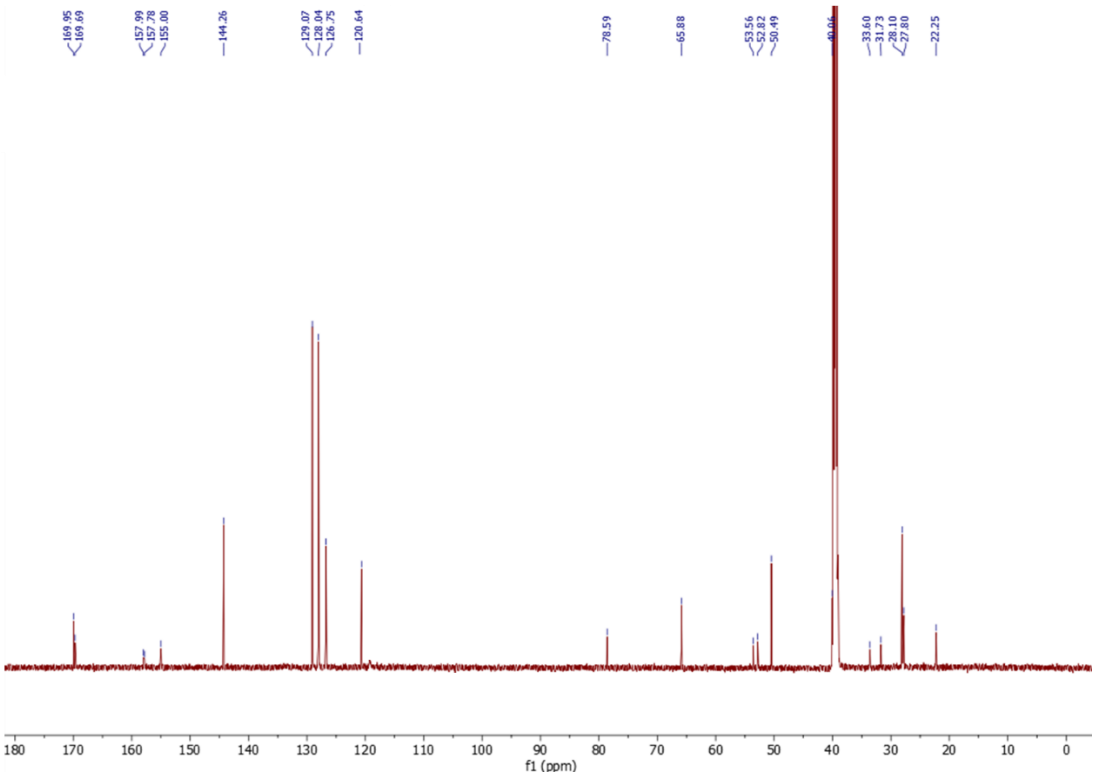

S90. ^{13}C NMR spectrum of compound 24 in DMSO-D_6.

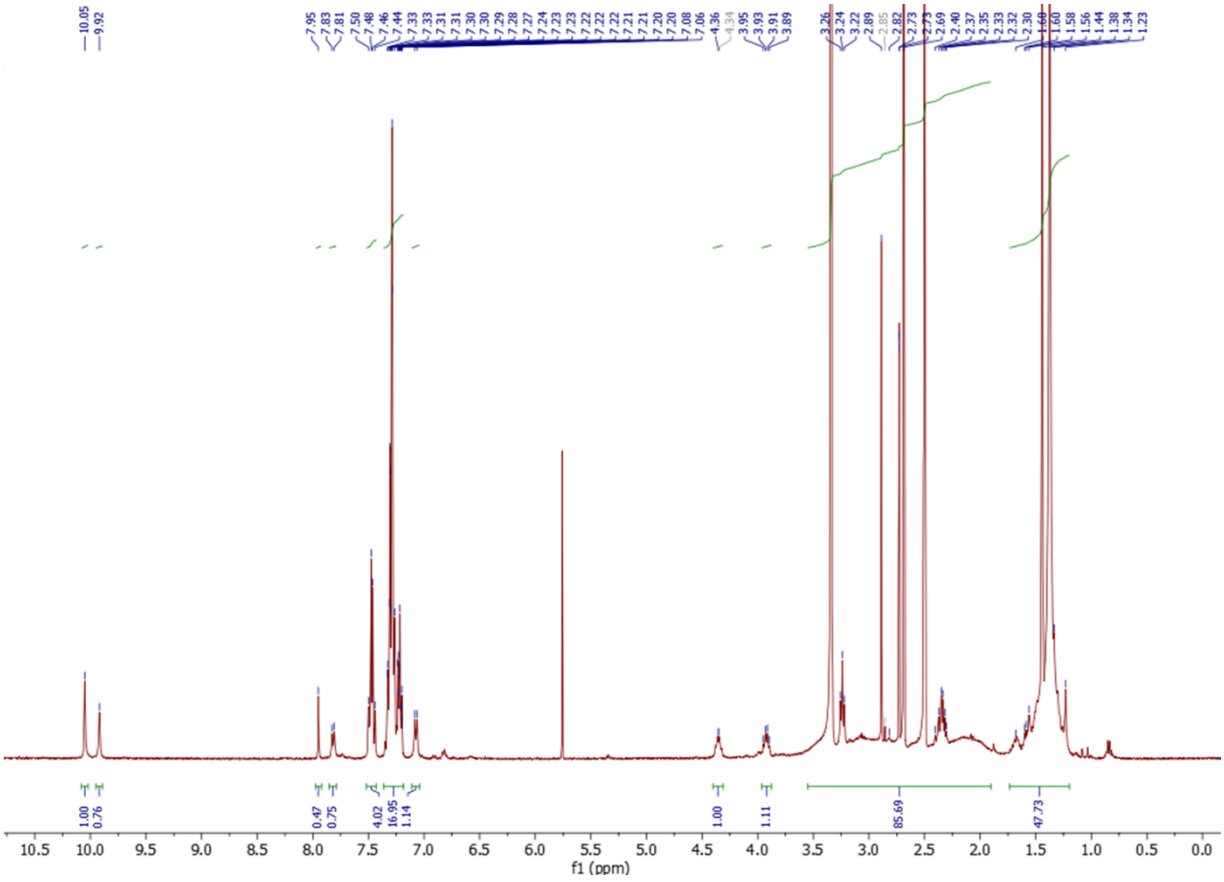

S91. ^{1}H NMR spectrum of compound 25 in DMSO-D_6. The signal at δ 5.76 ppm is due to the presence of CH_2Cl_2 in the sample.

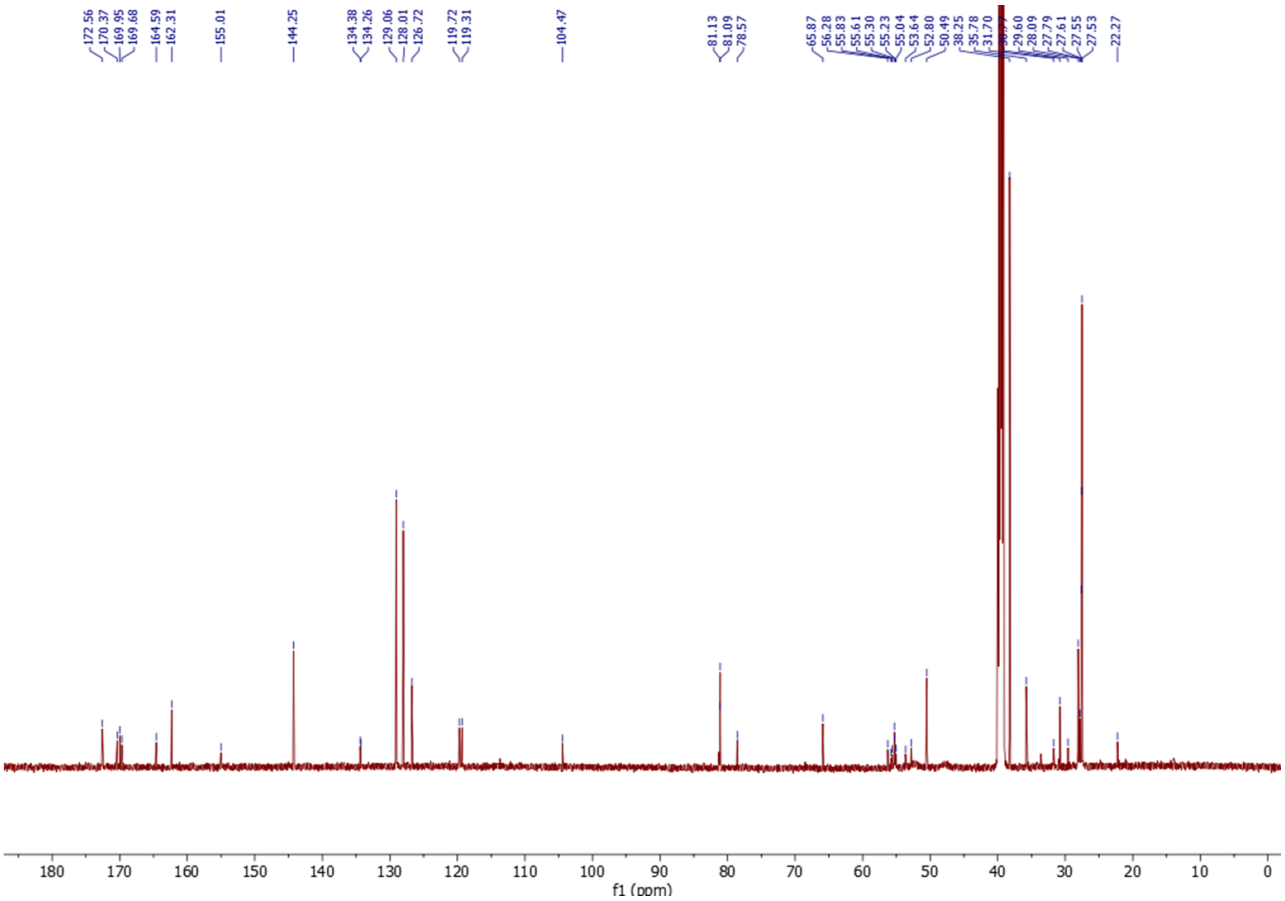

S92. ^{13}C NMR spectrum of compound 25 in DMSO-D_6.

4.9. Notes and References

(1) Bolcaen, J.; Kleynhans, J.; Nair, S.; Verhoeven, J.; Goethals, I.; Sathekge, M.; Vandevoorde, C.; Ebenhan, T. A Perspective on the Radiopharmaceutical Requirements for Imaging and Therapy of Glioblastoma. *Theranostics* **2021**, *11* (16), 7911–7947.

(2) Davis, M. E. Glioblastoma: Overview of Disease and Treatment. *Clin J Oncol Nurs* **2016**, *20* (5), S2–S8.

(3) Omuro, A.; DeAngelis, L. M. Glioblastoma and Other Malignant Gliomas: A Clinical Review. *JAMA* **2013**, *310* (17), 1842–1850.

(4) Urbańska, K.; Sokołowska, J.; Szmidt, M.; Sysa, P. Glioblastoma Multiforme – an Overview. *Contemp Oncol (Pozn)* **2014**, *18* (5), 307–312.

(5) Das, T.; Banerjee, S. Theranostic Applications of Lutetium-177 in Radionuclide Therapy. *Current Radiopharmaceuticals* **2016**, *9* (1), 94–101.

(6) McLendon, R.; Friedman, A.; Bigner, D.; Van Meir, E. G.; Brat, D. J.; M. Mastrogianakis, G.; Olson, J. J.; Mikkelsen, T.; Lehman, N.; Aldape, K.; Alfred Yung, W. K.; Bogler, O.; VandenBerg, S.; Berger, M.; Prados, M.; Muzny, D.; Morgan, M.; Scherer, S.; Sabo, A.; Nazareth, L.; Lewis, L.; Hall, O.; Zhu, Y.; Ren, Y.; Alvi, O.; Yao, J.; Hawes, A.; Jhangiani, S.; Fowler, G.; San Lucas, A.; Kovar, C.; Cree, A.; Dinh, H.; Santibanez, J.; Joshi, V.; Gonzalez-Garay, M. L.; Miller, C. A.; Milosavljevic, A.; Donehower, L.; Wheeler, D. A.; Gibbs, R. A.; Cibulskis, K.; Sougnez, C.; Fennell, T.; Mahan, S.; Wilkinson, J.; Ziaugra, L.; Onofrio, R.; Bloom, T.; Nicol, R.; Ardlie, K.; Baldwin, J.; Gabriel, S.; Lander, E. S.; Ding, L.; Fulton, R. S.; McLellan, M. D.; Wallis, J.; Larson, D. E.; Shi, X.; Abbott, R.; Fulton, L.; Chen, K.; Koboldt, D. C.; Wendl, M. C.; Meyer,

R.; Tang, Y.; Lin, L.; Osborne, J. R.; Dunford-Shore, B. H.; Miner, T. L.; Delehaunty, K.; Markovic, C.; Swift, G.; Courtney, W.; Pohl, C.; Abbott, S.; Hawkins, A.; Leong, S.; Haipek, C.; Schmidt, H.; Wiechert, M.; Vickery, T.; Scott, S.; Dooling, D. J.; Chinwalla, A.; Weinstock, G. M.; Mardis, E. R.; Wilson, R. K.; Getz, G.; Winckler, W.; Verhaak, R. G. W.; Lawrence, M. S.; O'Kelly, M.; Robinson, J.; Alexe, G.; Beroukhim, R.; Carter, S.; Chiang, D.; Gould, J.; Gupta, S.; Korn, J.; Mermel, C.; Mesirov, J.; Monti, S.; Nguyen, H.; Parkin, M.; Reich, M.; Stransky, N.; Weir, B. A.; Garraway, L.; Golub, T.; Meyerson, M.; Chin, L.; Protopopov, A.; Zhang, J.; Perna, I.; Aronson, S.; Sathiamoorthy, N.; Ren, G.; Yao, J.; Wiedemeyer, W. R.; Kim, H.; Won Kong, S.; Xiao, Y.; Kohane, I. S.; Seidman, J.; Park, P. J.; Kucherlapati, R.; Laird, P. W.; Cope, L.; Herman, J. G.; Weisenberger, D. J.; Pan, F.; Van Den Berg, D.; Van Neste, L.; Mi Yi, J.; Schuebel, K. E.; Baylin, S. B.; Absher, D. M.; Li, J. Z.; Southwick, A.; Brady, S.; Aggarwal, A.; Chung, T.; Sherlock, G.; Brooks, J. D.; Myers, R. M.; Spellman, P. T.; Purdom, E.; Jakkula, L. R.; Lapuk, A. V.; Marr, H.; Dorton, S.; Gi Choi, Y.; Han, J.; Ray, A.; Wang, V.; Durinck, S.; Robinson, M.; Wang, N. J.; Vranizan, K.; Peng, V.; Van Name, E.; Fontenay, G. V.; Ngai, J.; Conboy, J. G.; Parvin, B.; Feiler, H. S.; Speed, T. P.; Gray, J. W.; Brennan, C.; Socci, N. D.; Olshen, A.; Taylor, B. S.; Lash, A.; Schultz, N.; Reva, B.; Antipin, Y.; Stukalov, A.; Gross, B.; Cerami, E.; Qing Wang, W.; Qin, L.-X.; Seshan, V. E.; Villafania, L.; Cavatore, M.; Borsu, L.; Viale, A.; Gerald, W.; Sander, C.; Ladanyi, M.; Perou, C. M.; Neil Hayes, D.; Topal, M. D.; Hoadley, K. A.; Qi, Y.; Balu, S.; Shi, Y.; Wu, J.; Penny, R.; Bittner, M.; Shelton, T.; Lenkiewicz, E.; Morris, S.; Beasley, D.; Sanders, S.; Kahn, A.; Sfeir, R.; Chen, J.; Nassau, D.; Feng, L.; Hickey, E.; Zhang, J.; Weinstein, J. N.; Barker, A.; Gerhard, D. S.; Vockley, J.; Compton, C.; Vaught, J.; Fielding, P.; Ferguson, M. L.; Schaefer, C.; Madhavan, S.; Buetow, K. H.; Collins, F.; Good, P.; Guyer, M.;

Ozenberger, B.; Peterson, J.; Thomson, E. Comprehensive Genomic Characterization Defines Human Glioblastoma Genes and Core Pathways. *Nature* **2008**, *455* (7216), 1061–1068.

(7) Nayak, A.; Ralte, A. M.; Sharma, M. C.; Singh, V. P.; Mahapatra, A. K.; Mehta, V. S.; Sarkar, C. P53 Protein Alterations in Adult Astrocytic Tumors and Oligodendrogliomas. *Neurol India* **2004**, *52* (2), 228–232.

(8) Rajaraman, P.; Melin, B. S.; Wang, Z.; McKean-Cowdin, R.; Michaud, D.; Wang, S. S.; Bondy, M.; Houlston, R.; Jenkins, R. B.; Wrensch, M.; Yeager, M.; Ahlbom, A.; Albanes, D.; Andersson, U.; Freeman, L. E. B.; Buring, J. E.; Butler, M. A.; Braganza, M.; Carreon, T.; Feychting, M.; Fleming, S. J.; Gapstur, S. M.; Gaziano, J. M.; Giles, G. G.; Hallmans, G.; Henriksson, R.; Hoffman-Bolton, J.; Inskip, P. D.; Johansen, C.; Kitahara, C. M.; Lathrop, M.; Liu, C.; Le Marchand, L.; Linet, M. S.; Lonn, S.; Peters, U.; Purdue, M. P.; Rothman, N.; Ruder, A. M.; Sanson, M.; Sesso, H. D.; Severi, G.; Shu, X.-O.; Simon, M.; Stampfer, M.; Stevens, V. L.; Visvanathan, K.; White, E.; Wolk, A.; Zeleniuch-Jacquotte, A.; Zheng, W.; Decker, P.; Enciso-Mora, V.; Fridley, B.; Gao, Y.-T.; Kosel, M.; Lachance, D.; Lau, C.; Rice, T.; Swerdlow, A.; Wiemels, J.; Wiencke, J.; Shete, S.; Xiang, Y.-B.; Xiao, Y.; Hoover, R.; Fraumeni, J. F.; Chatterjee, N.; Hartge, P.; Chanock, S. J. Genome-Wide Association Study of Glioma and Meta-Analysis. *Hum Genet* **2012**, *131* (12), 1877–1888.

(9) Pearson, J. R. D.; Regad, T. Targeting Cellular Pathways in Glioblastoma Multiforme. *Sig Transduct Target Ther* **2017**, *2* (1), 1–11.

(10) Ran, D.; Mao, J.; Shen, Q.; Xie, C.; Zhan, C.; Wang, R.; Lu, W. GRP78 Enabled Micelle-Based Glioma Targeted Drug Delivery. *Journal of Controlled Release* **2017**, *255*, 120–131.

(11) Wang, M.; Ye, R.; Barron, E.; Baumeister, P.; Mao, C.; Luo, S.; Fu, Y.; Luo, B.; Dubeau, L.; Hinton, D. R.; Lee, A. S. Essential Role of the Unfolded Protein Response Regulator GRP78/BiP in Protection from Neuronal Apoptosis. *Cell Death Differ* **2010**, *17* (3), 488–498.

(12) Fu, Y.; Lee, A. S. Glucose Regulated Proteins in Cancer Progression, Drug Resistance and Immunotherapy. *Cancer Biology & Therapy* **2006**, *5* (7), 741–744.

(13) Lee, A. S. GRP78 Induction in Cancer: Therapeutic and Prognostic Implications. *Cancer Res* **2007**, *67* (8), 3496–3499.

(14) Kang, B. R.; Yang, S.-H.; Chung, B.-R.; Kim, W.; Kim, Y. Cell Surface GRP78 as a Biomarker and Target for Suppressing Glioma Cells. *Sci Rep* **2016**, *6* (1), 34922.

(15) Lee, H. K.; Xiang, C.; Cazacu, S.; Finniss, S.; Kazimirsky, G.; Lemke, N.; Lehman, N. L.; Rempel, S. A.; Mikkelsen, T.; Brodie, C. GRP78 Is Overexpressed in Glioblastomas and Regulates Glioma Cell Growth and Apoptosis. *Neuro Oncol* **2008**, *10* (3), 236–243.

(16) Mandelin, J.; Cardó-Vila, M.; Driessen, W. H. P.; Mathew, P.; Navone, N. M.; Lin, S.-H.; Logothetis, C. J.; Rietz, A. C.; Dobroff, A. S.; Proneth, B.; Sidman, R. L.; Pasqualini, R.; Arap, W. Selection and Identification of Ligand Peptides Targeting a Model of Castrate-Resistant Osteogenic Prostate Cancer and Their Receptors. *Proceedings of the National Academy of Sciences* **2015**, *112* (12), 3776–3781.

(17) Arap, M. A.; Lahdenranta, J.; Mintz, P. J.; Hajitou, A.; Sarkis, Á. S.; Arap, W.; Pasqualini, R. Cell Surface Expression of the Stress Response Chaperone GRP78 Enables Tumor Targeting by Circulating Ligands. *Cancer Cell* **2004**, *6* (3), 275–284.

(18) Liu, M.; Li, X.; Xie, Z.; Xie, C.; Zhan, C.; Hu, X.; Shen, Q.; Wei, X.; Su, B.; Wang, J.; Lu, W. D-Peptides as Recognition Molecules and Therapeutic Agents. *Chem Rec* **2016**, *16* (4), 1772–1786.

(19) Wen, P. Y.; Macdonald, D. R.; Reardon, D. A.; Cloughesy, T. F.; Sorensen, A. G.; Galanis, E.; Degroot, J.; Wick, W.; Gilbert, M. R.; Lassman, A. B.; Tsien, C.; Mikkelsen, T.; Wong, E. T.; Chamberlain, M. C.; Stupp, R.; Lamborn, K. R.; Vogelbaum, M. A.; van den Bent, M. J.; Chang, S. M. Updated Response Assessment Criteria for High-Grade Gliomas: Response Assessment in Neuro-Oncology Working Group. *J Clin Oncol* **2010**, *28* (11), 1963–1972.

(20) Zhao, X.; Jakobsson, V.; Tao, Y.; Zhao, T.; Wang, J.; Khong, P.-L.; Chen, X.; Zhang, J. Targeted Radionuclide Therapy in Glioblastoma. *ACS Appl. Mater. Interfaces* **2024**, *16* (31), 40391–40410.

(21) Banerjee, S.; Pillai, M. R. A.; Knapp, F. F. (Russ). Lutetium-177 Therapeutic Radiopharmaceuticals: Linking Chemistry, Radiochemistry, and Practical Applications. *Chem. Rev.* **2015**, *115* (8), 2934–2974.

(22) Sgouros, G.; Bodei, L.; McDevitt, M. R.; Nedrow, J. R. Radiopharmaceutical Therapy in Cancer: Clinical Advances and Challenges. *Nat Rev Drug Discov* **2020**, *19* (9), 589–608.

(23) Kneifel, S.; Cordier, D.; Good, S.; Ionescu, M. C. S.; Ghaffari, A.; Hofer, S.; Kretzschmar, M.; Tolnay, M.; Apostolidis, C.; Waser, B.; Arnold, M.; Mueller-Brand, J.; Maecke, H. R.; Reubi, J. C.; Merlo, A. Local Targeting of Malignant Gliomas by the Diffusible Peptidic Vector 1,4,7,10-Tetraazacyclododecane-1-Glutaric Acid-4,7,10-Triacetic Acid-Substance P. *Clinical Cancer Research* **2006**, *12* (12), 3843–3850.

(24) Dalm, S. U.; Bakker, I. L.; Blois, E. de; Doeswijk, G. N.; Konijnenberg, M. W.; Orlandi, F.; Barbato, D.; Tedesco, M.; Maina, T.; Nock, B. A.; Jong, M. de. 68Ga/177Lu-NeoBOMB1, a Novel Radiolabeled GRPR Antagonist for Theranostic Use in Oncology. *Journal of Nuclear Medicine* **2017**, *58* (2), 293–299.

(25) Placidi, M. P.; Villaraza, A. J. L.; Natrajan, L. S.; Sykes, D.; Kenwright, A. M.; Faulkner, S. Synthesis and Spectroscopic Studies on Azo-Dye Derivatives of Polymetallic Lanthanide Complexes: Using Diazotization to Link Metal Complexes Together. *J. Am. Chem. Soc.* **2009**, *131* (29), 9916–9917.

(26) Sørensen, T. J.; Kenwright, A. M.; Faulkner, S. Bimetallic Lanthanide Complexes That Display a Ratiometric Response to Oxygen Concentrations. *Chem. Sci.* **2015**, *6* (3), 2054–2059.

(27) Sørensen, T. J.; Tropiano, M.; Kenwright, A. M.; Faulkner, S. Triheterometallic Lanthanide Complexes Prepared from Kinetically Inert Lanthanide Building Blocks. *European Journal of Inorganic Chemistry* **2017**, *2017* (15), 2165–2172.

(28) Szíjjártó, C.; Pershagen, E.; Borbas, K. E. Functionalisation of Lanthanide Complexes via Microwave-Enhanced Cu(I)-Catalysed Azide–Alkyne Cycloaddition. *Dalton Trans.* **2012**, *41* (25), 7660–7669.

(29) Ye, D.; Shuhendler, A. J.; Cui, L.; Tong, L.; Tee, S. S.; Tikhomirov, G.; Felsher, D. W.; Rao, J. Bioorthogonal Cyclization-Mediated in Situ Self-Assembly of Small-Molecule Probes for Imaging Caspase Activity *in Vivo*. *Nature Chem* **2014**, *6* (6), 519–526.

(30) Fields, G. B. Methods for Removing the Fmoc Group. *Peptide Synthesis Protocols*; Pennington, M. W., Dunn, B. M., Eds.; Humana Press: Totowa, NJ, **1995**; pp 17–27.

(31) Luna, O. F.; Gomez, J.; Cárdenas, C.; Albericio, F.; Marshall, S. H.; Guzmán, F. Deprotection Reagents in Fmoc Solid Phase Peptide Synthesis: Moving Away from Piperidine? *Molecules* **2016**, *21* (11), 1542.

(32) Pires, D. A. T.; Bemquerer, M. P.; do Nascimento, C. J. Some Mechanistic Aspects on Fmoc Solid Phase Peptide Synthesis. *Int J Pept Res Ther* **2014**, *20* (1), 53–69.

(33) Hachmann, J.; Lebl, M. Alternative to Piperidine in Fmoc Solid-Phase Synthesis. *J Comb Chem* **2006**, *8* (2), 149.

(34) Tahoori, F.; Balalaie, S.; Sheikhnejad, R.; Sadjadi, M.; Boloori, P. Design and Synthesis of Anti-Cancer Cyclopeptides Containing Triazole Skeleton. *Amino Acids* **2014**, *46* (4), 1033–1046.

(35) Ishida, K.; Nakamura, Y.; Ohta, T.; Oe, Y. A Molecular Probe with Both Chromogenic and Fluorescent Units for Detecting Serine Proteases. *Molecules* **2021**, *26* (2), 482.

(36) Chi, H.; Takemoto, Y.; Nsiama, T. K.; Kato, T.; Nishino, N.; Ito, A.; Yoshida, M. Design and Synthesis of Peptide-MCA Substrates for a Novel Assay of Histone Methyltransferases and Their Inhibitors. *Bioorganic & Medicinal Chemistry* **2014**, *22* (4), 1268–1275.

(37) Yoo, B.; Sheth, V. R.; Pagel, M. D. An Amine-Derivatized, DOTA-Loaded Polymeric Support for Fmoc Solid Phase Peptide Synthesis. *Tetrahedron Lett* **2009**, *50* (31), 4459–4462.

(38) Hermanson, G. T. Chapter 3 - The Reactions of Bioconjugation. In *Bioconjugate Techniques (Third Edition)*; Hermanson, G. T., Ed.; Academic Press: Boston, **2013**; pp 229–258.

(39) Pringle, T. A.; Knight, J. C. The Effects of Buffer, pH, and Temperature upon SPAAC Reaction Rates. *Org. Biomol. Chem.* **2025**, *23* (10), 2432–2438.

(40) Scinto, S. L.; Bilodeau, D. A.; Hincapie, R.; Lee, W.; Nguyen, S. S.; Xu, M.; am Ende, C. W.; Finn, M. G.; Lang, K.; Lin, Q.; Pezacki, J. P.; Prescher, J. A.; Robillard, M. S.; Fox, J. M. Bioorthogonal Chemistry. *Nat Rev Methods Primers* **2021**, *1* (1), 1–23.

(41) Luu, T.; Gristwood, K.; Knight, J. C.; Jörg, M. Click Chemistry: Reaction Rates and Their Suitability for Biomedical Applications. *Bioconjugate Chem.* **2024**, *35* (6), 715–731.

(42) Rigolot, V.; Biot, C.; Lion, C. To View Your Biomolecule, Click inside the Cell. *Angewandte Chemie* **2021**, *133* (43), 23268–23289.

(43) Mushtaq, S.; Yun, S.-J.; Jeon, J. Recent Advances in Bioorthogonal Click Chemistry for Efficient Synthesis of Radiotracers and Radiopharmaceuticals. *Molecules* **2019**, *24* (19), 3567.

(44) McKinnon, K. M. Flow Cytometry: An Overview. *Current Protocols in Immunology* **2018**, *120* (1), 5.1.1-5.1.11.

(45) Thurston, D. E.; Jackson, P. J. M. Polycyclic Amides as Cytotoxic Agents. Patent Cooperation Treaty WO **2020**/049286.

Chapter 5: Synthesis of a Novel Cannabinoid Radiotracer with an Application across PET-CT Imaging

Emilie Marie Sophie Patit-Tha Brun [1, 2], Dominic Graf [1, 2], Rui Liu [3], Cory Harris [3] and Adam J. Shuhendler [1, 2, 3*]

[1]Dept. Chemistry & Biomolecular Sciences, University of Ottawa, Ottawa, Ontario, Canada. E-mail: adam.shuhendler@uottawa.ca

[2]University of Ottawa Heart Institute, Ottawa, Ontario, Canada

[3]Dept. Biology, University of Ottawa, Ottawa, Ontario, Canada

5.1. Overview of the Research Project Presented in this Chapter

Over the past decade, the increasing legalization of tetrahydroxannbinol (THC) across various countries has led to greater accessibility and usage. This trend highlights the need for a better understanding of THC's pharmacological and toxicological effects to effectively reduce associated risks. The pharmacological interaction of THC with the cannabinoid receptors CB_1 and CB_2, including their roles within the endocannabinoid system, is well studied. However, specific cannabinoid-based imaging probes have yet to be developed for scientific application in both research and diagnostic Positron Emission Tomography (PET) imaging. Radiotracers have been created using molecules distinct from the cannabinoids THC and cannabidiol (CBD), which interact with CB_1 receptors. These also includes THC analogues such as HU-210F and HU-211F. Based on this specificity, a new radiotracer with minimally modified chemical structure of Δ^8 and Δ^9-THC can be developed by incorporating a proton bioisostere, radioactive fluorine-18 (^{18}F), at the end of the cannabinoid aliphatic chain. This modification will enable the creation of radiotracers capable of quantifying biodistribution and receptor engagement using PET imaging.

5.2. Authors Contributions

E.M.S.P.B. performed the synthesis and characterization of every chemical compounds including the different purification attempts on HPLC and automated purification systems, with the support of D.G. R.L performed the separation of the sample on the analytical-scale fractions collector HPLC.

5.3. Abstract

An attempt to synthesize new THC-based radiotracers, [^{18}F]-ω-fluoro- Δ^8-THC and [^{18}F]-ω-fluoro- Δ^9-THC, has been made for PET-CT imaging to initially evaluate its biodistribution and receptor engagement in the endocannabinoid system. Based on *J. Med. Chem.* **2005**, (48:7389-7399), an intermediate, a brominated THC, was formed by converting a proton bioisostere to a bromine atom on the aliphatic chain, facilitating the subsequent conversion to fluorine. NMR characterization revealed the complexity of the aliphatic region, suggesting a mixture of both Δ^8-THC and Δ^9-THC isomers during the synthesis of brominated THC. Although the intermediates were synthesized according to the published procedure, additional purification steps through HPLC were required to obtain the desired pure brominated Δ^8-THC and Δ^9-THC. This necessitated a redesign of the initial project plan.

5.4. Introduction

After its legalization in Canada in 2018, cannabis has attracted increased research interest due to its increased use across demographics and its pharmacological and psychotropic effects [1]. Tetrahydrocannabinol (THC) is one of hundreds of phytocannabinoid compounds extracted from the female plant of *Cannabis sativa L.* and is known for its psychoactive properties. As a terpenophenolic compound with antibacterial, anti-inflammatory or analgesic properties [2], THC shows a high affinity for different receptors present in the endocannabinoid system (ECS). Multiple studies show that THC binds to the two main cannabinoids receptors (CB), the G protein-

coupled CB_1 and CB_2 [3]. THC activates both CB_1 and CB_2 receptors, with the CB_1 receptor, mostly found in the central nervous system (CNS), typically leading to the psychoactive effects associated with cannabis. In contrast, the CB_2 receptor is predominantly present in various immune cells, where it does not produce psychoactive effects, and is generally linked to protective biological functions [2, 4].

Due to its lipophilic nature, THC can be rapidly absorbed and accumulated in body's adipose tissue for extended periods [5]. In rodent studies, THC was found at higher concentrations in gonadal fat organs than in other tissue like the brain, liver or lungs, where it remains unmetabolized for several hours [6]. Human studies have detected THC in fat biopsies up to 28 days after cannabis exposure [7]. Although THC appears to transfer from fat tissue back into the bloodstream under normal physiological conditions, this specific cannabinoid can be released from adipocytes at higher concentrations in the blood during enhanced fat metabolism, such as lipolysis [8].

Although cannabinoids receptors are involved in psychiatric or neurological disorders, they also play a role in non-central nervous system pathologies such as liver fibrosis or metabolic disorders like diabetes and cancer [4]. THC has demonstrated several therapeutic effects, including pain relief due to its analgesic properties [9], making it a valuable option for patients with multiple sclerosis [10]. Additionally, THC can reduce nausea and vomiting notably benefiting patients suffering from conditions like HIV/AIDS [11]. It has also been shown to aid in mood regulation by decreasing anxiety and tension [12], and has potential applications in the treatment of conditions such as Alzheimer's [13] and Parkinsons's diseases [14]. However, THC's psychoactive properties, including euphoria and altered perception [12], can induce anxiety, paranoia and even psychotic symptoms in some individuals at high dose [15, 16]. These potential adverse effects highlight the need for better understanding and monitoring of THC's impact on the body. To date, specific

cannabinoid imaging probes have not yet been developed but they could have both research and diagnostic applications in the PET-CT imaging field. While related analogues to synthetic cannabinoids have been synthesized and characterized as potential agonists of CB_1 and CB_2 receptors [17], specific imaging probes are still lacking. These synthetic cannabinoids, which feature a terminal fluorine atom on their linear aliphatic chains, present higher pharmacological properties compared to their non-fluorinated analogs [17]. Radiotracers have been made based on molecules other than THC or cannabidiol (CBD) that engage the CB_1 receptor [18, 19], including THC analogues such as HU-210F and HU-211F [20].

This is why, one of the main goals of this project is to assess the biodistribution of cannabinoids through non-invasive, quantitative imaging techniques, and to investigate how factors like the age, sex and body mass index (BMI) could influence its biodistribution. By evaluating both Δ^8-THC and Δ^9-THC, a low and high potency cannabinoid respectively, and comparing them, this study aims to establish the evaluation of these radiotracers to applying [^{18}F]-ω-fluoro- Δ^8-THC and [^{18}F]-ω-fluoro- Δ^9-THC to PET imaging within mouse models.

5.5. Results and Discussion

Design and synthesis strategies for fluorinated tetrahydrocannabinol derivatives

To assess the biodistribution of cannabinoids and their receptor engagement , the primary objective of this project was to synthesize THC derivatives radiotracers. These radiotracers had minimally modified chemical structures of Δ^8-THC and Δ^9-THC, achieved by adding a proton bioisostere, a radioactive fluorine, to the end of the cannabinoid aliphatic chain. This generated [^{18}F]-ω-fluoro- Δ^8-THC and [^{18}F]-ω-fluoro- Δ^9-THC. Therefore, the synthesis of these radiotracers focused on established methods to obtain 3'-bromo-Δ^8-tetrahydrocannabinol (**41**) and 3'-bromo-Δ^8-tetrahydrocannabinol (**42**) (Figure 5.1) [21].

Based on a paper published in the Journal of Medicinal Chemistry in 2005 [21], where the authors developed a synthesis to produce THC and THC analogues for immunopharmacotherapy, the synthesis scheme presented in Figure 5.1 began with the *in situ* production of a Grignard reagent. This reagent reacted with 3,5-dimethoxybenzaldehyde affording 5-phenoxy-1-(3,5-dimethoxyphenyl)pentanol (**37**) with a 91% yield after purification. Following a dihydroxylation reaction using a combination of TMSCl and NaI, product **38** was obtained with a 90% yield after extraction and filtration. The resulting product **38** was then deprotected using the Lewis acid boron tribromide (BBr_3) etherate, which converted the methoxy groups into primary alcohols and the phenol group into a bromine, yielding the precursor 1-(3,5-dihydroxyphenyl)-5-bromopentane (**39**) after purification. The synthesis of brominated Δ^8-tetrahydrocannabinol and brominated Δ^9-tetrahydrocannabinol involved two separate steps with different reagents (Figure 5.1B). The synthesis of 3'-bromo-Δ^8-tetrahydrocannabinol (**41**) began with the coupling of (s)-cis-verbenol

and the precursor 1-(3,5-dihydroxyphenyl)-5-bromopentane (**39**) in the presence of *p*-toluenesulfonic acid (*p*-TSA), giving the intermediate (**40**), with a 24% yield after purification. This intermediate was then cyclized using boron fluoride etherate to form the brominated Δ^8-THC analogue (**41**). On the other hand, under the same acidic conditions used for the brominated Δ^8-THC analogue (**41**), the precursor 1-(3,5-dihydroxyphenyl)-5-bromopentane (**39**) was coupled with (+)-*p*-mentha-2,8-dien-1-ol to produce the brominated Δ^9-THC analogue (**42**) in one single step.

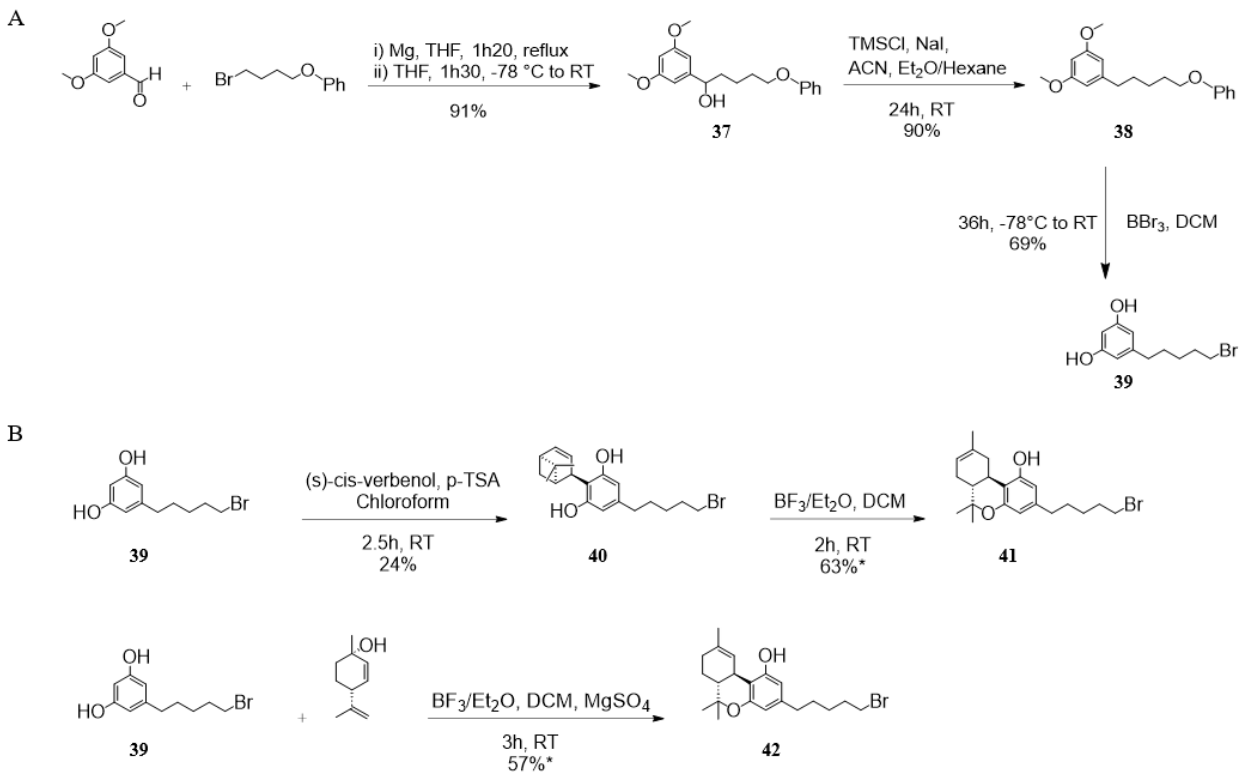

Figure 5.1 Chemical synthesis of bromine-labeled THC. (A) Synthesis scheme for the precursor 1-(3,5-dihydroxyphenyl)-5-bromopentane **39**. (B) Synthesis scheme for the final products 3'-bromo-Δ^8-tetrahydrocannabinol **41** and 3'-bromo-Δ^9-tetrahydrocannabinol **42**. *THF: tetrahydrofuran; TMSCl: trimethylsilyl chloride; NaI: sodium iodide; ACN: acetonitrile; Et_2O: diethyl ether; DCM: dichloromethane; p-TSA: p-toluenesulfonic acid.*

With the synthesis of the various brominated THC analogues, the next objective was to convert the bromine atom into fluorine. This process required careful selection of fluorinating agents and optimization of reaction conditions to ensure selective substitution without compromising the structural integrity of the THC analogues. This conversion was essential for

developing potential radiotracers, which will be used to map their biodistribution through PET-CT imaging. Multiple conditions and methodologies were explored to achieve the conversion of bromine to fluorine, as presented in Table 5.1, before identifying the most effective approach. As a nucleophilic substitution, the first approach involved using kryptofix with potassium fluoride (KF) in acetonitrile solvent [22]. The goal was to enhance the solubility of the fluoride ion by complexing the potassium ion with kryptofix [23, 24] due to its non-solubility in polar aprotic solvent like acetonitrile. However, this method did not yield to the desired product. This can be explained by the fact that, even with the presence of kryptofix, the solubility of KF in acetonitrile might not have been sufficient to provide enough reactive fluoride ions for the substitution reaction. Additionally, the reactivity of the fluoride ion might have been insufficient to displace the bromine atom under the given conditions, despite being more soluble with kryptofix.

The next attempt was realized with tetra-butylammonium fluoride (TBAF) in various solvents like 2-methyl-2-butanol [25] and tert-butanol [26], with different reaction times and temperatures. TBAF is known for its solubility in organic solvents and its ability to provide a reactive fluorine ion [27] which might offer a more reactive fluoride source and better conditions for the substitution to occur efficiently. Despite these advantages, LC-MS data showed that the nucleophilic substitution of bromine with fluorine ion was either incomplete or produced minimal desired product. After multiple trials on both brominated Δ^8-THC (**41**) and Δ^9-THC (**42**), TBAF in acetonitrile solvent emerged as the optimal combination. By closely monitoring the reaction progress using LC-MS, it was determined that setting up the reaction for 2 hours at 80 °C provided the best condition for an effective conversion. This method facilitated the nucleophilic substitution, yielding the non-pure desired fluorinated Δ^8-THC (**46**) and Δ^9-THC (**44**) (Figure 5.2).

Table 5.1 Overview of experimental procedure to synthesize [^{19}F]-ω-fluoro-Δ^8-THC and [^{19}F]-ω-fluoro-Δ^9-THC. All reactions were followed by LC-MS.

Solvent	Reagent	Reaction time	Temperature
Acetonitrile	KF + Kryptofix	1 h 30 min	80 °C
2-methyl-2-butanol	TBAF	30 min	70 °C
Tert-butanol	TBAF	1 h	80 °C
Acetonitrile	TBAF	30 min	80 °C
Acetonitrile	TBAF	2 h	80 °C

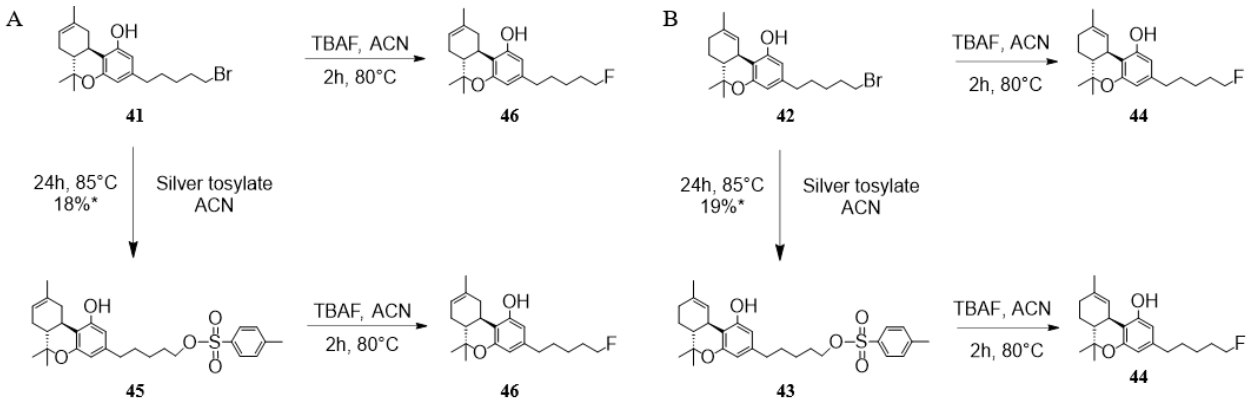

Figure 5.2 Chemical synthesis of fluorinated radiotracer THC analogues. (A) Synthesis scheme for fluorinated Δ^8-THC **46** through the tosylated intermediate **45**. (B) Synthesis scheme for fluorinated Δ^9-THC **44** through the tosylated intermediate **43**. *TBAF: tetra-n-butylammonium fluoride; ACN: acetonitrile.*

Evaluation and optimization of HPLC methods for the purification of tetrahydrocannabinol derivatives

Before proceeding with any further purification of the fluorinated THC, the crude product was injected into the analytical HPLC system to observe its chromatographic behavior. This step allowed for a comparison with the precursor, THC-Br, and standard THC, as a reference. By analyzing the retention times of these compounds under identical HPLC conditions, it was possible to evaluate how the fluorinated THC differed from its precursor and the standard.

According to the HPLC chromatograms obtained for Δ^9 THC and its analogues (Figure 5.3), it was observed that the brominated (Figure 5.3A) and fluorinated THC (Figure 5.3B) variants presented nearly identical retention times, even though the fluorinated THC was injected into the

HPLC system before further purification process. Furthermore, the chromatogram of the fluorinated THC (Figure 5.3B) revealed a shoulder peak, which could be potentially indicative of the presence of a mixture of fluorinated and brominated THC within the sample. The co-elution of these compounds complicated the separation process, as the resolution between the peaks is insufficient to achieve a clear distinction and separation. This similarity in the retention time could be attributed to the similar electronic and steric effects conferred by the bromine and fluorine substituents, both being halogens atoms [28], which may not change the overall polarity or molecular shape of THC. When compared to the THC standard (Figure 5.3A/B *vs* C), both brominated and fluorinated THC variants demonstrated a slight difference in retention time, observed as less than half a minute. This indicated that the halogenation of THC introduced changes in its chromatographic behavior, such as altered interactions with the stationary phase or modification in molecular polarity, due to the introduction of halogen to the molecule.

The conversion from brominated THC to fluorinated THC resulted in identical or very similar retention times on the HPLC, inducing a significant challenge for subsequent hot chemistry with radioactive fluorine. In radiochemistry, especially when working with short-lived isotopes like fluorine-18 ($t_{½}$ = 109.77 min) [29], it is important to have distinct retention times for the starting material and the product. The differentiation allows for efficient purification and isolation of the desired radiotracer from any unreacted precursor or by-products. Without a clear separation in retention time, ensuring the purity of the radiotracer becomes difficult. This purity is essential for accurate PET imaging and reliable biological studies due to its high sensitivity and specificity required for measuring different protein targets or receptors engagement [19]. To address this issue, an additional step was added to the synthesis by incorporating a tosylated intermediate (Figure 5.2). By converting the brominated THC precursor, both Δ^8 (**41**) and Δ^9 THC-Br (**42**), into their

corresponding tosylated form, the aim was to enhance the separation and purification of the compounds. This process involved a nucleophilic attack at the bromine position to generate the tosylate as a leaving group, facilitated by reaction with silver toluenesulfonate in acetonitrile [30]. This modification should lead to a difference in the retention time on the HPLC chromatograms. By achieving this separation, reaction progress could be monitored more effectively to ultimately obtain a pure radiotracer usable for *in vivo* studies in mouse models. This strategy ensured that both radiolabeled products, [^{18}F]-ω-fluoro-Δ^8-THC and [^{18}F]-ω-fluoro-Δ^9-THC, could be isolated with high purity and specificity activity, which are critical factors for PET imaging applications.

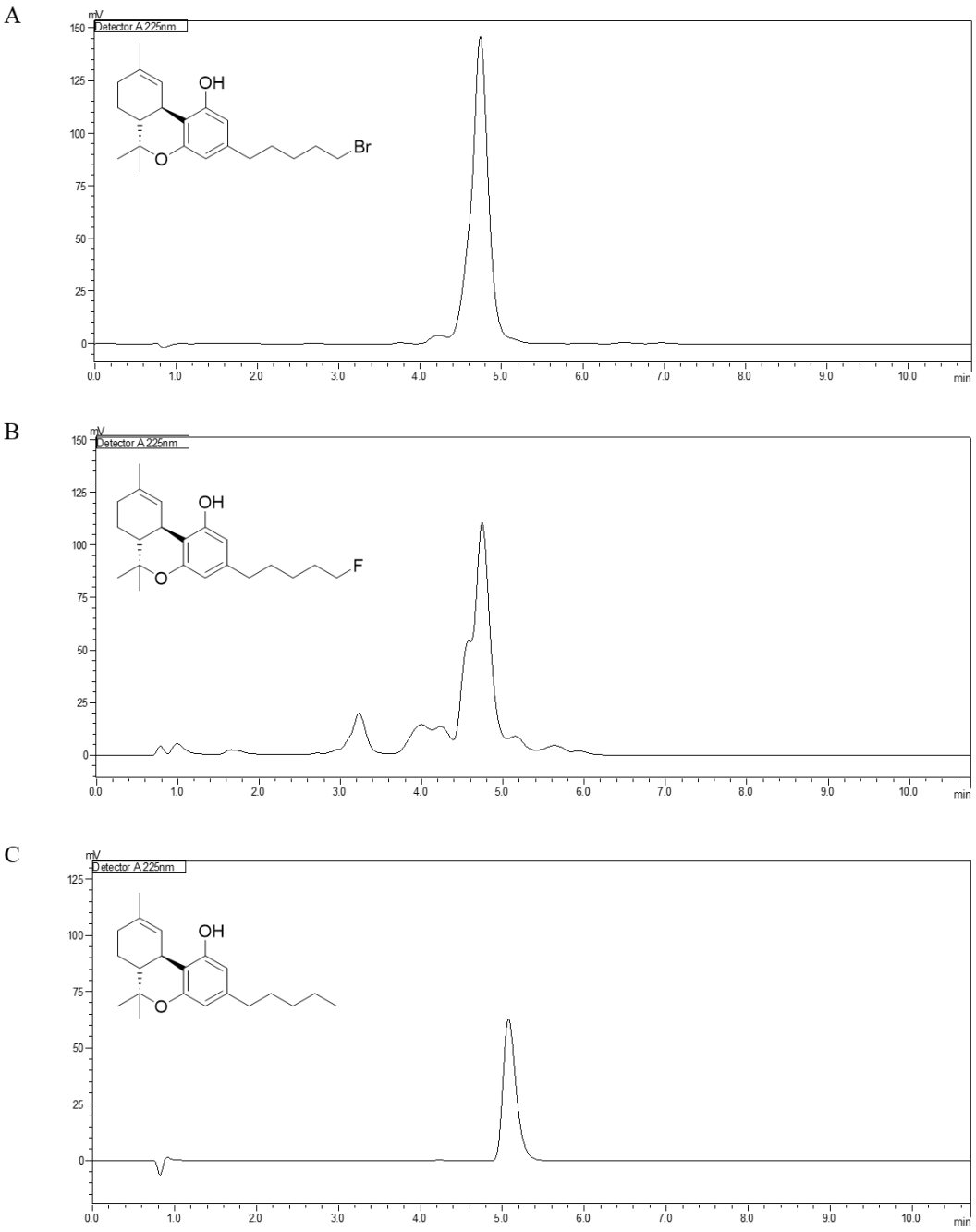

Figure 5.3 HPLC chromatograms comparing (A) brominated Δ^9 THC, (B) fluorinated Δ^9 THC and (C) Δ^9 THC as a reference. The chromatograms illustrate the retention times and peak intensities of each THC variant, highlighting differences in their chemical properties and purity levels.

Upon successfully synthesizing the intermediate THC-tosylate for both Δ^8 (**45**) and Δ^9 THC (**43**), the reaction mixture was purified using an automated Biotage system. This system is based on a specialized cannabinoid column with a methanol/water solvent mixture (Supplemental Figure S1), designed for cannabinoids and achieved effective separation of the tosylated intermediates from side products. Multiple fractions were collected from the Biotage system for both samples. Each fraction was individually analyzed by LC-MS to determine its composition. Once the fractions containing THC-tosylate were identified, they were pooled together to concentrate the product. This combined sample was then subjected to NMR spectroscopy for further structural characterization, confirming the presence of the tosylate group. The NMR spectra (Supporting Information) revealed the presence of characteristic doublets signals in the aromatic region, which corresponds to the protons on the benzene ring of the tosylate group and confirmed the successful formation of the tosylate intermediate. However, a closer examination of the NMR spectra revealed that the aliphatic region for both tosylated Δ^8 (**45**) and Δ^9 THC (**43**) appeared complex and disordered, indicating potential impurities or structural heterogeneity.

Further detailed analysis of the NMR spectra obtained from multiple purification attempts and precursor syntheses, including THC-OTs and THC-Br, revealed additional information. The complexity in the aliphatic region suggested the presence of a mixture of Δ^8 and Δ^9 isomers, likely resulting from the cyclization step during the synthesis (Figure 5.1B). Despite following published procedures for the synthesis of the precursor THC-Br [21], the presence of isomeric mixtures and the need for additional purification steps showed the importance of refining the synthesis and purification protocols from the previously published procedure [21]. This refinement was necessary to ensure the isolation of pure Δ^8 and Δ^9 THC-tosylate intermediates, which was crucial for subsequent radiolabeling studies where purity and structural integrity were essentials for receptor

engagement and biodistribution assay. Despite observing that the aliphatic regions in the NMR spectra of the tosylated products was complex, with multiple peaks resulting from a mixture of the two isomers, Δ^8 and Δ^9 THC intermediates, it was decided to proceed with the reaction to convert the tosylated intermediates to their fluorinated forms.

The decision to proceed with the fluorination reaction was driven by the expectation that the isomers could be effectively separated using HPLC purification. Multiple HPLC methods were explored, employing various gradient solvents, to achieve this separation for fluorinated Δ^8 THC (**46**) (Table 5.2) and fluorinated Δ^9 THC (**44**) (Table 5.3). The solvent system used was a mixture of acetonitrile with 0.1% TFA and water with 0.1% TFA. This method aimed to mimic established HPLC purification methods for cannabinoids to achieve effective separation and purification of the intermediates [31, 32]. The goal was to identify conditions under which fluorinated Δ^8 (**46**) and Δ^9 THC (**44**) isomers would elute at distinct retention times, enabling their separation and subsequent isolation.

Despite employing multiple solvents gradient systems for both fluorinated Δ^8 THC (**46**) and Δ^9 THC (**44**), achieving a clear separation between the two isomers remained difficult, where each chromatographic attempt presented unique challenges and outcomes. Concerning Δ^8 THC-F (**46**) (Figure 5.4), the chromatogram consistently presented a major peak at around 5 minutes. This peak was hypothesized to correspond to hydroxy-THC, a side product formed during the fluorination reaction. Following this initial peak, a broad and complex region was observed, which did not allow for the distinct separation of the two isomers. The absence of well-defined peaks in this region indicated co-elution or insufficient resolution under the tested conditions.

In the case of Δ^9 THC-F (**44**) (Figure 5.5), the gradient solvent system used were nearly identical. The only differences between the methods were the duration of the chromatographic

runs and the length of the 100 % acetonitrile (solvent B) plateau [33]. The goal of adjusting this plateau was to improve isomer separation and potentially obtained a major peak corresponding in this case to Δ^9 THC-F (**44**) with the most successful method for the final attempt (Figure 5.6).

It demonstrated a clear separation with two major peaks at approximately 15 and 17 minutes, along with several minor peaks that likely resulted from side products or contaminants from previous reactions. This method offered the best resolution among the attempts, suggesting its potential for isomer separation. However, multiple attempts were made to reproduce the results by adjusting the sample concentration or the injection's volume, with the aim of transitioning to a semi-preparative system for large-scale purification. Unfortunately, these efforts did not provide consistent results, highlighting the sensitivity of the separation process to subtle changes in experimental conditions.

Table 5.2 HPLC methods attempts for the separation of Δ^8 THC-F (**46**) at a flow rate of 1.5 mL/min, where solvent A is water + 0.1 % TFA and solvent B is acetonitrile + 0.1 % TFA.

Attempt	Solvent A (%)	Solvent B (%)	Time (min)
1	50 0	50 100	0.00 20.00 – 22.00
2	99 0 99	1 100 1	0.00 25.00 – 30.00 30.01 – 35.00
3	75 0 75	25 100 25	0.00 25.00 – 30.00 30.01 – 35.00

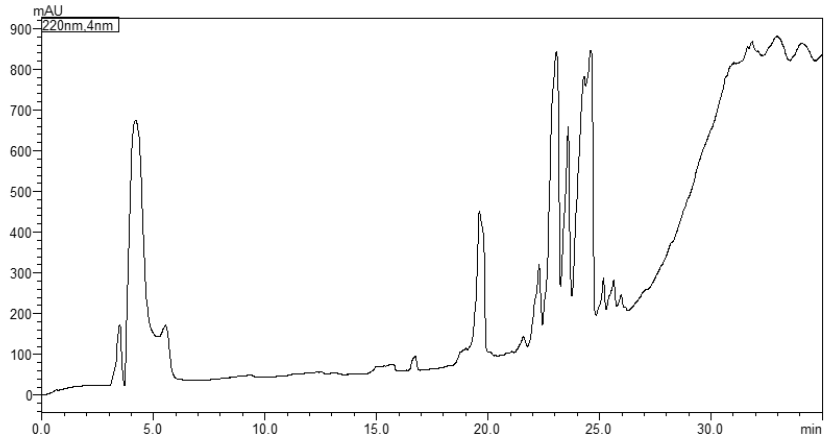

Figure 5.4 HPLC chromatogram of Δ^8 THC-F (**46**) with the gradient system of attempt 3, as detailed in Table 5.2. Chromatogram was acquired using a solvent system of water + 0.1 % TFA and acetonitrile + 0.1 % TFA, at a wavelength of 220 nm, a flow rate of 1.5 mL/min and a volume of injection of 10 µL.

Table 5.3 HPLC methods attempts for the separation of Δ^9 THC-F (**44**) at a flow rate of 1.5 mL/min, where solvent A is water + 0.1 % TFA and solvent B is acetonitrile + 0.1 % TFA. Each run was realized at a flow rate of 1.5 mL/min.

Attempt	Solvent A (%)	Solvent B (%)	Time (min)
1	50 0	50 100	0.00 23.00 – 29.00
2	50 0	50 100	0.00 24.00 – 40.00
3	50 0	50 100	0.00 7.00 – 15.00
4	50 0	50 100	0.00 7.00 – 20.00
5	99 0 99	1 100 1	0.00 25.00 – 30.00 30.01 – 35.00

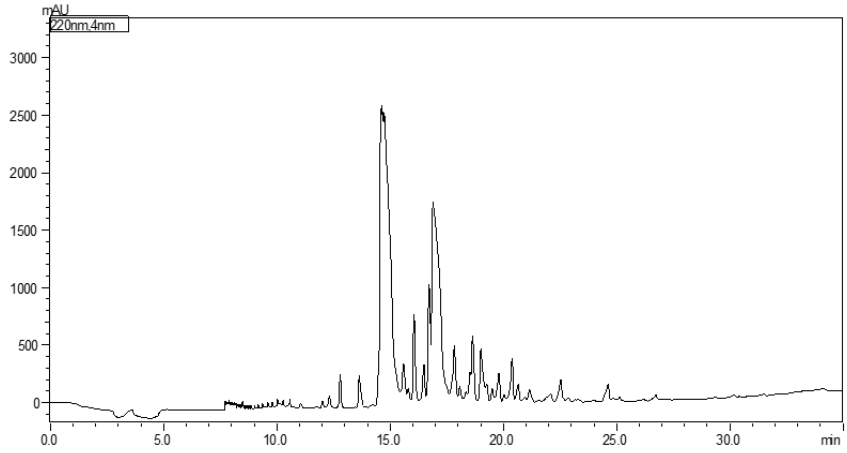

Figure 5.5 HPLC chromatogram of Δ^9 THC-F (**44**) with the gradient system of attempt 5, as detailed in Table 5.3. Chromatogram was acquired using a solvent system of water + 0.1 % TFA and acetonitrile + 0.1 % TFA, at a wavelength of 220 nm, a flow rate of 1.5 mL/min and a volume of injection of 10 µL.

Giving the challenges encountered in the purification of THC-F isomers and the observed complexity in the NMR spectra of THC-Br, even if the published procedure to obtain this intermediate was followed [21], efforts were redirected towards optimizing the purification of THC-Br using HPLC.

The synthesis of Δ^9 THC-Br (**42**) was produced through a single cyclization step, which was then followed by a straightforward filtration and flash chromatography for initial purification [21]. Considered a more practical starting point for HPLC purification attempts, this allowed the investigation and refinements of various HPLC gradients systems (Table 5.4) for Δ^9 THC-Br (**42**). The objective was to identify the best parameters for separating Δ^9 THC-Br (**42**) from its isomer, Δ^8 THC-Br (**41**).

Table 5.4 HPLC methods attempts for the separation of Δ^9 THC-Br (**42**) at a flow rate of 1.5 mL/min, where solvent A is water + 0.1 % TFA and solvent B is methanol + 0.1 % TFA. Each run was realized at a flow rate of 1.5 mL/min.

Attempt	Solvent A (%)	Solvent B (%)	Time (min)	Volume of Injection (µL)
1	20	80	0.00 – 23.00	100
2	20	80	0.00 – 23.00	10
3	25	75	0.00 – 30.00	50
4	30	70	0.00 – 20.00	50
5	60 20	40 80	0.00 20.00 – 30.00	10
6	60 20	40 80	0.00 20.00 – 30.00	100
7	60 10 10	40 90 90	0.00 – 15.00 15.01 – 17.00 17.01 – 30.00	10
8	30 15	70 85	0.00 20.00	10

A chromatogram (Figure 5.6A) was obtained with a reduced injection volume of 10 µL revealing a splitting peak at approximately 10 minutes. Based on the purity of the previously obtained intermediates, it was hypothesized that this splitting peak represented the isomers, Δ^8 (**41**) and Δ^9 THC-Br (**42**), presenting also the same peak shape of what can be found in the literature [34].

A new gradient profile was designed, starting with a plateau at 60% methanol (solvent B) for 15 minutes, followed by an increase to 90% and a second 15-minute plateau (Figure 5.6B). This approach aimed to provide more time for the compound to interact with the stationary phase and potentially improve separation. However, this gradient profile resulted in multiple broad peaks starting at 20 minutes and continuing to the end of the run, further complicating the separation.

Multiple factors may have contributed to the challenges in separating Δ^8 (**41**) and Δ^9 THC-Br (**42**) isomers using the initial HPLC methods. A primary reason was the similar polarity between these isomers since they have nearly identical chemical structures, which made it difficult to achieve effective separation using standard HPLC techniques. This similarity caused the isomer to interact with the stationary phase in almost identical ways, leading to overlapping peaks. In summary, different isocratic and gradient elution methods were explored to separate the Δ^8 (**41**) and Δ^9 THC-Br (**42**) isomers. While some adjustments led to changes in peak shape and retention time, none of the attempted methods successfully resolved the isomers into two distinct peaks. However, the splitting peak was observed on most of the chromatograms obtained, suggesting the association to both Δ^8 (**41**) and Δ^9 THC-Br (**42**) isomers. Therefore, it was decided to separate the samples using an analytical-scale fraction collector HPLC (Agilent), enabling their subsequent collection and validation through NMR.

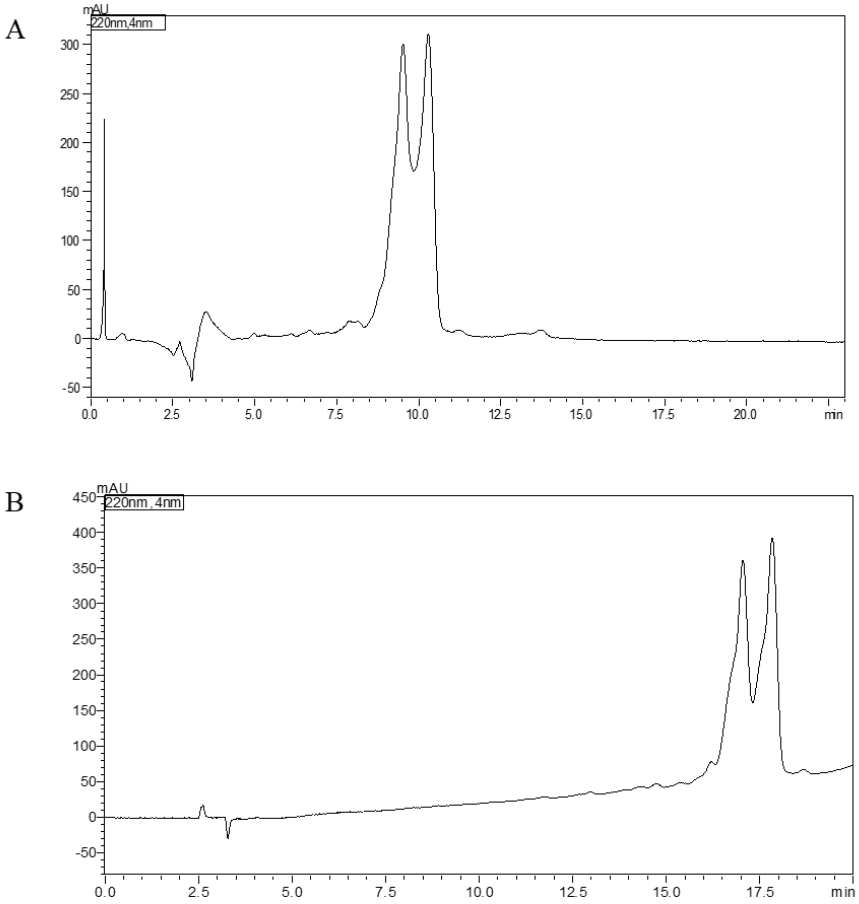

Figure 5.6 Comparative HPLC chromatograms of Δ^9 THC-F (**44**). (A) shows the gradient system of attempt 2 and (B) shows the gradient system of attempt 8, as detailed in Table 5.4. Chromatograms were acquired using a solvent system of water + 0.1 % TFA and methanol + 0.1 % TFA, at a wavelength of 220 nm and a flow rate of 1.5 mL/min.

To achieve the best separation possible of the isomers, multiple experiments were conducted to optimize HPLC conditions and provided baseline separation, as evident in the chromatograms for at least one of the samples (Figure 5.7 & Figure 5.8). In figure 5.7B, which represented the Δ^9 THC-Br (**42**) sample, two main peaks were observed on the chromatogram with nearly identical intensities. This observation suggested that the isomer mixture was present in approximately equal

proportions, indicating that the synthesis procedure resulted in a roughly 1:1 mixture of Δ^8 THC-Br (**41**) and Δ^9 THC-Br (**42**) isomers. This finding highlighted the challenge of selectively synthesizing one isomer over the other using the published method [21].

The HPLC system used a reversed-phase C18 column, known for separating compounds based on their hydrophobicity. Given that methanol is more polar than acetonitrile [35], its use as the organic solvent in the mobile phase influenced the retention times of the compounds. The presence of halogen atoms on the aliphatic chain of THC-Br isomers altered their polarity, affecting their interaction with the stationary phase of the C18 column. This resulted in later retention times compared to pure standard.

Based on these observations, the peaks in Figure 5.7B could be attributed as follows: Δ^9 THC-Br (**42**) eluted first (t_R = 9.5 minutes) and Δ^8 THC-Br (**41**) eluted second (t_R = 10.5 minutes). This attribution was supported by the known differences in polarity and interaction with the stationary phase [34, 36]. To validate the hypothesis that the synthesis step produced both isomers, the decision was made to collect these two peaks and to characterize them through NMR. Peak 1, characterized in Figure 5.7A, showed a singlet at 4.87 ppm that integrated for one hydrogen, which is specific to the double bond of Δ^9 THC-Br (**42**) [37, 38]. This observation, along with the matching integration values and chemical shifts, confirmed that peak 1 (t_R = 9.5 minutes) corresponded to Δ^9 THC-Br (**42**).

In contrast, peak 2, characterized in Figure 5.7C, showed a singlet at 5.43 ppm that integrated for one hydrogen, which is specific to the doublet bond of Δ^8 THC-Br Br (**41**) [37, 38]. However, upon closer examination, some chemical shifts and integration values in the NMR spectrum of peak 2 did not perfectly align with the expected values for Δ^8 THC-Br (**41**), particularly in the aliphatic region. While the NMR characterization of peak 1 confirmed its identity as Δ^9 THC-Br

(**42**), the identity of peak 2 remains less certain. It was possible that peak 2 represented a Δ^8 THC analogue or an incomplete cyclized product that closely resembled Δ^8 THC-Br (**41**). This ambiguity could be attributed to the fact that the sample was synthesized using the procedure intended for Δ^9 THC-Br (**42**) (Figure 5.1B). Since Δ^8 (**41**) and Δ^9 THC-Br (**42**) are produced through different synthesis steps, the presence of an analogue or incomplete cyclization product is plausible. The HPLC analysis and subsequent NMR characterization provided valuable insight into the composition of the synthesized samples. While Δ^9 THC-Br (**42**) was successfully isolated and characterized, the identity of the second peak required further investigation. Additional experiments, such as optimizing the synthesis conditions or employing alternative purification techniques, might be necessary to obtain pure Δ^8 THC Br (**41**) and confirm its structure.

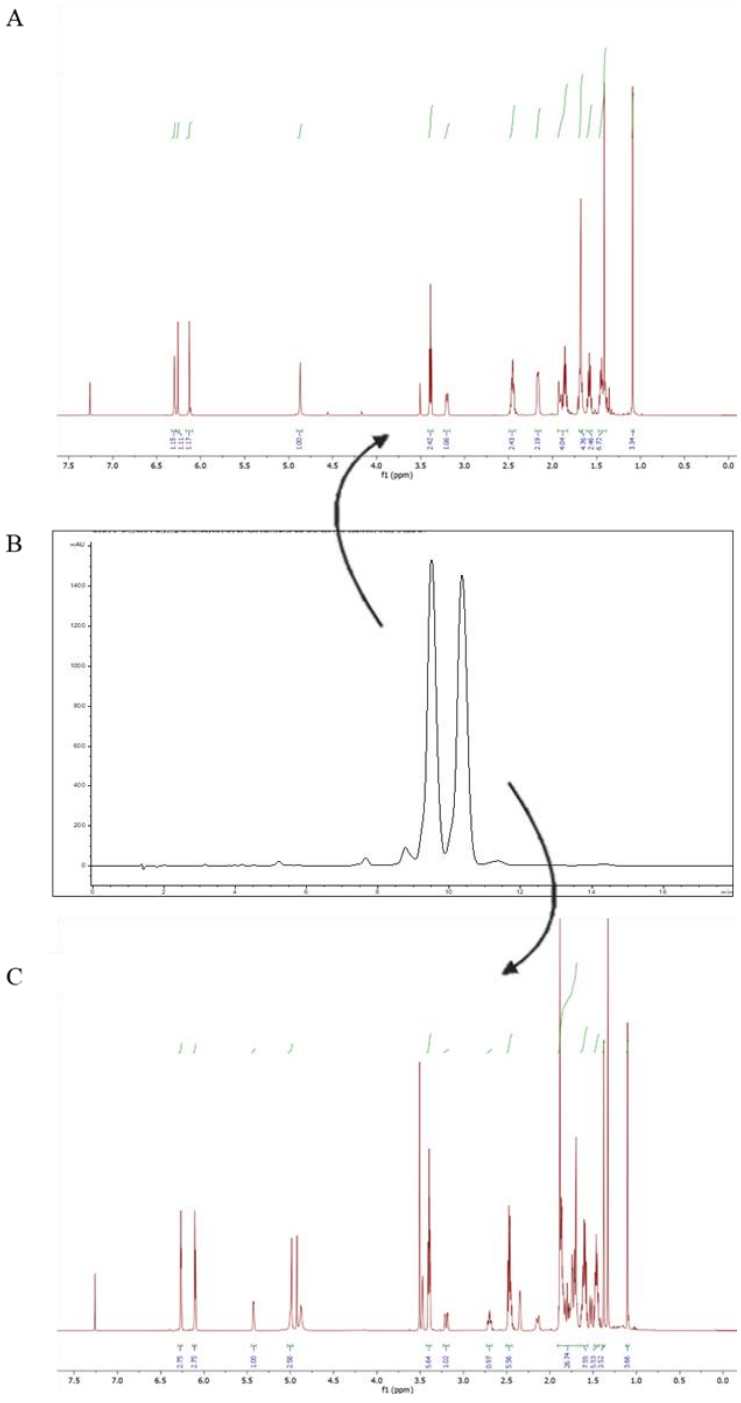

Figure 5.7 Isolation and Characterization of Δ^9 THC-Br (**42**). (A) ^{1}H NMR spectrum characterization of peak 1 (t_R = 9.5 minutes). (B) HPLC chromatogram of Δ^9 THC-Br (**42**) sample obtained on Agilent HPLC system. (C) ^{1}H NMR spectrum characterization of peak 1 (t_R = 10.5 minutes).

The same analytical procedure was applied to the Δ^8 THC-Br (**41**) sample, with the results presented in Figure 5.8. In Figure 5.8B, which represented the chromatogram of Δ^8 THC-Br (**41**) sample, two major peaks were observed at a retention times of 9.8 and 10.5 minutes. These peaks were presumed to correspond to the isomer mixture of Δ^8 (**41**) and Δ^9 THC-Br (**42**). Additionally, smaller peaks observed before 9.8 minutes were likely due to residual contaminants from the synthesis reactions, indicating the presence of impurities in the sample. Applying the same reasoning as before, it was suggested that the first peak (t_R = 9.8 minutes) might correspond to Δ^9 THC-Br (**42**), while the second peak (t_R = 10.5 minutes) corresponded to Δ^8 THC-Br (**41**). This observation indicated that the synthesis procedure for Δ^8 THC-Br (**41**) also resulted in a mixture of isomers, but with a different ratio compared to the Δ^9 THC-Br (**42**) sample. Specifically, there appeared to be a higher proportion of assumed Δ^9 THC-Br (**42**) relative to Δ^8 THC-Br (**41**) in this sample.

To validate the hypothesis that a mixture of isomers was obtained, both peaks were isolated and collected for characterization by NMR. The NMR spectrum of the second peak (Figure 5.8C) revealed the presence of a singlet at 5.46 ppm, which is characteristic of the specific double bond in Δ^8 THC-Br (**41**). This observation, along with the correct chemical shifts and integration values for all other signals in the spectrum [37, 38], confirmed that the second peak corresponded to Δ^8 THC-Br (**41**). However, a closer examination of the first peak and its characterization by NMR reveals some differences. The NMR spectrum of the first peak showed a signal at 4.87 ppm, which is expected to correspond to the double bond of Δ^9 THC-Br (**42**). Instead of the typical singlet observed for this bond, a doublet of doublet was presented, which still integrated for one hydrogen. This unusual splitting pattern and the fact that some integration values did not align perfectly with the expected values [37, 38] suggested that the first peak may not be pure Δ^9 THC-Br (**42**).

The synthesis of Δ^8 THC-Br (**41**) involved a separate chemical step (Figure 5.1B) designed to produce a higher yield of Δ^8 THC-Br (**41**). Therefore, the presence of Δ^9 THC-Br (**42**) in this sample is unexpected. It was possible that the first peak represented a derivative of Δ^9 THC-Br (**42**) or a side product that did not fully cyclize during the synthesis step. This hypothesis was supported by the presence of extra signals in the NMR spectrum of the first peak (Figure 5.8A), which exhibited chemical shifts and integration values that were not characteristic of Δ^9 THC-Br (**42**). These additional signals suggested the presence of impurities or side products that were not fully separated during the HPLC analysis. The complexity of the synthesis process and the potential for side reactions to happen may contribute to the formation of these byproducts. The HPLC and NMR analyses provided valuable insights into the composition of the Δ^8 THC-Br (**41**) sample. While the second peak was confirmed to be Δ^8 THC-Br (**41**) (Figure 5.8C), the first peak required further investigation to determine its identity. The presence of unexpected signals in the NMR spectrum and integration values of the first peak suggested that it may be a derivative or side product rather than pure Δ^9 THC-Br (**42**). Additional experiments will be necessary to fully characterize this peak and optimize the synthesis and purification of Δ^8 THC-Br (**41**).

In a word, both sets of peaks for both chromatograms (Figure 5.7 & Figure 5.8) were collected separately to validate the hypothesis via NMR analysis. The aim of this additional purification step was to determine if the HPLC separation reduced the complexity in the aliphatic region of the NMR spectra. By achieving better separation and purification, it was expected that the NMR spectra will be cleaner, allowing for more accurate identification and characterization of the individual isomers.

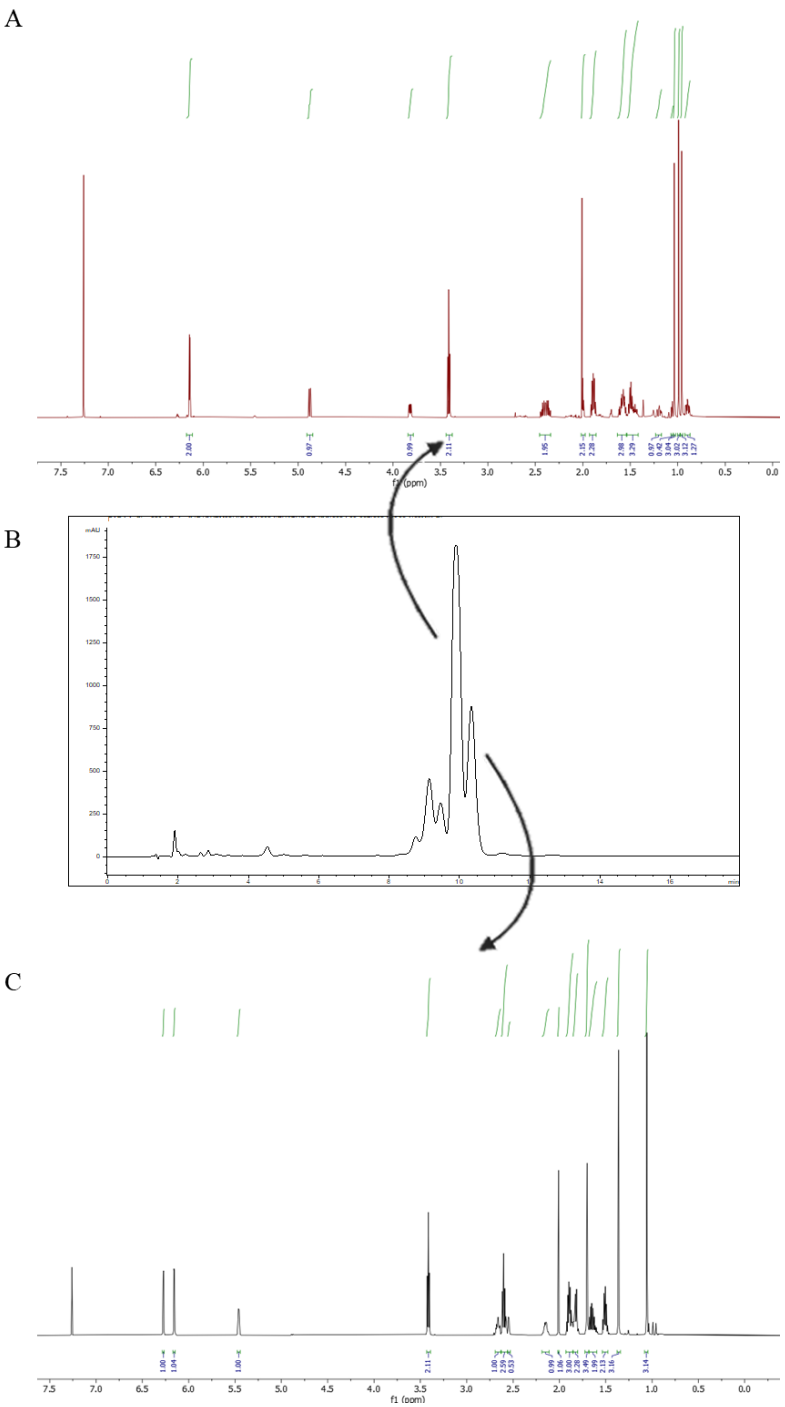

Figure 5.8 Isolation and Characterization of Δ^8 THC-Br (**41**). (A) ^{1}H NMR spectrum characterization of peak 1 (t_R = 9.8 minutes). (B) HPLC chromatogram of Δ^8 THC-Br (**41**) sample obtained on Agilent HPLC system. (C) ^{1}H NMR spectrum characterization of peak 1 (t_R = 10.5 minutes).

5.6. Conclusion

The primary focus of this project was to convert brominated THC analogues, based on a published method, to their fluorine counterparts to study their biodistribution and receptor engagements in the body. During the synthesis, HPLC analysis revealed the need for an additional step to generate tosylated Δ^8-THC and Δ^9-THC intermediates, based on their retention times. What was initially intended to be a straightforward replication of a published synthesis to produce brominated Δ^8-THC and Δ^9-THC turned into a whole purification process due to the presence of additional signals on the NMR characterization. This involved the addition of HPLC and automated flash column chromatography, highlighting the complexity of working with these molecules despite their prior publication. The next step of this project would be the addition of radioactive fluorine (^{18}F) to the end of the aliphatic chain, producing THC-based radiotracers with minimal modification of Δ^8 and Δ^9 THC.

5.7. Conflict of Interests

There are no conflicts to declare.

5.8. Supplementary Information

5.8.1. General Experimental Procedures

All materials were either purchased commercially or synthesized according to the methods outlined below. Solvents used were HPLC grade except for water (18.2 MΩ cm Millipore-grade). Volatile substances were removed using a rotary evaporator under reduced pressure. Thin-layer chromatography (TLC) was conducted on aluminum-backed silica gel plates, and compounds were visualized using Hanessian's stain and UV light. Concerning nuclear magnetic resonance (NMR) spectroscopy, ^{1}H NMR spectra were recorded using 400 or 600 MHz instruments, with chemical shifts values (δ) of 2.50 ppm for DMSO-D_6 and 7.26 ppm for $CDCl_3$. For ^{13}C NMR, the δ values were 39.50 ppm for DMSO-D_6 and 49.0 ppm for $CDCl_3$. High-resolution mass spectrometry (HRMS) data were acquired using electrospray ionization (ESI).

5.8.2. Synthetic Procedure

Preparation of 5-phenoxy-1-(3,5-dimethoxyphenyl)pentanol (37)

To a stirred suspension of magnesium (530.5 mg, 21.82 mmol) in THF (22 mL), a solution of 4-phenoxybutyl bromide (5.257 g, 21.82 mmol) was added dropwise in a flame-dried flask. The mixture was kept under reflux at 50 °C for 20 minutes followed by an additional hour at 70 °C. As the Grignard reagent cooled to room temperature, 3,5-dimethoxybenzaldehyde (2.13 g, 12.84 mmol) was dissolved with THF (43 mL). The Grignard solution was then transferred and stirred for 30 minutes at -78 °C. The mixture was warmed to room temperature and stirred for an additional hour. After 1 hour, the reaction was quenched by dropwise addition of saturated NH_4Cl (20 mL). The solution was then partitioned between brine (20 mL) and EtOAc (2 × 45 mL). The combined organic extracts were dried over Na_2SO_4 and concentrated. The residue was purified by flash column chromatography (FCC) on 60 g of silica gel using hexane/EtOAc 4:1 then 3:2 as the eluent. Evaporation of the collected fractions provided the 5-phenoxy-1-(3,5-dimethoxyphenyl)pentanol **37** as a colorless oil, 3.13 g, 77 %. ^{1}H NMR (600 MHz, $CDCl_3$) δ 7.27 – 7.23 (m, 2H), 6.90 (tt, *J* = 7.3, 1.1 Hz, 1H), 6.87 – 6.84 (m, 2H), 6.49 (d, *J* = 2.3 Hz, 2H), 6.36 (t, *J* = 2.3 Hz, 1H), 4.62 (ddd, *J* = 7.7, 5.5, 3.2 Hz, 1H), 3.93 (t, *J* = 6.5 Hz, 2H), 3.77 (s, 6H), 1.86 (d, *J* = 3.3 Hz, 1H), 1.84 – 1.71 (m, 4H), 1.64 – 1.55 (m, 1H), 1.51 – 1.42 (m, 1H). ^{13}C NMR (100 MHz, CDCl3) δ 161.00, 159.10, 147.50, 129.53, 120.64, 114.58, 103.86, 99.51, 74.69, 67.72, 55.46, 38.76, 29.27, 22.56.

Preparation of 5-phenoxy-1-(3,5-dimethoxyphenyl)pentane (38)

In a flask, TMSCl (7.52 mL, 59.22 mmol) and sodium iodide (8.9 g, 59.4 mmol) were mixed with acetonitrile (4 mL) and stirred for 15 minutes at room temperature. In a separate vial, compound **37** (3.1216 g, 9.87 mmol) was dissolved in a mixture of Et_2O (6.77 mL) and hexane (5.2 mL) before being transferred to the initial flask. The mixture was stirred at room temperature under argon for 24 hours. The reaction was quenched with water (30 mL) and the solution was extracted with Et_2O (4 × 25 mL). The combined organic extracts were washed with a saturated aqueous thiosulfate solution (3 × 50 mL) and brine (3 × 50 mL). The organic solution was dried over Na_2SO_4 and concentrated. Without any further purification, evaporation provided the 5-phenoxy-1-(3,5-dimethoxyphenyl)pentane **38** as a light-yellow oil, 2.6 g, 87%. ^{1}H NMR (400 MHz, $CDCl_3$) δ 7.32 – 7.23 (m, 2H), 6.97 – 6.86 (m, 3H), 6.37 (d, *J* = 2.3 Hz, 2H), 6.32 (t, *J* = 2.3 Hz, 1H), 3.96 (t, *J* = 6.5 Hz, 2H), 3.79 (s, 6H), 2.64 – 2.57 (m, 2H), 1.83 (dq, *J* = 8.1, 6.6 Hz, 2H), 1.75 – 1.65 (m, 2H), 1.58 – 1.47 (m, 2H). ^{13}C NMR (101 MHz, $CDCl_3$) δ 160.81, 159.15, 145.08, 129.51, 120.59, 114.56, 106.57, 97.73, 67.78, 55.32, 36.30, 31.14, 29.28, 25.87.

Preparation of 1-(3,5-dihydroxyphenyl)-5-bromopentane (39)

The product **38** (2.6 g, 9.58 mmol) was initially dissolved in dichloromethane (20.7 mL) and cooled to -78 °C before adding a 1 M BBr_3 solution (4.6 mL, 47.9 mmol). The mixture was slowly warmer to room temperature and stirred for 36 hours. The reaction was quenched with a dropwise saturated $NaHCO_3$ solution (60 mL) followed by an extraction with ether (3 × 60 mL). The combined organic extracts were washed with saturated NaHCO3 solution (3 × 50 mL) and brine (3 × 50 mL). The residue was purified by FCC on 60 g of silica using hexane/EtOAc 4:1 then 3:2

as the eluent. Evaporation of the collected fractions provided the 1-(3,5-dihydroxyphenyl)-5-bromopentane **39** as a light brown-oil, 2.02 g, 81%. ^{1}H NMR (400 MHz, $CDCl_3$) δ 7.54 (s, 2H), 6.32 (d, J = 3.7 Hz, 3H), 3.31 (t, J = 6.8 Hz, 2H), 2.39 (t, J = 7.6 Hz, 2H), 1.76 (p, J = 7.0 Hz, 2H), 1.47 (p, J = 7.5 Hz, 2H), 1.35 (q, J = 8.1 Hz, 2H). ^{13}C NMR (100 MHz, $CDCl_3$) δ 156.76, 145.60, 108.15, 100.48, 35.67, 33.97, 32.76, 30.25, 27.86.

Preparation of 2-[(1S-cis)-4,6,6-trimethylbicyclo[3.1.1]hept-3-en-2-yl]-5-(5-bromopentyl)resorcinol (40)

(S)-*cis* verbenol (237.4 mg, 1.56 mmol) was first dissolved in chloroform (4.5 mL) and then transferred to a flame-dried flask containing a solution of 1-(3,5-dihydroxyphenyl)-5-bromopentane **39** (403.9 mg, 1.56 mmol) and *p*-toluenesulfonic acid (30 mg, 0.156 mmol) in chloroform (9 mL). The mixture was stirred under argon at room temperature. After 2.5 hours, the reaction mixture was partitioned between $NaHCO_3$ (60 mL) and dichloromethane (2 × 40 mL). The combined organic layers were dried using Na_2SO_4 and concentrated. The resulting residue was purified by FCC on 50 g of silica using hexane/EtOAc 9:1 as the eluent. Evaporation of the collected fractions provided the 2-[(1S-cis)-4,6,6-trimethylbicyclo[3.1.1]hept-3-en-2-yl]-5-(5-bromopentyl)resorcinol **40** as a yellow oil, 168.4 mg, 27%. ^{1}H NMR (400 MHz, $CDCl_3$) δ 6.19 (s, 2H), 5.70 (dd, *J* = 3.1, 1.7 Hz, 1H), 3.91 (q, *J* = 2.6 Hz, 1H), 3.40 (t, *J* = 6.9 Hz, 2H), 2.46 (t, *J* = 7.6 Hz, 2H), 2.36 – 2.22 (m, 2H), 2.21 – 2.15 (m, 1H), 1.92 – 1.82 (m, 5H), 1.63 – 1.54 (m, 4H), 1.51 – 1.41 (m, 3H), 1.32 (s, 3H), 0.96 (s, 3H). ^{13}C NMR (100 MHz, CDCl3) δ 157.60, 154.86, 152.64, 143.26, 117.95, 116.97, 108.88, 102.01, 48.50, 47.93, 41.11, 39.75, 33.84, 32.95, 32.73, 31.73, 30.67, 28.40, 27.38, 26.11, 23.83, 22.79, 20.53, 14.27.

Preparation of 3'-bromo-Δ^8-tetrahydrocannabinol (41)

A solution of 2-[(1S-cis)-4,6,6-trimethylbicyclo[3.1.1]hept-3-en-2-yl]-5-(5-bromopentyl)resorcinol **40** (168.4 mg, 0.43 mmol) in dichloromethane (7.8 mL) was cooled to 0°C under argon. BF_3/Et_2O (105 µL, 0.86 mmol) was added, and the mixture was allowed to warm temperature before being stirred for 2 hours. The reaction mixture was then extracted with $NaHCO_3$ (45 mL) and DCM (2 × 30 mL). The combined organic extracts were dried over Na_2SO_4 and concentrated. The resulting residue was purified by FCC on 40 g of silica using DMC/hexane 75:25 as the eluent. Evaporation of the collected fractions provided the 3'-bromo-Δ^8-tetrahydrocannabinol **41**, as a yellow oil, 82.8 mg, 49% [isoform mixture]. ^{1}H NMR (600 MHz, CDCl3) δ 6.28 (d, *J* = 2.7 Hz, 1H), 6.15 (q, *J* = 2.2 Hz, 1H), 5.48 – 5.34 (m, 2H), 5.29 (s, 1H), 3.40 (td, *J* = 6.8, 2.3 Hz, 3H), 2.66 (ddd, *J* = 10.8, 8.8, 4.5 Hz, 1H), 2.58 (q, *J* = 7.4 Hz, 3H), 2.15 (ddt, *J* = 13.3, 7.2, 3.1 Hz, 1H), 1.92 – 1.77 (m, 8H), 1.69 (s, 4H), 1.67 – 1.58 (m, 4H), 1.50 (tt, *J* = 14.2, 3.4 Hz, 5H), 1.36 (s, 3H), 1.05 (s, 3H). ^{13}C NMR (100 MHz, $CDCl_3$) δ 154.74, 140.06, 119.38, 109.15, 106.80, 76.29, 45.78, 38.90, 33.95, 32.77, 30.49, 27.59, 23.66, 18.66.

Preparation of 3'-bromo-Δ^9-tetrahydrocannabinol (42)

(+)-*p*-mentha-2,8-dien-1-ol (158 mg, 1 mmol) was initially dissolved in DCM (12.35 mL) and then transferred to a flask containing 1-(3,5-dihydroxyphenyl)-5-bromopentane **39** (245.5 mg, 0.95 mmol). Magnesium sulfate (712.5 mg) was added, and the flask was cooled down to -3°C before dropwise addition of BF_3/Et_2O (56 µL, 0.123 mmol). The reaction was stirred for 2.5 hours at 0°C under argon, followed by the addition of anhydrous $NaHCO_3$ (308 mg). The mixture was warmed to room temperature and stirred for another 30 minutes, before being filtrate through Florisil. The

filtrate was concentrated under reduced pressure, and the residue was purified by FCC on 40 g of silica with hexane/ether 10:1 as the eluent. Evaporation of the collected fractions afforded the 3'-bromo-Δ^9-tetrahydrocannabinol **42**, as a light-yellow oil, 213.9 mg, 57% [isoform mixture]. ^{1}H NMR (400 MHz, CDCl3) δ 6.28 (dq, J = 10.0, 2.0 Hz, 4H), 6.15 – 6.08 (m, 3H), 5.43 (d, J = 5.1 Hz, 1H), 4.74 (s, 1H), 3.39 (ddt, J = 6.9, 4.4, 2.2 Hz, 5H), 3.24 – 3.14 (m, 2H), 2.52 – 2.41 (m, 6H), 2.14 (d, J = 14.6 Hz, 3H), 1.96 – 1.76 (m, 16H), 1.76 – 1.66 (m, 12H), 1.59 (d, J = 4.4 Hz, 8H), 1.52 – 1.40 (m, 10H), 1.10 (d, J = 5.4 Hz, 6H). ^{13}C NMR (100 MHz, $CDCl_3$) δ 155.02, 154.94, 142.08, 134.83, 123.80, 119.42, 110.07, 108.10, 107.68, 45.88, 37.12, 35.58, 35.55, 33.94, 33.68, 32.80, 31.67, 30.05, 27.65, 25.11, 23.62, 19.37.

Preparation of 3'-tosyloxy-Δ^9-tetrahydrocannabinol (43)

To a flame-dried flask, 3'-bromo-Δ^9-tetrahydrocannabinol **42** (118.9 mg, 0.3 mmol) was dissolved with acetonitrile (3 mL) before addition of silver tosylate (363 mg, 1.3 mmol). The whole mixture was heated to reflux for 24 hours under nitrogen. The flask was completely evaporated before purifying it through an automated flash chromatography system Biotage. After validation of the fractions by LC-MS, evaporation of the collected fractions afforded 3'-tosyloxy-Δ^9-tetrahydrocannabinol **43**, a light yellow oil, 26.2 mg, 18 % [isoform mixture]. ^{1}H NMR (600 MHz, $CDCl_3$) δ 7.78 (dd, *J* = 8.3, 1.8 Hz, 2H), 7.34 (d, *J* = 8.0 Hz, 2H), 6.21 (dd, *J* = 3.9, 1.5 Hz, 1H), 6.11 – 6.08 (m, 1H), 4.92 (d, *J* = 5.0 Hz, 1H), 4.01 (td, *J* = 6.4, 1.5 Hz, 3H), 3.23 – 3.17 (m, 1H), 2.44 – 2.37 (m, 3H), 1.89 – 1.77 (m, 5H), 1.69 – 1.62 (m, 5H), 1.58 (s, 3H), 1.55 – 1.48 (m, 4H), 1.37 (s, 2H), 1.10 (s, 2H).

Preparation of 3'-fluoro-Δ^9-tetrahydrocannabinol (44)

To a flame-dried flask, 3'-tosyloxy-Δ^9-tetrahydrocannabinol **43** (28.8 mg, 0.06 mmol) was dissolved with acetonitrile (1.2 mL) before addition of TBAF (22 mg, 0.08 mmol). The whole mixture was heated at 80 °C for 2 hours under nitrogen. The flask was completely evaporated before attempted purification through a preparative HPLC.

Preparation of 3'-tosyloxy-Δ^8-tetrahydrocannabinol (45)

To a flame-dried flask, 3'-bromo-Δ^8-tetrahydrocannabinol **41** (116 mg, 0.3 mmol) was dissolved with acetonitrile (3 mL) before addition of silver tosylate (360 mg, 1.29 mmol). The whole mixture was heated to reflux for 24 hours under nitrogen. The flask was completely evaporated before purifying it through an automated flash chromatography system Biotage. After validation of the fractions by LC-MS, evaporation of the collected fractions afforded 3'-tosyloxy-Δ^8-tetrahydrocannabinol **45**, a light yellow oil, 25.4 mg, 17 % [isoform mixture]. ^{1}H NMR (600 MHz, $CDCl_3$) δ 7.79 (d, *J* = 8.2 Hz, 2H), 7.34 (d, *J* = 8.0 Hz, 2H), 6.24 (d, *J* = 2.7 Hz, 1H), 6.15 (d, *J* = 2.7 Hz, 1H), 5.48 – 5.43 (m, 1H), 4.03 (t, *J* = 6.4 Hz, 3H), 2.67 – 2.58 (m, 4H), 2.45 (s, 4H), 2.19 – 2.11 (m, 1H), 1.87 – 1.77 (m, 3H), 1.37 (d, *J* = 8.2 Hz, 7H), 1.04 (d, *J* = 5.5 Hz, 4H). ^{13}C NMR (151 MHz, CDCl3) δ 155.12, 154.65, 143.09, 143.02, 134.47, 129.99, 128.03, 120.27, 108.97, 106.71, 76.28, 70.57, 44.74, 35.87, 35.34, 33.45, 33.10, 30.41, 27.60, 23.48, 21.79, 18.66.

Preparation of 3'-fluoro-Δ^8-tetrahydrocannabinol (46)

To a flame-dried flask, 3'-tosyloxy-Δ^8-tetrahydrocannabinol **45** (25.4 mg, 0.05 mmol) was dissolved with acetonitrile (1 mL) before addition of TBAF (19.4 mg, 0.073 mmol). The whole mixture was heated at 80 °C for 2 hours under nitrogen. The flask was completely evaporated before attempted purification through a preparative HPLC.

HPLC Analysis

Δ^9 THC standard, including brominated **42** and fluorinated Δ^9 THC **44** were analyzed through HLPC system (Shimadzu Prominence-I LC 2030C Plus) by preparing a 1 mg/mL solution in water. The analysis was realized on a polar C18 Scout Kinetex column (100 x 2.1 mm, particle size 2.6 μm, pore size 100 Å). The mobile phase is composed of water + 0.1 % TFA (mobile phase A) and acetonitrile + 0.1 % TFA (mobile phase B). Products are analyzed according to a gradient from 0.0 to 9.50 min 65 % B, 9.51 to 9.60 min 100 % B, 9.61 to 12.00 min 100-65 % B, followed by a 3 minute column equilibration after each run. Chromatograms were detected at 225 nm and a flow rate of 0.4 mL/min was set up with a 30 °C temperature.

Fluorinated Δ^8 **46** and Δ^9 THC **44** were analyzed through HPLC system (Shimadzu) by preparing a 1 mg/mL solution in water + 5 % acetonitrile. The analysis was realized on a polar C18 Phenomenex Luna column (250 x 4.6 mm, particle size 5 μm, pore size Å). The mobile phase is composed of water + 0.1 % TFA (mobile phase A) and acetonitrile + 0.1 % TFA (mobile phase B). Products are analyzed according to multiple solvent gradients presented in Table 5.2 and Table 5.3 depending on the sample. Chromatograms were detected at 220 nm with a flow rate of 1.5 mL/min and 25 °C temperature.

Brominated Δ^8 **41** and Δ^9 THC **42** were analyzed through HPLC system (Agilent) by preparing a 1 mg/mL solution in methanol. The analysis was realized on the same column conditions as the fluorinated samples. The mobile phase is composed of water + 0.1 % TFA (mobile phase A) and methanol + 0.1 % TFA (mobile phase B). Products are analyzed according to an isocratic gradient from 0.0 to 20.0 min 72 % B. Chromatograms were detected at 220 nm with a flow rate of 2 mL/min and a 40 ° C temperature.

Automated flash chromatography system

Tosylated Δ^8 **45** and Δ^9 THC **43** were purified through an automates flash chromatography system (Biotage) by preparing a 5 mg/mL solution in methanol. The purification was realized on a polar 20 g C4 ~ 8 CannFlash SW-5CAN-012-SP column (particle size 20 – 45 µm, pore size 100 Å). The mobile phase is composed of water + 0.1 % TFA (mobile phase A) and methanol + 0.1 % TFA (mobile phase B) Products are analyzed according to solvents gradients expressed in column volume (CV): a plateau of 2 CV 30 % B followed by 3 CV 30-50 % B, plateau of 1 CV 50 % B followed by 3 CV 50-70 % B, plateau of 2 CV 70 % B followed by 2.5 CV 70-90 % B, plateau of 2CV 90 % B followed by 1.5 CV 90-95 % B, plateau of 1 CV 95 % B followed by 2 CV 95-100 % B, plateau of 3 CV 100 % B followed by 1 CV 100-50 % B and 1 CV column equilibration at 50 % B. Chromatograms are detected at any wavelength between 200 and 400 nm with a flow rate of 13 mL/min at room temperature.

5.8.3. Supplementary Data

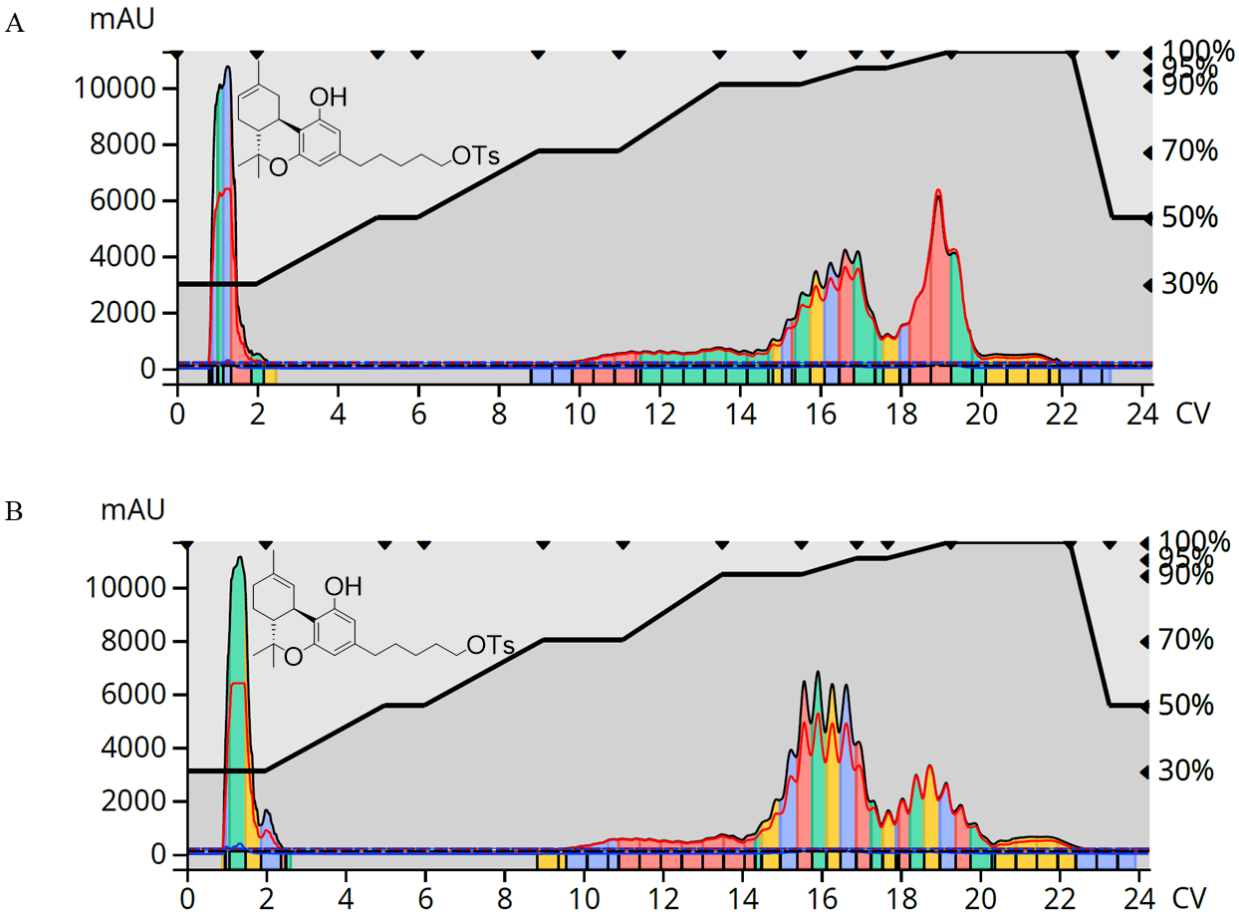

S93. Chromatograms obtained from the purification of (A) tosylated Δ^8 THC **45** and (B) tosylated Δ^9 THC **43** using an automated Biotage system. The chromatograms illustrate the separation of the reaction mixture into several fractions, each collected over time as the mobile phase, a methanol/water mixture, elutes through the CannFlash, a specialized cannabinoid column.

5.8.4. NMR Spectral Characterization

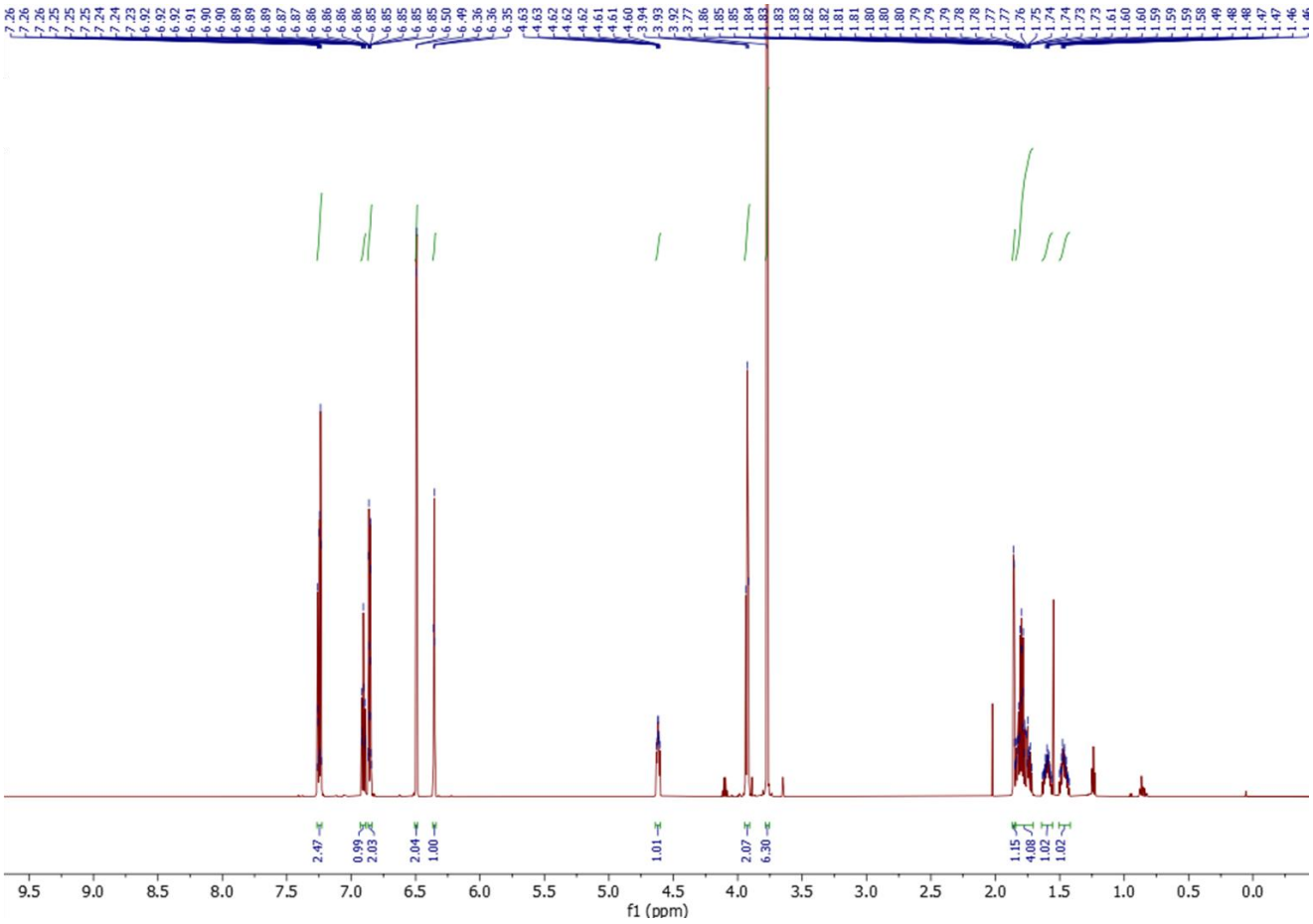

S94. ^{1}H NMR spectrum of compound 37 in $CDCl_3$. Signals at δ 1.26 ppm, 2.05 ppm and 4.12 ppm are due to the presence of ethyl acetate in the sample.

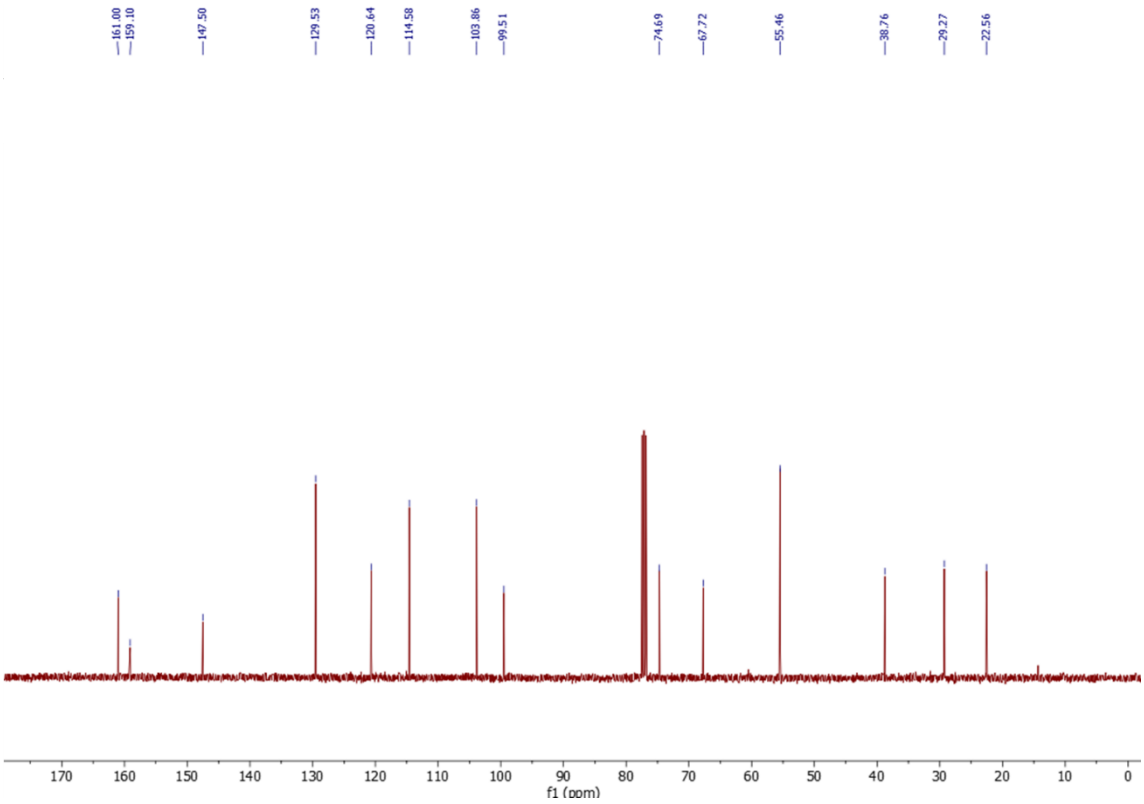

S95. ^{13}C NMR spectrum of compound 37 in $CDCl_3$.

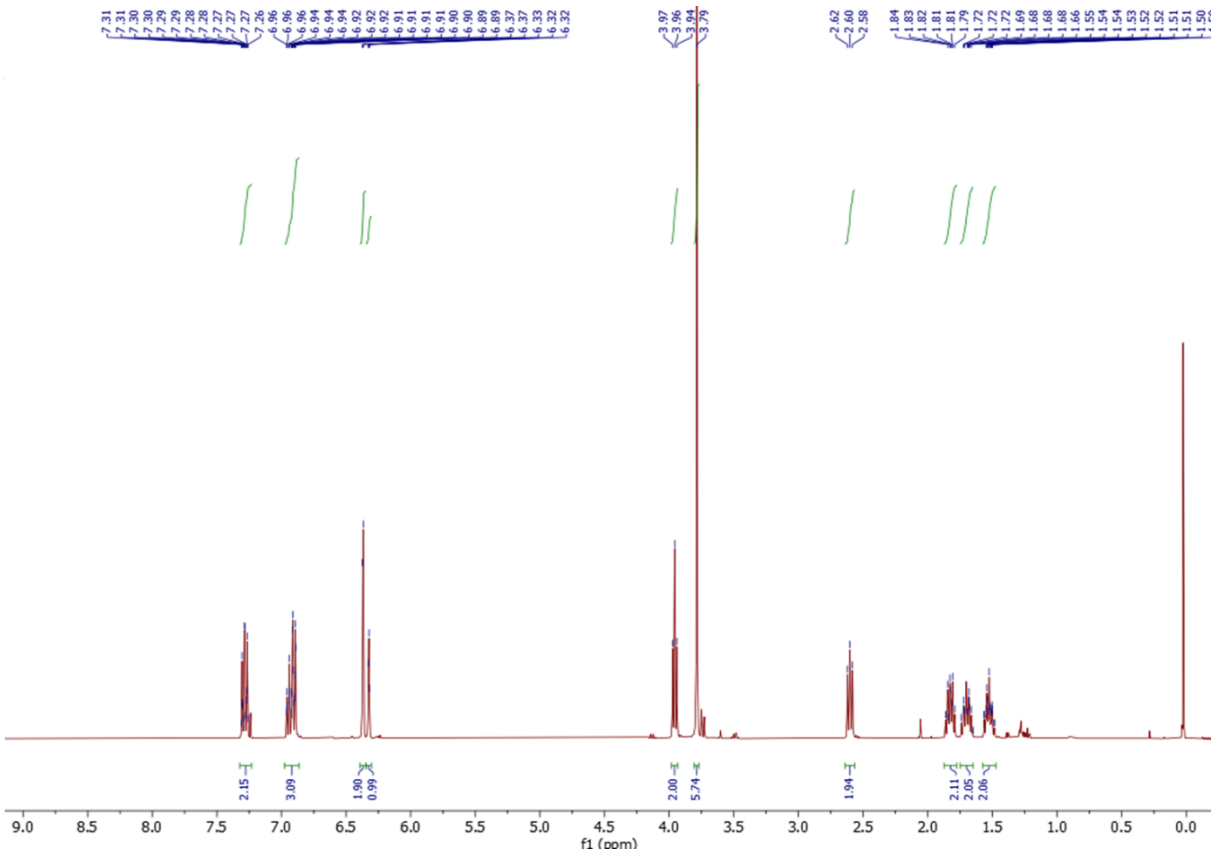

S96. ^{1}H NMR spectrum of compound 38 in $CDCl_3$. The signal at δ 0.0 ppm is due to the presence of tetramethylsilane in the sample.

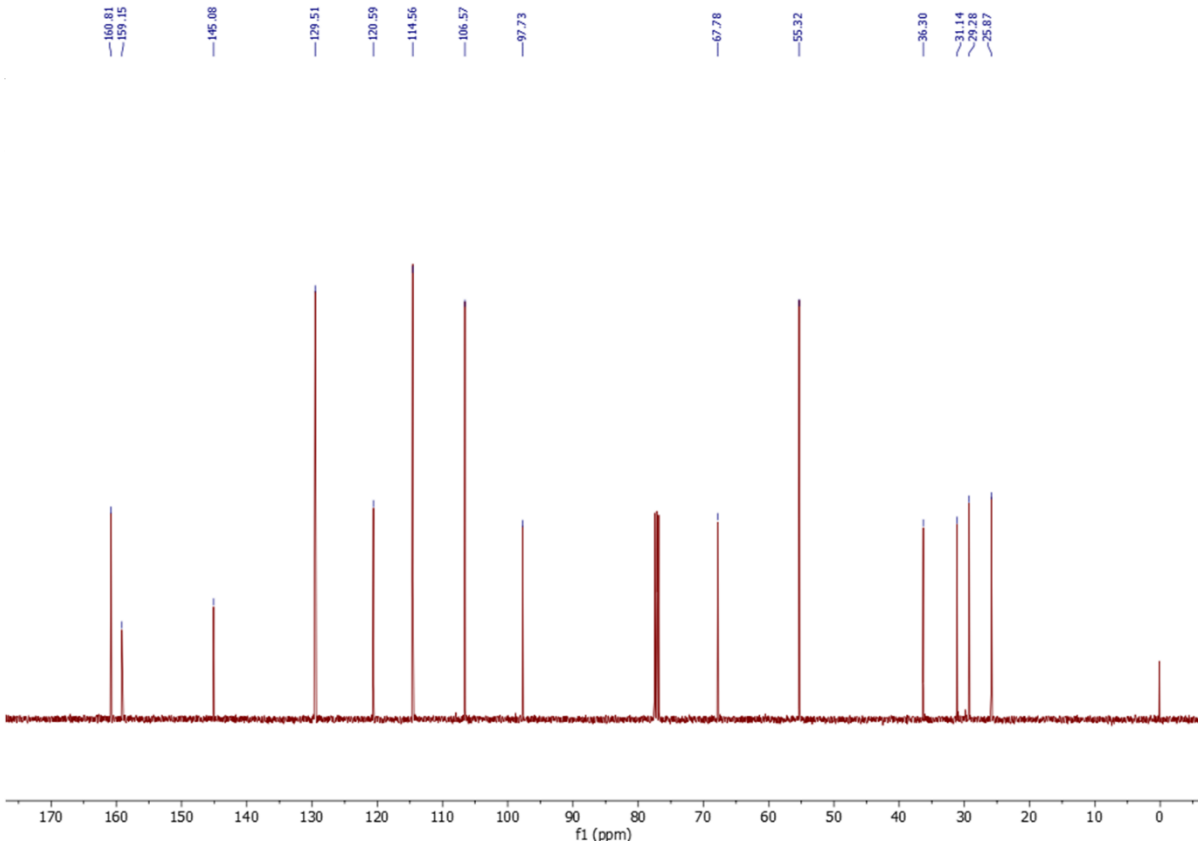

S97. ^{13}C NMR spectrum of compound 38 in $CDCl_3$.

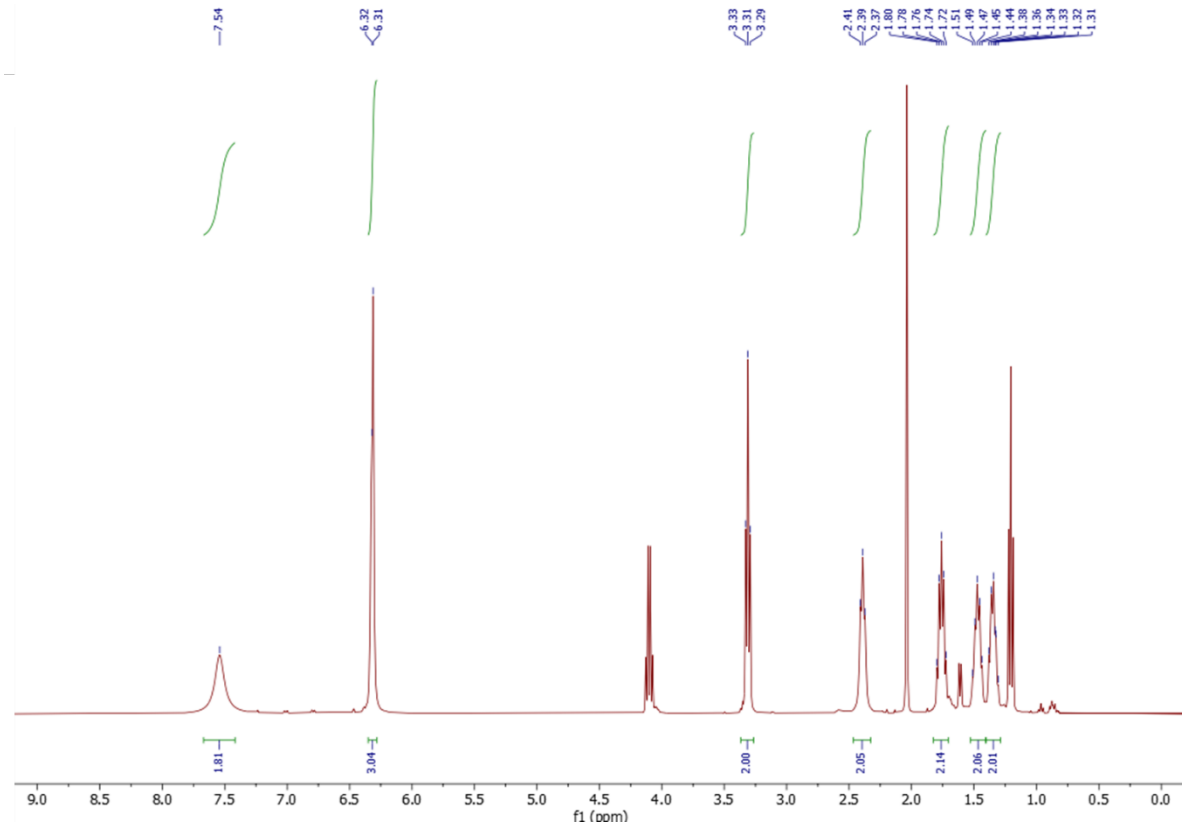

S98. ^{1}H NMR spectrum of compound 39 in $CDCl_3$. Signals at δ 1.26 ppm, 2.05 ppm and 4.12 ppm are due to the presence of ethyl acetate in the sample.

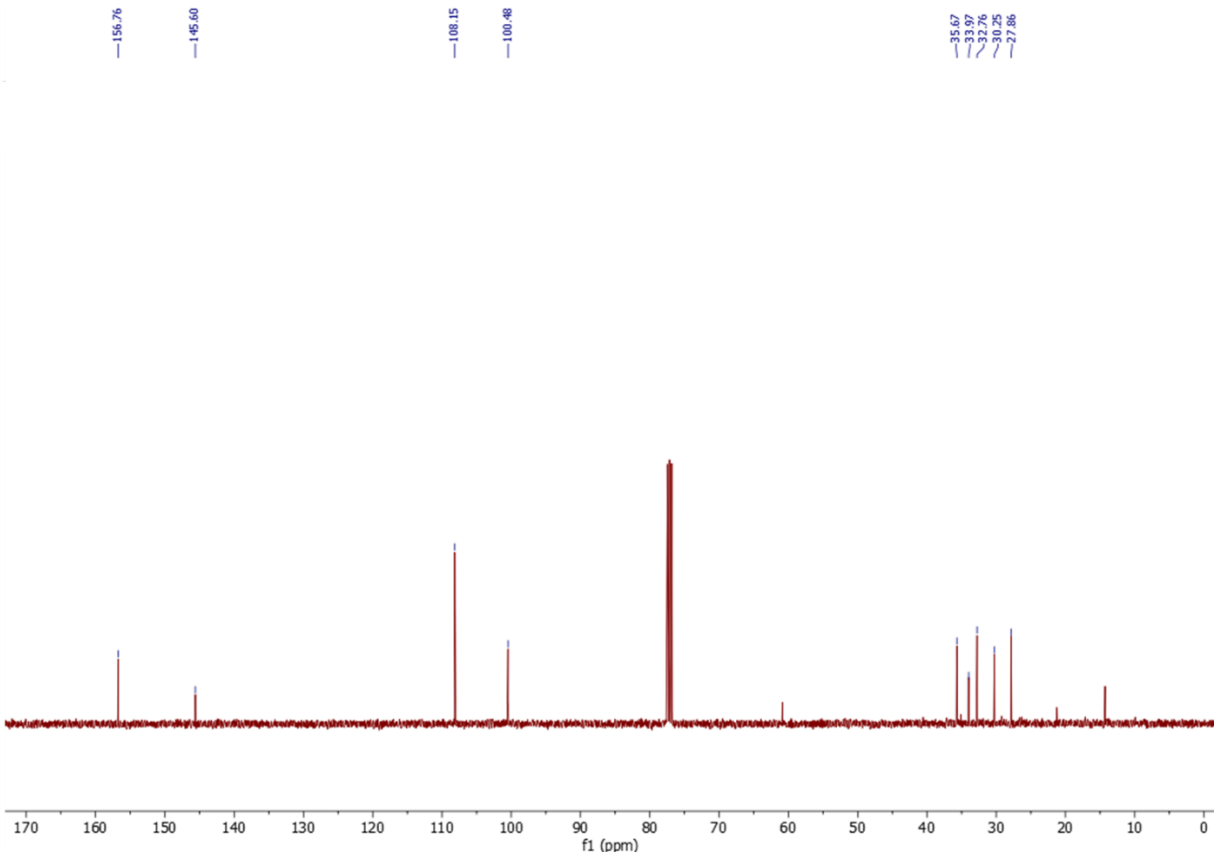

S99. ^{13}C NMR spectrum of compound 39 in $CDCl_3$. Signals at δ 14.19 ppm, 21.04 ppm and 60.49 ppm are due to the presence of ethyl acetate in the sample.

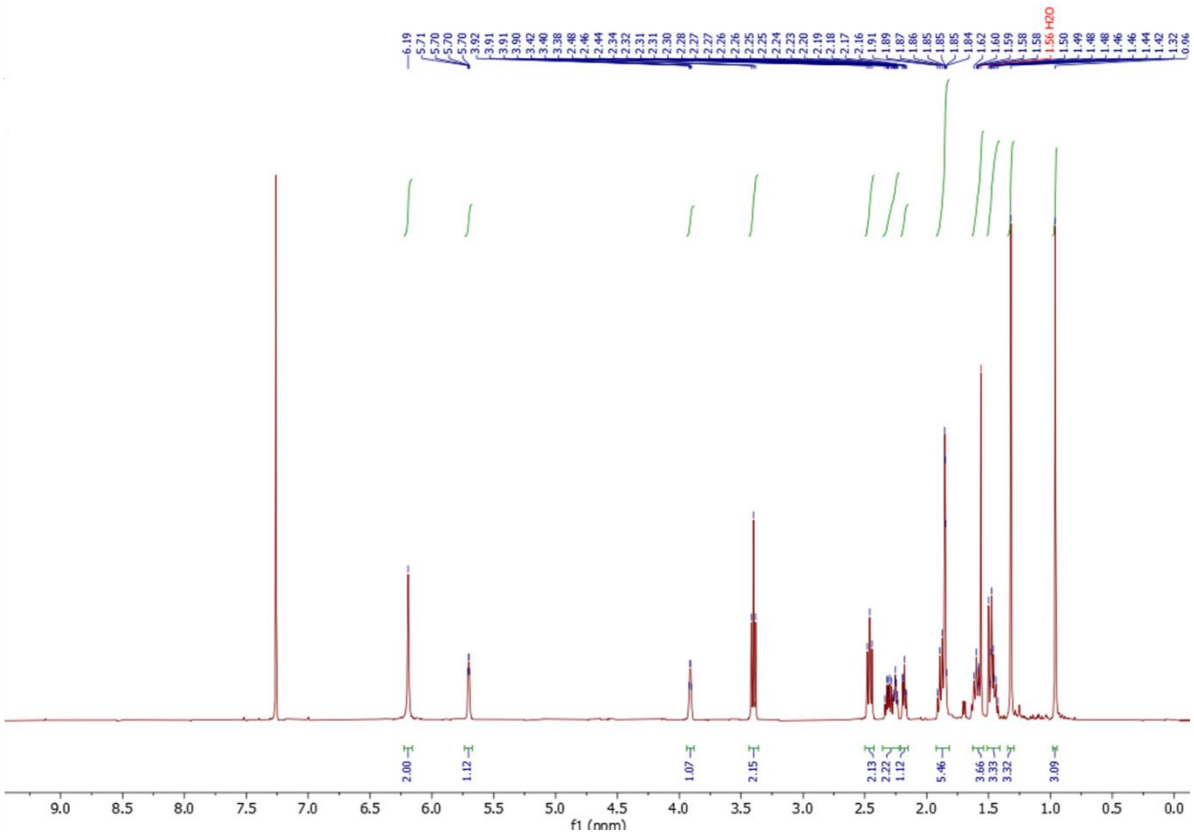

S100. ^{1}H NMR spectrum of compound 40 in $CDCl_3$.

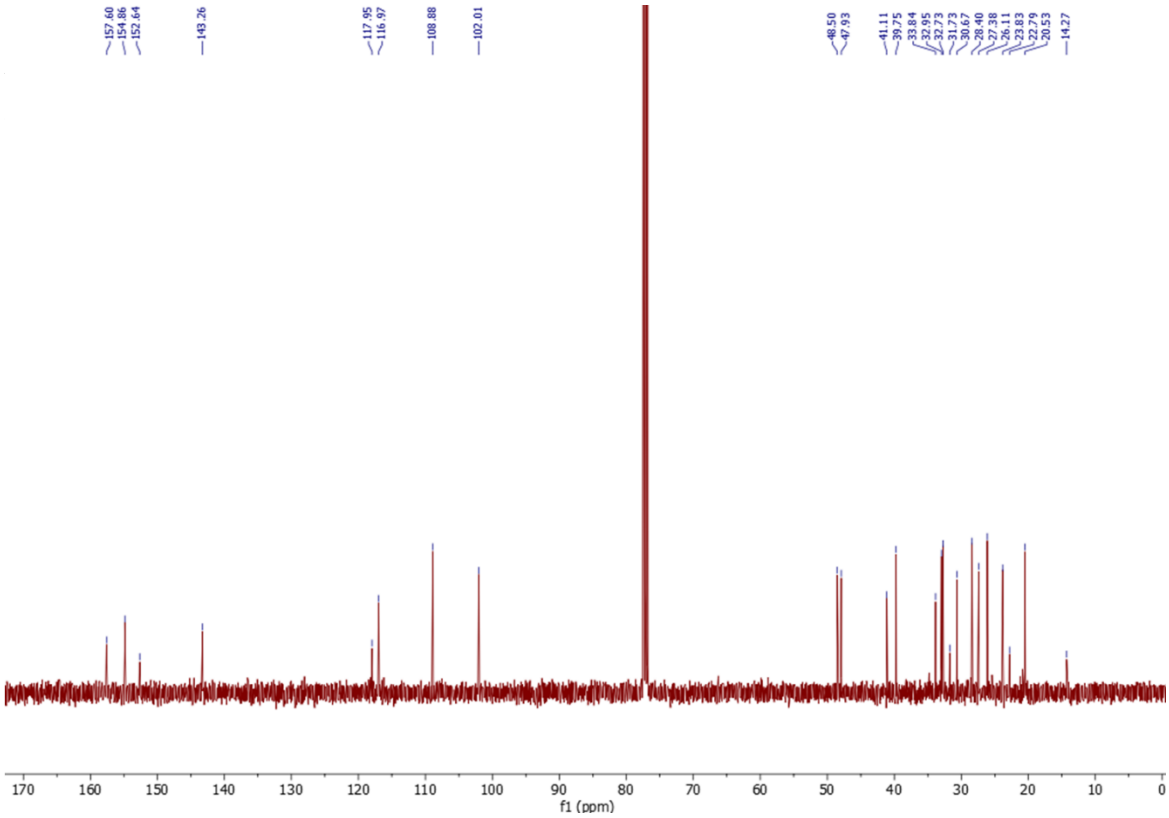

S101. ^{13}C NMR spectrum of compound 41 in $CDCl_3$.

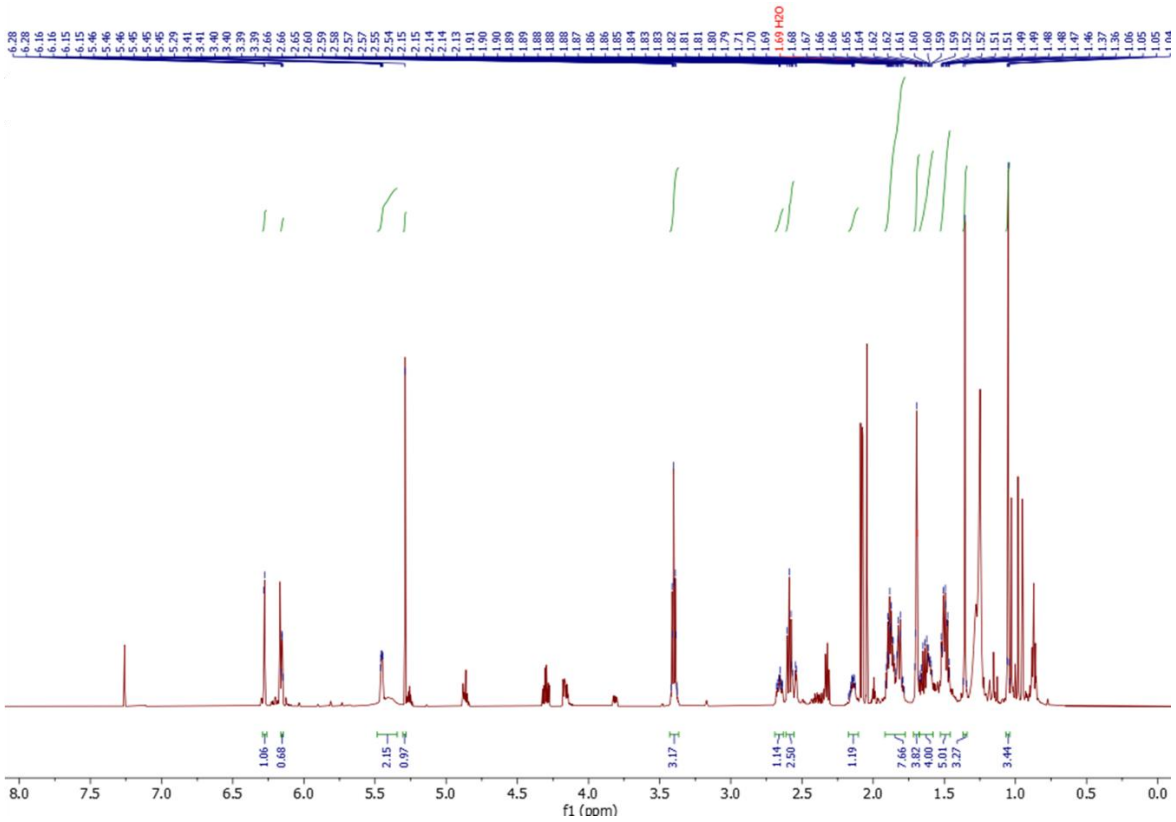

S102. ^{1}H NMR spectrum of compound 41 in $CDCl_3$ obtained after the first purification step using a chromatographic column, as per the published procedure [13]. This spectrum was recorded before HPLC purification. The extra peaks, which are not integrated, correspond to the isoform of the molecule, Δ^9 THC-Br **42**.

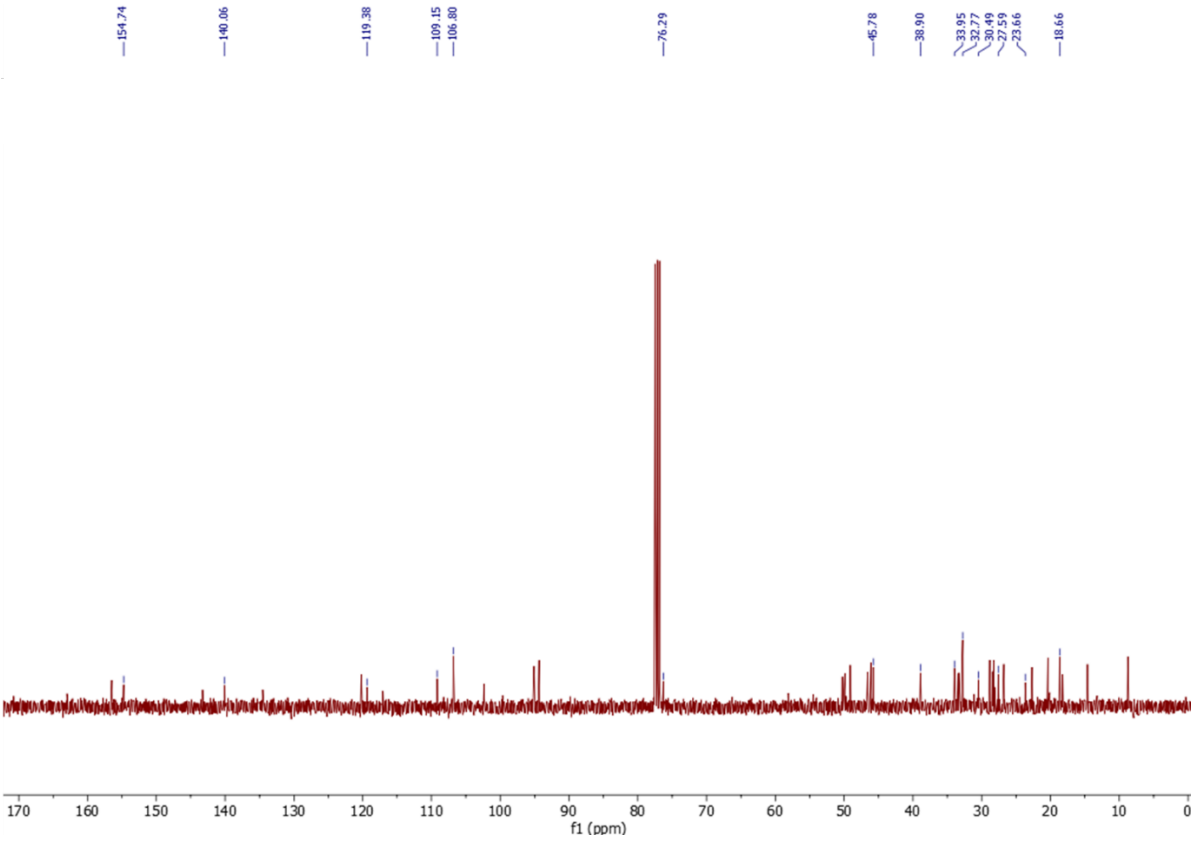

S103. ^{13}C NMR spectrum of compound 41 in $CDCl_3$ obtained after the first purification step using a chromatographic column, as per the published procedure [13]. This spectrum was recorded before HPLC purification. The extra peaks, which are not selected, correspond to the isoform of the molecule, Δ^9 THC-Br **42**.

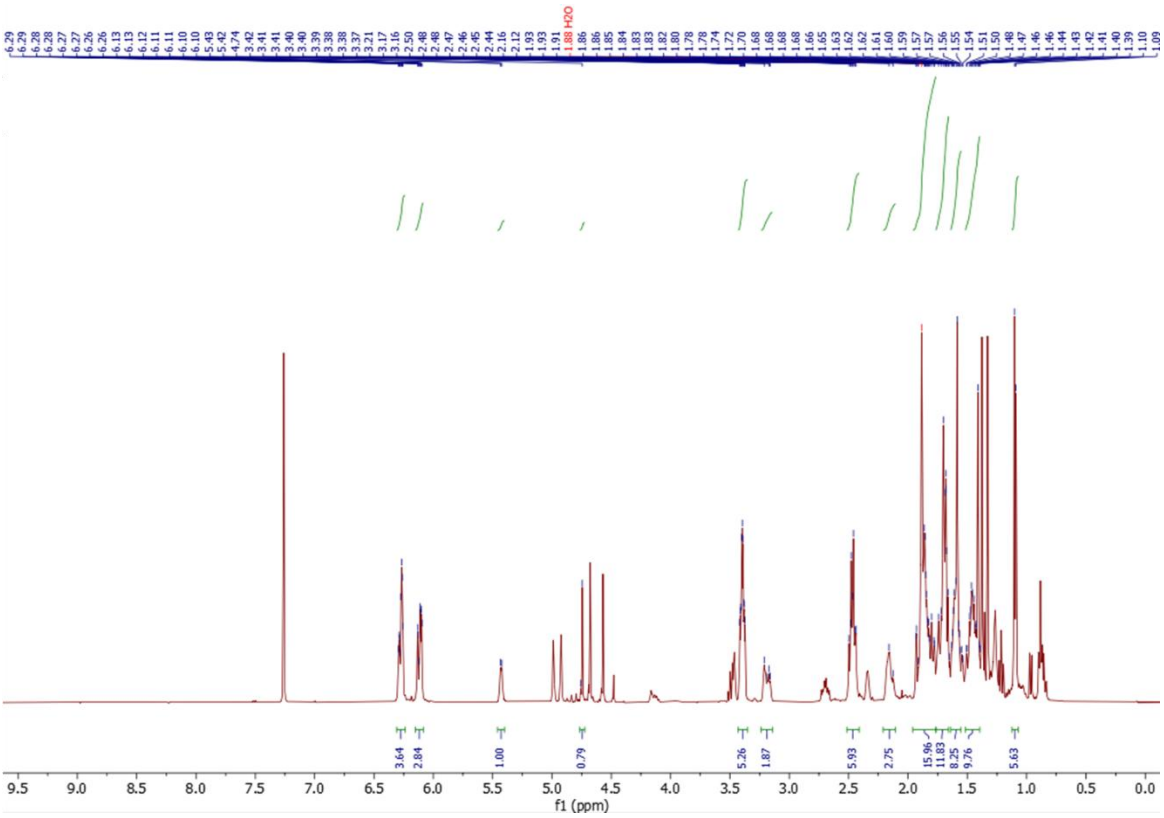

S104. ^{1}H NMR spectrum of compound 42 in $CDCl_3$ obtained after the first purification step using a chromatographic column, as per the published procedure [13]. This spectrum was recorded before HPLC purification. The extra peaks, which are not integrated, correspond to the isoform of the molecule, Δ^8 THC-Br **41**.

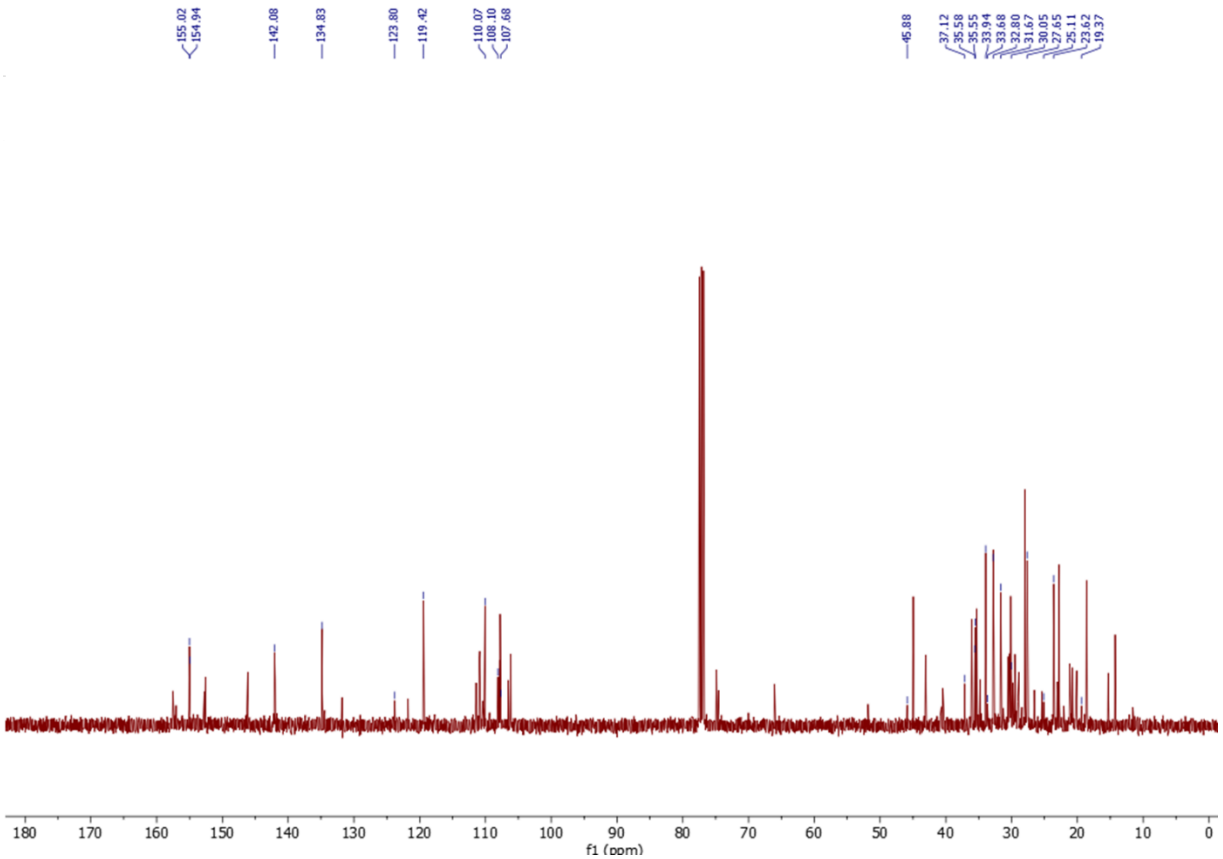

S105. ^{13}C NMR spectrum of compound 42 in $CDCl_3$ obtained after the first purification step using a chromatographic column, as per the published procedure [13]. This spectrum was recorded before HPLC purification. The extra peaks, which are not selected, correspond to the isoform of the molecule, Δ^8 THC-Br **41**.

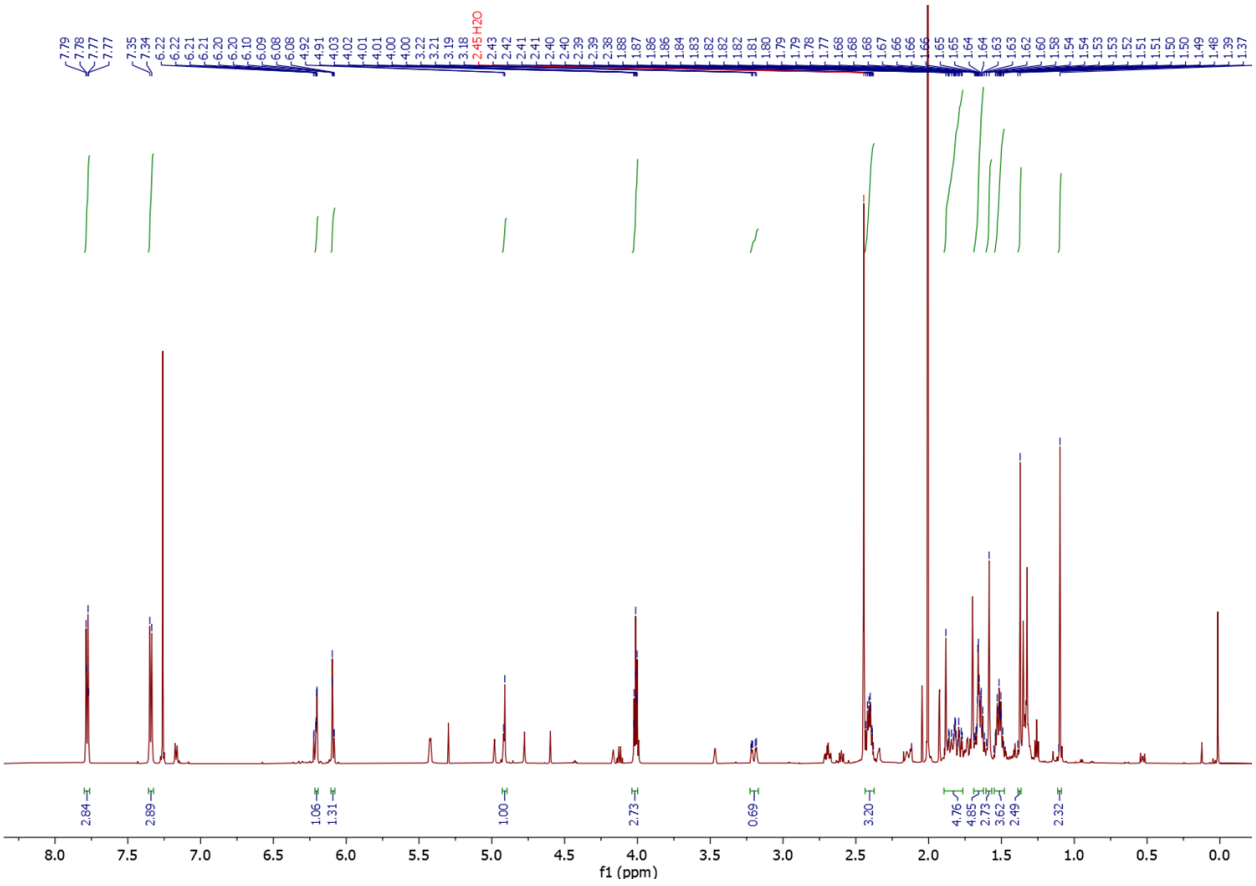

S106. ^{1}H NMR spectrum of compound 43 in $CDCl_3$. The extra peaks, which are not integrated, correspond to the isoform of the molecule, Δ^8 THC-OTs **45**.

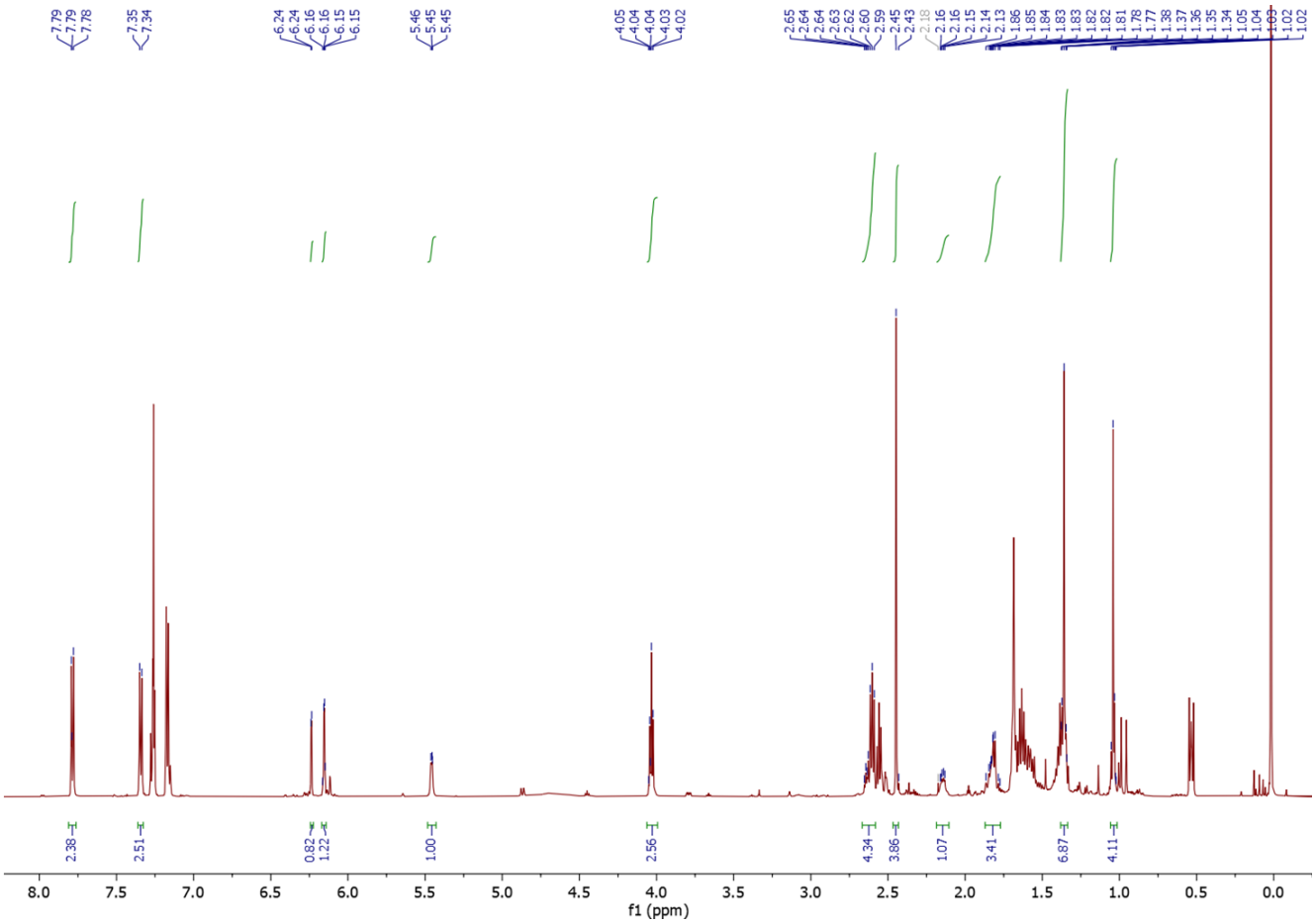

S107. ^{1}H NMR spectrum of compound 45 in $CDCl_3$. The extra peaks, which are not integrated, correspond to the isoform of the molecule, Δ^9 THC-OTs **43**.

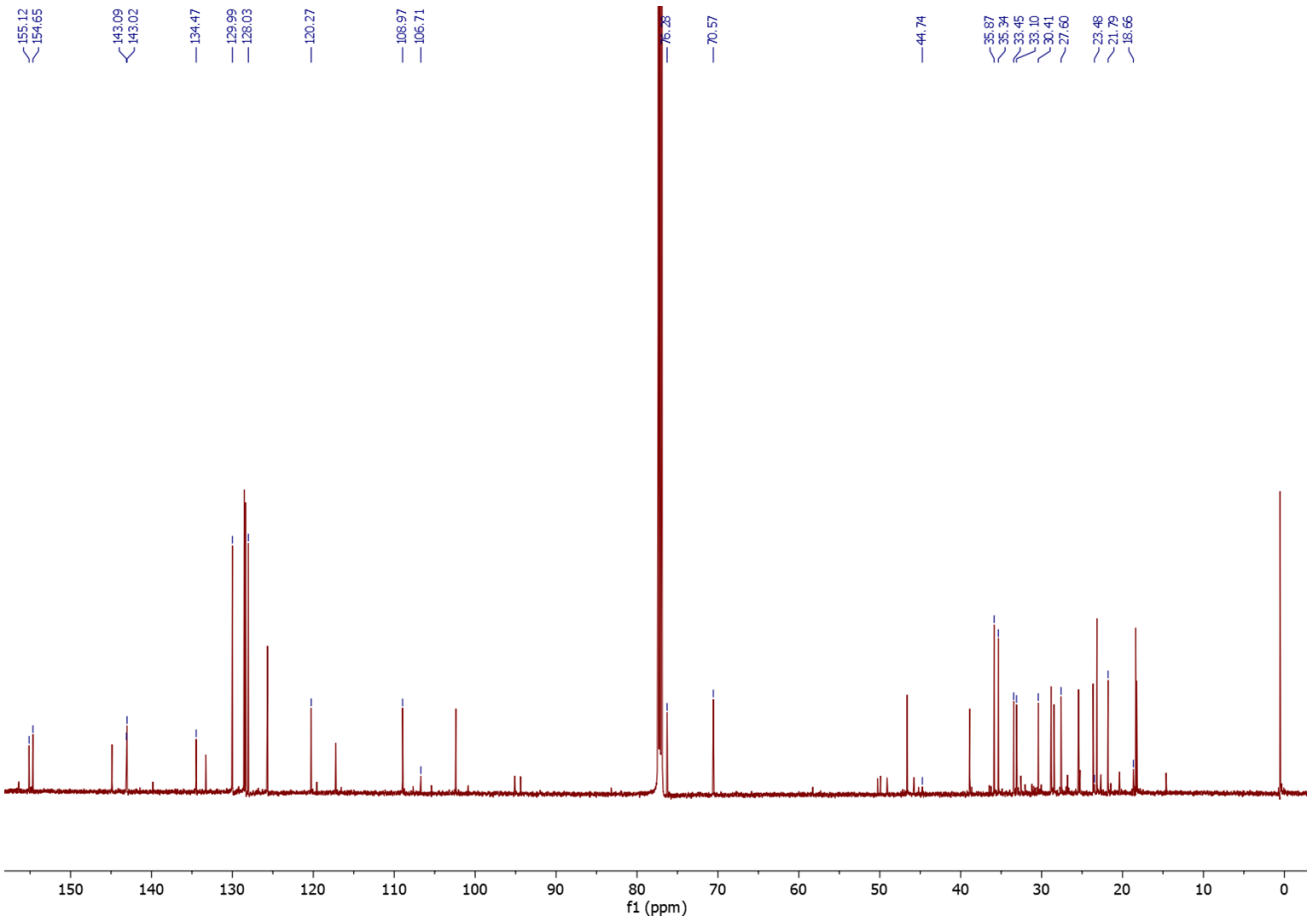

S108. ^{13}C NMR spectrum of compound 45 in $CDCl_3$. The extra peaks, which are not selected, correspond to the isoform of the molecule, Δ^9 THC-OTs **43**.

5.9. Notes and References

(1) Yimer, T. M.; Hoch, E.; Fischer, B.; Dawson, D.; Hall, W. The Adverse Public Health Effects of Non-Medical Cannabis Legalisation in Canada and the USA. *The Lancet Public Health* **2025**, *10* (2), e148–e159.

(2) Pacher, P.; Kogan, N. M.; Mechoulam, R. Beyond THC and Endocannabinoids. *Annu Rev Pharmacol Toxicol* **2020**, *60*, 637–659.

(3) Lu, H.-C.; Mackie, K. Review of the Endocannabinoid System. *Biological Psychiatry: Cognitive Neuroscience and Neuroimaging* **2021**, *6* (6), 607–615.

(4) Bie, B.; Wu, J.; Foss, J. F.; Naguib, M. An Overview of the Cannabinoid Type 2 Receptor System and Its Therapeutic Potential. *Curr Opin Anaesthesiol* **2018**, *31* (4), 407–414.

(5) Kreuz, D. S.; Axelrod, J. Delta-9-Tetrahydrocannabinol: Localization in Body Fat. *Science* **1973**, *179* (4071), 391–393.

(6) Rawitch, A. B.; Rohrer, R.; Vardaris, R. M. Delta-9-Tetrahydrocannabinol Uptake by Adipose Tissue: Preferential Accumulation in Gonadal Fat Organs. *General Pharmacology: The Vascular System* **1979**, *10* (6), 525–529.

(7) Johansson, E.; Norén, K.; Sjövall, J.; Halldin, M. M. Determination of Δ1-Tetrahydrocannabinol in Human Fat Biopsies from Marihuana Users by Gas Chromatography–Mass Spectrometry. *Biomedical Chromatography* **1989**, *3* (1), 35–38.

(8) Gunasekaran, N.; Long, L.; Dawson, B.; Hansen, G.; Richardson, D.; Li, K.; Arnold, J.; McGregor, I. Reintoxication: The Release of Fat-Stored Δ9-Tetrahydrocannabinol (THC) into

Blood Is Enhanced by Food Deprivation or ACTH Exposure. *British Journal of Pharmacology* **2009**, *158* (5), 1330–1337.

(9) Richter, G.; Hazzah, T.; Hartsel, J. A.; Eades, J.; Hickory, B.; Makriyannis, A. Cannabis Sativa: An Overview. *Nutraceuticals*; Academic Press, **2021**; pp 603–624.

(10) Jones, É.; Vlachou, S. A Critical Review of the Role of the Cannabinoid Compounds Δ9-Tetrahydrocannabinol (Δ9-THC) and Cannabidiol (CBD) and Their Combination in Multiple Sclerosis Treatment. *Molecules* **2020**, *25* (21), 4930.

(11) Vemuri, V. K.; Makriyannis, A. Medicinal Chemistry of Cannabinoids. *Clin Pharmacol Ther* **2015**, *97* (6), 553–558.

(12) Ashton, C. H. Pharmacology and Effects of Cannabis: A Brief Review. *The British Journal of Psychiatry* **2001**, *178* (2), 101–106.

(13) Cao, C.; Li, Y.; Liu, H.; Bai, G.; Mayl, J.; Lin, X.; Sutherland, K.; Nabar, N.; Cai, J. The Potential Therapeutic Effects of THC on Alzheimer's Disease. *Journal of Alzheimer's Disease* **2014**, *42* (3), 973–984.

(14) Cooray, R.; Gupta, V.; Suphioglu, C. Current Aspects of the Endocannabinoid System and Targeted THC and CBD Phytocannabinoids as Potential Therapeutics for Parkinson's and Alzheimer's Diseases: A Review. *Mol Neurobiol* **2020**, *57* (11), 4878–4890.

(15) Gorelick, D. A. Cannabis-Related Disorders and Toxic Effects. *New England Journal of Medicine* **2023**, *389* (24), 2267–2275.

(16) Johns, A. Psychiatric Effects of Cannabis. *The British Journal of Psychiatry* **2001**, *178* (2), 116–122.

(17) Longworth, M.; Banister, S. D.; Boyd, R.; Kevin, R. C.; Connor, M.; McGregor, I. S.; Kassiou, M. Pharmacology of Cumyl-Carboxamide Synthetic Cannabinoid New Psychoactive Substances (NPS) CUMYL-BICA, CUMYL-PICA, CUMYL-5F-PICA, CUMYL-5F-PINACA, and Their Analogues. *ACS Chem. Neurosci.* **2017**, *8* (10), 2159–2167.

(18) Varlow, C.; Boileau, I.; Wey, H.-Y.; Liang, S. H.; Vasdev, N. Classics in Neuroimaging: Imaging the Endocannabinoid Pathway with PET. *ACS Chem. Neurosci.* **2020**, *11* (13), 1855–1862.

(19) Hirvonen, J. *In Vivo* Imaging of the Cannabinoid CB1 Receptor with Positron Emission Tomography. *Clinical Pharmacology & Therapeutics* **2015**, *97* (6), 565–567.

(20) Zanato, C.; Pelagalli, A.; Marwick, K. F. M.; Piras, M.; Dall'Angelo, S.; Spinaci, A.; Pertwee, R. G.; Wyllie, D. J. A.; Hardingham, G. E.; Zanda, M. Synthesis, Radio-Synthesis and *in Vitro* Evaluation of Terminally Fluorinated Derivatives of HU-210 and HU-211 as Novel Candidate PET Tracers. *Org. Biomol. Chem.* **2017**, *15* (9), 2086–2096.

(21) Qi, L.; Yamamoto, N.; Meijler, M. M.; Altobell, L. J.; Koob, G. F.; Wirsching, P.; Janda, K. D. Δ9-Tetrahydrocannabinol Immunochemical Studies: Haptens, Monoclonal Antibodies, and a Convenient Synthesis of Radiolabeled Δ9-Tetrahydrocannabinol. *J. Med. Chem.* **2005**, *48* (23), 7389–7399.

(22) Mizuta, S.; Yamaguchi, T.; Ishikawa, T. Nucleophilic Fluorine Substitution Reaction of α-Carbonyl Benzyl Bromide, Phenylthiofluoroalkyl Bromide, and 2-Bromo-2-Phenoxyacetonitrile. *RSC Advances* **2024**, *14* (27), 19062–19066.

(23) Han, H. J.; Lee, S. S.; Kang, S. M.; Kim, Y.; Park, C.; Yoo, S.; Kim, C. H.; Oh, Y. H.; Lee, S.; Kim, D. W. The Effects of Structural Modifications of Bis-tert-alcohol-Functionalized Crown-

Calix[4]Arenes as Nucleophilic Fluorination Promotors and Relations with Computational Predictions. *European Journal of Organic Chem*istry **2020**, *6*, 728-735.

(24) Jadhav, V. H.; Jeong, H. J.; Choi, W.; Kim, D. W. Crown Ether Metal Complex Fluoride Salt as a Facile and Low Hygroscopic Fluoride Source for Nucleophilic Fluorination. *Chemical Engineering Journal* **2015**, *270*, 36–40.

(25) Kim, D. W.; Jeong, H.-J.; Lim, S. T.; Sohn, M.-H. Facile Nucleophilic Fluorination of Primary Alkyl Halides Using Tetrabutylammonium Fluoride in a *Tert*-Alcohol Medium. *Tetrahedron Letters* **2010**, *51* (2), 432–434.

(26) Kim, D. W.; Jeong, H.-J.; Lim, S. T.; Sohn, M.-H. Tetrabutylammonium Tetra(Tert-Butyl Alcohol)-Coordinated Fluoride as a Facile Fluoride Source. *Angewandte Chemie International Edition* **2008**, *47* (44), 8404–8406.

(27) Sun, H.; DiMagno, S. G. TBAF Fluorination for Preparing Alkyl Fluorides. *Fluorination*; Hu, J., Umemoto, T., Eds.; Springer: Singapore, **2020**; pp 605–613.

(28) Emeléus, H. J. The Chemistry of Fluorine and Its Compounds **2013** Elsevier.

(29) Li, Z.; Conti, P. S. Radiopharmaceutical Chemistry for Positron Emission Tomography. *Advanced Drug Delivery Reviews* **2010**, *62* (11), 1031–1051.

(30) Kopka, K.; Faust, A.; Keul, P.; Wagner, S.; Breyholz, H.-J.; Höltke, C.; Schober, O.; Schäfers, M.; Levkau, B. 5-Pyrrolidinylsulfonyl Isatins as a Potential Tool for the Molecular Imaging of Caspases in Apoptosis. *J. Med. Chem.* **2006**, *49* (23), 6704–6715.

(31) Zgair, A.; Wong, J. C. M.; Sabri, A.; Fischer, P. M.; Barrett, D. A.; Constantinescu, C. S.; Gershkovich, P. Development of a Simple and Sensitive HPLC–UV Method for the Simultaneous

Determination of Cannabidiol and Δ9-Tetrahydrocannabinol in Rat Plasma. *Journal of Pharmaceutical and Biomedical Analysis* **2015**, *114*, 145–151.

(32) Pittiglio, M. K.; Ramirez, G. A.; Tesfatsion, T. T.; Ray, K. P.; Cruces, W. HPLC Method for Better Separation of THC Isomers to Ensure Safety and Compliance in the Hemp Market. *ACS Omega* **2024**, *9* (23), 25390–25394.

(33) Nahar, L.; Onder, A.; Sarker, S. D. A Review on the Recent Advances in HPLC, UHPLC and UPLC Analyses of Naturally Occurring Cannabinoids (2010–2019). *Phytochemical Analysis* **2020**, *31* (4), 413–457.

(34) Gul, W.; Gul, S. W.; Radwan, M. M.; Wanas, A. S.; Mehmedic, Z.; Khan, I. I.; Sharaf, M. H. M.; ElSohly, M. A. Determination of 11 Cannabinoids in Biomass and Extracts of Different Varieties of Cannabis Using High-Performance Liquid Chromatography. *Journal of AOAC INTERNATIONAL* **2015**, *98* (6), 1523–1528.

(35) Aizpurua-Olaizola, O.; Omar, J.; Navarro, P.; Olivares, M.; Etxebarria, N.; Usobiaga, A. Identification and Quantification of Cannabinoids in Cannabis Sativa L. Plants by High Performance Liquid Chromatography-Mass Spectrometry. *Anal Bioanal Chem* **2014**, *406* (29), 7549–7560.

(36) Mandrioli, M.; Tura, M.; Scotti, S.; Gallina Toschi, T. Fast Detection of 10 Cannabinoids by RP-HPLC-UV Method in Cannabis Sativa L. *Molecules* **2019**, *24* (11), 2113.

(37) Bassetti, B.; Hone, C. A.; Kappe, C. O. Continuous-Flow Synthesis of Δ9-Tetrahydrocannabinol and Δ8-Tetrahydrocannabinol from Cannabidiol. *J Org Chem* **2023**, *88* (9), 6227–6231.

(38) Dethe, D. H.; Erande, R. D.; Mahapatra, S.; Das, S.; B, V. K. Protecting Group Free Enantiospecific Total Syntheses of Structurally Diverse Natural Products of the Tetrahydrocannabinoid Family. *Chem. Commun.* **2015**, *51* (14), 2871–2873.

Chapter 6: Conclusions and Future Directions

6.1. Chapter 2: Mapping Vitamin B_6 Metabolism by HydrazoCEST Magnetic Resonance Imaging

6.1.1. Conclusions to Chapter 2

In this chapter, we detailed the development and evaluation of a novel contrast agent for chemical exchange saturation transfer magnetic resonance imaging (CEST-MRI). Initially, our laboratory synthesized the first generation contrast agent, *N*-amino anthranilic acid (NA^3), which demonstrated the capability to form hydrazones under physiological conditions and exhibited a high affinity for detecting aldehydes through CEST-MRI, thereby defined as hydrazoCEST agent. Building upon the properties of NA^3, we made structural modifications to develop a second-generation probe, 2-hydrazinonicotinic acid (2-HYNIC). This new probe was tested for its selectivity for aromatic aldehydes using CEST-MRI. The results demonstrated that 2-HYNIC effectively produced a CEST signal from hydrazones derived from aromatic aldehydes. This property was evaluated at various concentrations and across a pH from 6.0 to 12.0, revealing a significant differentiation in the CEST signal between pyridoxal-derived hydrazone (5% at 20 mM) and pyridoxal phosphate-derived hydrazones (28% at 20 mM). *In vivo* testing was conducted using A549 and H460, two human non-small cell lung cancer cell lines. The results showed a higher signal in H460 cells, which was attributed to the higher intracellular PLP levels in H460 cells compared to A459 cells. The formation of hydrazones was confirmed by mass spectrometry and further validated through *in vivo* MRI of heterotopic A459 and H460 tumor xenografts. These

findings highlighted the potential of 2-HYNIC as a selective and effective contrast agent for detecting aromatic aldehydes in biological systems and especially mapping the metabolism of pyridoxal 5'-phosphate, paving the way for further applications in medical imaging and diagnostics.

6.1.2. Future Directions to Chapter 2

Currently, the majority of techniques used for diagnosing and detecting lung cancers are based on fluorodeoxyglucose (FDG) radiotracers. However, the discoveries made with the contrast agent 2-HYNIC, particularly its ability to map the metabolism of vitamin B_6, enable the development of more specific and selective diagnostic tools. The potential of 2-HYNIC to be adapted into a radiotracer for PET-CT imaging could significantly enhance the specificity and selectivity for non-small lung cancer compared to traditional FDG tracers, which may lack specificity. Our laboratory has already taken steps in this direction by developing a 2-HYNIC based [^{11}C] radiotracer designed for PET-CT imaging applications. This innovative radiotracer aims to measure changes in the expression levels of pyridoxal kinase, which can be monitored through PET-CT imaging. This approach allows for the assessment of cisplatin sensitivity during chemotherapy, providing valuables insights into treatment efficacy and resistance mechanisms. The development process involves the synthesis of -11-carbon-based radiotracers analogs of pyridoxine. These analogs are used to evaluate the biochemical and metabolic alterations of the cold standard derivatives through *in vitro* metabolomic analysis, leading to the understanding of the metabolic pathways and interactions within the cancer cells.

The next phase of the project involves transitioning to radiotracer standards, which will enable the testing of vitamin B_6 retention in tumor tissues. This step is essential for determining the association between vitamin B_6 retention and lung cancer resistance to cisplatin, a common chemotherapy drug. By understanding this relationship, we can gain insights into the mechanisms of drug resistance and identify potential targets for overcoming resistance. Once the hot standards is successfully developed, PET-CT imaging will be conducted on mouse models to evaluate the cancer resistance phenotype before and during cisplatin-based chemotherapy. This *in vivo* imaging will provide a comprehensive understanding of its potential for clinical applications.

The ultimate goal of this project is to utilize PET-CT imaging and advanced radiotracer development to quantify and imaging cisplatin-sensitive and resistant lung cancer. By achieving this, we aim to improve patient treatment outcomes by providing more accurate and personalized diagnostic and therapeutic strategies. This approach has the potential to significantly improve the way lung cancer is diagnosed and treated, leading to better patient prognosis and quality of life.

6.2. Chapter 3: Aqueous Click Chemistry for Controlled Synthesis of Homo- and Hetero-Bislanthanide Complexes: Magnetic and Optical Characterization

6.2.1. Conclusions to Chapter 3

In this chapter, the primary aim was to develop a novel methodology for combining two lanthanides, achieving a process that is both faster and simpler than those previously reported in the literature. While existing methods for combining two or more lanthanides employ diverse strategies, our approach is distinct as it is conducted in an aqueous environment through an uncatalyzed reaction that completes in under one hour. The individual synthons were synthesized separately before being subjected to the uncatalyzed click reaction. To validate our synthetic methodology for combining lanthanides in a 1:1 ratio, we successfully synthesized 17 hetero- and homo-bislanthanide complexes, utilizing lanthanides ranging from europium(III) to lutetium(III).

With these complexes in hand, we proceeded to investigate their MRI properties using an *in vitro* phantom, evaluating their T_1 and T_2 weighted images on a 3T MRI instrument, with a focus on gadolinium(III) chelated complexes, including the individual components. Our finding revealed no significant differences between the individual synthons and complexes, as they all demonstrated similar T_1-weighted contrast enhancement with limited T_2-weighted effects. To further explore their properties in a concentration-independent manner, we employed MRF. The results indicated that only Gd(III)-DOTA-CHQ-cysteine-DOTA-Gd(III) complex exhibited relaxivity data significantly different from the other bislanthanide complexes, with values of $r_1 = 15.4\ mM^{-1}s^{-1}$ and $r_2 = 22.2\ mM^{-1}s^{-1}$.

Additionally, we examined the optical properties of our complexes, given that their formation is based on the creation of 4,5-dihydrothiazole ring, which can act as a chromophore and potentially enhance lanthanide-based photoluminescence. Europium(III)-based complexes were synthesized due to europium(III)'s emissive properties and the chromophore's ability to promote fluorescence, depending on the molecular asymmetry of the bislanthanide complex.

6.2.2. Future Directions to Chapter 3

The advancement made in this project provide a foundation for several potential research directions. One possibility involves modifying the type of metal link on the complex to incorporate various metals, such as alkaline earth metals (e.g. calcium, magnesium) or transition metals (e.g. ion, copper, zinc). These metals play significant roles in physiological and biochemical processes, offering potential for developing drug delivery complexes that target specific sites in the body or modulate metal levels. For instance, calcium's role in regulating cellular process could be utilized to provide therapeutic benefits for conditions such as cancer, cardiovascular diseases, and neurological disorders. Another potential direction is the incorporation of actinides, particularly those with alpha-emitting isotopes like actinium-225 and thorium-227. These isotopes could be conjugated to target specific cancer cells, offering a targeted approach for precision oncology. The complexes developed in this project, once paired with the appropriate metal, have potential applications in targeted drug delivery, diagnostic imaging, and therapeutic interventions enhancing treatment efficacy and specificity.

The next phase of this project will focus on adding an extra amino acid to the complex, which could serve as a linker to connect the complex with various biomolecules such as peptides, proteins, antibodies or small molecules. This adaptation will further expand the biological applications of these complexes. The chemistry developed in Chapter 4, involving the generation of a homo-lutetium(III)-based complex and utilizing the properties of the lutetium-177 isotope for targeted glioblastoma therapy, demonstrates the potential of this approach.

6.3. Chapter 4: Second Generation Probe of Homo-Bislanthanide complexes – Potential Application for Glioblastoma Treatment

6.3.1. Conclusions to Chapter 4

In the continuation of the homo-/hetero-bislanthanide chemistry explored in chapter 3, we adapted the synthesis protocols for individual synthons to incorporate an additional amino acid, specifically an azide-modified lysine. This particular amino acid was chosen for its long side chain, which provides a functional group capable of linking to potential biomolecular targets, thereby enhancing the versatility and applicability of the synthesized complexes.

Consistent with the methodologies applied to the previous complexes, these newly developed lutetium(III)-based complexes are designed to leverage the unique properties lutetium(III), and specifically the isotope 177, as a theranostic agent. The synthesis of these complexes relies on the preparation of two distinct synthons: a cyanohydroxyquinoline (CHQ)-DOTA and a lysyl-DOTA moieties. As developed in chapter 3, the complexation process involves the formation of a 4,5-dihydrothiazole ring, which is crucial for the structural integrity and functionality of the final

complex. Initially, a synthesis scheme for the lysyl-DOTA moiety was developed. However, repeated unsuccessful attempts at Fmoc deprotection necessitated a comprehensive redesign of the synthesis pathway. This iterative process was essential to overcome the challenges encountered and to ultimately achieve the desired compound with the requisite purity and yield. With both synthons successfully synthesized, we proceeded to assemble the Lu(III) DOTA-quinoline-lysine-DOTA-Lu(III) complex. This complex shows significant promises for future applications in the therapy of glioblastoma, a particularly aggressive form of brain cancer. The successful synthesis and characterization of this complex mark a substantial advancements in our research, paving the way for potential therapeutic innovations.

6.3.2. Future Directions to Chapter 4

The next phase of this project will focus on functionalizing our Lu(III) DOTA-quinoline-lysine-DOTA-Lu(III) complex with DBCO-maleimide D-VAP and RI-VAP conjugates for targeted glioblastoma therapy. Initially, the synthesis of the homo-bislanthanide complex was completed to evaluate whether an azide-modified lysine interferes with the uncatalyzed click reaction necessary for forming the 4,5-dihydrothiazoline ring. Concurrently, the synthesis and purification of peptides that specifically bind to GRP78, a biomarker for glioblastoma, will be undertaken. Following this, the next step will involve combining the homo-bislanthanide complex with DBCO-maleimide peptide conjugates trough strain-promoted azide-alkyne cycloaddition (SPAAC) chemistry. With the new complex prepared and functionalized, we plan to test its efficacy in U87MG glioblastoma cell lines. The primary objective moving forward is to evaluate

the specificity and selectivity of ^{177}Lu as a theranostic agent for glioblastoma. Upon validation with the cold standard, we will transition to hot chemistry to produce our ^{177}Lu complex with testing in cell lines and potentially in mouse models with tumor xenografts, to assess *in vivo* efficacy and safety of our theranostic agent.

Given the potential of our complex to target glioblastoma cell lines and the therapeutic capabilities of ^{177}Lu as targeted radionuclide therapy agent, there is a promising opportunity to combine this approach with actinium-225. ^{225}Ac, a radioactive isotope used in nuclear medicine for targeted alpha therapy, could deliver highly localized radiation doses directly to tumors. To leverage the properties of ^{225}Ac, we plan to create complexes with a macropa-isothiocyanate chelator, facilitating the chelation of ^{225}Ac and enabling the generation of radiotracers for potential application in U87MG glioblastoma cell lines. Different complexes will be generated with ^{225}Ac on both side of the complex or even a combination of the two radionuclides in the same complex to see if there will be an impact on glioblastoma therapy by comparing the efficacy of an alpha and beta emitters between probes and on the same probe.

An alternative approach within this project involves incorporating gadolinium(III) on the lysyl-DOTA side and switching the lanthanides on the CHQ moiety of the complex. By utilizing the side chain of the lysyl-DOTA component, different particles sizes will be added to the complex, including a variant without any particles, through the complexation of amino polystyrene particles with DBCO acid and SPAAC chemistry. This approach aims to determine if MRF imaging can be used to distinguish the same contrast agent binding to different-sized targets. Additionally, we seek to investigate whether the use of MRF and varying of particle sizes affects the tumbling rate of the complexes, as a slower tumbling rate enhances relaxivity values, and thereby improving image contrast.

These strategic steps outline the future directions for advancing our targeted therapy for glioblastoma, setting the stage for subsequent experimental validations and potential therapeutic applications. By systematically addressing each of these steps, we aim to develop a highly effective and specific theranostic agent for glioblastoma, ultimately improving patient outcomes.

6.4. Chapter 5: Synthesis of a Novel Cannabinoid Radiotracer with an Application across PET-CT Imaging

6.4.1. Conclusions to Chapter 5

In this chapter, the primary objective of this project was to develop radiofluorinated THC-based probes for both Δ^8 and Δ^9 isomers. This involved the strategic addition of a proton bioisostere, a radioactive fluorine, at the terminus of the cannabinoid aliphatic chain. The main aim was to enable application in PET-CT imaging, leading to the visualization of the biodistribution of CB_1 and CB_2 receptors. Additionally, we attempted to investigate whether receptor engagement is influenced by physiological factors such as age, sex and body mass index. In the synthesis of our radiotracers, the first challenge was the separation of the brominated form from the fluorinated one. To address this, we incorporated an additional synthetic step, informed by the HPLC traces obtained and the close retention times between the two halogens. This step involved the formation of tosylated intermediates from the brominated precursors before generating the final fluorinated product for both Δ^8 and Δ^9 isomers.

During the purification process through HPLC and analysis of their characterized NMR spectra, we faced the presence of multiple signals that led us to realize the presence of a disordered

aliphatic region in both Δ^8 and Δ^9 fluorinated THC isomers. Initially, we believed we had successfully produced the final fluorinated THC-based probes, but additional analysis showed that was not the case. Ono of the precursor synthesis, the brominated THC, was based on a publish procedure (*J. Med. Chem*. **2005**, 48:7389-7399). A closer examination of the NMR spectra revealed a mixture of the two isomers in both Δ^8 and Δ^9 THC-Br isomers precursors due to the presence of multiple peaks in the aliphatic area. To overcome these challenges, we implemented multiple purification steps, with HPLC and automated flash column chromatography system, in the synthesis process. These steps were designed to separate the two isomers from each other and include the optimization of HPLC methods using various gradient systems and different solvent mixtures. This meticulous approach was essential to ensure the purity and efficacy of the final product.

6.4.2. Future Directions to Chapter 5

Despite adapting a published procedure to obtain the desired final product, a fluorinated THC-based probe for both Δ^8 and Δ^9 isomers, significant challenges were encountered during the purification process to separate the two isomers from each other. To overcome these difficulties and still achieve the project's objective of testing receptor engagement and the biodistribution of endocannabinoid receptors, it was decided to redesign the synthesis scheme. To avoid the isomerization problem between Δ^8 and Δ^9-THC, the two compounds will be synthesized separately through two distinct synthesis pathways. The synthesis of Δ^9-THC will begin with a Friedel-Crafts reaction between the chiral terpenoid *p*-Mentha-2,8-dien-1-ol and phloroglucinol. The hydroxy

group at the para position will need to be protected to facilitate the later addition of the aliphatic chain of THC. Consequently, the next step of the synthesis will involve a reaction with a regioselective triflate before the addition of the aliphatic chain through a Negishi coupling reaction with 5-bromopenta-1-ol, leading to the tosylated form of Δ^9-THC before any further fluorination reaction.

This new synthesis scheme for cold standards will be rigorously tested and optimized to obtain the best yield and fully characterized before being used in mouse models. The biodistribution of these probes will then be tracked using PET-CT imaging, providing valuable insights into the receptor engagement and biodistribution of endocannabinoid receptors. This approach aims to contribute to enhance our understanding of endocannabinoid receptors dynamics.

6.5. Overall Conclusion

In conclusion, the advancements in imaging modalities, driven by the design of multiple probes, show great potential for the future of medical imaging. This thesis illustrates the design and synthesis of multiple imaging probes with current or potentials applications in the multidisciplinary imaging field. While some of these probes have been successfully applied in disease models, others still require further development to be effectively utilized in biological models. Design and optimization of probes tailored for specific imaging modalities have opened new avenues for enhancing the sensitivity, specificity and resolution of imaging techniques. The synthesis and characterization of probes, coupled with their application in biological systems for some of them, demonstrate the translational potential of these imaging modalities. Whether through the use of fluorinated probes for PET-CT imaging, contrast agent for MRI or CEST-MRI, or targeted probes for optical imaging, each modality could offer unique insights into the structural and functional aspects of biological systems. The integration of these probes into imaging protocols has the potential to advance our understanding of disease mechanisms, facilitate early detection, and guide targeted interventions.